Exploring the Role of σ* Driven Photochemistry in Heteroaromatic Molecules

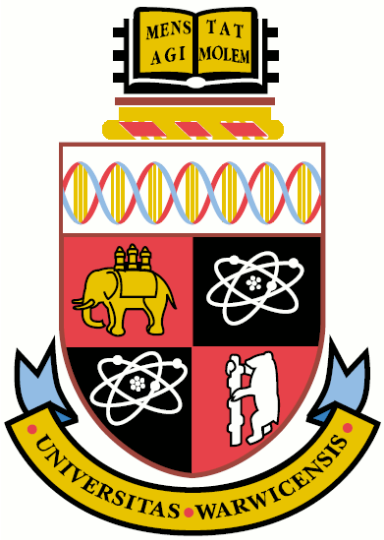

David John Hadden

Submitted for the Qualification of Doctor of Philosophy

University of Warwick

Department of Chemistry

January 2013

Contents

Contents 2
Lift of Figures 5
List of Tables 18
Acknowledgements 20
Declaration 22
Abstract 24
List of Abbreviations 25
1. Introduction 29
1.1 Molecular Dynamics 31
1.1.1 The Dynamics of Photophysical Processes 31
1.1.2 Femtochemistry and the Nobel Prize 35
1.2 Potential Energy Surfaces 38
1.2.1 The Born-Oppenheimer Approximation 39
1.2.2 Wavepackets 43
1.2.3 Electronic State Degeneracy and Non-Adiabatic Dynamics 46
1.3 Spectroscopic Techniques 51
1.3.1 Multiphoton Ionisation and Resonance Enhanced Multiphoton Ionisation 52
1.3.2 Photoproduct Kinetic Energy Detection 55
1.3.3 Velocity Map Imaging 59
1.4 Photochemical Processes in Biomolecule Sub-Units 60
1.4.1 Photodamage and Photostability 61
1.4.2 Studying $^{1}\pi\sigma^{*}$ States 71
1.5 Outlook of Thesis 76
1.6 References 79
2. Experimental 91
2.1 Laser Systems 92
2.1.1 The Femtosecond Laser 92
2.1.2 Non-Linear Optical Effects and Frequency Up-Conversion 95
2.1.3 Pump Probe Setup 99
2.1.4 Alignment and Focusing 101
2.2 Vacuum Chamber Setup 103
2.2.1 Molecular Beams 104

2.2.2 Velocity Map Imaging 108
2.3 Ultraviolet Absorption Spectrum 120
2.4 Calibration 120
2.4.1 Time of Flight Calibration 120
2.4.2 Velocity Map Imaging Calibration 122
2.4.3 Laser Cross Correlations and Time Zero 125
2.4 References 128
3. The Dynamics of Hydrogen Elimination in Imidazole and Methylated Imidazole Derivatives 130
3.1 Introduction to Imidazole Photodynamics 131
3.1.1 Previous Studies on Imidazole 131
3.1.2 Electronic Structure of Imidazole and its Derivatives 134
3.1.3 Aims and Procedure 136
3.2 Experimental Results and Discussion 137
3.2.1 Total Kinetic Energy Release Spectra 137
3.2.2 Hydrogen Transients 141
3.2.3 Anisotropy Parameters 145
3.2.4 The Effects of Ring Methylation 147
3.2.5 1-Methylimidazole Results 149
3.3 Conclusions 150
3.4 References 152
4. Time Resolved Velocity Map Imaging Studies of CH_3 Elimination from Photoexcited Anisole 154
4.1 Introduction to Anisole Studies 155
4.1.1 Aims and Procedure 156
4.2 Anisole Studies Results 158
4.2.1 Total Kinetic Energy Release Spectrum 158
4.2.2 High TKER Methyl Transients 161
4.2.3 Low TKER Methyl Transients 164
4.2.4 Evidence of Statistical Unimolecular Decay? 166
4.3 Conclusions 166
4.4 References 168
5. Exploring Quantum Phenomena in the σ* mediated Photochemistry of Thioanisole 170
5.1 Introduction to Thioanisole Studies 171
5.1.1 Previous Studies of Thioanisole 171
5.1.2 Aims and Procedure 174

5.2 Results of Thioanisole Studies 176
5.2.1 Comparison of fs TR-VMI and ns VMI results at the $^1\pi\pi^* \leftarrow {}^1\pi\pi$ Origin 176
5.2.2 Results at the "Dynamic Resonance" Transition Wavelength: 283.9 nm 180
5.2.3 CH_3 Elimination at 286.3, 279 and 275 nm 182
5.2.4 CH_3^+ Transients 183
5.2.5 Low TKER CH_3 signal 186
5.3 Conclusions 187
5.4 References 189
6. Competing $^1\pi\sigma^*$ mediated Dynamics in Mequinol 192
6.1 Introduction to Mequinol Studies 193
6.1.1 The Electronic Structure of Mequinol 194
6.1.2 Aims and Procedure 198
6.2 Results of Mequinol Studies 200
6.2.1 Hydrogen Elimination upon Excitation at λ = 280 – 298 nm 200
6.2.2 Hydrogen Elimination upon Excitation at λ = 254 and 264 nm 205
6.2.3 Hydrogen Elimination upon Excitation at λ = 200 – 245 nm 206
6.2.4 CH_3 Elimination 211
6.2.5 Low TKER Hydrogen and CH_3 Elimination 217
6.3 Conclusions 218
6.4 References 220
7. Concluding Remarks 223
7.1 Summary of Thesis 223
7.2 Outlook 227
7.3 References 229
Appendix I 231
Total Kinetic Energy Release Fitting Functions 231
Transient Signal Fitting Functions 232

Lift of Figures

Figure 1.1 – The structures of the molecules studied in this thesis, highlighting the specific nuclear coordinate(s) of interest. a) The dissociation of the N-H bond in imidazole serves as a model for the N_9-H coordinate in adenine. b) The structures of the anisole, thioanisole and mequinol, and how they relate to tyrosine and phenol. **30**

Figure 1.2 – A Jablonski diagram, summarising the possible photophysical processes for a molecule between the first three singlet states (S_0, S_1 and S_2) and the lowest triplet state (T_1). The photophysical processes shown are: absorption (blue), fluorescence (Dark Green), phosphorescence (Light Green), internal conversion (Brown), intersystem crossing (Red) and intramolecular vibrational energy redistribution (Orange). **31**

Figure 1.3 – Schematic representation of the ground (black - ionic) and first (red - covalent) excited electronic potential energy surfaces of NaI. Black dashed lines represent the presence of an adiabatic avoided crossing between the two potentials. Also shown is a pair of laser pulses represented by λ_{pump} and λ_{probe}, providing photoexcitation and inducing fluorescence ($h\nu$) respectively. Blue dashed line represents the path of a wavepacket trapped in the bound adiabatic potential. Inset is a representation of the step-wise rise in the laser induced fluorescence signal ($h\nu$) intensity as a function of pump probe delay. **37**

Figure 1.4 – PEC along a nuclear coordinate in a molecule with a vibronic transition shown between an initial and final electronic state. The favourable

overlap of the $\Psi'_{v=0}$ and $\Psi''_{v=4}$ wavefunctions leads to the largest Franck-Condon factor for this transition. **42**

Figure 1.5 – Wavepacket generation and evolution from a shaped (g(*E*)) pulse excitation from an initial electronic state to a range of vibrational eigenstates in the final electronic state, ΔE is the average spacing of vibrational levels over the range of the laser pulse for: a) a set of evenly distributed harmonic vibrational eigenstates which will evolve at an even rate; and b) a set of anharmonic vibrational eigenstates which evolve unevenly causing wavepacket dispersion. **45**

Figure 1.6 – An avoided crossing between two diabatic electronic states (grey dotted lines) as a function of nuclear displacement (*R*) in a diatomic. The black lines represent the adiabatic states. **47**

Figure 1.7 – A conical intersection between two electronic states as a function of *x* (the gradient difference) and *y* (the derivative coupling). **50**

Figure 1.8 – Multiphoton processes showing: a) two-photon absorption from an initial state (Ψ'') to a final state (Ψ') via a virtual state (Ψ_n), b) (1+1) multiphoton ionisation from an initial state (Ψ'') to an ionic state (Ψ^+) via a virtual state (Ψ_n) and c) (2+1) resonance enhanced multiphoton ionisation where two-photon absorption occurs from an initial state (Ψ'') to a resonant state (Ψ') via a virtual state (Ψ_n) before excitation to the ionic state (Ψ^+) **53**

Figure 1.9 – The structure of the four DNA bases and an example of a DNA base stack dinucleotide, base paired nucleotides, single oligonucleotide strand and double oligonucleotide strand. This figure is modified from reference [3]. **62**

Figure 1.10 – a) Cytosine-guanine hydrogen bonded base pair; b) schematic PECs along an N-H coordinate in hydrogen bonded guanine, showing the mechanism for ground state repopulation by accessing a charge transfer (CT) state upon N-H elongation. The schematic PECs are based upon those calculated and discussed in reference [98]. **65**

Figure 1.11 – Schematic PECs of the ground ($^1\pi\pi$) and first two singlet excited ($^1\pi\pi^*$ and $^1\pi\sigma^*$) electronic states in phenol with respect to O-H nuclear separation. Also labelled are the two relevant CIs and the radical photodissociation products. The schematic PECs are based on those calculated by Dixon *et al*. [8] **71**

Figure 1.12 – Schematic PEC depicting tunnelling (green arrow) between the first $^1\pi\pi^*$ and $^1\pi\sigma^*$ state along the O-H coordinate in phenol at the zero point energy of the O-H stretch, leading to photodissociation of a hydrogen atom. The PECs shown are based upon those used to model tunnelling dynamics in phenol by Dixon *et al*. [8] **75**

Figure 2.1 – Schematic of laser action in a Ti^{3+} ion within an Al_2O_3 lattice. Photon emission between ^2E and $^2T_2$ occurs over a wide range of wavelengths ($h\nu_o$) centred at 800 nm with a Gaussian distribution g(*E*). See text for details. **93**

Figure 2.2 – Spectrum of the output from the Spitfire XP regenerative amplifier. The feature is Gaussian in shape centred at 795 nm with a FWHM of ~30 nm **94**

Figure 2.3 – Schematic of the laser table layout for a) pumping at 200 nm and probing with the output of a TOPAS-C; b) pumping and probing with a pair of TOPAS-C. **94**

Figure 2.4 – Representation of the two non-linear processes used to generate pump and probe pulses; a) shows sum frequency generation (or second harmonic generation when $\omega_1 = \omega_2$) and b) shows optical parametric generation where the signal (ω_2) is amplified by a pump (ω_1) producing idler (ω_3) as a by-product. **96**

Figure 2.5 – The REMPI transitions employed in this thesis to selectively ionise a) hydrogen and b) methyl radicals. **101**

Figure 2.6 – Schematic of the vacuum chamber setup. The chamber to the left is the source chamber containing the pulsed solenoid valve; the chamber to the right is the interactions chamber containing the electrostatic lens setup and VMI detector. **104**

Figure 2.7 – Schematic of the pulsed solenoid valve, representation of the region of supersonic beam created and how skimming the centre of the distribution yields a molecular beam "packet" with high translational energy (E_{trans}) and a low internal energy (E_{int}). **105**

Figure 2.8 – Schematic of the velocity map imaging setup including the electrostatic lens electrodes (left); the field free flight path and deflector (middle); and the detector consisting of two MCPs, P-43 screen and CCD array. The laser pulses ($h\nu$) have an electric field polarised in the Z-axis. Projection of the ions is vertically in the laboratory frame (Y-axis). **109**

Figure 2.9 – Simulated ion trajectories for ions in an electrostatic lens field (shown as equipotential lines) with the same kinetic energy ejected at three different angles relative to the direction of flight. b-d) show zoomed-in sections of the trajectories. Reprinted with permission from reference [8]. **111**

Figure 2.10 – Velocity mapping of a 3D Newton sphere distribution of charged particles with velocity (v), which can be described in polar coordinate as the function $F(r,\theta,\phi)$. The distribution is required to be cylindrically symmetric around the Cartesian Z-axis. This distribution is then projected along the Y-axis and mapped as a 2D distribution in terms of a radius (R) and an angle (α) from the Cartesian Z-axis. **112**

Figure 2.11 – Schematic of the steps involved in image deconvolution. From a 2D image, an effective slice at $\phi = 0$ is taken and the 3D distribution determined. This is then converted to a 1D radial spectrum by integration over all angles. **113**

Figure 2.12 – A schematic of the 2D VMI images resulting from the photodissociation of a diatomic molecule whose transition dipole moment (TDM) is aligned a) parallel and b) perpendicular to the dissociating bond. The VMI images are representations of the image before deconvolution, in terms of α; but correspond to a 3D distribution where the maximum signal is located at a) $\theta = 0°$ and b) $\theta = 90°$. **115**

Figure 2.13 – Schematic representation of the various processes triggered by the a) 125 Hz laser TTL output pulses. These processes are b) the solenoid valve opening delayed by t_1; c) the voltage applied to MCP2 (gating the MCP gain) delayed by t_2 and d) the voltage on the deflector plates delayed by t_3. Included are representative times for the time of laser-molecule interaction (t_i) and the arrival time of a low mass (t_{lm}) and high mass ion (t_{hm}) at the detector. **119**

Figure 2.14 – The conversion of a a time of flight spectrum a) to one based on mass to charge b). The four peaks correspond to ^{129}Xe, ^{130}Xe, ^{131}Xe and ^{132}Xe ions. Calibration of mass to charge is based on the ^{132}Xe peak as a reference. **121**

Figure 2.15 – VMI calibration for hydrogen dissociation from hydrogen bromide: a) a spectrum in terms of *r*, showing four peaks corresponding to two different bromine dissociation channels at two dissociation wavelengths; b) a plot of the assigned H-KER for each feature against pixel radius squared (r^2); c) total kinetic energy release spectrum (TKER) for the same hydrogen bromide spectrum, including the resolution of the largest kinetic energy peak (7%)..... **122**

Figure 2.16 – VMI calibration for methyl dissociation from methyl iodide: a) a spectrum in terms of *r*, showing two peaks corresponding to two different iodine dissociation channels; b) a plot of the assigned CH_3-KER for each feature against pixel radius squared (r^2); c) TKER for the same methyl iodide spectrum..... **124**

Figure 2.17 – Cross correlations taken with a 200 nm pump and 243.1 nm probe in a) ethanol, b) methanol and c) ammonia..... **125**

Figure 2.18 – Cross correlations taken with a 256 nm pump and 243.1 nm probe in a) ^{131}xenon, b) ethanol and c) methanol..... **127**

Figure 3.1 – The molecular structures of a) imidazole; b) 2-methylimidazole; c) 4-methylimidazole; d) 2,4-dimethylimidazole and e) 1-methylimidazole..... **130**

Figure 3.2 – Schematic PEC along the N-H coordinate in imidazole, showing the ground ($^1\pi\pi$) state and the first two excited states ($^1\pi\sigma^*$ and $^1\pi\pi^*$). Also shown is the proposed N-H dissociation mechanism. The PECs are based upon those calculated by King *et al.*[5]..... **134**

Figure 3.3 – Vapour phase UV absorption spectra of a) imidazole; b) 2-methylimidazole; c) 4-methylimidazole; d) 2,4-dimethylimidazole; and e) 1-methylimidazole..... **135**

Figure 3.4 – Raw images for H^+ and corresponding TKER spectra following excitation at 200 nm and probing with 243.1 nm for a) imidazole, b) 2-MI, c) 4-MI and d) 2,4-DMI. The pump probe delay was set to +2 ps. The corresponding fits to the TKER spectra include a Boltzmann function (red) and a Gaussian distribution (blue). Also shown below each TKER spectrum is the associated β_2 anisotropy parameter as a function of TKER. The polarization of the pump laser relative to the image is shown by the double-headed arrow (**ε**)..... **139**

Figure 3.5 – H^+ transients as a function of pump (200 nm) probe (243.1 nm) delay for high and low TKER components, a) and b), respectively, in imidazole. Experimental data is fit with an exponential rise function convolved to the IRF (solid black line) giving time constants τ for the high (τ_H) and low (τ_L) TKER components of a) $\tau_H = 78 \pm 37$ fs and b) $\tau_L = 163 \pm 50$ fs, respectively. Error bars correspond to a 95% confidence limit..... **142**

Figure 3.6 – H^+ transients as a function of pump (200 nm) probe (243.1 nm) delay for high and low TKER components for a) and b) 2-MI; c) and d) 4-MI; e) and f) 2,4-DMI. Experimental data is fit with an exponential rise function convolved to the IRF (solid black line) giving time constants τ which are provided in table 3.2. Error bars correspond to a 95% confidence limit..... **145**

Figure 3.7 – a) Raw H^+ image and corresponding TKER spectrum for hydrogen elimination from 1-MI taken with a 200 nm pump and 243.1 nm probe at a pump probe delay of +2 ps. The polarization of the pump laser relative to the image is shown by the double-headed arrow (**ε**).The corresponding fit to the TKER spectrum is a Boltzmann function (red). b) H^+ transient of hydrogen eliminated from 1-MI at all TKER fit with an exponential rise function convolved to the IRF

(solid black line) giving a time constant $\tau < 50$ fs. Error bars correspond to a 95% confidence limit..... **149**

Figure 4.1 – a) Mass spectrum of anisole taken with a 200 nm pump and a 333.4 nm probe at a pump probe delay of 1.5 ps. The spectrum is not continuous across the axis break, the lower m/z signal was collected at higher detector voltages (V_{mcp1} and V_{mcp2}) b) Gas phase UV absorption spectrum of anisole. **157**

Figure 4.2 – a) Molecular structure of anisole. Velocity map images of CH_3^+ taken with a pump and probe of 200 and 333.4 nm, respectively, taken at a pump probe delay of b) + 1.5 ps and c) – 1.5 ps. **159**

Figure 4.3 – Total kinetic energy release spectra for anisole taken with a 200 nm pump and a 333.4 nm (solid line) or 322.5 nm (dashed line) probe at a pump probe delay of + 1.5 ps. The highlighted area shows the neutral CH_3 from 200 nm induced dissociation attributed to $^1\pi\sigma^*$ dissociation. **160**

Figure 4.4 – CH_3^+ transients as a function of pump (200 nm) probe delay for high TKER CH_3 molecules probed using a) 333.5 nm and b) 322.5 nm respectively. At negative delays, there is no appreciable 2-colour signal. Experimental data in a) and b) were fitted with an off resonance decay and step function with lifetimes $\tau_{ORdecay} < 65$ fs and $\tau_{ORstep} < 50$ fs, respectively and an additional step function in a) with $\tau_R = 91 \pm 36$ fs, where OR and R correspond to off-resonance and on-resonance respectively. **162**

Figure 4.5 – CH_3^+ transients as a function of pump (200 nm) probe delay for low TKER CH_3 molecules probed using a) 333.5 nm and b) 322.5 nm respectively. Experimental data in a) and b) were fitted with two off-resonance decay functions

and a step function having lifetimes of $\tau_{ORdecay1}$ = 85 ± 15 fs, $\tau_{ORdecay2}$ = 5.9 ± 0.7 ps and τ_{ORstep} < 50 fs respectively..... **165**

Figure 5.1 – a) Molecular structure of thioanisole. b) PES of the ground state ($^1\pi\pi$) and first two singlet excited states ($^1\pi\pi^*$ and $^1n\sigma^*$), with respect to the S-CH_3 separation ($R_{S\text{-}CH_3}$) and the out-of-plane C-C-S-CH_3 angle (ϕ). The "quasi-seam of intersection" CI1 (black dotted line) and $^1n\sigma^*$ / $^1\pi\pi$ CI (CI2) are shown. Also included is the pathway for channel [A] – dissociation to the $\tilde{A}$ state radical products (black arrows); and channel [B] – the formation of $\tilde{X}$ state product by excitation of the "dynamic resonance" ν_{7a} vibrational mode (black dashed arrows)..... **172**

Figure 5.2 – TKER spectra obtained following photoexcitation of thioanisole with a ns excitation pulse centred at a) 289.8 nm and b) 283.9 nm collected at $t \approx$ 20 ns. Solid black lines correspond to fits to the TKER spectra, with individual components of the fit associated with the channel [A] (red), channel [B] (blue) and Boltzmann-like background (dashed green) signals. β_2 anisotropy parameters (grey circles) extracted are provided below each spectrum. **173**

Figure 5.3 – a) Ultraviolet absorption spectrum for thioanisole, with the five excitation wavelengths highlighted (Gaussian distributions). The origin transition (green dashed line) and the "dynamic resonance" transition (red dashed line) are highlighted. b) Mass spectrum of thioanisole parent and methyl taken with a 279 nm pump and 333.4 nm probe, at t = 1.2 ns. The spectrum is not continuous over the break in axis and the lower m/z peak was collected at higher detector voltages (V_{mcp1} and V_{mcp2})..... **175**

Figure 5.4 – TKER spectra of the CH_3 radical products obtained following photoexcitation of thioanisole at 289.8 and REMPI-probing at 333.4 nm, recorded at t = 1.2 ns. Associated velocity map images from which the TKER spectra are derived are shown inset (left halves are raw recorded images, right halves are deconvoluted slices, white arrows represent **ε**). Solid black lines correspond to fits to the TKER spectra, with individual components of the fit associated with the channel [A] (red), channel [B] (blue) and Boltzmann-like background (dashed green) signals. β_2 anisotropy parameters (grey circles) extracted from the images are provided below. **177**

Figure 5.5 – TKER spectra of the CH_3 radical products obtained following photoexcitation of thioanisole at 283.9 and REMPI-probing at 333.4 nm, recorded at t = 1.2 ns. Associated velocity map images from which the TKER spectra are derived are shown inset (left halves are raw recorded images, right halves are deconvoluted slices, white arrows represent **ε**). Solid black lines correspond to fits to the TKER spectra, with individual components of the fit associated with the channel [A] (red), channel [B] (blue) and Boltzmann-like background (dashed green) signals. β_2 anisotropy parameters (grey circles) extracted from the images are provided below. **181**

Figure 5.6 – TKER spectra of the CH_3 radical products obtained following photoexcitation of thioanisole at a) 286.8, b) 279 and c) 275 nm and REMPI-probing at 333.4 nm, recorded at t = 1.2 ns. Associated velocity map images from which the TKER spectra are derived are shown inset (left halves are raw recorded images, right halves are deconvoluted slices and white arrows represent **ε**). Solid black lines correspond to fits to the TKER spectra, with individual components of

the fit associated with the channel [A] (red), channel [B] (blue) and Boltzmann-like background (dashed green) signals. β_2 anisotropy parameters (grey circles) extracted from the images are provided below. **182**

Figure 5.7 – a) Normalised integrated CH_3^+ signal transients for the CH_3 and $\tilde{A}$ state thiophenoxyl channel feature (circles) from fs TR-VMI following excitation centred at 289.8 (green), 286.8 (blue), 283.9 (red), 279 (orange) and 275 nm (grey) plotted as a function of pump probe delay (t). Error bars correspond to 2 standard deviations the mean signal values and the solid lines show kinetic fits which consist of two exponential rises (one <500 fs and one >50 ps) and an exponential decay convoluted with the IRF (see appendix I for details). b) Dissociation rate ($k = 1/\tau$) as a function of mean internal (vibrational) energy imparted to the $^1\pi\pi^*$ molecules by photoexcitation (red circles), compared to the calculated density of vibrational states in $^1\pi\pi^*$ at 25 cm^{-1} energy intervals (blue circles). **184**

Figure 5.8 – a) TKER spectra from thioanisole dissociation at 275 nm and probing at either 333.4 nm (red) or 323 nm (blue), at t = 1.2 ns. b) Transient CH_3^+ signal at varying t, taken with a 275 nm pump and probing at either 333.4 nm (red) or 323 nm (blue). **186**

Figure 6.1 – a) Molecular structure of mequinol, overlaid with arrows representing the direction of the transition dipole moment for excitation to the $1^1\pi\pi^*$ (red) and $2^1\pi\pi^*$ (green) states calculated using EOM-CCSD.[6] b) Vapour phase UV absorption spectrum of mequinol, with the excitation wavelengths studied using TR-VMI highlighted (Gaussian distributions). These highlighted wavelengths are assigned to a $1^1\pi\pi^* \leftarrow {}^1\pi\pi$ transition (red), a $2^1\pi\pi^* \leftarrow {}^1\pi\pi$

transition (green), a transition to a higher lying state (grey) and a $^1\pi\sigma^*_{O\text{-}CH_3} \leftarrow {}^1\pi\pi$ transition (blue). **194**

Figure 6.2 – PECs of the ground state and first four singlet excited states ($1^1\pi\pi^*$, $2^1\pi\pi^*$, $^1\pi\sigma^*_{O\text{-}H}$ and $^1\pi\sigma^*_{O\text{-}CH_3}$) in mequinol calculated at the CASPT2(12,11) level, with respect to a) O-H separation ($R_{O\text{-}H}$) and b) O-CH_3 separation ($R_{O\text{-}CH_3}$). Also labelled are the relevant CIs between states and the radical states that correspond to each asymptote.[5] **196**

Figure 6.3 – TKER spectra (circles), overlaid with 10 point averages (black lines), and corresponding H^+ velocity map images (inset) recorded for hydrogen elimination from mequinol at pump wavelengths of a) 298, b) 290 and c) 280 nm with a 1200 ps delayed probe of 243.1 nm. Also included are 10 point averaged TKER spectra taken with a 1 ps delayed probe (red lines). Vertical green arrows represent the predicted $TKER_{max}$ derived from equation 6.1 (see text). The inset images consist of raw (top) and deconvoluted images (bottom) where the pump electric field polarisation, **ε**, is indicated by the white arrow..... **201**

Figure 6.4 – H^+ signal transients in mequinol, taken at pump wavelengths of a) 298, b) 290 and c) 280 nm, with a probe of 243.1 nm. Transients are obtained by integrating the measured H^+ signal over the TKER range of 2000 cm^{-1} around the Gaussian-like feature peak at a series of pump probe delays (*t*). Error bars correspond to two standard deviations. **203**

Figure 6.5 – TKER spectra for hydrogen elimination in mequinol (circles) at pump wavelengths of a) 254 and b) 264 nm, with a 1200 ps delayed 243.1 nm probe. Data is overlaid with a 10 point average (black line). **206**

Figure 6.6 – TKER spectra for hydrogen elimination from mequinol (circles) at pump wavelengths of a) 245, b) 238 and c) 200 nm, with a 10 ps delayed probe of 243.1 nm. Spectra are overlaid with a 10 point average (black line). Corresponding images are shown inset and consist of raw (top) and deconvoluted images (bottom) with the pump electric field polarisation, **ε**, indicated by the white arrow. Vertical green arrows represent the predicted $TKER_{max}$ derived from equation 6.1 (see text). H^+ signal transients from the high TKER Gaussian feature are shown for d) 238 and e) 200 nm (circles), obtained by integrating signal over the TKER range 9500 - 11500 cm^{-1} for spectra recorded at a series of *t*. Error bars correspond to two standard deviations. Transients are fitted with an exponential rise function convoluted with the Gaussian IRF (black line)..... **207**

Figure 6.7 – TKER spectra obtained for CH_3 elimination from mequinol, taken at pump wavelengths of a) 280, b) 264, c) 254, d) 245, e) 238 and f) 200 nm, with a *t* = 1 (black), *t* = 10 (blue) and *t* = 1200 ps (red) delayed 333.3 nm probe. Spectra b) – e) show a 10 point average of the raw collected data (not shown). Vertical orange arrows in a) – e) indicate the predicted $TKER_{max}$ value determined from equation 6.3 (see text). g) CH_3^+ signal transient (circles) obtained by integrating in the TKER range 6000 - 8000 cm^{-1} taken with a 238 and 333.3 nm pump and probe arrangement. The black line in g) represents a kinetic fit to the data, while the inset CH_3^+ velocity map image was recorded at a 238 nm pump wavelength with *t* = 1200 ps. The pump electric field polarisation, **ε**, is shown by the white arrow. **212**

List of Tables

Table 2.1 – Wavelengths generated in the fourth harmonic generation process utilising a series of BBO crystals. Included in the table is the harmonic relative to the fundamental, the type of phase matching implemented to generate that harmonic and the relative polarisation of the harmonic. **98**

Table 2.2 – Summary of typical operating conditions for the molecules studied, including literature melting points and boiling points. **107**

Table 3.1 – TD-DFT, LR-CCSD and CCSD(3) vertical excitation energies for the $^1\pi\pi^* \leftarrow {}^1\pi\pi$ transition in imidazole, 2-MI, 4-MI and 2,4-DMI. TD-DFT calculations were performed at B3LYP/6-31G*//B3LYP/aug-cc-pVTZ level of theory. All other calculations were performed with a aug-cc-pVTZ basis set. Also included are the assigned experimental onsets for the transition, taken from figure 3.3. ..... **136**

Table 3.2 – Extracted time constants τ for the high (τ_H) and low (τ_L) TKER components obtained in imidazole, 2-MI, 4-MI, 2,4-DMI and 1-MI obtained through convolution of the IRF with an exponential rise (see appendix 1). Also shown are the integral widths for the high and low TKER components used to extract the associated time constants for imidazole and its methylated derivatives **144**

Table 5.1 – Adiabatic S–CH_3 dissociation to CH_3 and $\tilde{A}$ state thiophenoxyl time constants (τ) and associated dissociation rates ($k = 1/\tau$) obtained from kinetic fits to the CH_3^+ signal transients presented in Fig. 5(a). Errors correspond to 2 standard deviations. **185**

Table 6.1 – EOM-CCSD vertical energies (ΔE_{vert}) [6] and oscillator strengths (f) in addition to CASPT2(12/11) optimised energies (ΔE_{opt}) [5] for the singlet electronic state transitions in mequinol. Where available, experimentally determined values (Expt) are also provided from [a] reference [15] and [b] TR-VMI results. **195**

Acknowledgements

First and foremost, my immense gratitude goes to my supervisor Dr Vasilios Stavros, without whose tireless support, constant encouragement and vast patience the work achieved in my PhD studies would not have been possible.

I would also like to thank the various members of "Team Stavros". Many thanks go to Dr Kym Wells, Dr Azhar Iqbal and Dr Gareth Roberts, together with Vas, for teaching me all that I now know about spectroscopy and photochemistry. My gratitude also goes to Mr Craig Williams, Mr (Simon) Ed Greenough, Mr Adam Chatterley, Mr Jamie Young and the new guys, Dr Michael Staniforth and Mr Michael Horbury, for making the last 3½ years as enjoyable as possible and keeping me company when experiments ran into the early hours. Also thank you to the master students Mr Jeremy Brown, Mr Nicholas Harding, Mr Alex Bird and Miss Jenny Moore who I have been fortunate to work with.

I would also like to express my gratitude to Mr Tom White, Miss Ada Della Pia, Dr Mark Barrow, Dr Nataliya Kalashnyk and Mr Ben Moreton who have been tolerant enough to share an office with me. Furthermore my thanks go to the members of the Department of Chemistry machine and electronic workshops, along with Dr Alex Colburn, for their help in repairing the parts of the lab that broke and assistance in keeping the lab running.

My thanks also go to Dr Mike Nix, Ms Therese Bergendahl, Prof. Martin Paterson, Mr Tolga Karsili, Prof. Mike Ashfold, Dr Andreas Wenge and Miss Stephanie Harris who I have collaborated with on published work.

I also wish to express my gratitude to my family and friends who have supported and encouraged me throughout all my studies and driven me to achieve what have so far. Finally, my thanks go to the numerous friends, housemates, acquaintances, teammates (if I ever made the team), drinking buddies and the local purveyors of food / beverages for providing numerous (and often too many) distractions from my studies.

Declaration

This thesis is submitted to the University of Warwick in support of my application for the degree of Doctor of Philosophy. It has been composed by myself and has not been submitted in any previous application for any degree.

The work presented (including data generated and data analysis) was carried out by the author except in the cases outlined below:

- Theoretical calculations and analysis discussed in chapters 3, 5 and 6 were performed by Dr G. M. Roberts at the University of Warwick and Ms L. T. Bergendahl and Prof. M. J. Paterson at Heriot-Watt University.

- Theoretical calculations and analysis discussed in chapter 6 were performed by Mr T. N. V. Karsili and Prof. M. N. R. Ashfold at the University of Bristol.

- Complementary experimental results and analysis discussed in chapter 5 were performed by Dr. A. M. Wenge, Miss S. J. Harris, Mr T. N. V. Karsili and Prof. M. N. R. Ashfold at the University of Bristol.

Parts of this thesis have been published by the author:

- Time resolved velocity map imaging of methyl elimination from photoexcited anisole **-** D. J. Hadden, C. A. Williams, G. M. Roberts and V. G. Stavros, *Phys. Chem. Chem. Phys.*, **13** (2011) 4494.

- Time resolved velocity map imaging of H-atom elimination from photoexcited imidazole and its methyl substituted derivatives **-** D. J. Hadden, K. L. Wells, G. M. Roberts, L. T. Bergendahl, M. J. Paterson and V. G. Stavros, *Phys. Chem. Chem. Phys.*, **13** (2011) 10342.

- Competing $^{1}\pi\sigma^{*}$ mediated dynamics in mequinol: O-H versus O-CH3 photodissociation pathways **-** D. J. Hadden, G. M. Roberts, T. N. V. Karsili, M. N. R. Ashfold and V. G. Stavros, *Phys. Chem. Chem. Phys.*, **14**, (2012) 13415

- Exploring quantum phenomena and vibrational control in σ^{*} mediated photochemistry **-** G. M. Roberts, D. J. Hadden, L. T. Bergendahl, A. M. Wenge, S. J. Harris, T. N. V. Karsili, M. N. R. Ashfold, M. J. Paterson and V. G. Stavros, *Chem. Sci.*, **4** (2013) 993

Abstract

$^1\pi\sigma^*$ or $^1n\sigma^*$ mediated dissociation of X-H and X-CH_3 bonds (where X = N, O or S) has been studied herein, progressing previous work into the role of $^1\pi\sigma^*$ and $^1n\sigma^*$ states as mediators for excited state relaxation. By investigating the role of these states in excited state dynamics of sub-units and analogues of biomolecular systems, spectroscopic signatures can be observed with greater ease. These signatures may then be extended to elucidate the role of these dissociative states in excited state relaxation processes of more realistic systems, namely DNA bases and amino acids.

The work undertaken in this thesis specifically focuses on $^1\pi\sigma^*$ mediated hydrogen elimination from imidazole and mequinol, as well as $^1\pi\sigma^*$ or $^1n\sigma^*$ mediated CH_3 elimination in anisole, thioanisole and mequinol. Through the use of time resolved velocity map imaging, the timescale for these dissociation processes can be determined by independently measuring the radicals produced with a characteristic kinetic energy. From these timescales, information about the rate of coupling to these $^1\pi\sigma^*$ and $^1n\sigma^*$ states can be inferred. The results obtained show that population of these states can occur via several different mechanisms including: direct excitation; coupling through conical intersections; and tunnelling. The results also project the importance of $^1\pi\sigma^*$ or $^1n\sigma^*$ mediated processes in much larger biological systems, strongly suggesting the need to extend these measurements and begin to bridge the gap between the microscopic, such as DNA bases and amino acids, and the macroscopic, such as oligonucleotides and polypeptides.

List of Abbreviations

UV	Ultraviolet
DNA	Deoxyribonucleic Acid
IC	Internal Conversion
ISC	Intersystem Crossing
IVR	Intramolecular Vibrational Energy Redistribution
LIF	Laser Induced Fluorescence
CI	Conical Intersection
PES	Potential Energy Surface
PEC	Potential Energy Cut
TDM	Transition Dipole Moment
FWHM	Full Width at Half Maximum
1D	One Dimensional
2D	Two Dimensional
3D	Three Dimensional
IP	Ionisation Potential
REMPI	Resonance Enhanced Multiphoton Ionisation

D_0	Bond Dissociation Energy
TKER	Total Kinetic Energy Release
HRA-PTS	High Rydberg Atom Photofragment Translational Spectroscopy
VUV	Vacuum Ultraviolet
A / G / C / T / U	Adenine / Guanine / Cytosine / Thymine / Uracil
RNA	Ribonucleic Acid
CT	Charge Transfer
CW	Continuous Wave
SFG	Sum Frequency Generation
SHG	Second Harmonic Generation
OPG	Optical Parametric Generation
BBO	β-Barium Borate
IR	Infrared
VMI	Velocity Map Imaging
TOF	Time of Flight
MCP	Microchannel Plate
CCD	Charge Couple Device

POP	Polar Onion Peeling
TR-IY	Time Resolved Ion Yield
TTL	Transistor-Transistor Logic
TR-VMI	Time Resolved Velocity Map Imaging
1-MI	1-Methylimidazole
2-MI	2-Methylimidazole
4-MI	4-Methylimidazole
2,4-DMI	2,4-Dimethylimidazole
TD-DFT	Time Dependent Density Functional Theory
LR-CCSD	Linear Response Couple Cluster Singles and Doubles
CCSD(3)	Non-Iterative Corrected Triples CCSD
IRF	Instrument Response Functions
RRKM	Rice-Ramsperger-Kassel-Marcus
MPI	Multiphoton Ionisation
$TKER_{max}$	Maximum Total Kinetic Energy Release
EOM-CCSD	Equations of Motion Couple Cluster Singles and Doubles
CASPT2	Complete Active Space with Second Order Perturbation Theory

vFC	Vertical Franck-Condon
ZPE	Zero Point Energy
BKW	Brillouin-Kramers-Wentzel

1. Introduction

One of the major aims of chemical physics has been to resolve chemical and physical processes in molecules by their timescales. This has been aided by advances in experimental techniques which enable temporal resolution on the timescale of nuclear motion. Obtaining a fundamental understanding of the factors that govern nuclear displacement can lead to a better understanding of how the atoms that make up a molecule rearrange during a chemical reaction. Measurements on the timescale for nuclear motion, typically femtoseconds (where 1 fs = 10^{-15} s), were first achieved using ultrashort laser pulses (typically lasting a few hundred femtoseconds) in the early 1980s.[1] The implementation of femtosecond laser systems allowed experimentalists to study how electronic structure influences nuclear motion. In doing so, these studies highlighted the importance of competing photophysical processes resulting in population transfer between different electronic states. Indeed early studies showed how competing excited state decay processes play a vital role in several biological systems, following ultraviolet (UV) radiation absorption, including bond dissociation in peptide residues and molecular photostability in deoxyribonucleic acid (DNA) bases.[2, 3]

The work in this thesis aims to study the competition between different decay processes of photoexcited electronic states in a range of model biomolecules through determining their excited state relaxation timescales. This is achieved by measuring the timescale for the formation of photoproducts following UV irradiation. In particular, this work strives towards a fundamental understanding of the dynamical interplay between different excited electronic states, some of which have previously

been identified in biological systems and have been linked to theorised non-radiative relaxation pathways in excited DNA bases. The use of gas phase techniques allows one to study the dynamics of excited electronic states, independent of intermolecular interactions such as solvent effects. However, generating large biomolecules in the gas phase is very difficult and hence the majority of the work herein focuses on model systems or subunits of biomolecules. These studies are based upon previous work in adenine [4] and tyrosine [5] whose chromophores, imidazole and phenol respectively, have been the subject of numerous studies.[6-9] The structures of the molecules studied and how they relate to adenine, tyrosine and phenol are shown in figure 1.1.

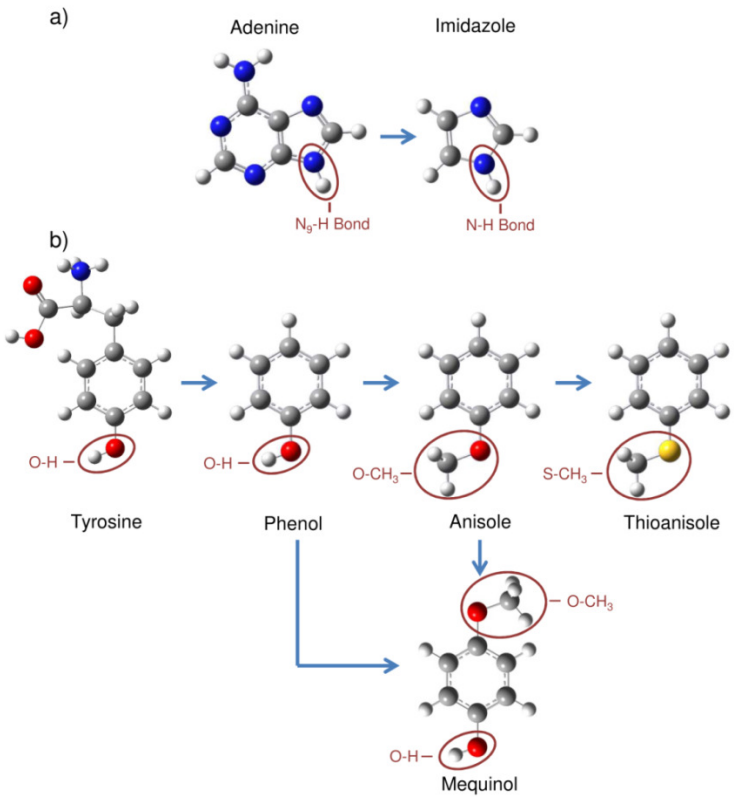

Figure 1.1 – The structures of the molecules studied in this thesis, highlighting the specific nuclear coordinate(s) of interest. a) The dissociation of the N-H bond in imidazole serves as a model for the N_9-H coordinate in adenine. b) The structures of the anisole, thioanisole and mequinol, and how they relate to tyrosine and phenol.

1.1 Molecular Dynamics

1.1.1 The Dynamics of Photophysical Processes

The evolution of an electronically excited state, once populated by the absorption of a photon, can occur via several different mechanisms depending on the vibrational level promoted, the density of vibrational states, the proximity in energy to other electronic states and the degree of spin-orbit coupling. [10, 11] The timescale for the initial photon absorption is sub-femtosecond ($<1 \times 10^{-15}$ s), far quicker than other electronic state transfer mechanisms (see Franck-Condon Principle in section 1.2.1).

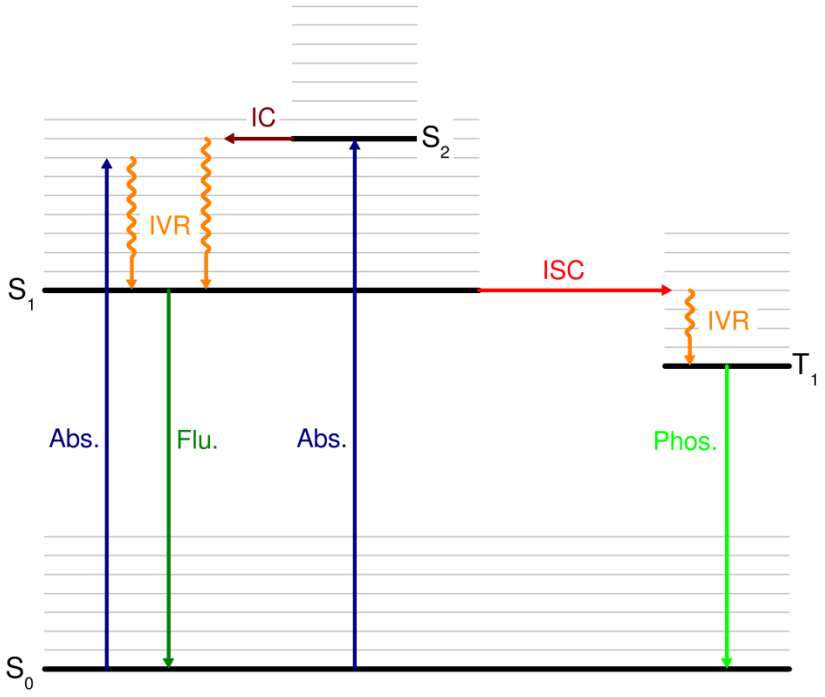

Figure 1.2 – A Jablonski diagram, summarising the possible photophysical processes for a molecule between the first three singlet states (S_0, S_1 and S_2) and the lowest triplet state (T_1). The photophysical processes shown are: absorption (blue), fluorescence (Dark Green), phosphorescence (Light Green), internal conversion (Brown), intersystem crossing (Red) and intramolecular vibrational energy redistribution (Orange).

Several of these processes can be summarised in a Jablonski diagram, such as that shown in figure 1.2, and in many molecules competition between these processes takes place with the overall mechanism governed by the rate of each component. Possible mechanisms that results in population transfer between two electronic states include: fluorescence, phosphorescence, internal conversion (IC) and intersystem crossing (ISC). Also occurring on a similar timescale to these electronic state transfer mechanisms is intramolecular vibrational energy redistribution (IVR), where energy in a particular vibrational mode is redistributed amongst the other (3*N*−7) vibrational degrees of freedom, where *N* is the number of atoms in the molecule.[12] The timescale of each of these processes can be estimated from previous studies and a summary of each mechanism will now be discussed.

Radiative Processes: Fluorescence and Phosphorescence

There are two radiative processes, described as fluorescence and phosphorescence, depending on whether there is a change in spin multiplicity between the initial and final electronic states, following the emission of a photon.

Fluorescence has been a widely studied phenomenon for centuries, with scientists as early as the 16th century observing a characteristic luminescent signal in the medicinal wood derivative *lignum nephriticum*.[13] The term fluorescence was originally coined by G. G. Stokes [14] to describe the changing of wavelength of an incident beam of light when passing through a photoluminescent medium, such as fluorite crystals and quinine solutions. Quantum mechanically, fluorescence corresponds to population transfer from an excited electronic state (usually the lowest excited electronic state of the appropriate spin multiplicity, forming the basis

of Kasha's Rule [15]) to the electronic ground state, with the energy conserved by the spontaneous emission of a photon with the corresponding frequency. The defining factor in fluorescence is that the spin multiplicity of the excited and ground states are the same. As a result, the process is "spin-allowed" and the lifetime for the excited state is relatively short, typically ranging from 10^{-12} to 10^{-6} s.[16] The emitted photon is typically red-shifted from the initially absorbed photon due to losses through IC and IVR; and this is used as a spectroscopic technique forming the basis of laser induced fluorescence spectroscopy (LIF).[17]

Phosphorescence is a similar radiative process occurring between electronic states of different spin multiplicity. In the case of closed shell molecules this typically occurs from a triplet excited state to the ground singlet state. As with fluorescence, spontaneous emission occurs at a longer wavelength than the initially absorbed photon since energy is lost through ISC and IVR. Due to the difference in spin multiplicity, the emission process is "spin-forbidden"; as a result the lifetime of an excited state undergoing phosphorescence is longer than fluorescence, usually taking 10^{-6} to 10^{-1} s in organic molecules.[16] Due to the longer lifetime, quenching of phosphorescence by intermolecular processes tends to reduce the amount of emission, particularly in condensed phase systems. The rate of phosphorescence is highly dependent on spin-orbit coupling and is therefore more likely to be observed in molecules containing heavy atoms, exhibiting large orbital angular momentum.

Non-Radiative Processes: Internal Conversion and Intersystem Crossing

Transitions between electronic states can also occur non-radiatively, without photon emission.[18] IC takes place between states of the same spin multiplicity. IC

has been shown to underpin many transitions to charge transfer or dissociative excited states in organic molecules. Most of these mechanisms rely on avoided crossings and conical intersections (CI, discussed below) to funnel population into the desired electronic state. Therefore the rate for IC depends greatly on the proximity to avoided crossings and CIs, with studies showing transfer can occur within tens of femtoseconds. CIs often occur between excited states in organic molecules and have been shown to account for several notable processes, such as the *cis-trans* isomerisation of the retinal pigment in rhodopsin, which is one of the first stages in the eye's perception of light,[19] or the fast depletion of the S_1 state population in azulene.[20, 21] In the absence of any CI, the rate has been shown to be dependent on the density of vibrational states in the initial and final states, which fits a Fermi's golden rule model.[10, 11] In this case IC usually occurs faster than the timescale required for fluorescence of higher lying excited states (i.e. not the first excited state); and generally fluorescence is only observed from the lowest singlet excited state.[15] The excited state relaxation of isolated DNA bases is speculated to involve IC between three different singlet states allowing for non-radiative repopulation of the ground state and understanding the dynamics that mediates this IC process is one of the driving forces behind this thesis. Given the importance of IC via avoided crossings and CIs, this area will be expanded upon below.

Non-radiative crossing between electronic states of different spin multiplicities, such as a singlet to a triplet state, requires a change in electron spin, and, as discussed, is termed ISC. As with phosphorescence the transition is "spin-forbidden" and requires a significant degree of spin-orbit coupling. As a result the rate of ISC is usually less than IC, though studies on heavy metal complexes (such as

iridium or ruthenium based) have measured ISC taking place within hundreds of femtoseconds. ISC also accounts for some of the excited state dynamics of benzene.

Intramolecular Vibrational Energy Redistribution

The remaining intramolecular process shown in figure 1.2 is IVR, where vibrational energy isolated in a single vibrational coordinate is transferred to other vibrational degrees of freedom. For a non-linear polyatomic molecule these correspond to the remaining $3N-7$ vibrational degrees of freedom.[12] However the rate of IVR is typically larger than the rate of fluorescence, and as a result fluorescence is mostly observed from the zero point energy of the lowest electronically excited state.[15]

1.1.2 Femtochemistry and the Nobel Prize

The photophysical processes described above can potentially lead to a change in the atomic positions within a molecule, with dissociation or nuclear rearrangement to a minimum energy molecular geometry a common outcome from photoexcitation to an electronically excited state. Given that nuclear rearrangements occur on the timescale of vibrational motion and given that a typical vibration has a frequency of 10^{14} Hz, nuclear rearrangement can occur on the order of tens of femtoseconds. With the development, in the early 1980s, of lasers that can generate pulses of light on a similar timescale to nuclear motion, it became possible to measure the evolution of excited electronic states following photoexcitation. This work was pioneered by Professor Ahmed Zewail at Caltech, whose seminal work in the early 1980s on pump probe spectroscopy of electronically excited states in NaI [22, 23] and ICN [24-26]

gave rise to a new area of chemistry. This lead to Professor Zewail being awarded the 1999 Nobel Prize in Chemistry [27] for the development of femtochemistry.[1]

Pump Probe Spectroscopy

The technique implemented by Professor Zewail utilises two femtosecond laser pulses, termed the pump and probe pulses. The pump pulse provides the initial photoexcitation. The probe pulse provides a means of detection. Selecting an adequate approach to probe the evolution of the system of interest is essential; with the probe potentially inducing photoionisation (detecting ions or electrons), inducing photoluminescence (fluorescence or phosphorescence) or undergoing a detectable modulation of probe photons (by absorption or stimulated emission). By varying the time delay between the pump and probe laser pulses, it is possible to build up a picture of how the initially prepared electronically excited state evolves after photoexcitation. One of the original experiments by Professor Zewail's group was on the dissociation of NaI, [22] performed in a heated quartz cell of gaseous sample.

NaI: An Example of Pump Probe Spectroscopy

The potential energy curves of NaI, shown in figure 1.3, contains a pair of electronic states of distinctly different characteristics, the ground electronic state showing strong ionic character and the first electronically excited state strong covalent character. Excitation to the first electronically excited state (~4 eV) can lead to the creation of a vibrational wavepacket (see Section 1.2.2) which will propagate to larger Na – I separation. At increased Na – I separation, the two electronic states approach each other at which point the states can either cross or avoid each other.

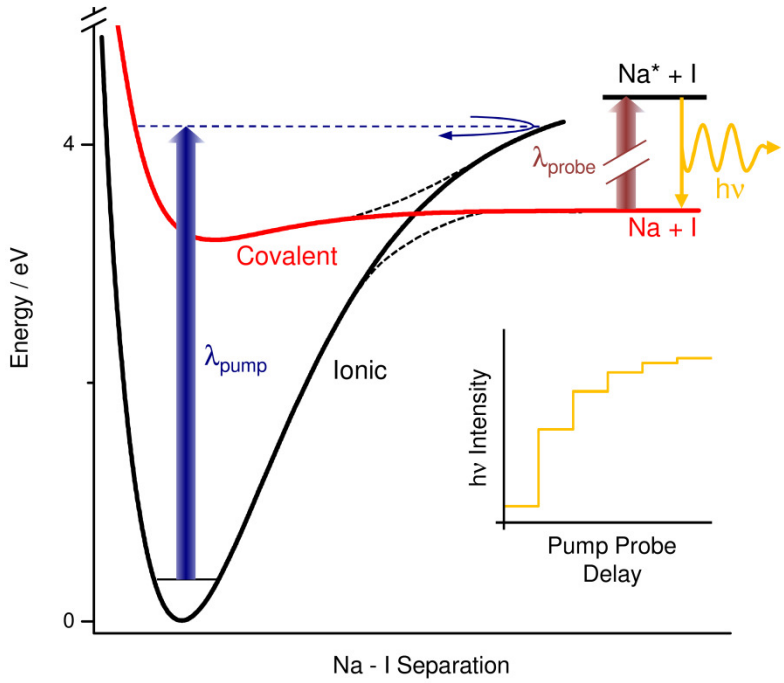

Figure 1.3 – Schematic representation of the ground (black - ionic) and first (red - covalent) excited electronic potential energy surfaces of NaI. Black dashed lines represent the presence of an adiabatic avoided crossing between the two potentials. Also shown is a pair of laser pulses represented by λ_{pump} and λ_{probe}, providing photoexcitation and inducing fluorescence (hν) respectively. Blue dashed line represents the path of a wavepacket trapped in the bound adiabatic potential. Inset is a representation of the step-wise rise in the laser induced fluorescence signal (hν) intensity as a function of pump probe delay.

The excited state wavepacket can thus propagate along two possible pathways; the first involves relaxation along a diabatic pathway (solid red line), leading to dissociation, to form radical products (Na and I). The second involves motion along an adiabatic pathway (black dashed line), in which the electronic states avoid each other. This leads to trapping of the wavepacket on the upper adiabatic potential (as illustrated by the dotted blue line) where the wavepacket oscillates, periodically returning to the avoiding crossing and potentially transferring population along the diabatic pathway. By measuring the production of Na atoms through LIF (by a 589 nm probe), a stepwise signal for Na production is thus observed (see inset

schematic in figure 1.2.).[23] The period of the step in the Na signal corresponds to the time taken for the wavepacket to oscillate on the upper adiabatic potential energy curve. The example of NaI illustrated the unique ability of femtochemistry for studying the dynamics of a system that shows competing adiabatic and non-adiabatic dynamics (along the diabatic pathway). However the potential energy curves of NaI are relatively simple as they only depend on one nuclear coordinate; larger molecules with many degrees of freedom can show far more complex dynamics with the possibility for forming CIs.

1.2 Potential Energy Surfaces

By determining the topography of a molecule's potential energy surfaces (PESs) it is possible to predict how the molecule's structure will evolve during a chemical reaction or physical process. A PES is a map of the potential energy of an electronic state throughout all nuclear degrees of freedom ($3N-6$). However calculation or spectroscopic determination of a molecules PESs for a system with many nuclear coordinates is not always possible and potential energy cuts (PECs) along a particular coordinate are usually determined to provide a simplified model. The concept of a PES relies on the principle that the electronic and nuclear motion in molecules is separable allowing for construction of a surface where the energy of each electronic state is defined solely by the nuclear displacement. This separation of electronic and nuclear terms forms the bases of the Born-Oppenheimer approximation for quantum mechanical systems. Consideration of the Born-Oppenheimer approximation when dealing with transitions between different electronic states leads to the derivation of the Franck-Condon principle which

governs the probability of a transition to a particular vibrational eigenstate (vibronic transition).

1.2.1 The Born-Oppenheimer Approximation

The Born-Oppenheimer approximation allows the determination of an estimate for the molecular wavefunction for a system, without explicitly solving the Schrödinger equation.[16, 28-30] The Schrödinger equation for a molecular wavefunction $\Psi(R,r)$ can be written, with the Hamiltonian separated into its constituent parts, as:

$$\left[\mathrm{T}_n(R)+\mathrm{T}_e(r)+\mathrm{V}_{ne}(R,r)+\mathrm{V}_{nn}(R)+\mathrm{V}_{ee}(r)\right]\Psi(R,r)=E\Psi(R,r) \tag{1.1}$$

where T_n and T_e are the kinetic energy operators for nuclei and electrons, respectively, and V_{ne}, V_{nn} and V_{ee} are the potential energy operators for the various Coulombic interactions, all in terms of nuclear displacement (R) and electronic displacement (r). The Born-Oppenheimer approximation states that, due to the vast difference in mass (at least 10^3 times), nuclear motion is far slower than electronic motion and the two components are separable.[31, 32] As such, the molecular wavefunction can be separated into two components, a nuclear (ψ_n) and an electronic (ψ_e) wavefunction:

$$\Psi(R,r)=\psi_e(R,r)\psi_n(R) \tag{1.2}$$

where only the terms dependent on the electronic displacement in equation 1.1 at a fixed nuclear configuration (R) operate on the electronic wavefunction, to give the electronic Schrödinger equation:

$$\left[\mathrm{T}_e(r)+\mathrm{V}_{ne}(R,r)+\mathrm{V}_{ee}(r)\right]\psi_e(R,r)=\mathrm{E}_e(R)\psi_e(R,r) \tag{1.3}$$

The nuclear wavefunction is dependent on the nuclear displacement terms, with the potential energy between each nucleus and electron contained in the term $E_e(R)$. This results in the nuclear Schrödinger equation:

$$\left[T_n(R) + V_{nn}(R) + E_e(R)\right]\psi_n(R) = E\psi_n(R) \tag{1.4}$$

The internuclear potential term ($V_{nn}(R)$) and the energy of the electronic wavefunction ($E_e(R)$) combine to give the molecular potential energy ($U(R)$) and it is this potential term as a function of all possible nuclear displacements that gives the PES.[31] This separation of wavefunctions is only possible while the nuclear motion is negligible relative to the electronic motion, forming part of the adiabatic theorem; the solution for the electronic wavefunction is preserved as long as perturbation of the molecule (in this case nuclear motion) is in infinitesimally small steps. When the speed of nuclear motion becomes comparable to that of the electrons, the adiabatic theorem is no longer valid and non-adiabatic dynamics can occur; this is the basis of avoided crossings and CIs.

Vibronic Transitions and the Franck-Condon Principle

The Franck-Condon principle is born through of the assumption that nuclear motion is separable from the electronic motion, [33-35] leading to the notion that photoexcitation to (or photoemission from) an electronic state occurs "vertically" in energy at a fixed point on a PES, with no nuclear rearrangement. It can be shown that a radiative transition is dependent on the overlap of the wavefunctions of the corresponding vibrational eigenstates. The probability (P) for a transition between an initial (Ψ'') and final (Ψ') electronic state is given by the overlap integral:

$$\mathrm{P} = \int \Psi'(R,r)\boldsymbol{\mu}\Psi''(R,r)\,\mathrm{d}\tau \tag{1.5}$$

where $\boldsymbol{\mu}$ is the molecular dipole moment operator and can be split into an electronic ($\boldsymbol{\mu}_\mathbf{e}$) and nuclear ($\boldsymbol{\mu}_\mathbf{n}$) component. The transition probability is not an easy quantity to calculate and breaking it down into components can allow for approximation of the electronic and nuclear contributions independently. Separation of the total wavefunction into electronic and nuclear wavefunctions, leads to the following:

$$\mathrm{P} = \int \psi'_v(R)\psi'_e(R,r)(\boldsymbol{\mu}_\mathbf{e} + \boldsymbol{\mu}_\mathbf{n})\psi''_v(R)\psi''_e(R,r)\,\mathrm{d}\tau \tag{1.6}$$

Expanding equation 1.6 gives an overlap integral of each wavefunction with the electronic and nuclear dipole moment separately. In this case the $\boldsymbol{\mu}_\mathbf{n}$ dependent integral is removed as it contains an overlap of two orthogonal electronic wavefunction (i.e $\int \psi'_e\psi''_e\,\mathrm{d}\tau = 0$). Therefore, the only factors remaining are:

$$\mathrm{P} = \int \psi'_e(R,r)\boldsymbol{\mu}_\mathbf{e}\psi''_e(R,r)\,\mathrm{d}\tau \int \psi'_v(R)\psi''_v(R)\,\mathrm{d}\tau \tag{1.7}$$

The first of these integrals is the electronic component, dependent on the spatial overlap of electronic wavefunctions of the initial and final states. Also included is the electronic component of the dipole moment operator ($\boldsymbol{\mu}_\mathbf{e}$) which is a summation of all positions of the electrons, and given by:

$$\boldsymbol{\mu}_\mathbf{e} = -\mathrm{e}\sum_i r_i \tag{1.8}$$

where e is the charge of an electron and r_i is the displacement of the *i*th electron. The square of this first term in equation 1.7 is the electronic transition dipole moment (TDM) for the transition to each electronic state, which corresponds to the directionality and magnitude of electron rearrangement in the transition. It is this first term, along with spin considerations, that can vary considerably between electronic

states in the same molecule and leads to the large disparities between optically "dark" (low transition probability) and "bright" (high transition probability) electronic states. The second integral in equation 1.7 is the overlap between the vibrational wavefunctions in the initial and final electronic states and is called the Franck-Condon factor. The Franck-Condon factor is specific to each pair of vibrational eigenstates in the initial and final electronic states.

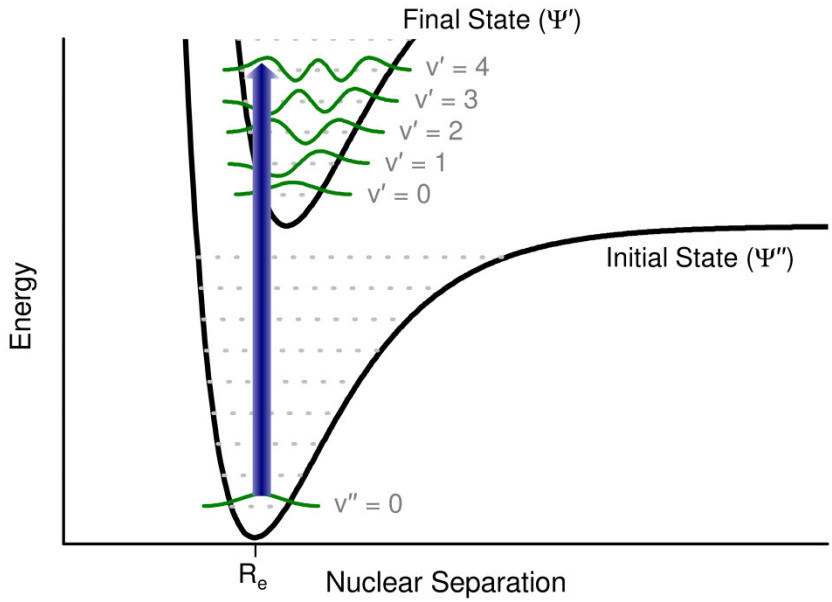

Figure 1.4 – PEC along a nuclear coordinate in a molecule with a vibronic transition shown between an initial and final electronic state. The favourable overlap of the $\Psi'_{v=0}$ and $\Psi''_{v=4}$ wavefunctions leads to the largest Franck-Condon factor for this transition.

Due to the "vertical" nature of a transition, excitation from the lowest vibrational eigenstate in the initial state, at its equilibrium geometry, may correspond to a high lying vibrational eigenstate in the final state, whose minimum energy geometry may be far off in nuclear coordinate space.[35] An example of this is shown in figure 1.4 where the lowest vibrational eigenstate (v = 0) in the initial state has a wavefunction centred at R_e. Excitation will occur preferentially to the vibrational eigenstate in the final state that has the largest overlap with the initial

wavefunction. In this case, the v = 4 vibrational level will be most favoured, as the optimum bond length in the excited electronic state is far from R_e.[36]

1.2.2 Wavepackets

The Franck-Condon principle above dictates the preferential excitation of a particular vibrational eigenstate in a final electronic state. To achieve excitation of a single vibrational level monochromatic light is used, with a narrower energy bandwidth than the spacing of vibrational levels; this forms the basis of some frequency resolved spectroscopy (discussed in section 1.3.2). However, this is not possible with short pulses due to the time energy uncertainty principle, resulting in excitation of multiple vibrational eigenstates simultaneously. In such cases, a coherent superposition of the vibrational eigenstates is formed that evolves in time. This superposition of eigenstates is called a wavepacket.

Time Energy Uncertainty and Bandwidth Limitation

The ability to measure dynamics on the timescale of nuclear motion requires lasers with pulse lengths of tens of femtoseconds. The temporal length of femtosecond laser pulses is limited by the time energy uncertainty principle and as a result wide energetic bandwidths are required to generate pulses of tens of femtoseconds. The laser system used to generate such pulses is discussed later (Section 2.1). The full width at half maximum (FWHM) in frequency ($\Delta\nu$) of a Gaussian profile laser pulse is given by the relationship:

$$\Delta\nu = \frac{0.441}{\Delta t} \tag{1.9}$$

where Δt is the temporal FWHM. For the creation of tens of femtosecond pulses, an energy bandwidth of hundreds of wavenumbers is required (for Δt = 50 fs; this give $\Delta\nu \approx 8$ THz or an energy of ~300 cm^{-1}). With energy bandwidths of this order, the excitation of multiple vibrational levels in organic molecules typically occurs, forming a superposition of vibrational eigenstates, thus generating a vibrational wavepacket.

Wavepacket Generation

The superposition of vibrational eigenstates introduces time-dependent behaviour to the total wavefunction. The time-dependent wavefunction ($\Psi(t)$) of the wavepacket is given by the sum of the n time-independent wavefunctions for each vibrational eigenstate accessed in the photoexcitation:

$$\Psi(t) = \sum_n A_n \psi'_{v=n} e^{-iE_n t/\hbar} \tag{1.10}$$

where A_n is the expansion coefficient, which determines the contribution of each eigenstate n, $\psi'_{v=n}$ is the time-independent wavefunction for each vibrational eigenstate, and E_n is the energy of each eigenstate. The expansion coefficients are dependent, in part, on the laser excitation pulse and are given by:

$$A_n = g(E) \int \psi'_{v=n} (\boldsymbol{\mu} \cdot \boldsymbol{\varepsilon}) \psi'' \, d\tau \tag{1.11}$$

In equation 1.11, $\boldsymbol{\mu}$ is the dipole moment operator and $\boldsymbol{\varepsilon}$ is the electric field vector of the excitation pulse. Therefore, the integral is the overlap between the initial state (ψ'') and final state vibrational eigenstate ($\psi'_{v=n}$) wavefunction with the dipole moment operator and electric field vector. $g(E)$ is a shape function that accounts for

the energetic distribution of the laser pulse; typically this will be Gaussian and an example of excitation to a range of vibrational eigenstates is shown in figure 1.5 a).

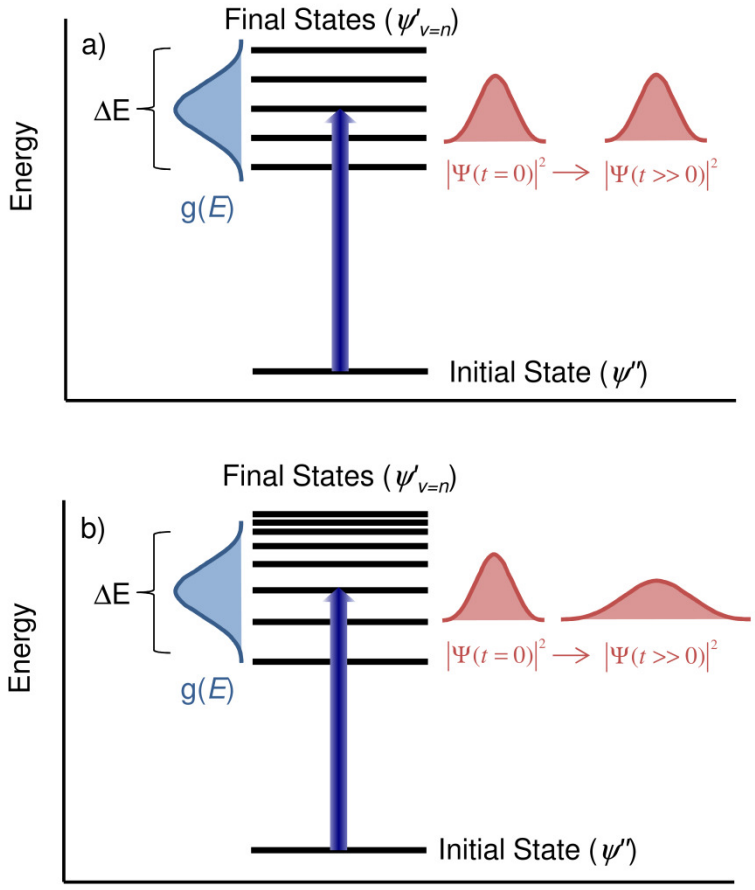

Figure 1.5 – Wavepacket generation and evolution from a shaped (g(*E*)) pulse excitation from an initial electronic state to a range of vibrational eigenstates in the final electronic state, ΔE is the average spacing of vibrational levels over the range of the laser pulse for: a) a set of evenly distributed harmonic vibrational eigenstates which will evolve at an even rate; and b) a set of anharmonic vibrational eigenstates which evolve unevenly causing wavepacket dispersion.

Wavepacket Evolution

Wavepacket formation in a molecule upon excitation to a single electronic state can be considered as a superposition of vibrational eigenstates that constructively interfere in a localised region of the PES while destructively interfering everywhere else.[32] The region of constructive interference (given by the

observable $\left|\Psi(R,t)\right|^2$) is governed by the summation of the exponential term in equation 1.10 which oscillates in time, the periodicity of which can be can be derived through Euler's relationship ($e^{-ix} = \cos x - i \sin x$). By applying Euler's formula to the expansion of the sum in equation 1.10, the wavepacket motion can be shown to depend on time, by the following expression:

$$\left|\Psi(R,t)\right|^2 \propto \left|\cos(\Delta E t/\hbar)\right|^2 \tag{1.12}$$

where ΔE is the average spacing of vibrational eigenstates over the energy range of the excitation pulse. As predicted by equation 1.12, the smaller spacing between the vibrational eigenstates, the lower the frequency of the wavepacket oscillation.[32] For a harmonic set of vibrational eigenstates, the contribution of each eigenstate should remain defined by the initial distribution (A_n) and the wavepacket should maintain the same spatial (in terms of R) shape indefinitely; an example of this is shown in figure 1.5 a) where the $\left|\Psi(t)\right|^2$ maintains the same distribution. However for unevenly spaced vibrational eigenstates, such as in an anharmonic region of a PES, the non-uniform distribution of eigenstates leads to wavepacket dispersion, as the higher energy eigenstates superposed have a different periodicity to the lower energy eigenstates superposed, as depicted by figure 1.5 b). As a result, the wavepacket will disperse causing its position to smear out.

1.2.3 Electronic State Degeneracy and Non-Adiabatic Dynamics

The dynamics of numerous photochemical reactions involve the evolution of vibrational wavepackets along various coordinates of a PES and are governed by the interplay of electronic states. In many regions of the PES two electronic states interact in a way that allows for population transfer, depending on the PES. These

interactions are: (a) an avoided crossing between states of the same symmetry in a one dimensional (1D) PEC or (b) a CI between states in a multidimensional PES.

Avoided Crossings

Within the formulation of the Born-Oppenheimer approximation it can be shown that in a 1D PEC, such as one dependent on nuclear separation in a diatomic molecule, two electronic states of the same spin multiplicity and symmetry cannot reach a point of degeneracy. By applying the adiabatic theorem, where the change in nuclear displacement (R) is considered as infinitesimally small, it can be shown that the electronic states will avoid the point of degeneracy. This is shown in figure 1.6 where the two adiabatic states (ψ_1 and ψ_2) repel each other and curve to avoid the point of degeneracy. Passing along one adiabatic surface changes the wavefunction from one diabatic state to the other (i.e. along ψ_1 the wavefunction changes from ϕ_1 on the left hand side to ϕ_2 on the right hand side).

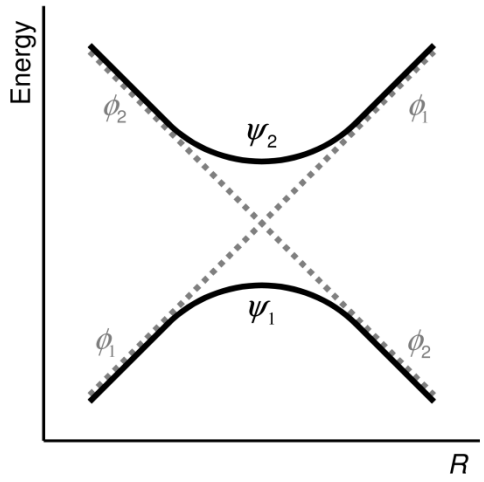

Figure 1.6 – An avoided crossing between two diabatic electronic states (grey dotted lines) as a function of nuclear displacement (R) in a diatomic. The black lines represent the adiabatic states.

In the curved region, the total wavefunction for the electronic state is a linear combination of the two diabatic surfaces. However, the adiabatic theorem can break down if the nuclear motion is quick, allowing for motion along the diabatic state (grey dashed lines in figure 1.6) through the point of degeneracy.[22, 23, 37, 38]

The non-crossing rule can be derived by variational treatment of this linear combination to give the adiabatic states. The adiabatic wavefunction (ψ) for each electronic state can be thought of as a linear combination of the two diabatic states (ϕ), such that:

$$\begin{aligned} \psi_1 &= c_{11}\phi_1 + c_{12}\phi_2 \\ \psi_2 &= c_{21}\phi_1 + c_{22}\phi_2 \end{aligned} \tag{1.13}$$

where c_{ij} is the coefficient for each diabatic state contribution. As a linear combination of states, a variation theory method may be used to find the energy of the adiabatic wavefunction. The energy can be determined from the Hamiltonian (H) by the secular determinant:

$$\begin{vmatrix} H_{11} - E & H_{12} \\ H_{21} & H_{22} - E \end{vmatrix} = 0 \tag{1.14}$$

in which the H_{ij} is given by the overlap integral:

$$H_{ij} = \int \phi_i H \phi_j d\tau \tag{1.15}$$

The secular determinant can be solved, yielding two roots corresponding to the energy of each state:

$$E = \frac{1}{2}(H_{11} + H_{22}) \pm \frac{1}{2}[(H_{11} - H_{22})^2 + 4H_{12}^2]^{\frac{1}{2}} \tag{1.16}$$

To reach a point of degeneracy between the two states the second term in equation 1.16 must equal zero. For this to be the case two conditions must be met: $H_{11} = H_{22}$; and $H_{12} = 0$. For two states of the same spin multiplicity and symmetry it is very unlikely that both these conditions can be met when R is one dimensional. [31, 37, 39] However if the states have different symmetry or spin multiplicity, then H_{12} will equal zero for all nuclear separation and a crossing can be reached at a specific value of R.[39] Avoided crossings are not exclusive to diatomic molecules and have mathematically been shown to exist in polyatomic molecules by Naqvi, [40] however the extra dimensionality to R in polyatomic molecules can lead to a change in molecular symmetry allowing states to cross.

Conical Intersections

The addition of more dimensionality to R may allow for a degeneracy between two electronic states, as the two requirements for a degeneracy in equation 1.16 may be met by varying the two degrees of freedom, x and y. If the degeneracy occurs at a point where $H_{11} = H_{22}$ and $H_{12} = 0$, then the secular determinant in equation 1.14 can be written as:

$$\begin{vmatrix} W + h_1 x - E & ly \\ ly & W + h_2 x - E \end{vmatrix} = 0 \qquad (1.17)$$

In the above expression, W is the energy at the point of intersection ($x = 0$ and $y = 0$), h_1 and h_2 are the gradients of H_{11} and H_{22} in x, respectively, and l is the gradient of H_{12} in y. If h_1 and h_2 are then defined in terms of the average gradient and the difference in gradient m and k, respectively, so that $m = (h_1 + h_2)/2$ and $k = (h_1 - h_2)/2$, then equation 1.17 becomes:

$$\begin{vmatrix} W+(m+k)x-E & ly \\ ly & W+(m-k)x-E \end{vmatrix} = 0 \qquad (1.18)$$

The set of parameters in the diagonal and off-diagonal represent the branching space of the CI, with the terms dependent on k called the gradient difference (a measure of the difference in steepness of the two surfaces) and the l terms related to the derivative coupling (a measure of the non-adiabatic coupling between the two surfaces). The two solutions for the energy of each surface are given by:

$$E = W + mx \pm (k^2x^2 + l^2y^2)^{\frac{1}{2}} \qquad (1.19)$$

The last term in equation 1.19 is the geometric equation for a cone, either increasing or decreasing in energy from its vertex depending on whether it is the positive or negative root. This means that the energy of each surface extends as a cone above and below the point of degeneracy at $x = 0$, $y = 0$ and $E = W$. This is depicted in figure 1.7 as a double cone and is termed a CI.[31, 41]

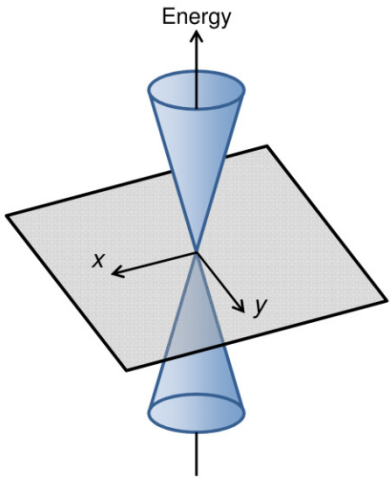

Figure 1.7 – A conical intersection between two electronic states as a function of x (the gradient difference) and y (the derivative coupling).

CIs are non-adiabatic features relying on vibronic coupling of the nuclear and electronic motion; in particular, the population of vibrational modes that govern the derivative coupling and gradient difference motion (which from the branching space).[42-44]

1.3 Spectroscopic Techniques

The dynamics of excited electronic state population, its evolution along PESs, avoided crossings and through CIs has become a wide area of study in recent years, with a myriad of experimental techniques implemented. To understand the processes that can occur in individual molecules, it is beneficial to study isolated systems. Typically this involves preparing molecules in a molecular beam where intermolecular interactions are removed. The preparation of a molecular beam usually involves the expansion of analyte molecules in a seed gas (such as noble gases) that lowers the rotational and vibrational energy of the target molecule through collisional energy transfer. For spectroscopic analysis it is favourable to study molecules with a narrow spread of internal energies, providing better energy resolution. The formation of molecular beams with minimal vibrational and rotational energy guarantees this narrow distribution of internal energy. Details on molecular beams will be discussed later in the experimental section 2.2.1.

A brief summary of techniques for studying the dynamics of excited states will now be discussed. Some of these techniques are applicable to time resolved studies and form the basis of the work presented in this thesis. Complementary techniques, particularly those providing high energy resolution are also discussed, as

they form the background to many of the existing studies into the molecules investigated herein.

1.3.1 Multiphoton Ionisation and Resonance Enhanced Multiphoton Ionisation

Virtual States and Two Photon Absorption

The absorption probability of a single photon (A) to populate a particular state, or superposition of states (wavepacket) in an excited electronic state is dependent on the probability for the transition, determined from equation 1.5, the intensity of the incident light (I) and electric field vector of the incident light ($\boldsymbol{\varepsilon}$). Combining these three factors gives:

$$A = I\left|\int \Psi'(\boldsymbol{\mu}\boldsymbol{\varepsilon})\Psi'' d\tau\right|^2 \tag{1.20}$$

However, excitation to some final states can also occur through two-photon excitation, where a virtual state is accessed by the first photon (which borrows intensity from nearby states) and the second photon then promotes the electron from the virtual state to the final state.[45-48] Due to the process involving two photons, a different set of selection rules apply to two-photon transitions (such as those governing the change in angular quantum number – L: $\Delta L = 0, \pm 2$), while the virtual state that is accessed is governed by one-photon selection rules. The lifetime of the virtual state is very short and the total process requires the two photons to be absorbed simultaneously. Two-photon excitation is schematically illustrated in figure 1.8 a) involving excitation from an initial state (Ψ'') to a final state (Ψ') by populating a virtual state (Ψ_n) that lies halfway between the two.

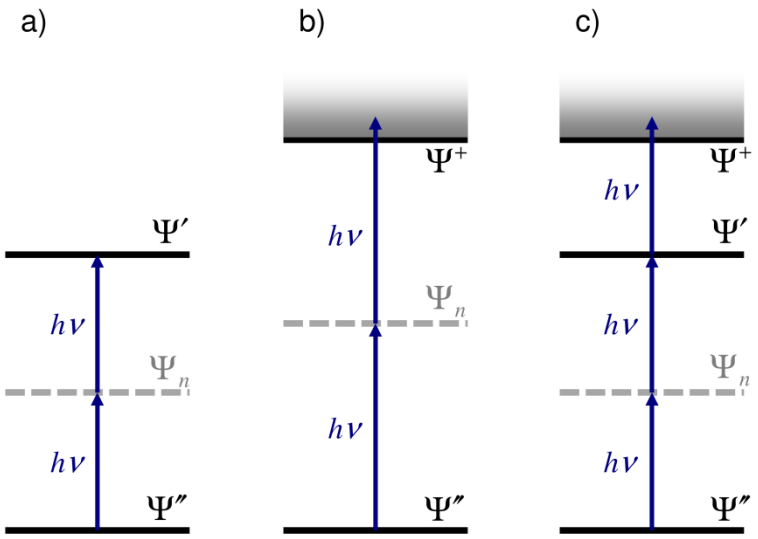

Figure 1.8 – Multiphoton processes showing: a) two-photon absorption from an initial state (Ψ'') to a final state (Ψ') via a virtual state (Ψ_n), b) (1+1) multiphoton ionisation from an initial state (Ψ'') to an ionic state (Ψ^+) via a virtual state (Ψ_n) and c) (2+1) resonance enhanced multiphoton ionisation where two-photon absorption occurs from an initial state (Ψ'') to a resonant state (Ψ') via a virtual state (Ψ_n) before excitation to the ionic state (Ψ^+).

The absorption for a two-photon transition (A) can be expressed as a pair of overlap integrals, each similar to the equation for a one-photon transition (equation 1.20), as:

$$A \propto I^2 \left| \sum_n \frac{\int \Psi_n (\boldsymbol{\mu}\boldsymbol{\varepsilon}) \Psi'' d\tau \int \Psi' (\boldsymbol{\mu}\boldsymbol{\varepsilon}) \Psi_n d\tau}{E' - E_n - h\nu} \right|^2 \qquad (1.21)$$

In the above expression $\boldsymbol{\mu}$ is the dipole moment operator and $\boldsymbol{\varepsilon}$ is the electric field vector of the light with intensity I. E' and E_n are the energy of the final and virtual states, respectively, and $h\nu$ is the photon energy. The probability is a sum over n, giving a range of possible virtual states accessed during the excitation, to account for the energetic bandwidth of the incident light. From equation 1.21 it is clear that the overall probability for the transition is dependent on the square of the light

intensity.[47] Furthermore, it is apparent that the transition probability is dependent on the relative angle between the vectors $\boldsymbol{\mu}$ and $\boldsymbol{\varepsilon}$ if polarised light is being used.

Multiphoton Ionisation

In a similar mechanism to two-photon excitation to an electronically excited state, it is also possible to undergo two-photon excitation to an ionic state, to generate a photoelectron and cation. This case is shown in figure 1.8 b) and has less specificity on $h\nu$ as the final state is a continuum. The continuum has the form of the first cationic state (Ψ^+) and the wavefunction for a free electron. The electron will have a kinetic energy equal to the difference between the energy absorbed by the molecule (combined energies of the photons) and the molecules' ionisation potential (IP).[48] The case shown in figure 1.8 b) illustrates a two photon process, that obeys similar constraints as two-photon absorption. Multiphoton ionisation can occur with more than two photons, although the probability of ionisation is significantly reduced as the likelihood of more photons being absorbed simultaneously is less.

Resonance Enhanced Multiphoton Ionisation

The third case in figure 1.8 c) shows multiphoton ionisation, requiring 3 photons, via a resonant electronic state. (2+1) resonance enhanced multiphoton ionisation (REMPI) occurs through two-photon absorption to a resonant state followed by ionisation with a third photon. The probability of ionisation is usually governed by equation 1.21, for two-photon absorption (in this case the final state Ψ' is the resonant state), as the probability of absorbing the third photon is typically far higher than the first two photons. REMPI is very sensitive to the level of the resonant state, which greatly increases the ionisation probability compared to non-resonant

multiphoton ionisation. Due to this, REMPI can be used to elucidate the transition energy to a particular electronic state and specific vibrational eigenstate by varying the photon energy and measuring the increase/decrease in ion or electron yield.

REMPI is extensively used as a probing technique in this thesis as a means of selectively ionising particular radical products. An example of this selectivity is the ionisation of hydrogen generated through photodissociation, where three photons of 41100 cm^{-1} are used to preferentially ionise hydrogen through a two-photon transition to the 2s level. A similar mechanism is also employed to detect methyl radicals by a (2+1) REMPI mechanism through a two-photon transition to the 3p $^2A_2''$ state, using three photons with a photon energy of 30000 cm^{-1}.

1.3.2 Photoproduct Kinetic Energy Detection

While REMPI spectroscopy can be used to elucidate the transition energy to a particular state, the evolution of that state requires the implementation of other forms of spectroscopy. These studies are typically based upon photoelectron spectroscopy or photofragment translational spectroscopy, where the kinetic energy and angular dependence of either electrons or ions is measured.

Photoelectron spectroscopy relies on extraction of an electron from a particular electronic state. Measurement of the electron's kinetic energy can then be compared to the molecule's IP to determine the energy of the electronic state. The kinetic energy of the electron (eKE) is given by equation 1.22, which was originally determined from the photoelectric effect.[49]

$$\mathrm{eKE} = h\nu - \mathrm{IP} = \frac{1}{2} m_e v^2 \tag{1.22}$$

In the above equation $h\nu$ is the photon energy, IP will be the difference between the emitting electronic state and the first cationic state, m_e is the mass of the electron and v is the electron velocity. Photoelectron spectroscopy is a very powerful technique as it can be used to detect optically "dark" and non-fluorescing states, due to the relaxed selection rules associated with the ionisation process relative to other techniques. It also allows one to track excited state energies of a molecule as it undergoes nuclear rearrangement when utilised as part of a pump probe scheme. In such studies, photoelectron kinetic energy is usually detected by time of flight (TOF) detection techniques or velocity map imaging (VMI). Photoelectron spectroscopy can provide complementary information to photofragment spectroscopy that is employed in the studies herein.[32, 50-52]

Photofragment Translational Spectroscopy

Photofragment translational spectroscopy can be used to detect the kinetic energy of a particular fragment after photodissociation. Typical experiments involve photoexcitation to a dissociative (or pre-dissociative) region of a PES and measurement of kinetic energy release of the resulting photofragments. In these cases the kinetic energy release of the photoproducts can be used to determine the electronic state of each fragment formed and infer information about the photodissociation mechanism.

Similar to photoelectron spectroscopy, discussed above, TOF mass spectrometry techniques are often employed to study the kinetic energy release of photofragments from a photoexcited molecule.[53, 54] Techniques of this type can prove useful for determining which photofragments are formed and in which

electronic state they are formed, as the difference between the photon energy and the photofragment kinetic energy release will provide information about the internal energy of the fragment. The total energy in the excitation/dissociation process is conserved and thus can be expressed by:

$$E_{AB} + h\nu = D_0 + E_A + E_B + TKER \tag{1.23}$$

where E_{AB}, E_A and E_B are the internal energies of the parent molecule and the two photofragments, respectively, D_0 is the bond dissociation energy and TKER is the total kinetic energy release. The TKER is the kinetic energy of both fragments combined, which will be partitioned between the two fragments to due to conservation of momentum, such that:

$$TKER = KER_A\left(\frac{M_A + M_B}{M_A}\right) = KER_B\left(\frac{M_B + M_A}{M_B}\right) \tag{1.24}$$

where KER_A and KER_B is the kinetic energy release of each fragment and M_A and M_B is the mass of each fragment. If the molecule of interest is studied in a molecular beam, E_{AB} is close to zero and the vibrational energy can be assumed to be zero. The terms on the right of equation 1.23 are then equal to the photon energy ($h\nu$) which is known. When D_0 is well-defined, the total internal energy of both fragments can be inferred as the TKER can be determined from the experiment. However, it is very difficult to determine the internal energy of each fragment as there may be numerous ways the internal energy can be partitioned between the two photofragments; this can be avoided when one of the fragments is hydrogen (see below).[55]

The kinetic energy of the photofragment can be measured, much like photoelectrons, by its translational velocity (proportional to the square root of the

kinetic energy release). Many methods for measuring the translational velocity exist. The main techniques used are high Rydberg atom photofragment translation spectroscopy (HRA-PTS),[55] spatial (multimass) imaging [56] and VMI.[57] A brief outline of these techniques will now be discussed, with VMI discussed further in Chapter 2 as this forms the basis of the experiments performed herein.

HRA-PTS [55] overcomes the Coulombic interactions between ions by ionising the neutral hydrogen fragments just before detection at the end of the TOF. The ionisation is achieved by exciting the hydrogen fragment to a high Rydberg level in the interaction region, in which it remains for the duration of the TOF.[55, 58] The highly excited hydrogen is then "field ionised" from this Rydberg level by an electric field in front of the ion detector. HRA-PTS relies on the ability to field ionise a long lived Rydberg state of hydrogen; for molecular fragments the presence of vibrational modes can prevent a neatly resolved field ionisation process. As a result, HRA-PTS has mostly been employed to study the dissociation of hydrogen atoms, as a high Rydberg level can be easily prepared and then ionised.[59, 60] The study of hydrogen dissociation from a number of heteroatom hydride species by HRA-PTS has been extensive in recent years, as this allows for the accurate detection of the co-fragment's internal energy.

Multimass imaging is another method for measuring the translational energy of each fragment (though with poorer resolution than HRA-PTS) and involves the imaging of fragments that are spatially separated by their mass. Photofragments are generated and then ionised, with a vacuum ultraviolet (VUV) laser at a fixed time and spatial separation. The ions are then mapped by their position (using a series of electrostatic plates) onto an imaging detector. The distance in the spatial image from

the central point of photofragment generation can then be related to the velocity of each photofragment.[56, 61] One advantage of using spatial imaging is that the fragments can also be mapped onto the detector by their mass; this allows simultaneous detection of multiple fragments, which is not possible through HRA-PTS and most VMI setups.

1.3.3 Velocity Map Imaging

Another technique that allows the detection of photoproduct kinetic energy is VMI, which can be implemented to study both photoelectrons and photofragments. Previous studies have shown the versatility of VMI as a means of performing high energy resolution spectroscopy, particularly in photofragment studies;[57, 62-67] while it has also been used as a detection scheme in pump probe experiments, with energy resolution limited by the time energy uncertainty of the laser pulses.[66-70] VMI was pioneered by Eppink and Parker,[57] who first suggested modification of a Wiley-McLaren type TOF spectrometer [58] to map charged particles by their velocity, independently of their initial spatial coordinates. Although the use of TOF electrodes and imaging was previously implemented to study photodissociation processes, [71] it was the conversion of these TOF electrodes to a set of Einzel lenses that could focus charged particles onto a position sensitive detector that was crucial for VMI. VMI works through projecting a three dimensional (3D) distribution of charged particles onto a position sensitive detector. The resulting two dimensional (2D) distribution is then deconvoluted to determine the ion's radius in the original 3D distribution, which can be related to the particle's velocity.[72] Although a very useful technique VMI also has its limitations, one of which is the need for deconvolution which reduces the signal levels significantly. Further information

about a photodissociation pathway can be gleaned by measuring the photoproducts angular distribution (which is retained in velocity mapping) relative to the electric field vector of the dissociating light. In particular the angular dependence provides details about the state (or states) accessed in the photoexcitation.[73] A discussion about the origins of the angular distribution of photoproducts and further details about the experimental setup implemented herein can be found in section 2.2.2.

1.4 Photochemical Processes in Biomolecule Sub-Units

All of the techniques discussed above can be employed to study the photochemical processes that underpin the photostability of numerous biomolecules and their sub-units. By studying the evolution of an excited electronic state following photoexcitation with UV radiation, techniques such as time resolved photoelectron spectroscopy, HRA-PTS and VMI, enables one to study how the population of an excited state can dissipate harmful UV energy through non-radiative processes and can lead to either ground state repopulation or photodissociation. By employing HRA-PTS and VMI, it is possible to study the mechanisms involved in the photodissociation process, assess what states are involved and infer information about possible excited state depopulation mechanisms mediated by these states. This is of particular relevance to the study of biological building blocks, such as DNA bases and amino acids, which demonstrate a low level of fluorescence upon photoexcitation, suggesting that fast non-radiative processes are operative.[2, 3, 74-77]

1.4.1 Photodamage and Photostability

The absorption of UV photons by large biological structures, such as DNA strands, can lead to a multitude of harmful processes due to the higher reactivity of excited electronic states. However, previous studies have shown that only a small fraction (<1%) of photoexcited DNA undergoes photoreactions, resulting in photolesions and DNA mutations that can lead to carcinogenesis.[78, 79] The photostability comes from the way that evolution has set in place protective mechanisms that can dissipate the energy of each photon, returning molecules to their less reactive electronic ground state. Furthermore, various repair mechanisms are present to mend damaged sites whilst skin pigments exist to absorb the majority of UV radiation, thereby acting as a front line defence to UV exposure.[80-82]

The absorption of DNA mononucleotides (the base, sugar and phosphate) and nucleosides (the base and sugar) in the UV region typically involves a singlet excitation from an occupied π orbital to a π antibonding orbital ($^1\pi\pi^*$) on the DNA base. The photostability mechanisms are theorised to involve fast non-radiative processes from this $^1\pi\pi^*$ state that can repopulate the electronic ground state of the molecule and allow the photon energy to be dissipated through intermolecular interactions with the surrounding solvent, ultimately leading to less harmful, thermal energy.[2, 3] Much of the work in this area has originated from earlier studies which show that the fluorescence quantum yield of individual DNA bases is particularly low upon excitation in the near UV.[83] This suggests that fast non-radiative dynamics occur within independent bases, implying that the dynamics observed in complete mononucleotides and nucleosides is dominated by the dynamics of the base. However studies have also examined the fluorescence quantum yield of larger

oligonucleotides (single strands of many nucleotides) and found that they also possess this abnormally low fluorescence quantum yield. While a contribution from the mononucleotide photorelaxtion processes are observed in oligonucleotides, the formation of strands can lead to an increase in potential relaxation mechanisms.[77, 83-85] A vast area of study has now arisen to investigate how the structure of biomolecule sub-units influences the non-radiative relaxation processes.

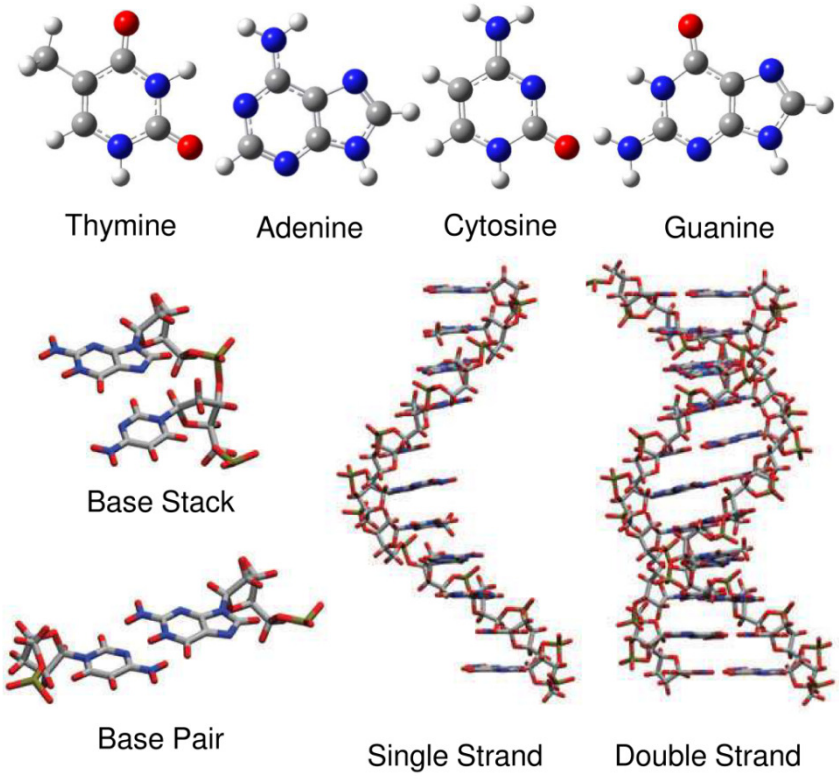

Figure 1.9 – The structure of the four DNA bases and an example of a DNA base stack dinucleotide, base paired nucleotides, single oligonucleotide strand and double oligonucleotide strand. This figure is modified from reference [3].

These studies encompass investigation of synthesised single and double DNA oligonucleotide strands (studied in solution), hydrogen bonded DNA base pairs, the individual mononucleotides / nucleosides and the bases: adenine (A), guanine (G), cytosine (C) and thymine (T) (also the ribonucleic acid (RNA) base uracil (U)). The

structures of these various DNA components are shown in figure 1.9 and a summary of these studies will now be discussed.

DNA Intrastrand Studies

Numerous studies have been carried out to examine which electronic states are accessed (and their lifetimes) when a single strand of DNA is excited with a photon of UV light. The majority of these have looked at well-defined strands that have been synthetically produced to only contain a single DNA base or a controlled distribution of two bases. Due to the size of the DNA strands, typically 2 to 20 nucleotides, these experiments have been carried out in solution, usually aqueous, and studied with a combination of LIF and transient absorption.[86-89]

Studies on single DNA strands aim to look at the influence of base stacking on the lifetime of the initially accessed excited electronic state. Numerous studies have shown that the lifetime of the initially excited state (a localised $^{1}\pi\pi^{*}$) in polynucleotides is short. While a similar non-radiative mechanism to that of isolated bases may contribute (discussed below), in a significant proportion of polynucleotide systems studied, the timescale for repopulation of the electronic ground state is far longer than for an isolated base or nucleotide. The suggested mechanism for these systems is that the initially $^{1}\pi\pi^{*}$ state decays into a series of excimer or exciplex states, where a significant amount of charge transfer (CT) occurs between bases in the base stack allowing for the photon energy to disperse. Excimer states are CT states between a dimer (or polymer) of identical bases and exciplex states are CT states between different bases. Work by Crespo-Hernandez *et al.* has shown that it is these excimer or exciplex states which are long lived, leading to the long timescale

for ground state repopulation.[3, 87] Studies have also shown that the overlap between the bases determines how effective the excimer or exciplex state is at dispersing the UV photon energy and that the CT state lifetime is dependent on the base sequence of the strand, with the guanine and thymine bases showing less excimer/exciplex contribution.[86, 87] The lifetime of these long lived states has been measured to be between tens of picoseconds and nanoseconds. Phillips and co-workers originally speculated that these excimer and exciplex states allow for fast dissipation of the photon energy into a state that can slowly fluoresce at a greatly red-shifted (less harmful) wavelength rather than via heat transfer.[86]

These investigations by Crespo-Hernandez *et al*. have also looked at the effect of excimer/exciplex states on the lifetime of excited states in hydrogen bonded double stranded DNA (double helix) and found similar dynamics to that observed in single strands. A recently proposed mechanism that relies on electron and proton transfer between hydrogen bonded bases has led to debate as to whether the base stacking mechanism dominates double stranded DNA dynamics. However contribution of excimer and exciplex states has been observed in the majority DNA double strands studied, showing similarities to previous work on DNA single strands.[3, 87, 89]

Interstrand Base-Base Interactions

An alternative mechanism proposed for the dissipation of photon energy and ground state repopulation in DNA is proton coupled electron transfer between hydrogen bonded base pairs. Numerous experimental [90-95] and theoretical studies [96-100] have been performed on hydrogen bonded DNA nucleotide pairs, or models

thereof, to measure the timescale for ground state repopulation. The major focus of these works has been on the hydrogen bonded G-C base pair (shown in figure 1.10 a)) and the 2-aminopyridine dimer which serves as a model base pair system.[96, 98]

Experimental work by Temps and co-workers on the G-C base pair in solution has shown that the rate of excited $^1\pi\pi^*$ state depopulation is quicker than either cytosine or guanine monomer.[93] Work on the G-C base pair and the RNA A-U base pair have also shown that the rate of intermolecular vibrational redistribution is increased when a base pair is formed, suggesting that vibrational cooling is efficient once ground state repopulation is achieved.[90, 95]

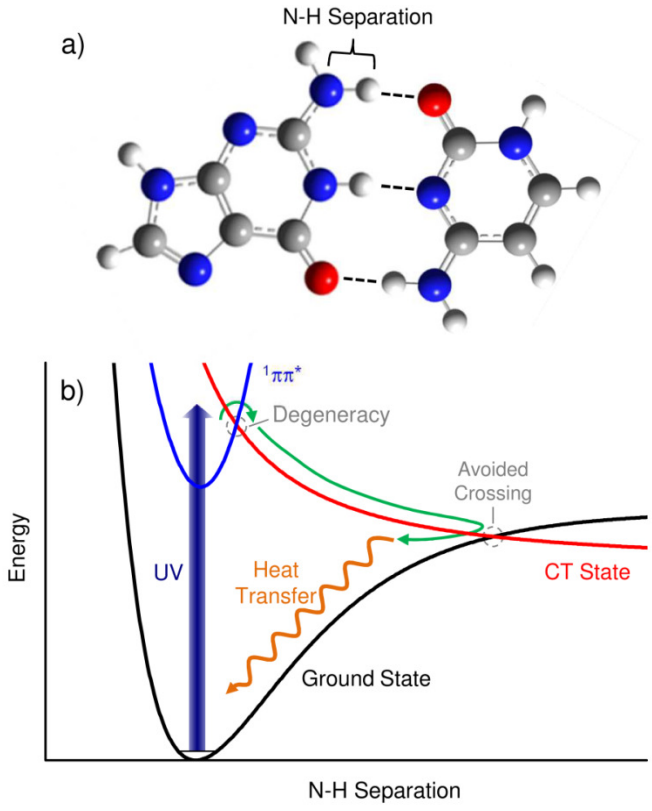

Figure 1.10 – a) Cytosine-guanine hydrogen bonded base pair; b) schematic PECs along an N-H coordinate in hydrogen bonded guanine, showing the mechanism for ground state repopulation by accessing a charge transfer (CT) state upon N-H elongation. The schematic PECs are based upon those calculated and discussed in reference [98].

Schultz and co-workers have performed gas phase studies and observed that monomer-like dynamics still play a major role in analogous model A-T base pairs, proposing a two step decay mechanism via an $^1n\pi^*$ state similar to isolated DNA bases (see below).[92, 97] These authors also see a small contribution from a long lived state that they attribute to a CT state between the hydrogen bonded bases.[92, 94]

Theoretical work on DNA base pairs has suggested a mechanism by which repopulation of the ground state may occur. Work by Sobolewski *et al.* on the G-C DNA base pair [98] and other model systems [96, 97] has shown that a CT state exists, induced by electron transfer between bases. Upon elongation of one of the hydrogen bonded N-H coordinates (towards either N or O on the complementary base pair), this CT state forms a weakly avoided crossing with the electronic ground state. Non-adiabatic dynamics can repopulate the ground state, potentially leading to recapture of the "dissociated" proton within the hydrogen bond, and heat dissipation through intermolecular vibrational energy redistribution. [96-101] The overall process for ground state repopulation is shown schematically in figure 1.10 b).

Although the experimental studies in this area seem to show that base pairing leads to a change in excited state lifetime, direct experimental observation of hydrogen transfer has yet to be performed. This has led to some contention as to whether base pairing or base stacking is the dominant pathway that controls the excited state dynamics.[2, 3] However the proposed theory for proton coupled electron transfer between base pairs shows similarities to a proposed mechanism for isolated DNA bases, which also relies on the elongation of a heteroatom-hydrogen bond coordinate. In this case however, there is no hydrogen bond with an opposing

heteroatom to "recapture" the dissociated hydrogen, and thus full dissociation can occur. As a result, studies on hydrogen photodissociation may provide a "bottom up" approach for studying the viability of this base pair mechanism; an approach which is central to the work described in this thesis.

Photostability in Single DNA Bases and Mononucleotides

DNA bases (with the exception of guanine) have been studied extensively due to the ease with which they can be introduced into vacuum for gas phase studies and dissolved in solution for liquid phase studies. As previously discussed, the fluorescence quantum yield of DNA is unusually low, upon near UV excitation, but time resolved studies of individual nucleotides, nucleosides and bases were not performed until the early 2000s. These studies measured the lifetime of the first $^1\pi\pi^*$ state in all four nucleotides following photoexcitation in the near UV.[102] In all four nucleotides studied, results implicate the localised electronic structure of the bases as governing the photorelaxation process and measured excited state lifetimes of less than a picosecond in all cases.[103, 104] This work suggests an IC mechanism is causing ground state repopulation on an ultrafast timescale. The results were loosely attributed to the involvement of IC to an optically "dark" $^1n\pi^*$ states accessed via a CI - the $^1n\pi^*$ state corresponds to a transfer of an electron out of a lone pair orbital into a π antibonding orbital.

$^1n\pi^*$ states in DNA bases have been studied using various theoretical approaches which find that they typically lie lower in energy that the first $^1\pi\pi^*$ state. This enables $^1n\pi^*$ states to act as mediators for ground state repopulation. Originally, work by Broo on adenine [105] suggested that a crossing between the first $^1\pi\pi^*$ state

and the first $^1n\pi^*$ state forms a CI that can lead to depopulation of the initially excited $^1\pi\pi^*$ state. Theoretical studies have found that access to this $^1\pi\pi^*$ / $^1n\pi^*$ CI exists along ring deformation coordinates and that a similar set of CIs are present in all DNA bases.[99-101, 105-113]

The presence of $^1n\pi^*$ states in DNA bases have been experimentally measured by various groups through transient absorption (in the condensed phase) and other pump probe techniques.[114-118] These studies have determined that the $^1\pi\pi^* \rightarrow {}^1n\pi^*$ IC an ultrafast process that accounts for a large proportion of excited state relaxation.[107, 114, 115, 119, 120] These studies also account for the disparities in lifetimes of the $^1\pi\pi^*$ states for different bases, due to the relative efficiency of accessing the theoretically predicted $^1\pi\pi^*$ / $^1n\pi^*$ CI, in particular highlighting the longer lifetimes observed in the pyrimidine bases where this mechanism is less favoured.[102, 121, 122] While experimental and theoretical studies have shown that $^1n\pi^*$ states may determine excited state lifetimes in DNA bases there is still some contention, largely based upon an alternative excited state relaxation pathway suggested by Sobolewski and Domcke, based on dissociative $^1\pi\sigma^*$ states (see below). As both mechanisms have been supported by numerous experimental studies, there is some disagreement about the favoured relaxation process.[2, 3, 112]

The complementary theory is based on the presence of $^1\pi\sigma^*$ states, formed by the excitation of an electron from a π orbital to a σ antibonding orbital centred on a heteroatom hydride bond (i.e. X-H coordinates, where X is O, N or S). Initial work on model malonaldehyde [123] showed the presence of a $^1\pi\pi^*$ / $^1\pi\sigma^*$ CI accessed by

elongation of the O-H coordinate. It was also theorised that access to this $^1\pi\sigma^*$ state may allow rapid ground state repopulation.[123, 124] Further studies then concluded that a similar $^1\pi\pi^*$ / $^1\pi\sigma^*$ CI mediated relaxation pathway may be operative in numerous heteroaromatic systems, such as the isolated DNA bases and aromatic amino acids.[60, 125-129] The suggested pathway for ground state repopulation relies on fast non-adiabatic coupling through a $^1\pi\pi^*$ / $^1\pi\sigma^*$ CI at an elongated heteroatom hydride bond length. Subsequently, further elongation leads to a crossing between the $^1\pi\sigma^*$ state and the ground state forming a $^1\pi\sigma^*$ / $^1\pi\pi$ CI which allows non-adiabatic repopulation of the ground state. $^1\pi\sigma^*$ mediated relaxation bears similarities to the hydrogen bonded base pair relaxation mechanism discussed above, as that too requires elongation of a heteroatom hydride coordinate. However, as noted above in isolated bases, no hydrogen transfer can occur and the elongation of the heteroatom hydride coordinate leads to elimination of hydrogen. This proves useful for studying the dynamics that govern the non-adiabatic passage through the $^1\pi\pi^*$ / $^1\pi\sigma^*$ and $^1\pi\sigma^*$ / $^1\pi\pi$ CIs as it is possible to measure the formation of the hydrogen photofragment and ultimately determine the timescale and energetics of the IC mechanism through pump probe spectroscopy.

Numerous experimental studies have looked at the role of $^1\pi\sigma^*$ states in DNA bases and have shown that it accounts for a significant proportion of the depopulation dynamics from the initially excited $^1\pi\pi^*$ electronic states (estimated to contributed 45 – 90 % in adenine [120]). While the overall photophysics of all DNA bases have been investigated [121, 122, 130, 131] many of the studies have focused on adenine. The dominance of only one adenine conformer in the gas phase has triggered a plethora of experimental and theoretical work on this molecule.[4, 119,

120, 132-139] Time dependent pump probe photoelectron and photofragment studies on adenine have shown that IC via the $^1\pi\pi^*$ / $^1\pi\sigma^*$ CI provides an ultrafast (sub-picosecond) pathway for depopulation of the initially populated $^1\pi\pi^*$ state. However, work on the isolated adenine base has raised questions about the relevance of such studies when compared to nucleotides and nucleosides. The reason for this is that one of the $^1\pi\sigma^*$ states studied extensively in adenine is localized along the N_9-H coordinate (see figure 1.1); in DNA bound adenine the N_9-H coordinate is replaced by a glycosidic (N_9-C) bone to the sugar-phosphate backbone. However. studies that focus on the NH_2 moiety have been performed which show similar hydrogen elimination dynamics to those along the N_9-H coordinate.[4, 127, 128] With the realisation that $^1\pi\sigma^*$ states occur ubiquitously throughout heteroaromatic systems, the current motivation for research has been to study model systems and chromophores of DNA bases, as these are easier to work with and allow for a "bottom-up" approach towards understanding excited state dynamics involving $^1\pi\sigma^*$ states in these systems.[60]

Aromatic Amino Acids

Similar $^1\pi\sigma^*$ mediated relaxation processes have been postulated for the photostability of the aromatic amino acids tyrosine, tryptophan and histidine.[5, 75, 76, 140] The number of studies on these molecules is limited, largely due to the reduced likelihood for significant photodamage (photolesions and carcinogenesis) from protein photoreactions in comparison to DNA photoreaction. However a few notable studies of $^1\pi\sigma^*$ mediated dynamics in the amino acid chromophores phenol, indole and imidazole have been performed.[59, 60]

In recent years a large number of studies have been performed on phenol. Phenol is largely responsible for the UV induced excited state dynamics in tyrosine and is an exemplar system to study the role of $^1\pi\sigma^*$ mediated dynamics, discussed below.

1.4.2 Studying $^1\pi\sigma^*$ States

The ubiquitous nature of $^1\pi\sigma^*$ states in heteroaromatic molecules has presented spectroscopists and theoreticians with a plethora of potential systems to study, with the aim of developing a general picture of the extent to which these states contribute to the photophysics and photochemistry of larger biomolecules. $^1\pi\sigma^*$ states localised on X-H coordinates have a distinct topography with respect to the X-H coordinate. This is illustrated in figure 1.11, which shows schematic PECs of the three lowest-lying singlet electronic states in phenol.

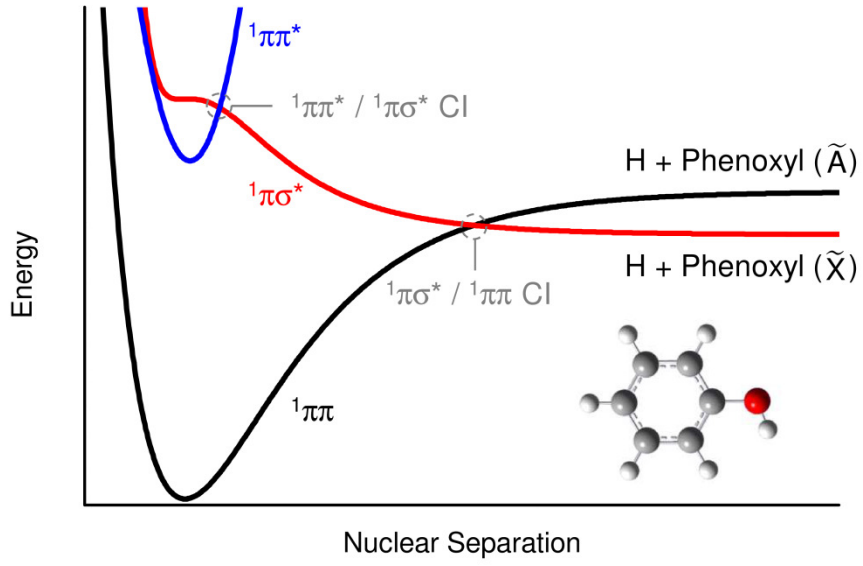

Figure 1.11 – Schematic PECs of the ground ($^1\pi\pi$) and first two singlet excited ($^1\pi\pi^*$ and $^1\pi\sigma^*$) electronic states in phenol with respect to O-H nuclear separation. Also labelled are the two relevant CIs and the radical photodissociation products. The schematic PECs are based on those calculated by Dixon *et al*. [8]

The plateau region of the $^1\pi\sigma^*$ state in the vertical Franck-Condon region is formed by the mixing of a $^1\pi$3s Rydberg state (4s in sulphur containing species) with the $^1\pi\sigma^*$ valence state localised along the X-H coordinate.[60, 141] In some cases, the mixing is very strong leading to a quasi-bound region supporting vibrational eigenstates, a notable example of which is aniline (aminobenzene).[142-146] Far from the vertical Franck-Condon region, the topography of the $^1\pi\sigma^*$ state is purely dissociative. Once this region is accessed, propagation to longer X-H separation shows repulsive character similar to purely dissociative states in simple heteronuclear diatomics.

Due to the localisation of the electronic state along a single X-H coordinate, $^1\pi\sigma^*$ states typically have low oscillator strengths upon photoexcitation from the electronic ground state. While in some molecules (such as aniline,[143-146], pyrrole [59, 147-150] and imidazole [59, 60, 151]) direct absorption to the $^1\pi\sigma^*$ state, via intensity borrowing, is observed (albeit very weakly), access to $^1\pi\sigma^*$ states typically relies on IC from nearby singlet excited states, such as $^1\pi\pi^*$ states, via a CI.

Conical Intersection Mediated Photodissociation

The study of $^1\pi\sigma^*$ mediated dynamics has mostly concentrated on photodissociation along X-H bond coordinates. This is certainly the case in phenol, which will serve in this initial discussion as a prototypical example for such dynamics. When excitation to the $^1\pi\pi^*$ state occurs in the Franck-Condon region (see figure 1.11), electronic state population can transfer to, and evolve along, the $^1\pi\sigma^*$ state towards a $^1\pi\sigma^*$ / $^1\pi\pi$ CI found at larger X-H separation. Motion adiabatically avoiding the $^1\pi\sigma^*$ / $^1\pi\pi$ CI can occur, traversing along the upper adiabatic state, or

passing non-adiabatically through the CI. Both cases can lead to the formation of hydrogen atoms and the phenoxyl radical co-fragment. Measuring the timescale and/or energy of the photodissociating hydrogen atoms can be used to infer the lifetime and energetics for $^1\pi\pi^*$ to $^1\pi\sigma^*$ transfer and radical formation processes.[8, 152, 153] By measuring the TKER following photodissociation it is also possible to determine the branching ratio of possible photoproducts and gain insight into the dynamics at the the$^1\pi\sigma^*$ / $^1\pi\pi$ CI. As shown in figure 1.11, non-adiabatic dynamics at the $^1\pi\sigma^*$ / $^1\pi\pi$ CI, will lead to the ground state radical co-fragment asymptote (phenoxyl ($\widetilde{X}$)). Adiabatic dynamics correlate to the excited electronic state radical asymptote (phenoxyl ($\widetilde{A}$)).[154] The branching between these two photoproduct channels will rely on the amount of non-adiabatic coupling, which is dependent on the velocity of nuclear motion and the gradient of the intersecting states (see section 1.2.3). It is important to note however that a particular channel at the CI may be inaccessible due to a geometric phase effect; a wavepacket bifurcates, destructively interferes with itself and extinguishes a particular branching channel.[44, 155, 156]

The presence of a $^1\pi\pi^*$ / $^1\pi\sigma^*$ CI may allow IC from the $^1\pi\pi^*$ state to the $^1\pi\sigma^*$ state if the photoexcitation energy exceeds the CI energy. Typical gas phase experiments on heteroaromatics have shown that, when excitation occurs above the $^1\pi\pi^*$ / $^1\pi\sigma^*$ CI, IC can occur within tens to hundreds of femtoseconds.[6, 7] There are a multitude of heteroaromatic molecules that can be found in nature, which have similar (but not identical) electronic structures, allowing for the study of how small changes in the electronic structure can affect the overall photodissociation process. In some cases however, the energies of the $^1\pi\pi^*$ and $^1\pi\sigma^*$ states can vary considerably,

with the relative ordering (in energy) switching between the two.[59, 151, 157] In such cases the excited state dynamics show marked differences.

Photoexcitation to higher lying excited states, such as higher energy $^1\pi\pi^*$ states resulting from different $\pi^* \leftarrow \pi$ transitions, can also yield photofragments formed via coupling to the $^1\pi\sigma^*$ state from these high lying states. [6, 7, 60, 61, 140, 158-160] This can complicate experimental results, particularly in studies performed at shorter wavelengths, as the observed signal may contain contributions from the excited state dynamics of multiple closely lying excited states. Furthermore, it can prove difficult to ascertain at what energy dissociation from the first $^1\pi\pi^*$ states (as discussed above) "switches-off" and the influence of these high lying states (or direct $^1\pi\sigma^*$ state population) begins. Dissociation following photoexcitation to these higher lying $^1\pi\pi^*$ states forms the basis for the experiments presented in chapters 3 and 4.

Tunnelling Between Electronic States

Quantum tunnelling can occur between electronic states when the excitation energy is below a barrier to dissociation. Using phenol as an example once more, and illustrated schematically in figure 1.12, this occurs from the region of the $^1\pi\pi^*$ state that lies (energetically) below the $^1\pi\pi^*$ / $^1\pi\sigma^*$ CI, resulting in the population of the $^1\pi\sigma^*$ state at extended O-H separation by hydrogen atom tunnelling. Once on the $^1\pi\sigma^*$ state, the molecule can proceed through to O-H dissociation.[8, 9] While tunnelling is observed in other molecules such as ammonia,[161, 162] tunnelling between different electronic states onto a dissociative $^1\pi\sigma^*$ state has mostly been studied in phenol and substituted phenol systems.[8, 163] The timescale for dissociation can be used to distinguish tunnelling mediated dynamics from $^1\pi\pi^*$ /

$^1\pi\sigma^*$ CI dynamics; typically the timescale for tunnelling will be significantly slower, between tens of picoseconds to several nanoseconds.[162-164]

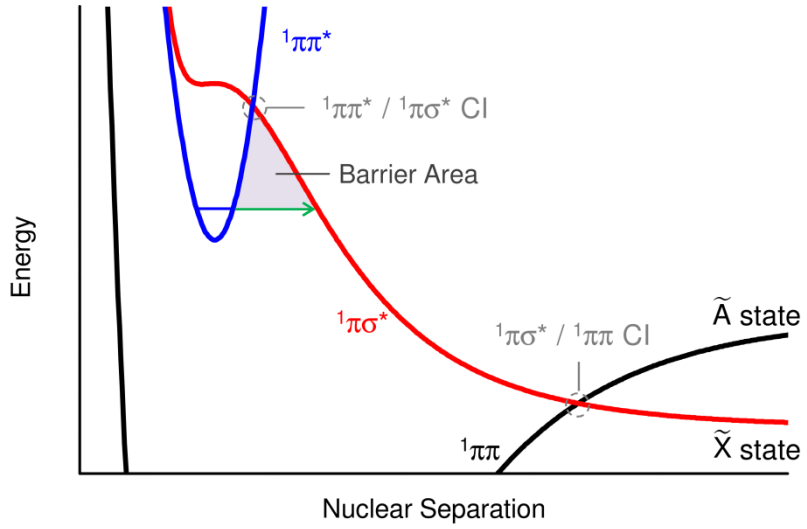

Figure 1.12 – Schematic PEC depicting tunnelling (green arrow) between the first $^1\pi\pi^*$ and $^1\pi\sigma^*$ state along the O-H coordinate in phenol at the zero point energy of the O-H stretch, leading to photodissociation of a hydrogen atom. The PECs shown are based upon those used to model tunnelling dynamics in phenol by Dixon *et al*. [8]

Other Heteroatom Coordinates

From the initial studies performed in systems possessing a $^1\pi\sigma^*$ state localised along a heteroatom hydride coordinate, it became apparent that $^1\pi\sigma^*$ mediated dynamics may play a crucial role in accounting for the excited state relaxation dynamics observed. However, similar $^1\pi\sigma^*$ states are also present along other heteroatom coordinates, such as X-CH_3 bonds and aryl halide systems.[165, 166] The study of these systems is also possible through photofragment detection as $^1\pi\sigma^*$ mediated dynamics may lead to bond dissociation, for example yielding CH_3 radicals. So far there have been fewer reports of research on $^1\pi\sigma^*$ mediated dynamics on X-CH_3 systems; however these studies have shown that methyl dissociation is a

possible pathway for excited state relaxation.[167-173] These studies may also prove useful for predicting photorelaxation pathways in the nucleoside, adenosine (and nucleotides thereof). Given that the N_9-H coordinate is replaced by a base-to-ribose N_9-C bond in adenosine, understanding the role of $^1\pi\sigma^*$ states localised along X-C coordinates will provide a "stepping stone" for studying more realistic systems. [120, 131] This will be discussed in more detail in chapters 4 and 5, which presents studies into the heteroatom-methyl systems anisole and thioanisole.

1.5 Outlook of Thesis

Chapter 1 of this thesis has provided a background to the potential photophysical and photochemical processes that underpin the dynamics of excited electronic states in molecules and highlighted how both time and energy resolved experiments can provide detailed insight of how excited states evolve. The role of non-adiabatic dynamics at CIs in biologically relevant systems has been extensively studied in an attempt to explain the ultrafast non-radiative excited state decay observed in many of these systems. One of the main relaxation pathways implicated involves $^1\pi\sigma^*$ states as a mediator for ground state repopulation. The ubiquitous nature of $^1\pi\sigma^*$ states has led to a multitude of possible systems to study, allowing for extensive characterisation of the factors effecting $^1\pi\sigma^*$ state mediated dynamics. The role of $^1\pi\sigma^*$ states is the main focus of this thesis, in particular, how the relative energetics of a $^1\pi\sigma^*$ state compared to other PESs can determine the evolution of photoexcited molecules.

In chapter 2 an outline of the experimental setup utilised to study $^1\pi\sigma^*$ mediated dynamics is provided. This will present a brief summary of the laser system implemented and an overview of the molecular beam source and TR-VMI setup. Furthermore an explanation of how the apparatus is calibrated and the procedure for data analysis will also be discussed.

Chapter 3 will focus on the effects of methyl substitution on the excited state dynamics in imidazole, following 200 nm photoexcitation. In particular, these studies seek to understand how differences in electronic structure determine the timescale for photodissociation. Imidazole links well with previous studies as it is a model for the five-membered ring of adenine, as shown in figure 1.1 a).

The potential for $^1\pi\sigma^*$ mediated dynamics along non-hydride heteroatom coordinates will be discussed in chapter 4, which looks at the dynamics that leads to $^1\pi\sigma^*$ mediated O-CH_3 dissociation in anisole (see figure 1.1 b)). This work, also following photoexcitation at 200 nm, highlights the relevance of the small number of studies on X-CH_3 centred $^1\pi\sigma^*$ states.

The presence of the sulphur atom takes centre stage in chapter 5, which focuses on how a $^1\pi\sigma^*$ state, now localised along the S-CH_3 coordinate influences the excited state dynamics of thioanisole. To conclude the discussion of the experimental results, chapter 6 presents TR-VMI results of the competing dissociation along two heteroatom containing coordinates (an O-H and O-CH_3 bond) in mequinol. This work provides insight into how different substituents, each having a localized $^1\pi\sigma^*$ state along their respective coordinates, affects the

photodissociation mechanism. Work in mequinol neatly ties together the work in anisole and previous studies into the excited state dynamics of phenol.

Finally chapter 7 of this thesis will present some concluding remarks about the role of $^1\pi\sigma^*$ states in photochemistry and present an outlook for future experiments in this rapidly growing area of research.

1.6 References

[1] A. H. Zewail, *J. Phys. Chem. A*, **104**, 5660 (2000).

[2] C. E. Crespo-Hernandez, B. Cohen, P. M. Hare and B. Kohler, *Chem. Rev.*, **104**, 1977 (2004).

[3] C. T. Middleton, K. de La Harpe, C. Su, Y. K. Law, C. E. Crespo-Hernandez and B. Kohler, *Annu. Rev. Phys. Chem.*, **60**, 217 (2009).

[4] K. L. Wells, D. J. Hadden, M. G. D. Nix and V. G. Stavros, *J. Phys. Chem. Lett.*, **1**, 993 (2010).

[5] A. Iqbal and V. G. Stavros, *J. Phys. Chem. Lett.*, **1**, 2274 (2010).

[6] A. Iqbal, L. J. Pegg and V. G. Stavros, *J. Phys. Chem. A*, **112**, 9531 (2008).

[7] A. Iqbal, M. S. Y. Cheung, M. G. D. Nix and V. G. Stavros, *J. Phys. Chem. A*, **113**, 8157 (2009).

[8] R. N. Dixon, T. A. A. Oliver and M. N. R. Ashfold, *J. Chem. Phys.*, **134**, 194303 (2011).

[9] G. M. Roberts, A. S. Chatterley, J. D. Young and V. G. Stavros, *J. Phys. Chem. Lett.*, **3**, 348 (2012).

[10] P. A. M. Dirac, *Proc. R. Soc. Lond. A*, **114**, 243 (1927).

[11] G. S. Beddard, G. R. Fleming, O. L. J. Gijzeman and G. Porter, *Chem. Phys. Lett.*, **18**, 481 (1973).

[12] D. Boyall and K. L. Reid, *Chem. Soc. Rev.*, **26**, 223 (1997).

[13] B. Valeur and M. N. Berberan-Santos, *J. Chem. Educ.*, **88**, 731 (2011).

[14] G. G. Stokes, *Phil. Trans.*, **142**, 463 (1852).

[15] M. Kasha, *Faraday Discuss.*, **9**, 14 (1950).

[16] P. Atkins and J. de Paula, *Physical Chemistry, 7th Edition*, Oxford University Press, 2002.

[17] J. L. Kinsey, *Annu. Rev. Phys. Chem.*, **28**, 349 (1977).

[18] M. Bixon and J. Jortner, *J. Chem. Phys.*, **48**, 715 (1967).

[19] D. Polli, P. Altoe, O. Weingart, K. M. Spillane, C. Manzoni, D. Brida, G. Tomasello, G. Orlandi, P. Kukura, R. A. Mathies, M. Garavelli and G. Cerullo, *Nature*, **467**, 440 (2010).

[20] G. Viswanath and M. Kasha, *J. Chem. Phys.*, **24**, 574 (1956).

[21] M. J. Bearpark, F. Bernardi, S. Clifford, M. Olivucci, M. A. Robb, B. R. Smith and T. Vreven, *J. Am. Chem. Soc.*, **118**, 169 (1996).

[22] T. S. Rose, M. J. Rosker and A. H. Zewail, *J. Chem. Phys.*, **88**, 6672 (1988).

[23] T. S. Rose, M. J. Rosker and A. H. Zewail, *J. Chem. Phys.*, **91**, 7415 (1989).

[24] N. F. Scherer, J. L. Knee, D. D. Smith and A. H. Zewail, *J. Phys. Chem.*, **89**, 5141 (1985).

[25] M. Dantus, M. J. Rosker and A. H. Zewail, *J. Chem. Phys.*, **89**, 6128 (1988).

[26] M. J. Rosker, M. Dantus and A. H. Zewail, *Science*, **241**, 1200 (1988).

[27] A. H. Zewail, *Angew. Chem. Int. Ed.*, **39**, 2587 (2000).

[28] P. Atkins and R. Friedman, *Molecular Quantum Mechanics, 5th Edition*, Oxford University Press, 2011.

[29] M. Born and J. R. Oppenheimer, *Ann. Physik*, **389**, 457 (1927).

[30] C. Eckart, *Phys. Rev.*, **46**, 383 (1934).

[31] D. M. Hirst, *Potential Energy Surfaces: Molecular Structure and Reaction Dynamics*, Taylor & Francis Ltd., 1985.

[32] G. R. Wu, P. Hockett and A. Stolow, *Phys. Chem. Chem. Phys.*, **13**, 18447 (2011).

[33] J. Franck, *Trans. Faraday Soc.*, **21**, 536 (1925).

[34] E. U. Condon, *Phys. Rev.*, **28**, 1182 (1926).

[35] E. U. Condon, *Phys. Rev.*, **32**, 858 (1928).

[36] J. M. Hollas, *Modern Spectroscopy*, John Wiley & Sons Ltd., 2004.

[37] C. Zener, *Proc. R. Soc. Lond. A*, **137**, 696 (1932).

[38] C. Wittig, *J. Phys. Chem. B*, **109**, 8428 (2005).

[39] K. R. Naqvi and W. B. Brown, *Int. J. Quantum Chem.*, **6**, 271 (1972).

[40] K. R. Naqvi, *Chem. Phys. Lett.*, **15**, 634 (1972).

[41] E. Teller, *J. Phys. Chem.*, **41**, 109 (1937).

[42] D. R. Yarkony, *Rev. Mod. Phys.*, **68**, 985 (1996).

[43] G. A. Worth and L. S. Cederbaum, *Annu. Rev. Phys. Chem.*, **55**, 127 (2004).

[44] W. Domcke, D. R. Yarkony and H. Köppel, *Conical Intersections: Theory, Computation and Experiments*, World Scientific Publishing Co. Pte. Ltd., 2011.

[45] M. Göppert-Mayer, *Ann. Physik*, **401**, 273 (1931).

[46] W. Demtröder, *Laser Spectroscopy*, Springer-Verlag Berlin Heidelberg, 1981.

[47] J. M. Hollas, *High Resolution Spectroscopy*, Butterworth & Co Ltd., 1982.

[48] S. H. Lin, Y. Fujimura, H. J. Neusser and E. W. Schlag, *Multiphoton Spectroscopy of Molecules*, Academic Press Inc., 1984.

[49] A. Einstein, *Ann. Physik*, **17**, 132 (1905).

[50] V. Blanchet, M. Z. Zgierski, T. Seideman and A. Stolow, *Nature*, **401**, 52 (1999).

[51] D. M. Neumark, *Annu. Rev. Phys. Chem.*, **52**, 255 (2001).

[52] A. Stolow, A. E. Bragg and D. M. Neumark, *Chem. Rev.*, **104**, 1719 (2004).

[53] M. N. R. Ashfold and J. E. Baggott, *Molecular Photodissociation Dynamics*, The Royal Society of Chemistry, 1987.

[54] R. Schinke, *Photodissociation Dynamics*, Cambridge University Press, 1993.

[55] H. J. Krautwald, L. Schnieder, K. H. Welge and M. N. R. Ashfold, *Faraday Discuss.*, **82**, 99 (1986).

[56] S.-T. Tsai, C.-K. Lin, Y. T. Lee and C.-K. Ni, *Rev. Sci. Instrum.*, **72**, 1963 (2001).

[57] A. T. J. B. Eppink and D. H. Parker, *Rev. Sci. Instrum.*, **68**, 3477 (1997).

[58] W. C. Wiley and I. H. McLaren, *Rev. Sci. Instrum.*, **26**, 1150 (1955).

[59] M. N. R. Ashfold, B. Cronin, A. L. Devine, R. N. Dixon and M. G. D. Nix, *Science*, **312**, 1637 (2006).

[60] M. N. R. Ashfold, G. A. King, D. Murdock, M. G. D. Nix, T. A. A. Oliver and A. G. Sage, *Phys. Chem. Chem. Phys.*, **12**, 1218 (2010).

[61] C. M. Tseng, Y. T. Lee, M. F. Lin, C. K. Ni, S. Y. Liu, Y. P. Lee, Z. F. Xu and M. C. Lin, *J. Phys. Chem. A*, **111**, 9463 (2007).

[62] A. T. J. B. Eppink and D. H. Parker, *J. Chem. Phys.*, **109**, 4758 (1998).

[63] T. Gougousi, P. C. Samartzis and T. N. Kitsopoulos, *J. Chem. Phys.*, **108**, 5742 (1998).

[64] K. T. Lorenz, D. W. Chandler, J. W. Barr, W. W. Chen, G. L. Barnes and J. I. Cline, *Science*, **293**, 2063 (2001).

[65] T. N. Kitsopoulos, C. R. Gebhardt and T. P. Rakitzis, *J. Chem. Phys.*, **115**, 9727 (2001).

[66] B. J. Whitaker, *Imaging in Molecular Dynamics: Technology and Applications*, Cambridge University Press, 2003.

[67] M. N. R. Ashfold, N. H. Nahler, A. J. Orr-Ewing, O. P. J. Vieuxmaire, R. L. Toomes, T. N. Kitsopoulos, I. A. Garcia, D. A. Chestakov, S. M. Wu and D. H. Parker, *Phys. Chem. Chem. Phys.*, **8**, 26 (2006).

[68] T. Suzuki, L. Wang and H. Kohguchi, *J. Chem. Phys.*, **111**, 4859 (1999).

[69] L. Wang, H. Kohguchi and T. Suzuki, *Faraday Discuss.*, **113**, 37 (1999).

[70] R. de Nalda, J. G. Izquierdo, J. Dura and L. Banares, *J. Chem. Phys.*, **126**, 021101 (2007).

[71] D. W. Chandler and P. L. Houston, *J. Chem. Phys.*, **87**, 1445 (1987).

[72] G. M. Roberts, J. L. Nixon, J. Lecointre, E. Wrede and J. R. R. Verlet, *Rev. Sci. Instrum.*, **80**, 053104 (2009).

[73] R. N. Zare, *Angular Momentum: Understanding Spatial Aspects in Chemistry and Physics*, Wiley-Blackwell, 1988.

[74] M. Daniels and W. Hauswirt, *Science*, **171**, 675 (1971).

[75] D. Creed, *Photochem. Photobiol.*, **39**, 537 (1984).

[76] D. Creed, *Photochem. Photobiol.*, **39**, 563 (1984).

[77] P. R. Callis, *Annu. Rev. Phys. Chem.*, **34**, 329 (1983).

[78] F. R. de Gruijl, *Eur. J. Cancer*, **35**, 2003 (1999).

[79] G. P. Pfeifer, Y. H. You and A. Besaratinia, *Mutat. Res.- Fund. Mol. M.*, **571**, 19 (2005).

[80] A. Sancar, *Chem. Rev.*, **103**, 2203 (2003).

[81] N. Agar and A. R. Young, *Mutat. Res.*, **571**, 121 (2005).

[82] Z. Liu, C. Tan, X. Guo, Y.-T. Kao, J. Li, L. Wang, A. Sancar and D. Zhong, *Proc. Natl. Acad. Sci. USA*, **108**, 14831 (2011).

[83] T. I. Aoki and P. R. Callis, *Chem. Phys. Lett.*, **92**, 327 (1982).

[84] P. Vingy and J. P. Ballini, in *Excited States in Organic Chemistry and Biochemistry*, eds. B. Pullman and N. Goldblum, D. Reidel Publishing Company, 1977, p. 1.

[85] A. Anders, *Chem. Phys. Lett.*, **81**, 270 (1981).

[86] R. Plessow, A. Brockhinke, W. Eimer and K. Kohse-Hoinghaus, *J. Phys. Chem. B*, **104**, 3695 (2000).

[87] C. E. Crespo-Hernandez, B. Cohen and B. Kohler, *Nature*, **436**, 1141 (2005).

[88] W. M. Kwok, C. S. Ma and D. L. Phillips, *J. Am. Chem. Soc.*, **128**, 11894 (2006).

[89] N. K. Schwalb and F. Temps, *Science*, **322**, 243 (2008).

[90] S. Woutersen and G. Cristalli, *J. Chem. Phys.*, **121**, 5381 (2004).

[91] E. Samoylova, H. Lippert, S. Ullrich, I. V. Hertel, W. Radloff and T. Schultz, *J. Am. Chem. Soc.*, **127**, 1782 (2005).

[92] N. Gador, E. Samoylova, V. R. Smith, A. Stolow, D. M. Rayner, W. G. Radloff, I. V. Hertel and T. Schultz, *J. Phys. Chem. A*, **111**, 11743 (2007).

[93] N. K. Schwalb and F. Temps, *J. Am. Chem. Soc.*, **129**, 9272 (2007).

[94] E. Samoylova, T. Schultz, I. V. Hertel and W. Radloff, *Chem. Phys.*, **347**, 376 (2008).

[95] M. Yang, L. Szyc, K. Rottger, H. Fidder, E. T. J. Nibbering, T. Elsaesser and F. Temps, *J. Phys. Chem. B*, **115**, 5484 (2011).

[96] A. L. Sobolewski and W. Domcke, *Chem. Phys.*, **294**, 73 (2003).

[97] T. Schultz, E. Samoylova, W. Radloff, I. V. Hertel, A. L. Sobolewski and W. Domcke, *Science*, **306**, 1765 (2004).

[98] A. L. Sobolewski and W. Domcke, *Phys. Chem. Chem. Phys.*, **6**, 2763 (2004).

[99] H. Saigusa, *J. Photochem. Photobio. C.*, **7**, 197 (2006).

[100] L. Serrano-Andres and M. Merchan, *J. Photochem. Photobio. C.*, **10**, 21 (2009).

[101] F. Plasser, M. Barbatti, A. J. A. Aquino and H. Lischka, *Theor. Chem. Acc.*, **131**, 1073 (2012).

[102] S. Ullrich, T. Schultz, M. Z. Zgierski and A. Stolow, *Phys. Chem. Chem. Phys.*, **6**, 2796 (2004).

[103] J. M. L. Pecourt, J. Peon and B. Kohler, *J. Am. Chem. Soc.*, **122**, 9348 (2000).

[104] J. M. L. Pecourt, J. Peon and B. Kohler, *J. Am. Chem. Soc.*, **123**, 10370 (2001).

[105] A. Broo, *J. Phys. Chem. A*, **102**, 526 (1998).

[106] N. Ismail, L. Blancafort, M. Olivucci, B. Kohler and M. A. Robb, *J. Am. Chem. Soc.*, **124**, 6818 (2002).

[107] C. M. Marian, *J. Chem. Phys.*, **122**, 104314 (2005).

[108] L. Serrano-Andres, M. Merchan and A. C. Borin, *Chem. Eur. J.*, **12**, 6559 (2006).

[109] L. Blancafort, *Photochem. Photobiol.*, **83**, 603 (2007).

[110] L. Serrano-Andres, M. Merchan and A. C. Borin, *J. Am. Chem. Soc.*, **130**, 2473 (2008).

[111] G. Zechmann and M. Barbatti, *J. Phys. Chem. A*, **112**, 8273 (2008).

[112] M. Barbatti, A. J. A. Aquino, J. J. Szymczak, D. Nachtigallova, P. Hobza and H. Lischka, *Proc. Natl. Acad. Sci. USA*, **107**, 21453 (2010).

[113] I. Conti, M. Garavelli and G. Orlandi, *J. Am. Chem. Soc.*, **131**, 16108 (2009).

[114] H. Kang, K. T. Lee, B. Jung, Y. J. Ko and S. K. Kim, *J. Am. Chem. Soc.*, **124**, 12958 (2002).

[115] H. Kang, B. Jung and S. K. Kim, *J. Chem. Phys.*, **118**, 6717 (2003).

[116] C. Canuel, M. Mons, F. Piuzzi, B. Tardivel, I. Dimicoli and M. Elhanine, *J. Chem. Phys.*, **122**, 074316 (2005).

[117] P. M. Hare, C. E. Crespo-Hernandez and B. Kohler, *J. Phys. Chem. B*, **110**, 18641 (2006).

[118] P. M. Hare, C. E. Crespo-Hernandez and B. Kohler, *Proc. Natl. Acad. Sci. USA*, **104**, 435 (2007).

[119] H. Satzger, D. Townsend, M. Z. Zgierski, S. Patchkovskii, S. Ullrich and A. Stolow, *Proc. Natl. Acad. Sci. USA*, **103**, 10196 (2006).

[120] C. Z. Bisgaard, H. Satzger, S. Ullrich and A. Stolow, *ChemPhysChem*, **10**, 101 (2009).

[121] M. Schneider, R. Maksimenka, F. J. Buback, T. Kitsopoulos, L. R. Lago and I. Fischer, *Phys. Chem. Chem. Phys.*, **8**, 3017 (2006).

[122] M. Schneider, C. Schon, I. Fischer, L. Rubio-Lago and T. Kitsopoulos, *Phys. Chem. Chem. Phys.*, **9**, 6021 (2007).

[123] A. L. Sobolewski and W. Domcke, *Chem. Phys. Lett.*, **310**, 548 (1999).

[124] A. L. Sobolewski and W. Domcke, *Chem. Phys. Lett.*, **300**, 533 (1999).

[125] A. L. Sobolewski and W. Domcke, *Chem. Phys.*, **259**, 181 (2000).

[126] A. L. Sobolewski, W. Domcke, C. Dedonder-Lardeux and C. Jouvet, *Phys. Chem. Chem. Phys.*, **4**, 1093 (2002).

[127] S. Perun, A. L. Sobolewski and W. Domcke, *Chem. Phys.*, **313**, 107 (2005).

[128] S. Perun, A. L. Sobolewski and W. Domcke, *J. Am. Chem. Soc.*, **127**, 6257 (2005).

[129] S. Yamazaki, W. Domcke and A. L. Sobolewski, *J. Phys. Chem. A*, **112**, 11965 (2008).

[130] E. Sarantopoulou, Z. Kollia, A. C. Cefalas, S. Kobe and Z. Samardzija, *J. Biol. Phys.*, **29**, 149 (2003).

[131] J. C. Marcum, A. Halevi and J. M. Weber, *Phys. Chem. Chem. Phys.*, **11**, 1740 (2009).

[132] M. Zierhut, W. Roth and I. Fischer, *Phys. Chem. Chem. Phys.*, **6**, 5178 (2004).

[133] M. G. D. Nix, A. L. Devine, B. Cronin and M. N. R. Ashfold, *J. Chem. Phys.*, **126**, 124312 (2007).

[134] K. L. Wells, G. M. Roberts and V. G. Stavros, *Chem. Phys. Lett.*, **446**, 20 (2007).

[135] M. Barbatti and H. Lischka, *J. Am. Chem. Soc.*, **130**, 6831 (2008).

[136] N. L. Evans and S. Ullrich, *J. Phys. Chem. A*, **114**, 11225 (2010).

[137] W. M. I. Hassan, W. C. Chung, N. Shimakura, S. Koseki, H. Kono and Y. Fujimura, *Phys. Chem. Chem. Phys.*, **12**, 5317 (2010).

[138] M. Barbatti and S. Ullrich, *Phys. Chem. Chem. Phys.*, **13**, 15492 (2011).

[139] S. Lobsiger, R. K. Sinha, M. Trachsel and S. Leutwyler, *J. Chem. Phys.*, **134**, 114307 (2011).

[140] C.-M. Tseng, Y. T. Lee, C.-K. Ni and J.-L. Chang, *J. Phys. Chem. A*, **111**, 6674 (2007).

[141] H. Reisler and A. I. Krylov, *Int. Rev. Phys. Chem.*, **28**, 267 (2009).

[142] T. Ebata, C. Minejima and N. Mikami, *J. Phys. Chem. A*, **106**, 11070 (2002).

[143] G. A. King, T. A. A. Oliver and M. N. R. Ashfold, *J. Chem. Phys.*, **132**, 214307 (2010).

[144] G. M. Roberts, C. A. Williams, J. D. Young, S. Ullrich, M. J. Paterson and V. G. Stavros, *J. Am. Chem. Soc.*, **134**, 12578 (2012).

[145] R. Spesyvtsev, O. M. Kirkby, M. Vacher and H. H. Fielding, *Phys. Chem. Chem. Phys.*, **14**, 9942 (2012).

[146] R. Spesyvtsev, O. M. Kirkby and H. H. Fielding, *Faraday Discuss.*, **157**, 165 (2012).

[147] J. Wei, A. Kuczmann, J. Riedel, F. Renth and F. Temps, *Phys. Chem. Chem. Phys.*, **5**, 315 (2003).

[148] B. Cronin, M. G. D. Nix, R. H. Qadiri and M. N. R. Ashfold, *Phys. Chem. Chem. Phys.*, **6**, 5031 (2004).

[149] J. Wei, J. Riedel, A. Kuczmann, F. Renth and F. Temps, *Faraday Discuss.*, **127**, 267 (2004).

[150] H. Lippert, H. H. Ritze, I. V. Hertel and W. Radloff, *ChemPhysChem*, **5**, 1423 (2004).

[151] A. L. Devine, B. Cronin, M. G. D. Nix and M. N. R. Ashfold, *J. Chem. Phys.*, **125**, 184302 (2006).

[152] M. G. D. Nix, A. L. Devine, B. Cronin, R. N. Dixon and M. N. R. Ashfold, *J. Chem. Phys.*, **125**, 133318 (2006).

[153] M. L. Hause, Y. H. Yoon, A. S. Case and F. F. Crim, *J. Chem. Phys.*, **128**, 104307 (2008).

[154] J. G. Radziszewski, M. Gil, A. Gorski, J. Spanget-Larsen, J. Waluk and B. J. Mroz, *J. Chem. Phys.*, **115**, 9733 (2001).

[155] M. G. D. Nix, A. L. Devine, R. N. Dixon and M. N. R. Ashfold, *Chem. Phys. Lett.*, **463**, 305 (2008).

[156] M. Abe, Y. Ohtsuki, Y. Fujimura, Z. G. Lan and W. Domcke, *J. Chem. Phys.*, **124**, 224316 (2006).

[157] D. J. Hadden, K. L. Wells, G. M. Roberts, L. T. Bergendahl, M. J. Paterson and V. G. Stavros, *Phys. Chem. Chem. Phys.*, **13**, 10342 (2011).

[158] C. A. Williams, G. M. Roberts, H. Yu, N. L. Evans, S. Ullrich and V. G. Stavros, *J. Phys. Chem. A*, **116**, 2600 (2011).

[159] G. M. Roberts, C. A. Williams, M. J. Paterson, S. Ullrich and V. G. Stavros, *Chem. Sci.*, **3**, 1192 (2012).

[160] G. A. King, T. A. A. Oliver, M. G. D. Nix and M. N. R. Ashfold, *J. Chem. Phys.*, **132**, 064305 (2010).

[161] M. F. Manning, *J. Chem. Phys.*, **3**, 136 (1935).

[162] R. P. Bell, *The Tunnel Effect in Chemistry*, Chapman-Hall, New York, 1980.

[163] G. A. Pino, A. N. Oldani, E. Marceca, M. Fujii, S. I. Ishiuchi, M. Miyazaki, M. Broquier, C. Dedonder and C. Jouvet, *J. Chem. Phys.*, **133**, 124313 (2010).

[164] M. F. Hineman, G. A. Brucker, D. F. Kelley and E. R. Bernstein, *J. Chem. Phys.*, **97**, 3341 (1992).

[165] A. G. Sage, T. A. A. Oliver, D. Murdock, M. B. Crow, G. A. D. Ritchie, J. N. Harvey and M. N. R. Ashfold, *Phys. Chem. Chem. Phys.*, **13**, 8075 (2011).

[166] D. Murdock, M. B. Crow, G. A. D. Ritchie and M. N. R. Ashfold, *J. Chem. Phys.*, **136**, 124313 (2012).

[167] A. G. Sage, M. G. D. Nix and M. N. R. Ashfold, *Chem. Phys.*, **347**, 300 (2008).

[168] G. Piani, L. Rubio-Lago, M. A. Collier, T. N. Kitsopoulos and M. Becucci, *J. Phys. Chem. A*, **113**, 14554 (2009).

[169] C. M. Tseng, Y. T. Lee and C. K. Ni, *J. Phys. Chem. A*, **113**, 3881 (2009).

[170] J. S. Lim and S. K. Kim, *Nature Chem.*, **2**, 627 (2010).

[171] D. J. Hadden, C. A. Williams, G. M. Roberts and V. G. Stavros, *Phys. Chem. Chem. Phys.*, **13**, 4494 (2011).

[172] D. J. Hadden, G. M. Roberts, T. N. V. Karsili, M. N. R. Ashfold and V. G. Stavros, *Phys. Chem. Chem. Phys.*, **14**, 13415 (2012).

[173] Y.-C. Ho, Y. A. Dyakov, W.-H. Hsu, C.-K. Ni, Y.-L. Sun and W.-P. Hu, *J. Chem. Phys.*, **137**, 194309 (2012).

2. Experimental

The details of the experimental setup utilised in this thesis are described below. The laser setup implemented in this thesis, outlined in section 2.1, consists of a Ti:sapphire oscillator and amplifier. Pump and probe wavelengths are obtained through the use of non-linear optical techniques, such as sum frequency generation and optical parametric generation. Section 2.2 includes information about: molecular beam generation, in this case formed by a pulsed solenoid valve; the vacuum chamber setup; the electrostatic lens (ion optics) setup within the interaction region; and the velocity map imaging setup utilised. A summary of how the time of flight and velocity map imaging system is calibrated is provided. Finally included is a section on the characterisation of the laser pulses to yield the instrument response function.

2.1 Laser Systems

2.1.1 The Femtosecond Laser

A Ti:sapphire (Ti^{3+} in Al_2O_3) oscillator (Spectra-Physics Tsunami) [1] produces pulses (4.7 nJ/pulse, 0.36 W) centred at 800 nm, with a pulse duration of ~80 fs at a repetition rate of 76 MHz. The oscillator is pumped by a frequency doubled continuous wave (CW) Nd:YVO_4 laser (Spectra-Physics Millenia), the output of which is set at 5 W centred at a wavelength of 532 nm. The ~80 fs pulses from the oscillator are formed by passive Kerr lens-modelocking, where the high electric field intensity of the pulses causes self-focusing within the lasing medium, allowing for selective amplification of these short pulses instead of the low electric field intensity, longer pulses (or CW modes).[2] A schematic representing laser action in a Ti:sapphire medium is shown in figure 2.1. The excited ^2E level is accessed with a 532 nm pump. Internal vibrational energy redistribution (IVR) then leads to population of a lower vibrational level. The ^2E state then undergoes stimulated emission back to the $^2T_2$ ground state before undergoing IVR to a low vibrational level completing a four level system. The interaction between the Ti^{3+} and Al_2O_3 lattice leads to a large range of vibrational levels (phonon modes) within each electronic level allowing a wide spectral bandwidth for the emission, which is necessary for the generation of short laser pulses.

Amplification of the pulse output from the oscillator is performed using a regenerative amplifier (Spectra-Physics Spitfire XP). The oscillator output or “seed” pulses are first temporally stretched to generate pulses on the order of picoseconds. 1 pulse in every 76,000 pulses of the seed pulse train are then amplified in a second

Ti:sapphire crystal, which is pumped by a frequency doubled, pulsed Nd:YLF laser (Spectra-Physics Empower) that outputs 100 nanosecond long pulses of ~30 W at 527 nm. Finally, the amplified pulses are then recompressed to short-pulse duration. This provides femtosecond pulses (3 mJ/pulse) centred at 800 nm, with pulse durations of ~40 fs and a repetition rate of 1 kHz. The pulses produced by the regenerative amplifier have a Gaussian spectral shape with a full width at half maximum (FWHM) of ~500 cm^{-1}. A representative spectrum of the outputted pulses is shown in figure 2.2, collected with an OceanOptics HR4000 spectrometer.

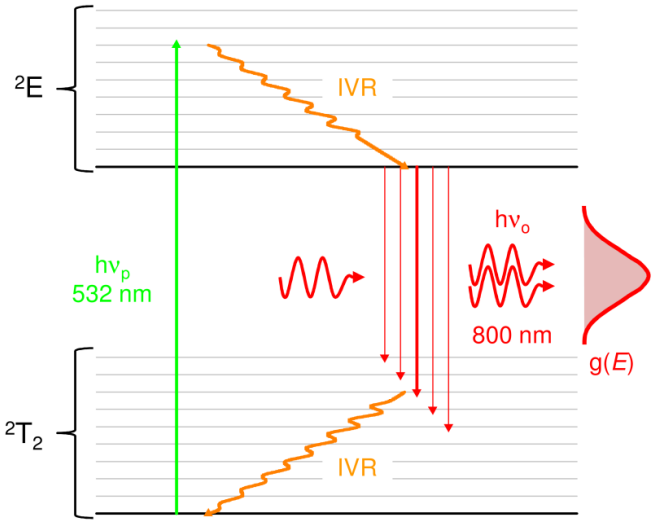

Figure 2.1 – Schematic of laser action in a Ti^{3+} ion within an Al_2O_3 lattice. Photon emission between ^2E and $^2T_2$ occurs over a wide range of wavelengths ($h\nu_o$) centred at 800 nm with a Gaussian distribution g(*E*). See text for details.

Due to the broad spectral absorption exhibited by the molecules studied the ability to photoexcite these molecules using a variety of wavelengths can be useful for understanding their electronic structure and how this drives the photodissociation pathway. To achieve this variety of pump wavelengths two laser setups are

employed. A simplified overview of the two laser setups in shown in figure 2.3 for the different pump generation mechanisms (see below).

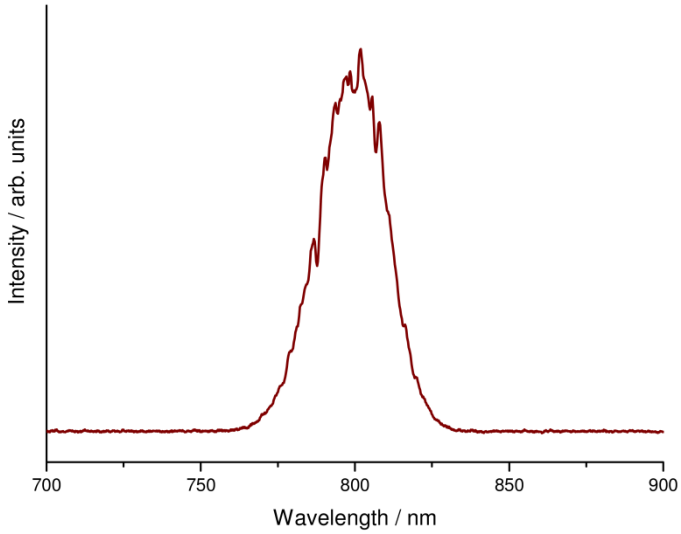

Figure 2.2 – Spectrum of the output from the Spitfire XP regenerative amplifier. The feature is Gaussian in shape centred at 795 nm with a FWHM of ~30 nm

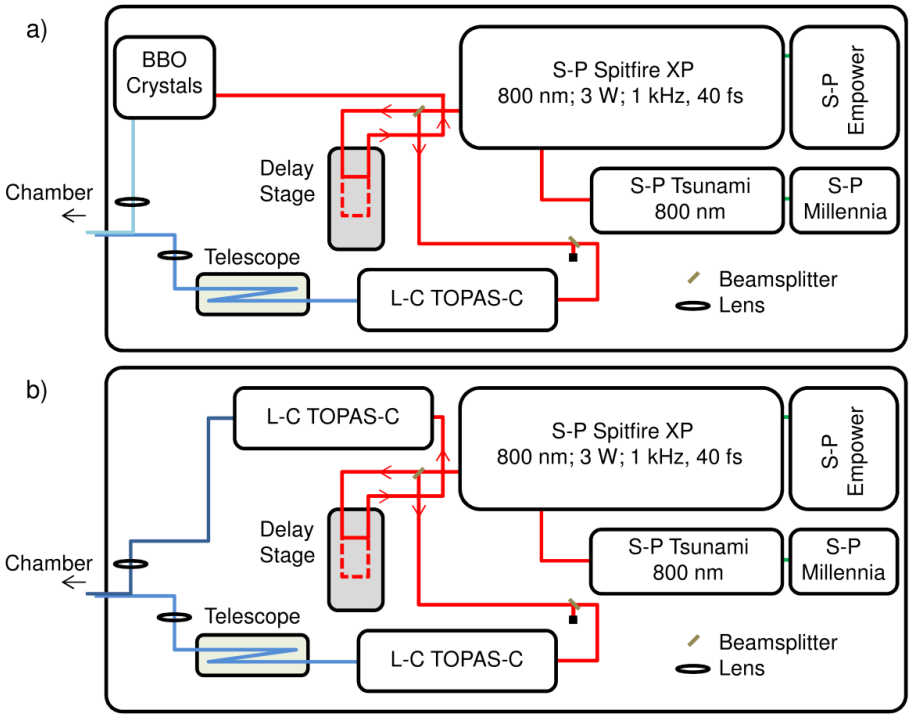

Figure 2.3 – Schematic of the laser table layout for a) pumping at 200 nm and probing with the output of a TOPAS-C; b) pumping and probing with a pair of TOPAS-C.

2.1.2 Non-Linear Optical Effects and Frequency Up-Conversion

The energy of a typical $\pi^* \leftarrow \pi$ transition is far greater than the photon energy of 800 nm light, output from the regenerative amplifier. As a result frequency up-conversion to the near ultraviolet (UV) wavelength region is required. The generation of femtosecond UV laser pulses relies on the use of non-linear optical effects in a non-linear material to frequency up-convert the fundamental 800 nm output from the regenerative amplifier. The non-linear processes used herein are either sum frequency generation (SFG), of which second harmonic generation (SHG) is a subset, or optical parametric generation (OPG).

Sum Frequency Generation

As the name suggests, SFG is used to produce light that has a frequency that is the sum, in this case, of two incident beams.[2-4] SHG is a specific case of SFG. SHG occurs in materials whose higher order electric susceptibility ($\chi^{(n)}$; where n > 1) is large. χ is the parameter that determines how a material's dielectric polarisation **P**, changes when an electric field **E**, is applied. In the case of an electric field from a laser pulse interacting with a non-linear medium, the polarisation is given by the equation:

$$\mathbf{P} = \varepsilon_0(\chi^{(1)}\mathbf{E} + \chi^{(2)}\mathbf{E}^2 + \ldots) \tag{2.1}$$

where ε_0 is the permittivity of free space. Equation 2.1 implies that the polarisation is dependent on a Taylor series that includes the higher order electric susceptibilities. The electric field of the laser pulses, **E**, can be described by the relationship:

$$\mathbf{E} = \mathbf{E_0}\sin(\omega t) \tag{2.2}$$

where ω is the laser frequency. Equation 2.2 can be substituted into equation 2.1 to give:

$$\begin{aligned}\mathbf{P} &= \varepsilon_0(\chi^{(1)}\mathbf{E_0}\sin\omega t + \chi^{(2)}\mathbf{E_0}^2\sin^2\omega t + \ldots) \\ &= \varepsilon_0(\chi^{(1)}\mathbf{E_0}\sin\omega t + \frac{1}{2}\chi^{(2)}\mathbf{E_0}^2(1-\cos 2\omega t) + \ldots)\end{aligned} \tag{2.3}$$

In the second term of equation 2.3 the trigonometric function depends on 2ω, implying that as **E** oscillates at ω, the dielectric polarisation oscillates at the second harmonic of this frequency. The medium undergoing this oscillating dielectric polarisation can then re-radiate photons at twice the fundamental frequency (and therefore energy). It is this behaviour that enables SHG, the overall process of which can be thought of as the summation of two photons of the same energy, to give one photon of double the initial photons' energy.[5] This is shown in figure 2.4 a), whereby for SHG $\omega_3 = 2\omega_1 = 2\omega_2$, when $\omega_1 = \omega_2$.

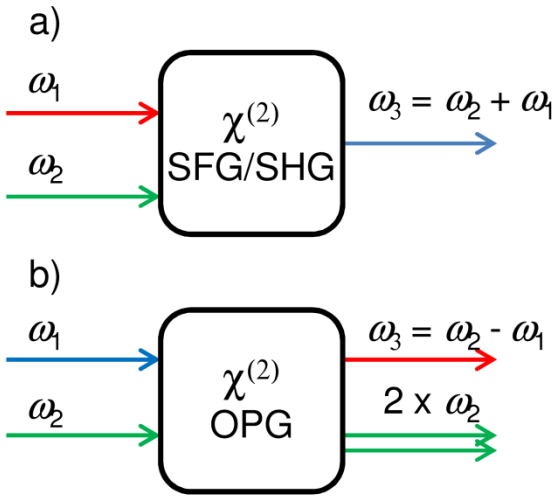

Figure 2.4 – Representation of the two non-linear processes used to generate pump and probe pulses; a) shows sum frequency generation (or second harmonic generation when $\omega_1 = \omega_2$) and b) shows optical parametric generation where the signal (ω_2) is amplified by a pump (ω_1) producing idler (ω_3) as a by-product.

Certain considerations need to be taken into account when selecting a non-linear medium. Firstly, second order susceptibility will only occur if the medium does not possess a centre of symmetry; if **P** changes symmetrically with **E**, the even terms of the Taylor expansion in equation 2.1 will be zero. Also care has to be taken to find a material where the fundamental and second harmonic have the same phase velocity otherwise the second harmonic, generated as the fundamental propagates through the medium, will destructively interfere. To allow this to occur, birefringent crystals are employed, cut at a specific angle to allow phase matching between the fundamental and second harmonic. For this case, the fundamental and second harmonic output are orthogonally polarised and this is termed type-I phase matching.

In a similar mathematical treatment to that discussed above, it can be shown that under the correct conditions, two laser beams of frequencies ω_1 and ω_2 can result in the formation of a beam of frequency $\omega_1 + \omega_2$. This is SFG, where the energy of the resultant photon is the sum of the two incident photons. For SFG a further constraint is put upon the phase matching conditions as the medium will possess different refractive indices at the two frequencies of the incident beams. In some cases, the electric field of two incident beams are orthogonally polarised allowing easier phase matching. This is termed type-II phase matching.

Both SHG and SFG are employed to generate photons at the fourth harmonic (200 nm) by utilising a series of three β-barium borate (BBO) crystals of varying thickness and angle at which the crystal is cut. The 200 nm beam is formed by SHG of the 800 nm fundamental to give 400 nm. The 400 nm beam then undergoes SFG with the fundamental to give the third harmonic of the fundamental at 267 nm. Finally SFG between the 267 nm and fundamental 800 nm gives the fourth harmonic

200 nm. The polarisations of each stage in the fourth harmonic generation process, relative to the "ordinary" (vertical in the lab frame) fundamental polarisation, are given in table 2.1 which also lists the phase matching implemented in each crystal. The setup utilising this fourth harmonic generation process is shown in figure 2.3 a).

Table 2.1 – Wavelengths generated in the fourth harmonic generation process utilising a series of BBO crystals. Included in the table is the harmonic relative to the fundamental, the type of phase matching implemented to generate that harmonic and the relative polarisation of the harmonic.

Wavelength (Energy)	**Harmonic of Fundamental**	**Phase Matching Type**	**Polarisation**
800 nm ($12500\ cm^{-1}$)	Fundamental (1st)	N/A	Ordinary
400 nm ($25000\ cm^{-1}$)	2nd	Type I	Extraordinary
266 nm ($37500\ cm^{-1}$)	3rd	Type II	Ordinary
200 nm ($50000\ cm^{-1}$)	4th	Type I	Extraordinary

Optical Parametric Generation

The second class of non-linear optical effect employed in this thesis is OPG. As in SFG, OPG relies on the higher order electric susceptibility dependence of the dielectric polarisation. OPG can be considered as the reverse process of SFG, in which light of frequency ω_1 is split into two beams of frequencies ω_2 and ω_3, such that $\omega_1 = \omega_2 + \omega_3$. Even if the input frequency, ω_1, is fixed there is still a wide range of values that ω_2 and ω_3 can take. However, selection of particular values for ω_2 and ω_3 can be achieved through the tuning of the phase matching angle within the medium or by passing a beam of frequency ω_2 into the medium to stimulate emission at this frequency. A representation of the OPG process for generating a beam with the difference in frequencies between two input beams (ω_1 and ω_2) is shown in figure

2.4 b). As OPG will produce photons at lower energy than the input photons, it is often used to generate beams in the infrared (IR).[4]

Based on the schematic in figure 2.4 b) it is straightforward to see that by passing the desired frequency ω_2 into a medium that is being seeded by a higher frequency beam (ω_1), an amplification of the desired frequency is achieved. In this case the input beams are called the pump (ω_1) and signal (ω_2) beams, while the output "by-product" beam is called the idler (ω_3). For every photon of pump and signal input, two signal photons and an idler photon are produced.[2, 4]

Optical parametric amplifiers (Light Conversion (L-C) TOPAS-C) are used for the experiments within this thesis to obtain tuneable wavelengths in the near UV. The TOPAS-C works by taking a small fraction of the fundamental, 800 nm beam, and generating an IR continuum by passing it through a sapphire crystal. A section of this white light continuum is then picked out and amplified through OPG. The remainder of the fundamental is used as the pump, ultimately resulting in an intense pulse in the IR. The IR beam then undergoes up conversion by passing through two BBO crystals using either SFG or SHG to produce the desired wavelengths within the wavelength range of interest, 238 – 340 nm.

2.1.3 Pump Probe Setup

The selection of pump and probe wavelengths are dependent on the specific molecule that is being studied. Two pump probe setups are employed in this thesis shown in figures 2.3a) and b). In each case the pump and probe beams are generated using 1 mJ/pulse (i.e. a third) of the 800 nm fundamental. This is made possible through the use of a 33:66 and a 50:50 pair of beam splitters. The first setup, as

shown by figure 2.3 a), has pump pulses at 200 nm (<1 μJ/pulse), formed by a series of three type I, type II and type I BBO crystals (as described above), and probe pulses provided by a TOPAS-C at either 243.1 or 333.4 nm (~7 μJ/pulse). The second setup, shown in figure 2.3 b), implements the same probe pulses, but utilises a second TOPAS-C to generate pump pulses within the range 238 – 288 nm (4 – 8 μJ/pulse).

The choice of probe wavelength used is either 243.1 or 333.4 nm, which correspond to resonance enhanced multiphoton ionisation (REMPI) transitions in hydrogen and methyl radicals, respectively. The use of REMPI allows for selective ionisation of a particular fragment as resonant ionisation will have a far higher probability than non-resonant ionisation. The REMPI transition in hydrogen is a 2+1 ionisation mechanism via the 2s ← 1s two-photon transition, at an excitation energy of 82236 cm^{-1} (very close to the Lyman-α transition), before ionisation by a third photon. The REMPI transition in the methyl radical is a 2+1 ionisation mechanism via the $3p\ ^2A_2'' \leftarrow \widetilde{X}\ ^2A_2''$ two-photon transition, before ionisation by a third photon. These transitions are illustrated in figure 2.5.

A temporal delay between the pump and probe pulses is controlled by a hollow-gold retroreflector mounted on a motorised delay stage (Physik-Instrumente M-521.DD). The minimum step size typically used for these experiments is ~4 μm or 25 fs. The hollow-gold retroreflector varies the optical path length of the 800 nm pump beam (before frequency conversion). Control of the delay stage is achieved through a purpose built LabVIEW program that also controls the data acquisition at each pump probe delay.

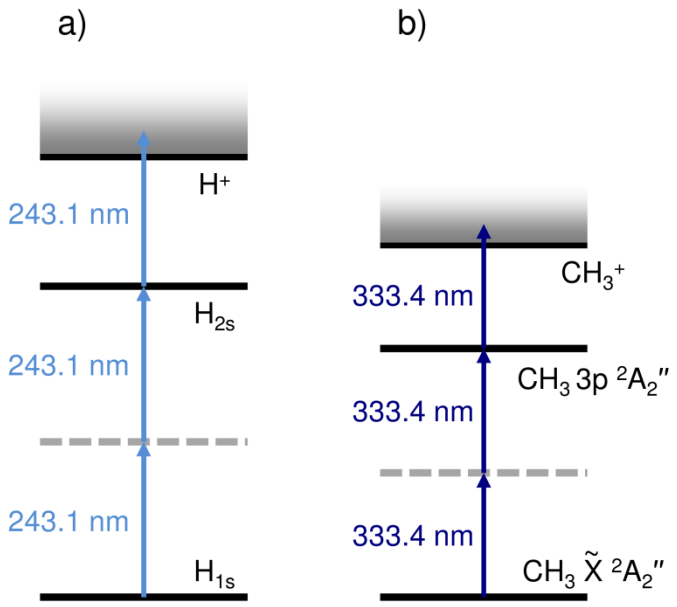

Figure 2.5 – The REMPI transitions employed in this thesis to selectively ionise a) hydrogen and b) methyl radicals.

2.1.4 Alignment and Focusing

The pump and probe beams are focused into the vacuum chamber setup by a pair of 500 mm plano-convex lenses made of MgF_2 and CaF_2, respectively. MgF_2 is used for the pump beam as it has a lower dispersion at 200 nm than CaF_2, reducing the amount of temporal dispersion. The 200 nm output and each TOPAS-C output have beam diameters of ~2 and ~3 mm, respectively. However as probing is a three-photon process, a higher photon density is desired at the focus of the probe. This is achieved by expanding the probe beam 3-fold (9 mm diameter) using a Galilean telescope, allowing for much tighter focusing.

The diameter of the beams at focus can be calculated using equation 2.4 [3]:

$$D_f = \frac{4\lambda F}{\pi D_0} \tag{2.4}$$

where D_f and D_0 are the beam diameter at focus and at the lens, respectively. F is the focal length of the lens (500 mm in this case) and λ is the wavelength. From equation 2.4 it is apparent that a 3-fold increase in the beam diameter of the probe leads to a 3-fold reduction in the diameter at the focus and therefore a 9-fold increase in intensity. Under typical experimental conditions the 200 nm pump, the TOPAS-C pump and the TOPAS-C probe outputs correspond to 1 μJ/pulse, 6 μJ/pulse (at 275 nm) and 6 μJ/pulse (at 243.1 nm), respectively. The corresponding focal diameters produced will be ~60, ~55 and ~20 μm, and associated beam intensities at the focus of 3.6×10^{11} W cm^{-2}, 2.5×10^{12} W cm^{-2} and 2×10^{13} W cm^{-2}, respectively. It is important to note the much greater intensity of the probe beam in comparison to the pump beams. [3, 6]

Two approaches are used to combine the pump and probe beams before sending them into the vacuum chamber, the choice of which depends on the wavelengths of each beam. The first is to use a dichroic mirror to combine the beams collinearly and is typically used when the pump and probe beams differ sufficiently in wavelength (e.g. 200 nm pump and 243.1 nm probe). The second approach is to align the beams vertically displaced in the lab frame. This approach is used when the pump and probe beams are very similar in wavelength (e.g. 238 nm pump and 243.1 nm probe). To realize the latter approach, a half-mirror is used to reflect the pump beam whilst allowing the probe beam to follow the pump beam, albeit slightly displaced vertically. Overlap between the pump and probe beams is achieved by redirecting both beams directly before entering the vacuum chamber (using a retractable mirror) through a 50 μm pinhole situated at the focal point of both beams.

2.2 Vacuum Chamber Setup

The vacuum chamber setup employed in these studies is shown in figure 2.6 and consists of a pair of differentially pumped chambers, termed the source and interaction chambers. Within the source chamber is housed the molecular beam source, an Even-Lavie (E-L) pulsed solenoid valve,[7] and this chamber is pumped by a turbo pump (Oerlikon Leybold Mag W 2200) which maintains a pressure of $<5 \times 10^{-6}$ mbar when the valve is operating. The interaction chamber is separated from the source chamber by a 2 mm skimmer that samples the centre of the molecular beam. Within the interaction chamber are the electrostatic lens electrodes that form the velocity map imaging (VMI) setup.[8] CaF_2 windows on either side of the chamber allow for alignment of the laser beams into the interaction chamber, intersecting the molecular beam in the centre of the electrostatic lens setup. The interaction chamber is pumped by a turbo pump (Oerlikon Leybold Turbovac Mag W 700), maintaining a pressure of $<2 \times 10^{-7}$ mbar when the valve is operating. Both turbo pumps are backed by a two-stage rotary pump (Oerlikon Leybold Trivac D 40-B), which maintains a backing pressure of $<2 \times 10^{-2}$ mbar.

Mounted vertically above the interaction chamber is a time of flight (TOF) tube at the terminus of which is the VMI detector, which lies approximately 500 mm away from the centre of the electrostatic lens. The TOF and detector setup can be employed to either provide VMI data or, by measuring the arrival time of a particular ion, it can also be employed as a basic mass spectrometer. Further details on VMI arrangement will be discussed (in section 2.2.2).

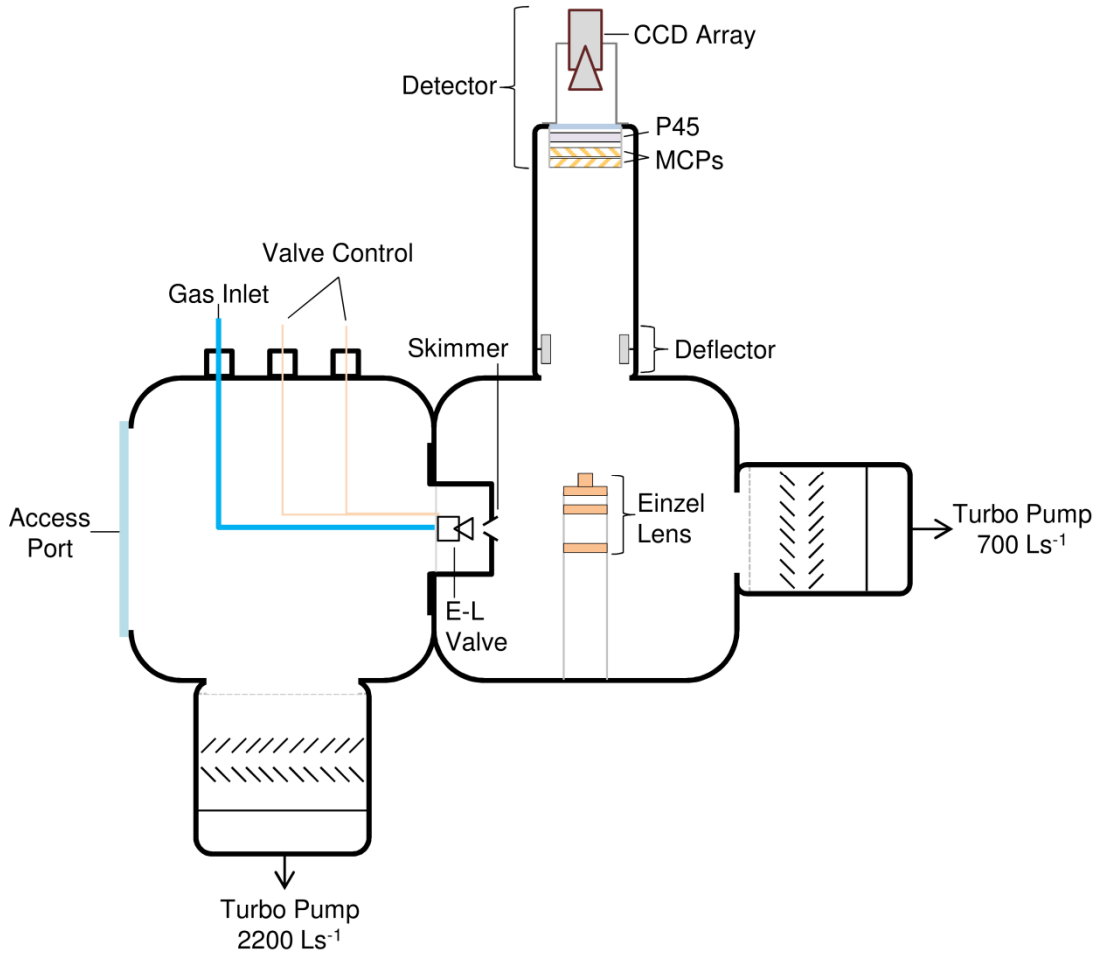

Figure 2.6 – Schematic of the vacuum chamber setup. The chamber to the left is the source chamber containing the pulsed solenoid valve; the chamber to the right is the interactions chamber containing the electrostatic lens setup and VMI detector.

2.2.1 Molecular Beams

The desire to study the energetics of isolated molecular systems typically requires that the molecules have a well-defined internal energy. Often in spectroscopy the aim is to carry out studies on molecules starting in low vibrational and rotational eigenstates. As the population of vibrational and rotational levels will be governed by a Boltzmann factor ($P \propto e^{-\Delta E/KT}$) it is clear that low internal temperatures are required to ensure population of the lowest vibrational and rotational levels. One way to achieve this is through the use of seeded molecular

beams in which the molecule of interest (analyte) is discharged in a beam of seed gas through a nozzle into a vacuum, a schematic of which is shown in figure 2.7.

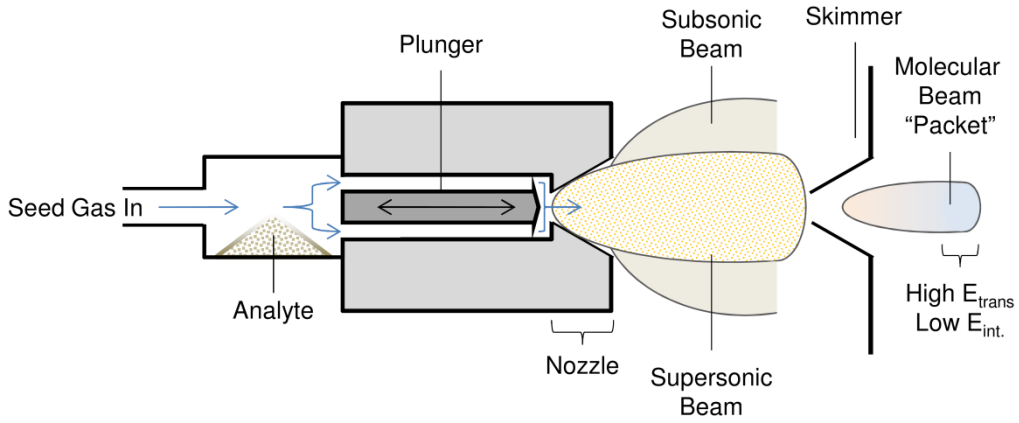

Figure 2.7 – Schematic of the pulsed solenoid valve, representation of the region of supersonic beam created and how skimming the centre of the distribution yields a molecular beam "packet" with high translational energy (E_{trans}) and a low internal energy (E_{int}).

If the pressure difference on either side of the nozzle is large enough, supersonic beam velocities can be achieved. Upon entering vacuum, the beam undergoes an expansion that transfers the internal energy of the molecules (E_{int}) to the translational energy (E_{trans}) of the seed gas through inelastic collisions. This transfer of energy ensures the low vibrational and rotational temperatures required for spectroscopy, particularly if the translationally quickest molecules are studied. By introducing a skimmer that removes the subsonic sections of the molecular beam, it is possible to sample the coldest segment of the beam which possesses a narrow range of beam velocities. The physics behind molecular beam generation is quite extensive and will not be discussed here, however they are comprehensively reviewed in reference [9].

The use of molecular beams has proven useful in many areas of spectroscopy, however using a continuous beam can cause problems as the large volume of gas necessitates large vacuum pumps in order to maintain high vacuum, and large

samples of analyte which can be costly. One solution to this problem is to use a pulsed valve that is synchronised with the means of detection, allowing for the study of small "packets" of molecular beam without the large through-put of gas. Furthermore the use of a pulsed system allows for detection of the front edge of a molecular beam "packet" which will have the highest translational velocity and therefore lowest internal temperature. The experiments herein implement a pulsed solenoid valve (Even-Lavie) operating at 125 Hz (N.B. synchronising with 1 in 8 laser pulses), the design of which allows for high seed gas pressures and controlled analyte heating. Previous studies with the Even-Lavie valve have suggested rotational temperature as low as <1 K can be achieved.[7] The valve works by retracting a spring-loaded magnetic plunger with a solenoid-induced magnetic field. The plunger is then returned by the spring mechanism once the field is removed.

The choice of seed gas for a molecular beam greatly affects the beam velocity and composition. In all the experiments herein a helium seed gas was used, which gives a beam velocity of ~1780 ms^{-1} which is obtained by using equation 2.5 [10, 11]:

$$\frac{1}{2}mv^2 = \frac{5}{2}k_B T_{valve} \tag{2.5}$$

where m is the atomic mass of the seed gas, v is the beam velocity, k_B is the Boltzmann constant and T_{valve} is the temperature of the pulsed-valve. The use of argon as a seed gas was considered in the studies presented, however due to the much slower beam velocities achieved a larger number of molecular clusters were formed. The opening of the valve was triggered relative to the laser pulses by the output from a digital delay generator (Stanford DG535) allowing for optimisation of

the valve opening time so that the front edge of the molecular beam arrives in the interaction region at the same time as the laser pulses. For more details on timing see below.

Typical Operating Conditions

For each molecule studied the temperature and the opening time of the pulsed valve was optimised to produce a sufficient amount of sample in the molecular beam. A summary of typical operating conditions for all the molecules studied in this thesis are shown in table 2.2, along with the melting and boiling point for each molecule.

Table 2.2 – Summary of typical operating conditions for the molecules studied, including literature melting points and boiling points.

Molecule	Melting Point / °C	Boiling Point / °C	Operating Temperature / °C	Valve Opening Time / μs
Imidazole	90	256	100	13.5
4 – Methylimidazole	142	267	140	12.5
2 – Methylimidazole	45	263	150	13.5
2,4 – Dimethylimidazole	86	266	100	14.5
1 – Methylimidazole	-6	198	100	15
Anisole	-37	154	80	14
Mequinol	55	243	120	14
Thioanisole	-15	188	80	12

All chemicals were above 98 % purity and purchased from Sigma-Aldrich. Solid samples were inserted as powders into the Even-Lavie valve sample tube between the seed gas inlet and solenoid valve mechanism (See figure 2.7). For the liquid samples, 1 – Methylimidazole, Anisole and Thioanisole, a sample was absorbed onto a piece of filter paper and inserted into the sample tube.

2.2.2 Velocity Map Imaging

As discussed earlier the desire to measure the kinetic energy of photofragments can be achieved through several techniques. For the work in this thesis VMI is employed as this allows for the detection of a photofragment's kinetic energy and angular distribution. Furthermore VMI can be employed to study fragments of varying mass (which is not always possible with high Rydberg time of flight techniques, as discussed in section 1.3.2). Imaging of photoproducts was first performed by Chandler and Houston [12] during the 1980s using a gridded set of Wiley-McLaren type electrodes. However, it was the development of the electrostatic lens setup by Eppink and Parker [8] that allowed for velocity mapping, yielding a significant improvement in kinetic energy resolution.

The VMI setup utilised in this thesis is schematically shown in figure 2.8. The electrostatic lens is shown on the left and consists of two electrodes, termed the repeller and extractor, which are based on a pair of grid-less Wiley-McLaren TOF electrodes. Furthermore, a ground electrode is included further down the flight tube to shield against stray electric fields (similar to a Wiley-McLaren setup [13]). The typical operating voltages applied to the repeller (V_r) and extractor (V_e) are 5000 and 3570 V, respectively, which is provided by a pair of Stanford PS350 high voltage supplies. The VMI detector, on the right-hand side of figure 2.8, consists of a pair of

microchannel plates (MCP), which serve to amplify the ion signal through a cascade of electron impacts, and a phosphor P-43 (Gd_2O_2S:Tb) screen which luminesces upon electron impact. The luminescence is then capture by a charge couple device (CCD) array (Basler A-312-f) and recorded by a purpose built LabVIEW program. Typical operating voltages for the MCP vary from 600 to 800 V behind the first MCP (V_{mcp1}) and from 1200 to 1600 V behind the second MCP (V_{mcp2}). The voltage on V_{mcp2} is kept at double that of V_{mcp1} ensuring a consistent gain over both MCP plates. The P-43 screen is maintained at 5 kV.

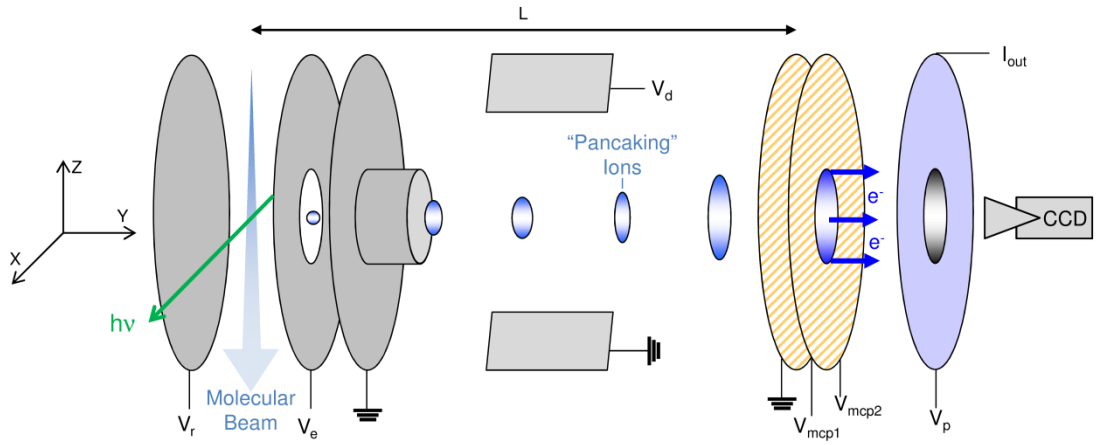

Figure 2.8 – Schematic of the velocity map imaging setup including the electrostatic lens electrodes (left); the field free flight path and deflector (middle); and the detector consisting of two MCPs, P-43 screen and CCD array. The laser pulses (hν) have an electric field polarised in the Z-axis. Projection of the ions is vertically in the laboratory frame (Y-axis).

The VMI setup is situated within the interaction chamber so that the propagating molecular beam (in the Z-axis in figure 2.8) and laser beam (propagating in the X-axis – with an electric field polarised along the Z-axis) intersect in the middle of the electrostatic lens. The electrostatic lens projects the Newton sphere of charged particles along the Y-axis. The Wiley-McLaren type electrode setup causes

the ion Newton sphere to become temporally compressed while in flight, leading to a "pancaking" of ions as they impact upon the detector (see figure 2.8).

Velocity Mapping

The equations governing the projection of charged particles along a TOF setup were originally provided by Wiley-McLaren. These state that for an optimised setup (V_e/V_r) an ion of specific m/z will be temporally focused onto the position sensitive detector, at the end of a TOF tube length L ($L \approx 500$ mm), independently of the initial position within the molecule-laser interaction region. The TOF (t_{tof}) for a particular fragment is given by:

$$t_{tof} \approx L\sqrt{\frac{m}{2eV_r}} \tag{2.6}$$

where m is the mass of the fragment and e is the elementary charge on an electron. For the electrostatic lens used in VMI the velocity of the photofragment within the Newton sphere will be mapped onto a specific position on the detector. The radius of the "pancaked" Newton sphere of an ion upon impact is given by:

$$r \approx av_{xz}t_{tof} \approx aL\sqrt{\frac{KER}{eV_r}} \tag{2.7}$$

The radius is therefore dependent on t_{tof}, the ion's velocity perpendicular to the flight axis (v_{xz}) and a magnification factor (a). From this it can be shown that the kinetic energy release (KER) of an ion can be related to r^2. This latter relationship is key for extracting a TKER spectrum from the 2D distribution and calibration of the VMI setup (see below). a is characteristic of the velocity mapping conditions and typically has values of ~1.4 for the length of TOF tube employed. The implication of equation

2.7 is that the mapping of an ion's velocity is independent of the ion's position within the molecule-laser interaction region. This significantly improves the *KER* resolution of the experiment as it overcomes the limits imposed by the size of the laser focus or the Doppler broadening from the molecular beam's motion. The independence from the ion's initial position is nicely illustrated in figure 2.9, taken from the original Eppink and Parker paper,[8] which shows Simion-calculated trajectories for the same ion at different initial positions within the electrostatic lens for an electrode setup with a voltage ratio $V_e/V_r = 0.75$.

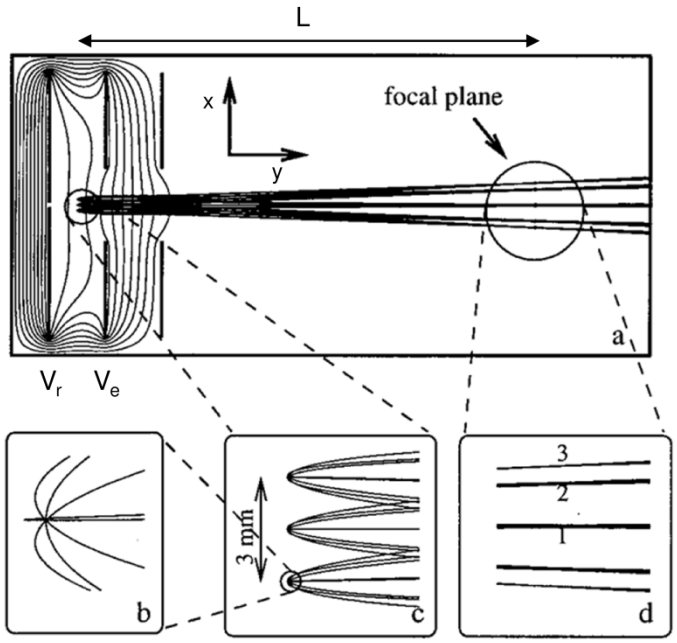

Figure 2.9 – Simulated ion trajectories for ions in an electrostatic lens field (shown as equipotential lines) with the same kinetic energy ejected at three different angles relative to the direction of flight. b-d) show zoomed-in sections of the trajectories. Reprinted with permission from reference [8].

The Need for Image Reconstruction

The mapping of ions from a three dimensional (3D) distribution of ions on a Newton sphere to a 2D image can be described, with reference to figure 2.10, by the conversion from a 3D polar distribution, $F(r,\theta,\phi)$, where θ and ϕ are the zenith and

azimuthal angles and r is the radius of the sphere, to a 2D projection $G(R,\alpha)$ where α is the angle and R is the radius of the circle. The projection of the Newton sphere of ions causes a reduction of dimensionality. As a result the contribution from signal with a non-zero azimuthal angle ($\phi \neq 0$) will become convoluted into the 2D distribution $G(R,\alpha)$ at a reduced R from $\phi = 0$ signal (and imposing upon signal with a lower 3D radius (r)).

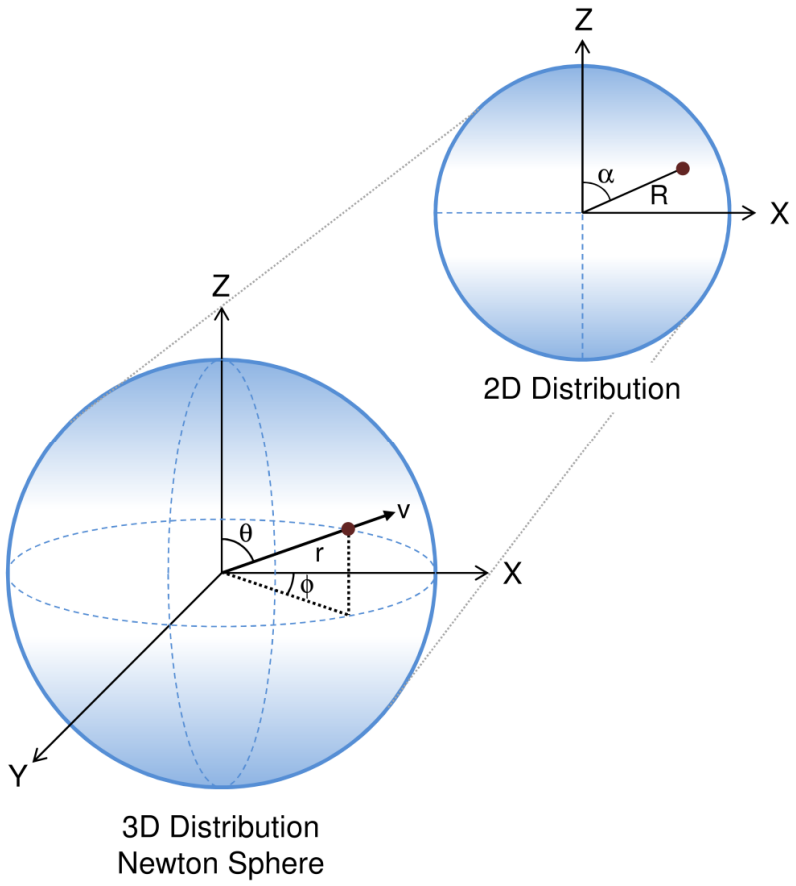

Figure 2.10 – Velocity mapping of a 3D Newton sphere distribution of charged particles with velocity (v), which can be described in polar coordinate as the function $F(r,\theta,\phi)$. The distribution is required to be cylindrically symmetric around the Cartesian Z-axis. This distribution is then projected along the Y-axis and mapped as a 2D distribution in terms of a radius (R) and an angle (α) from the Cartesian Z-axis.

The angles θ and α are defined relative to the polarisation of the laser's electric field (Z-axis in figure 2.10) that lies perpendicular to the VMI projection axis (Y-axis in figure 2.10). A laser polarisation perpendicular to the VMI projection axis is essential otherwise distinction of the θ and ϕ contribution to the convoluted 2D distribution is not possible.

As implied by equation 2.7 a one dimensional radial spectrum is proportional to $\sqrt{KER}$, therefore determining the ion signal intensity as a function of r can yield a spectrum of the photofragments *KER*. The intensity of the 1D radial distribution $I(r)$ is given by:

$$I(r) = \int_0^{2\pi}\int_0^{\pi} F(r,\theta,\phi)d\theta d\phi \tag{2.8}$$

Obtaining the distribution $F(r,\theta,\phi)$ from its projection $G(R,\alpha)$ is therefore essential to determining $I(r)$ and from it a KER spectrum. Attaining $F(r,\theta,\phi)$ from $G(R,\alpha)$ can be achieved through image deconvolution, which involves a series of transformations. A schematic of the basic steps are shown in figure 2.11.

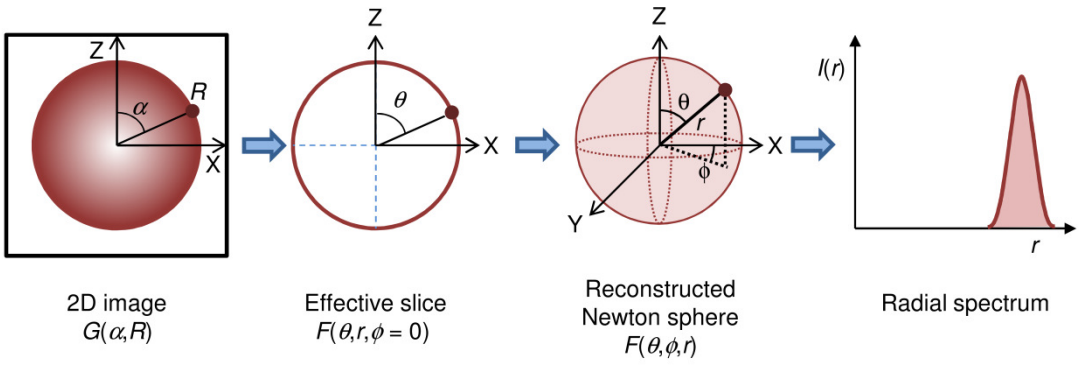

Figure 2.11 – Schematic of the steps involved in image deconvolution. From a 2D image, an effective slice at ϕ = 0 is taken and the 3D distribution determined. This is then converted to a 1D radial spectrum by integration over all angles.

The first stage in deconvolution is to account for the reduction in dimensionality and remove the contribution from signal with $\phi \neq 0$ in the initial Newton sphere, yielding $F(\theta,r,\phi = 0)$. This can be achieved through one of numerous mathematical algorithms.[14-17] The work in this thesis uses a polar onion peeling (POP) algorithm developed by Roberts *et al.*[18] Once the effective slice through the signal at $\phi = 0$ is determined the distribution of the initial Newton sphere, $F(r,\theta,\phi)$, can be recovered. Finally, by employing equation 2.8 it is possible to convert $F(r,\theta,\phi)$ to a 1D radial spectrum, which can yield a *KER* spectrum through conversion with a known calibration factor. The calibration factor is derived from analysis of a system with a known dissociation energy (hydrogen bromide and methyl iodide – see calibration section 2.4.2).

Photoproduct Angular Dependence

The angular distribution of photoproducts relative to the electric field vector of the light (defined in the Z-axis in figures 2.8 and 2.10) can be indicative of the nature of the electronic states accessed upon photoexcitation. Photofragment angular distributions arise due to the directionality of the transition dipole moment (TDM) of the pump transition, which was discussed earlier in relation to equation 1.5 for a case where unpolarised light is used. Within the Franck-Condon principle it can be shown that the probability of an electronic transition induced by polarised light is proportional to the electric field vector by:

$$P \propto \int \psi'_e(\boldsymbol{\mu}_e \boldsymbol{\varepsilon})\psi''_e \mathrm{d}\,\tau \qquad (2.9)$$

where $\boldsymbol{\varepsilon}$ is the electric field vector of the polarised light, $\boldsymbol{\mu}_e$ is the electronic dipole moment operator (defined in equation 1.8), ψ''_e and ψ'_e are the electronic

wavefunctions for the ground and excited electronic state, respectively. As $\boldsymbol{\mu}_e$ and $\boldsymbol{\varepsilon}$ are vectors, transitions will preferentially occur in molecules when the two vectors are parallel to each other. Typically it is easy to consider the alignment of $\boldsymbol{\varepsilon}$ and the observable, the TDM (where $\mathrm{TDM} = \left| \int \psi''_e \boldsymbol{\mu}_e \psi'_e \mathrm{d}\tau \right|^2$) for the transition. In a gaseous sample, this alignment leads to the formation of a set of molecules in an excited electronic state that are aligned in a particular direction relative to the laser polarisation, which is polarised along the Z-axis (see figure 2.8) of the laboratory frame. If the excited electronic state results in dissociation, this alignment is maintained in the distribution of photoproducts, with the photofragment's position dependent on the angle between the TDM (for the transition) and the dissociating bond.

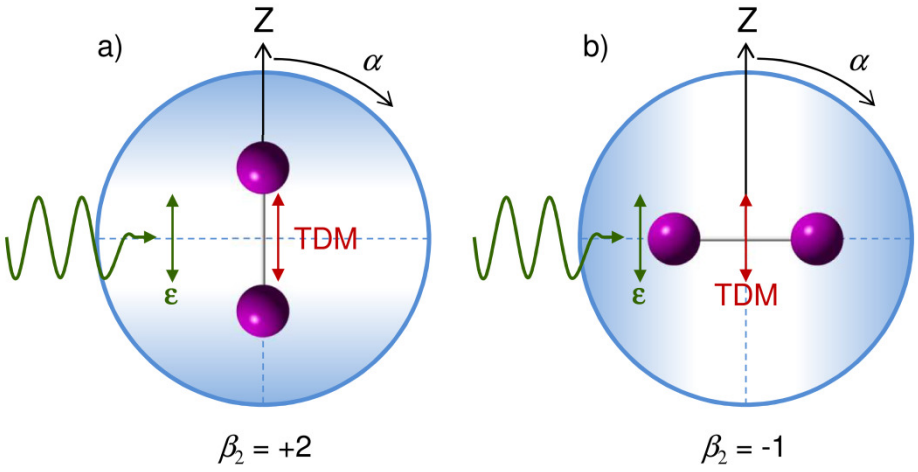

Figure 2.12 – A schematic of the 2D VMI images resulting from the photodissociation of a diatomic molecule whose transition dipole moment (TDM) is aligned a) parallel and b) perpendicular to the dissociating bond. The VMI images are representations of the image before deconvolution, in terms of α, but correspond to a 3D distribution where the maximum signal is located at a) $\theta = 0°$ and b) $\theta = 90°$.

The angular distribution that results from a one-photon excitation has a cosine-squared dependence on the angle between the electric field vector of the laser pulse and the TDM. Due to this, the two limiting cases of ion distribution can be described by a $\cos^2\theta$ distribution for a system where the TDM is parallel to the dissociating bond and $\sin^2\theta$ distribution when the TDM in perpendicular to the dissociating bond. The VMI images arising from these two limiting cases are shown in figure 2.12, where 2.12 a) is the parallel and 2.12 b) the perpendicular case.[14]

Typically for larger molecules the distribution of photofragments does not fit a limiting case. This occurs when: i) the absorption to two electronic states takes place; ii) the TDM lies at an angle between 0° and 90° to the dissociating bond; or iii) when the rotational period of the molecule is on a comparable timescale to the dissociation. To obtain a quantitative measure of how the photofragments are angularly distributed, the intensity of photofragments ($I(\theta)$) is fit to the lowest even term of the Legendre polynomial ($P_2(x)$) for a cosine distribution:

$$I(\theta) = \frac{1}{4\pi}[1 + \beta_2 P_2(\cos\theta)] = \frac{1}{4\pi}[1 + \beta_2 \frac{1}{2}(3\cos^2\theta - 1)] \qquad (2.10)$$

where β_2 is the anisotropy parameter for a one-photon dissociation process and quantifies the angular distribution. β_2 can take values between -1 and 2, where -1 corresponds to a photofragment distribution perpendicular to $\boldsymbol{\varepsilon}$ and 2 corresponds to a photofragment distribution parallel to $\boldsymbol{\varepsilon}$. A β_2 value of zero refers to an isotropic distribution which can arise from one of three possible situations: 1) a dissociation occurring far slower than the rotational period of the molecule; 2) excitation to a set of closely lying electronic states whose TDM combine to give an isotropic

distribution; or 3) a TDM that lies at 54.7° ("magic" angle) with respect to the dissociating bond.[14, 18-20]

It is important to note that the value of β_2 describes the distribution I(θ) relative to the $\boldsymbol{\varepsilon}$ of the polarised light. However, from this the angular relationship between the TDM and the dissociating bond can be inferred. The TDM can be derived from first principles (symmetry arguments) or calculated by various computational techniques. By comparing the calculated TDM to I(θ) it is possible to distinguish the excited state that is accessed prior to dissociation.[14, 18] It is also important to note that higher order evens terms of the Legendre polynomial and corresponding beta parameters (β_4, β_6…) to characterise I(θ) are required when considering multiphoton excitation.

Time of Flight Mass Spectrometry

Along with VMI, the experimental setup can be used to obtain a mass spectrum of the generated photofragments by measuring the current output from the phosphor screen (I_{out}) relative to the laser pulse trigger through an oscilloscope (LeCroy Waverunner LT372). By selecting an individual mass and measuring its intensity as a function of pump probe delay, time resolved ion-yield (TR-IY) experiments can be performed. Typically TR-IY experiments are performed to determine the cross correlation of the laser pulses, which in turn yields the instrument response function (see section 2.4.3). Alternatively, by varying the pump probe delay (t) it is possible to measure the decay of excited state population in a molecule after photoexcitation by the pump. TR-IY of the molecular parent ion is

extensively used to study the dynamics of the parent molecule, following one-photon excitation.

Gating and Timing Considerations

As a combined TOF mass- and VMI spectrometer, it is possible to gate the VMI detection setup to observe a single m/z ion. Gating onto a particular m/z is achieved through a combination of two gating techniques. Firstly a pair of deflector plates ($V_d \approx 400$ V) deflect ions that possess an *m*/*z* different from the fragment of interest using a purpose built delay generator and high voltage switch. The second means of gating is performed by switching V_{mcp2} from $V_{mcp2} = 2 \times V_{mcp1}$ to $V_{mcp2} = V_{mcp1}$. When $V_{mcp2} = V_{mcp1}$ no gain in ion signal is produced by the second MCP preventing detection of any measurable signal on the CCD array or when measuring I_{out}. Switching off this voltage is carried out using a high voltage switch (Behlke GHTS 60) and a purpose built delay generator.

Triggering the Even-Lavie valve to open and the two high voltage gates to switch is achieved using the 125 Hz transistor-transistor logic (TTL) electrical pulse from the output-switch of the laser. This ensures synchronization of the critical components of the experimental setup. The relative timings are summarised in figure 2.13. The time between the TTL pulse output (figure 2.13 a)) and the laser molecule interaction time (t_i) is essentially the time it takes for the laser pulse to travel from the output of the laser cavity to the interaction region. The valve opening is triggered at a delay (t_1) so that the molecular beam reaches the interaction region simultaneously with the subsequent laser pulse at t_i. t_1 is typically ~7.8 ms.

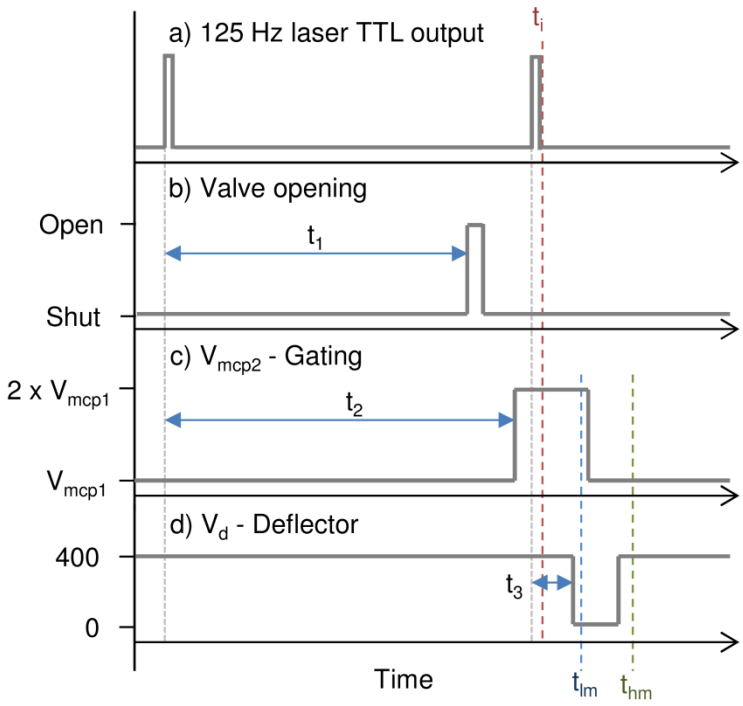

Figure 2.13 – Schematic representation of the various processes triggered by the a) 125 Hz laser TTL output pulses. These processes are b) the solenoid valve opening delayed by t_1; c) the voltage applied to MCP2 (gating the MCP gain) delayed by t_2 and d) the voltage on the deflector plates delayed by t_3. Included are representative times for the time of laser-molecule interaction (t_i) and the arrival time of a low mass (t_{lm}) and high mass ion (t_{hm}) at the detector.

Gating the gain on the second MCP, by varying $V_{mcp2,}$ is triggered by a delayed signal at t_2. This essentially turns the detector on for a period of time from before the laser molecule interaction time until the desired m/z fragment arrives at the detector. t_2 is typically 7.98 ms. The voltage supplied to deflector plates (V_d) is turned off by a third delay generator, at delay t_3, which occurs soon after the laser TTL output. t_3 is usually only a few hundred nanoseconds to prevent deflection of low mass fragments.

The two gating methods are used in conjunction so that the deflector plates remove the large intensity high m/z fragments (which would still impact upon the detector) and the low mass fragments (such as at m/z = 1 when performing VMI on

the methyl fragment). The gating of V_{mcp2} is fine tuned to remove closely neighbouring m/z peaks to the peak of interest. By gating onto a particular region of the TOF, a high mass fragment (at t_{hm}) contribution may be removed while still detecting a low mass fragment (at t_{lm}), and is shown in figure 2.13 c) and d).

2.3 Ultraviolet Absorption Spectrum

For all molecules studied a gas phase UV absorption spectrum was acquired using a commercial UV-Visible absorption spectrometer (Perkin Elmer Lambda 25) providing a 1 nm resolution. Samples were placed in a fused silica sample tube and, where necessary, heated until a significant vapour was produced to record a spectrum.

2.4 Calibration

2.4.1 Time of Flight Calibration

As discussed above, the VMI setup can also provide mass resolution allowing for detection of a particular fragment ion's yield by implementation as a standard Wiley-McLaren spectrometer.[13] The mass of a particular fragment can be determined from its arrival time at the terminus of the 500 mm flight tube by comparison to the arrival time of a known reference mass and *vice versa* through equations 2.11:

$$T_A = \left[\sqrt{\frac{m_i}{m_{ref}}} \times \left(T_{ref} - T_L\right)\right] + T_L$$
$$m_A = \left(\frac{T_{ref} - T_L}{T_i - T_L}\right)^2 \times m_{ref} \qquad (2.11)$$

where T_A and T_{ref} are the arrival times of the fragment and reference signal, respectively. m_A and m_{ref} are the mass of the fragment and reference, respectively, and T_L is the delay between triggering the oscilloscope to collect a TOF and the laser pulses arriving (typically ~335 ns).

During daily operation, the TOF spectrometer is used to check the mass of fragments by comparison to the parent ion signal to ensure that the correct fragment is selected by the two gating methods. A typical spectrum, in terms of TOF and m/z, is shown in figure 2.11 for four isotopes of xenon, each peak intensity approximately matches the isotopic abundance ratios of 6.5 : 1 : 5.5 : 6.5 for ^{129}Xe, ^{130}Xe, ^{131}Xe and ^{132}Xe, respectively. Conversion from TOF to m/z is carried out by referencing the ^{132}Xe isotope. The maximum resolving power of the mass spectrometer setup is ~550 m/z (based upon a peak FWHM of ~0.24 *m/z* for the ^{129}Xe peak).

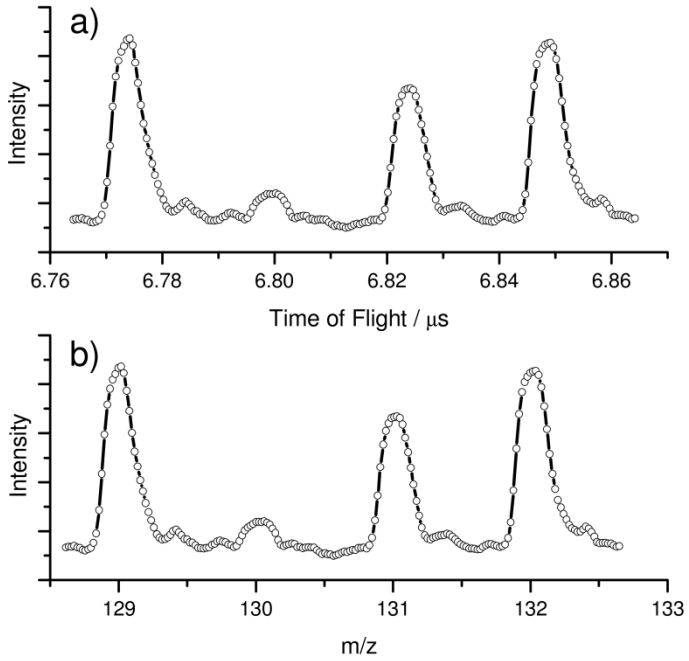

Figure 2.14 – The conversion of a a time of flight spectrum a) to one based on mass to charge b). The four peaks correspond to ^{129}Xe, ^{130}Xe, ^{131}Xe and ^{132}Xe ions. Calibration of mass to charge is based on the ^{132}Xe peak as a reference.

2.4.2 Velocity Map Imaging Calibration

Image deconvolution of a 2D VMI image yields a spectrum in terms of pixel radius (r) after conversion to a 1D spectrum through the appropriate Jacobian transformation. However, conversion from a 1D spectrum in terms of r to *KER* requires calibration with a known reference, from which a calibration factor from r^2 to *KER* can be obtained. In theory the calibration factor should be independent of the fragment mass.

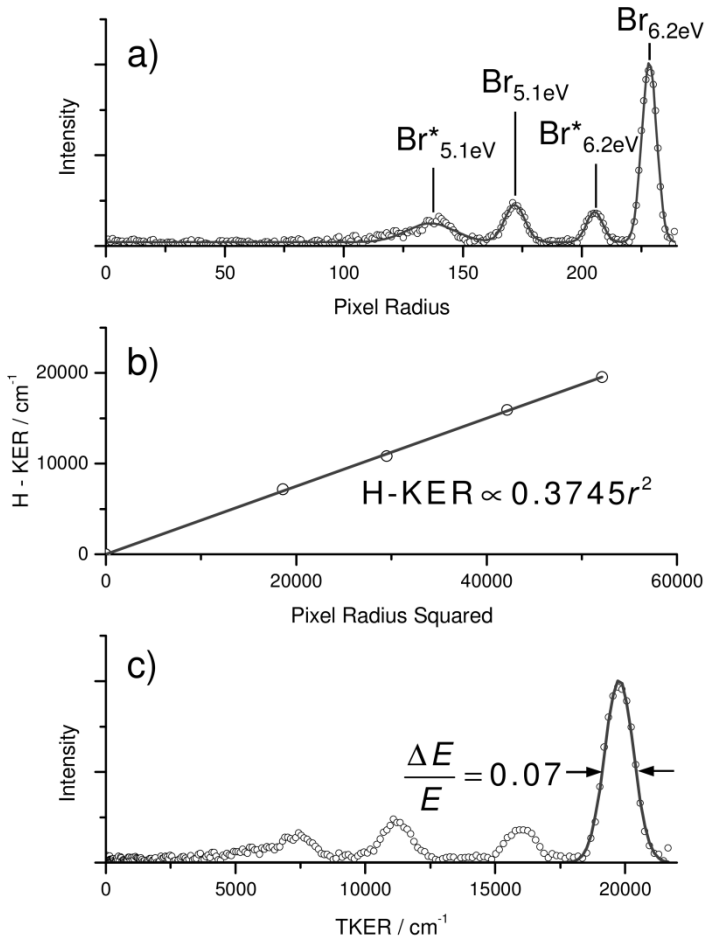

Figure 2.15 – VMI calibration for hydrogen dissociation from hydrogen bromide: a) a spectrum in terms of r, showing four peaks corresponding to two different bromine dissociation channels at two dissociation wavelengths; b) a plot of the assigned H-KER for each feature against pixel radius squared (r^2); c) total kinetic energy release spectrum (TKER) for the same hydrogen bromide spectrum, including the resolution of the largest kinetic energy peak (7%).

However, fragments of different masses can, in some cases, require different calibration factors. As a result, separate hydrogen and methyl radical calibrations were performed for each of these fragments. For hydrogen VMI calibration, hydrogen bromide is used. Following excitation in the UV, hydrogen bromide dissociates to yield hydrogen atoms and bromine atoms in both spin-orbit coupled states (Br-$^2P_{3/2}$ and Br-$^2P_{1/2}$). The D_0 of hydrogen bromide and difference in energy between spin-orbit coupled states in bromine are known to be 30210 and 3685 cm^{-1}, respectively, making calibration straightforward.[21, 22] The 1D spectrum, in terms of *r*, of hydrogen dissociation from hydrogen bromide using a 200 (6.2 eV photon energy) and 243 nm (5.1 eV) pump probe scheme is shown in figure 2.15 a). The four peaks in this spectrum correspond to 243 nm induced dissociation into the excited and ground bromine states (labelled $Br^*_{5.1eV}$ and $Br_{5.1eV}$, respectively) and 200 nm induced dissociation into the excited and ground bromine states (labelled $Br^*_{6.2eV}$ and $Br_{6.2eV}$, respectively). By plotting the hydrogen KER for each peak against pixel radius squared (figure 2.15 b)), this gives the calibration factor, in this case 0.3745.

Conversion from hydrogen KER to total kinetic energy release (TKER) can be achieved by accounting for conservation of momentum between the two fragments during bond dissociation using equation 2.12:

$$TKER = KER_H\left(\frac{m_H + m_{Br}}{m_H}\right) = KER_{Br}\left(\frac{m_{Br} + m_H}{m_{Br}}\right) \qquad (2.12)$$

where KER_H and KER_{Br} is the kinetic energy of each fragment, hydrogen and bromine; whilst m_H and m_{Br} is the mass of each fragment. The TKER spectrum for hydrogen bromide dissociation is shown in figure 2.15 c).

A similar methodology can be applied to methyl iodide to obtain methyl VMI calibration. The D_0 of CH_3-I and the difference in energy between spin-orbit coupled states in iodine ($I\text{-}^2P_{3/2}$ to $I\text{-}^2P_{1/2}$) are known to be 19440 and 7600 cm^{-1}, respectively.[22-24] The corresponding intensity versus *r*, methyl KER versus r^2 and TKER plots are shown in figure 2.16 for methyl iodide dissociation when photoexcited at 273.4 nm and probed at 333.4 nm. The methyl calibration factor calculated is 0.3599.

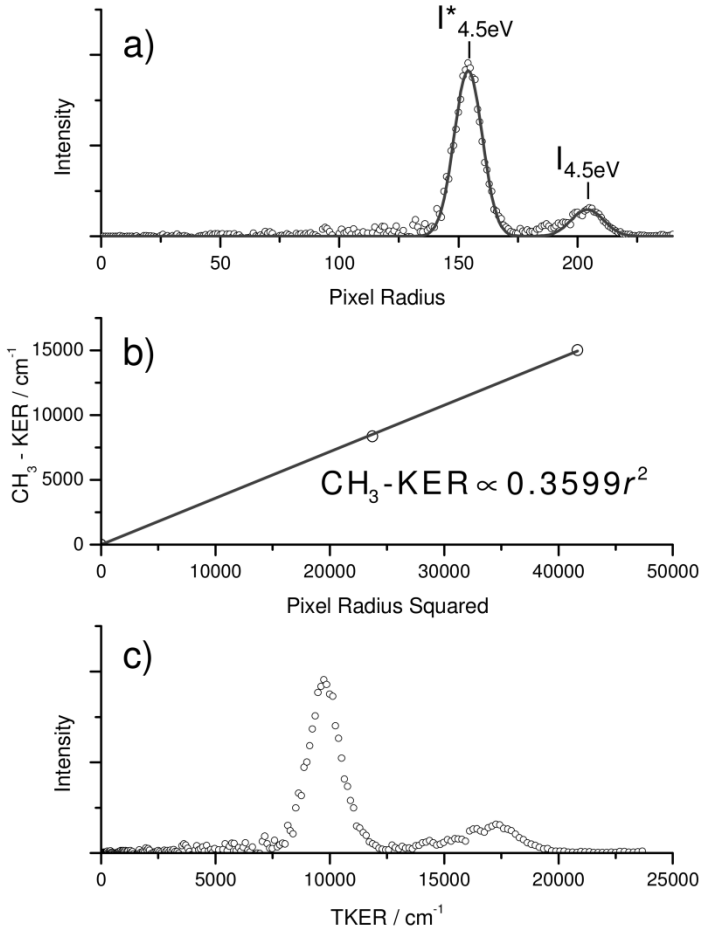

Figure 2.16 – VMI calibration for methyl dissociation from methyl iodide: a) a spectrum in terms of *r*, showing two peaks corresponding to two different iodine dissociation channels; b) a plot of the assigned CH_3-KER for each feature against pixel radius squared (r^2); c) TKER for the same methyl iodide spectrum.

2.4.3 Laser Cross Correlations and Time Zero

The temporal resolution and hence the instrument response function (IRF) of the experiments in this thesis is obtained from the cross correlation of the pump and probe pulses. A cross correlation is obtained by measuring the parent ion signal of a molecule as a function of pump probe delay (Δt). Ideally a molecule that does not contain an excited-state resonance at the pump and probe wavelengths should be used, as this can potentially distort the cross correlation. For two identical, Gaussian laser pulses, the convolution of two pulses will result in a cross correlation with a FWHM that is $\sqrt{2}$ times the FWHM of the original pulses.

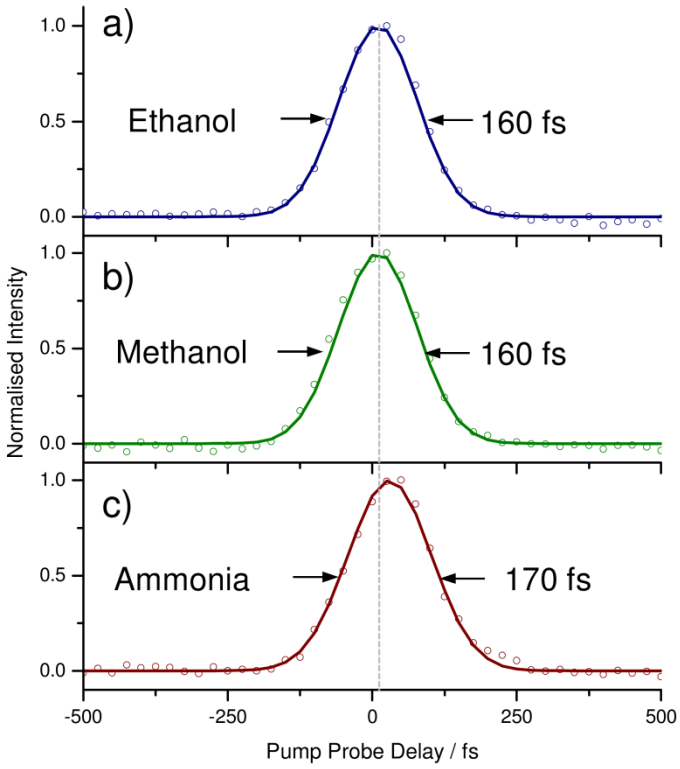

Figure 2.17 – Cross correlations taken with a 200 nm pump and 243.1 nm probe in a) ethanol, b) methanol and c) ammonia.

To obtain cross correlations when pumping at 200 nm and probing at 243.1 nm, ethanol, methanol or ammonia are employed and the results of these are shown

in figure 2.17. The FWHM is determined by fitting to a Gaussian function (for fitting details see appendix I) and yields a FWHM of ~160 fs for methanol and ethanol. However, the results in ammonia show a slight broadening (and temporal shift) due to the slight influence of a vibrational resonance in its first excited electronic state which lies close to the 200 nm photon energy.

Non-resonant parent ion yield cross correlations are also employed to determine the time zero of the experiment, which is the point at which the pump and probe pulses arrive simultaneously at the sample. The assigned time zero is shown as a vertical grey line in figure 2.17, which was assigned to the centre of Gaussian distributions fitted to the ethanol and methanol cross correlations. The ammonia cross correlation is slightly shifted due, once again, to the influence of an excited electronic state resonance. However this shift is < 20 fs and can be accounted for by a linear offset in the data analysis. Ammonia is often used to determine time zero as it produces far larger ion signal than ethanol and methanol and is more practical to use.

When pumping and probing with UV pulses generated by the two TOPAS-Cs, a different set of cross correlations are produced, and an example of these are shown in figure 2.18 taken in xenon, ethanol and methanol with a pump probe setup of 256 and 243.1 nm, respectively. The cross correlation measured is 120 – 135 fs. These values are shorter than those for a 200 nm pump pulse suggesting that the 200 nm pump pulse is temporally longer than the pump pulse output from the TOPAS-C. The time zero obtained from all three sets of cross correlations are in good agreement. The majority of experiments in this thesis utilising both TOPAS-Cs used

methanol to determine the time zero, as this yielded adequate signal at a range of pump and probe wavelengths.

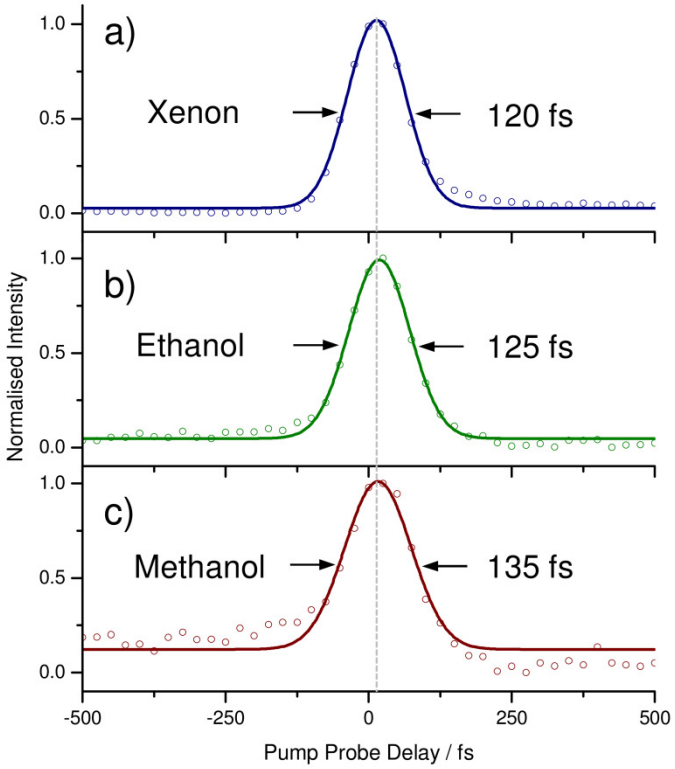

Figure 2.18 – Cross correlations taken with a 256 nm pump and 243.1 nm probe in a) ^{131}xenon, b) ethanol and c) methanol.

2.4 References

[1] P. F. Moulton, *J. Opt. Soc. Am. B*, **3**, 125 (1986).

[2] J. Wilson and J. F. B. Hawkes, *Optoelectronics: An Introduction 3rd Ed.*, Prentice Hall, 1997.

[3] E. Hecht, *Optics 4th Ed.*, Addison Wesley, 2003.

[4] R. Paschotta, *Encyclopedia for Photonics and Laser Technology*, Wiley-VCH, 2008.

[5] P. A. Franken, A. E. Hill, C. W. Peters and G. Weinreich, *Phys. Rev. Lett.*, **7**, 118 (1961).

[6] J. R. Meyer-Ardent, *Introduction to Classical and Modern Optics 4th Ed.*, Prentice Hall, 1994.

[7] U. Even, J. Jortner, D. Noy, N. Lavie and C. Cossart-Magos, *J. Chem. Phys.*, **112**, 8068 (2000).

[8] A. T. J. B. Eppink and D. H. Parker, *Rev. Sci. Instrum.*, **68**, 3477 (1997).

[9] G. Scoles, *Atomic and Molecular Beam Methods Vol. 1*, Oxford University Press, 1988.

[10] N. F. Ramsey, *Molecular Beams*, Oxford Univeristy Press, 1956.

[11] W. Christen and K. Rademann, *Phys. Rev. A*, **77**, 012702 (2008).

[12] D. W. Chandler and P. L. Houston, *J. Chem. Phys.*, **87**, 1445 (1987).

[13] W. C. Wiley and I. H. McLaren, *Rev. Sci. Instrum.*, **26**, 1150 (1955).

[14] B. J. Whitaker, *Imaging in Molecular Dynamics: Technology and Applications*, Cambridge University Press, 2003.

[15] V. Dribinski, A. Ossadtchi, V. A. Mandelshtam and H. Reisler, *Rev. Sci. Instrum.*, **73**, 2634 (2002).

[16] G. A. Garcia, L. Nahon and I. Powis, *Rev. Sci. Instrum.*, **75**, 4989 (2004).

[17] K. Zhao, T. Colvin, W. T. Hill and G. Zhang, *Rev. Sci. Instrum.*, **73**, 3044 (2002).

[18] G. M. Roberts, J. L. Nixon, J. Lecointre, E. Wrede and J. R. R. Verlet, *Rev. Sci. Instrum.*, **80**, 053104 (2009).

[19] R. N. Zare, *Angular Momentum: Understanding Spatial Aspects in Chemistry and Physics*, Wiley-Blackwell, 1988.

[20] M. N. R. Ashfold, N. H. Nahler, A. J. Orr-Ewing, O. P. J. Vieuxmaire, R. L. Toomes, T. N. Kitsopoulos, I. A. Garcia, D. A. Chestakov, S. M. Wu and D. H. Parker, *Phys. Chem. Chem. Phys.*, **8**, 26 (2006).

[21] P. M. Regan, S. R. Langford, A. J. Orr-Ewing and M. N. R. Ashfold, *J. Chem. Phys.*, **110**, 281 (1999).

[22] J. E. Sansonetti and W. C. Martin, *J. Phys. Chem. Ref. Data*, **34**, 1559 (2005).

[23] A. T. J. B. Eppink and D. H. Parker, *J. Chem. Phys.*, **109**, 4758 (1998).

[24] A. T. J. B. Eppink and D. H. Parker, *J. Chem. Phys.*, **110**, 832 (1998).

3. The Dynamics of Hydrogen Elimination in Imidazole and Methylated Imidazole Derivatives

Time resolved velocity map imaging (TR-VMI) studies have been employed to study and explain the observed dynamics of excited electronic state population, in imidazole, 2-methylimidazole (2-MI), 4-methylimidazole (4-MI), 2,4-dimethylimdazole (2,4-DMI) and 1-methylimidazole (1-MI) following photoexcitation at 200 nm. Ultrafast hydrogen elimination was observed from the N-H coordinate in imidazole. This was detected as characteristic high total kinetic energy release (TKER) signal which is attributed to dissociation mediated by a $^1\pi\sigma^*$ state, yielding hydrogen with a time constant of 78 ± 37 fs. This suggests that the initially excited state is accessing the $^1\pi\sigma^*$ state that is dissociative along the N-H coordinate, via a conical intersection (CI), within tens of femtoseconds. In comparison the methylated derivatives 2-MI, 4-MI and 2,4-DMI show hydrogen elimination on a slower timescale. It is concluded that the presence of methyl groups on the imidazole ring slows down the rate of internal conversion (IC) from the initial state to the $^1\pi\sigma^*$ state.

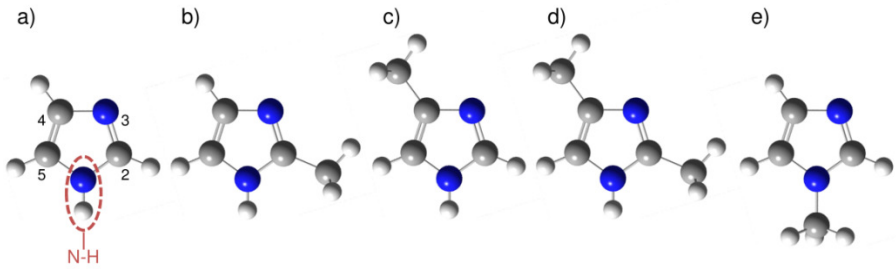

Figure 3.1 – The molecular structures of a) imidazole; b) 2-methylimidazole; c) 4-methylimidazole; d) 2,4-dimethylimidazole and e) 1-methylimidazole.

3.1 Introduction to Imidazole Photodynamics

The aim of this chapter is to look at the $^1\pi\sigma^*$ state [1, 2] driven photochemistry of imidazole (a subunit of both adenine and histidine) and methylated derivatives thereof, in order to assess: (i) the role of the $^1\pi\sigma^*$ state in the excited state dynamics of imidazole following photoexcitation to the optically "bright" $^1\pi\pi^*$ state; (ii) the influence of increasing degrees of freedom, introduced by the addition of methyl groups, on the excited state dynamics; and (iii) the role of statistical unimolecular decay pathways on short timescales (<100 ps). The desire to study imidazole originates from the numerous studies already performed on the photodynamics of the deoxyribonucleic acid (DNA) base adenine. The N-H coordinate in imidazole serves as a model for the N_9-H coordinate in adenine (see chapter 1.4.2) potentially providing an insight into $^1\pi\sigma^*$ mediated dynamics along only this N_9-H (azole) coordinate in adenine without contributing dynamics from the $^1\pi\sigma^*$ state localised along the amino coordinate upon the six membered ring (see section 1.4.1).[3]

3.1.1 Previous Studies on Imidazole

Following excitation at a range of wavelengths ($210 \leq \lambda \leq 240$ nm and $\lambda = 193$ nm), the hydrogen elimination dynamics of imidazole were studied using high Rydberg atom photofragment translation spectroscopy (HRA-PTS) by Ashfold and co-workers.[4, 5] These studies showed a bimodal distribution in the TKER spectra, the two components attributed to high TKER and low TKER hydrogen. The corresponding mechanisms assigned to these two channels were direct dissociation through the $^1\pi\sigma^*$ state and indirect dissociation in which highly vibrationally excited

$^1\pi\pi$ ground state molecules undergo statistical unimolecular decay, respectively. In addition, the relative intensity of the high TKER component was found to decrease markedly in the spectra recorded at $\lambda \leq 210$ nm. These authors also observed that the onset for direct absorption into the $^1\pi\pi^*$ state was at $\lambda \sim 220$ nm and corresponded to a large increase in absorption cross-section in the gas phase absorption spectrum (see section 3.1.2.).[4] For $\lambda > 220$ nm, direct absorption to the $^1\pi\sigma^*$ state was observed by intensity borrowing from the $^1\pi\pi^*$ state, in a similar mechanism to the direct $^1\pi\sigma^*$ state population previously observed in pyrrole.[6-8]

Time resolved studies have also been performed in imidazole to understand the photodynamics when excited at 250 – 217 nm [9] and 200 nm.[10] Both of these experiments showed that excited state depopulation is occurring on an ultrafast (<1 ps) timescale. However the authors of both papers stress that N-H dissociation is not the only relaxation process and a direct $^1\pi\pi^* \rightarrow {}^1\pi\pi$ IC pathway may also occur, mediated by a CI found along ring-puckering or ring-opening nuclear coordinates.

Theoretical Studies

These experiments have been complemented by high level *ab initio* calculations by Barbatti *et al.*[11] These show that direct excitation to the $^1\pi\sigma^*$ state can only access the $^1\pi\sigma^*$ / $^1\pi\pi$ CI, constituting the main pathway to both direct dissociation and ground state repopulation, ultimately leading to high and low TKER hydrogen, respectively. However, excitation to the $^1\pi\pi^*$ state cannot access the $^1\pi\sigma^*$ / $^1\pi\pi$ CI directly. Barbatti *et al.*[11] also showed that out-of-plane and in-plane distortions of the ring can lead to crossing of the $^1\pi\pi^*$ and $^1\pi\sigma^*$ states providing an indirect route to the $^1\pi\sigma^*$ / $^1\pi\pi$ CI, via a $^1\pi\pi^*$ / $^1\pi\sigma*$ CI. While this pathway can once

again lead to high TKER hydrogen through similar mechanisms as outlined above, the dominance of hydrogen elimination is not assured with other deactivation pathways via ring deformations now possible.

These theoretical investigations also explored the electronic structure of imidazole along ring-puckering and ring-opening coordinates. These showed that motion out-of-plane by either the N_3 or C_5 atoms and the extension of N_1-C_2 coordinate (see figure 3.1 a)) can lead to a $^1\pi\pi^*$ / $^1\pi\pi$ CI. However, a combination of theoretical non-adiabatic dynamics simulations and time resolved photoelectron spectroscopy has shown that these ring-puckering/ring-opening mechanisms form a minor pathway for excited state depopulation.[12] Therefore, the dominant pathway for excited state depopulation is expected to be via $^1\pi\pi^* \rightarrow {}^1\pi\sigma^*$ IC, followed by N-H elongation to the $^1\pi\sigma^*$ / $^1\pi\pi$ CI (see figure 3.2) and this mechanism was invoked to explain HRA-PTS results obtained in imidazole by Ashfold *et al.* [4]

Statistical Unimolecular Decay

A significant low TKER hydrogen signal has been observed in imidazole at a long time delay after photoexcitation (~10 ns) by Ashfold and co-workers, who attributed this to statistical unimolecular decay.[4] The work by Ashfold and co-workers suggest a mechanism for statistical fragmentation where IC to the $^1\pi\pi$ ground state leaves the molecule in a set of high vibrational eigenstates. This high level of vibrational energy may lead to "statistical boil-off" of hydrogen with low TKER if the vibrational energy is localised in the N-H coordinate through intramolecular vibrational energy redistribution (IVR).

Work by Roberts *et al.* [13] has shown that the timescale for statistical unimolecular decay in imidazole (and its structural isomer, pyrazole) takes hundreds of picoseconds, far longer than the typical pump probe delays employed in ultrafast time resolved studies. They also note that the onset of the low TKER hydrogen rises bi-exponentially, with an ultrafast component (<2.5 ps) and a much slower component (>270 ps).[13] The origin of low TKER hydrogen in ultrafast studies will be discussed further below.

3.1.2 Electronic Structure of Imidazole and its Derivatives

Schematic potential energy cut (PEC) of the $^1\pi\pi$, $^1\pi\sigma*$ and $^1\pi\pi*$ electronic states in imidazole with respect to the N-H coordinate is shown in figure 3.2. Also included is a representation of the high TKER hydrogen photodissociation process that was previously proposed by Ashfold *et al.* upon excitation at $\lambda < 220$ nm, which is supported by the calculations performed by Barbatti *et al.*[4, 11]

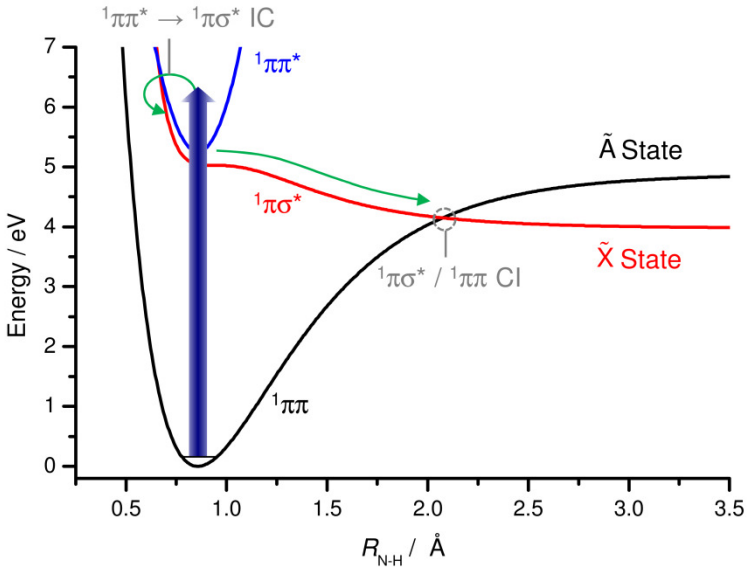

Figure 3.2 – Schematic PEC along the N-H coordinate in imidazole, showing the ground ($^1\pi\pi$) state and the first two excited states ($^1\pi\sigma*$ and $^1\pi\pi*$). Also shown is the proposed N-H dissociation mechanism. The PECs are based upon those calculated by King *et al.*[5]

Dissociation of the N-H coordinate in 2-MI, 4-MI and 2,4-DMI is predicted to proceed via a similar mechanism to imidazole. However, the energies of both the $^1\pi\sigma^*$ and $^1\pi\pi^*$ states, relative to the $^1\pi\pi$ state, are expected to vary between derivatives. This is apparent in the gas phase UV absorption spectra shown in figure 3.3 a) - d) and in the $^1\pi\pi^* \leftarrow {}^1\pi\pi$ vertical transitions in table 3.1.[14]

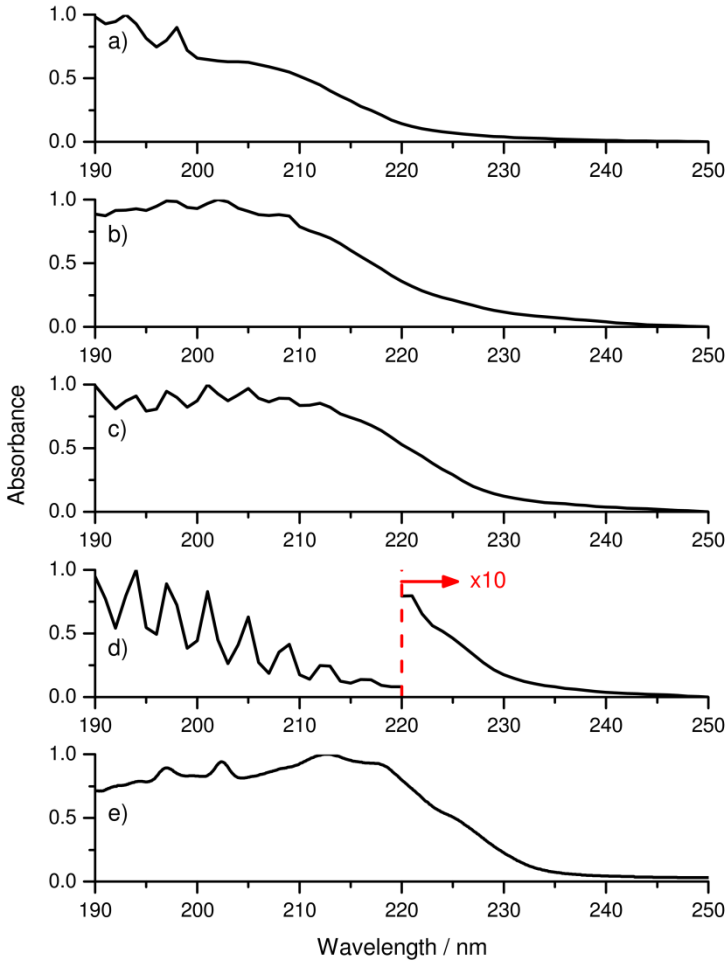

Figure 3.3 – Vapour phase UV absorption spectra of a) imidazole; b) 2-methylimidazole; c) 4-methylimidazole; d) 2,4-dimethylimidazole; and e) 1-methylimidazole.

The feature observed in figures 3.3 a) – e) beginning in the range 235 – 220 nm is attributed to the absorption of the optically "bright" $^1\pi\pi^*$ state, as this is

expected to have a far higher absorption cross-section than the optically "dark" $^1\pi\sigma^*$ state.

Also apparent from the UV spectra of the methylated imidazole derivatives (figures 3.3 b) – e)) is that the transition energy for $^1\pi\pi^* \leftarrow {}^1\pi\pi$ excitation is reduced (red-shifted) when compared to "bare" imidazole (figure 3.3 a)). This is attributed to the stabilisation of the $^1\pi\pi^*$ state induced by the presence of an electron donating methyl group(s). A similar trend for the $^1\pi\pi^* \leftarrow {}^1\pi\pi$ vertical transition energy is observed in the calculated energies in table 3.1, which use time dependent density functional theory (TD-DFT), linear response coupled cluster singles and doubles (LR-CCSD) and non-iterative corrected triples CCSD (CCSD(3)) theory. Also included are the experimental onsets for the $^1\pi\pi^* \leftarrow {}^1\pi\pi$ transitions from figure 3.3.

Table 3.1 – TD-DFT, LR-CCSD and CCSD(3) vertical excitation energies for the $^1\pi\pi^* \leftarrow {}^1\pi\pi$ transition in imidazole, 2-MI, 4-MI and 2,4-DMI. TD-DFT calculations were performed at B3LYP/6-31G*//B3LYP/aug-cc-pVTZ level of theory. All other calculations were performed with a aug-cc-pVTZ basis set. Also included are the assigned experimental onsets for the transition, taken from figure 3.3.

Molecule	Calculated $^1\pi\pi^* \leftarrow {}^1\pi\pi$ Vertical Transition / eV			Experimental Determined Onset / eV
	TD-DFT	LR-CCSD	CCSDR(3)	
Imidazole	6.16	6.55	6.44	~5.55
2-MI	5.95	6.58	6.51	~5.50
4-MI	5.87	6.30	6.20	~5.45
2,4-DMI	5.69	6.23	6.19	~5.35

3.1.3 Aims and Procedure

The use of TR-VMI provides the means to monitor the dynamics of hydrogen production on an ultrafast timescale providing detailed insight into factors that

control the efficiency of the photofragmentation process. Utilising such techniques should allow the study of how the proposed ring distortion mechanism governs population transfer from $^1\pi\pi^*$ to $^1\pi\sigma^*$, and whether substituting hydrogen atoms on the ring for more sterically hindering methyl groups alters the timescale of this population transfer. In addition the ability to measure the amount of high and low TKER hydrogen at very short times (<1 ps) may provide information about the efficiency of $^1\pi\sigma^*$ mediated dissociation and the suggested statistical unimolecular decay process, respectively.[15]

The experimental procedure was carried out as described in chapter 2 and the operating conditions for the valve are summarised in table 2.2. Studies utilised excitation at 200 nm using a series of β-barium borate (BBO) crystals (as describe in section 2.1.2) and probing at 243.1 nm by (2+1) resonance enhanced multiphoton ionisation (REMPI) via the 2s electronic state. As shown in figure 3.3, excitation at 200 nm corresponds to a transition with a significant absorption cross-section ($^1\pi\pi^* \leftarrow {}^1\pi\pi$) in imidazole and all derivatives. Significant amounts of H^+ signal were observed for all molecules in both the VMI and time of flight (TOF) mass spectrometer setup.

3.2 Experimental Results and Discussion

3.2.1 Total Kinetic Energy Release Spectra

Figures 3.4 a) – d) show raw images of H^+ and corresponding TKER spectra for imidazole, 2-MI, 4-MI and 2,4-DMI, respectively, following photoexcitation at 200 nm and probing with 243.1 nm. The pump probe delay (t) was set at 2 ps. When

the probe precedes the pump, there is negligible two-colour H^+ signal and this applies to all measurements discussed herein. As is evident from all the images, there is considerable H^+ signal in the centre of the image, which corresponds to hydrogen with low TKER following photodissociation (~1000 cm^{-1}). In addition, there is a clear outer ring, which results from hydrogen with higher TKER following photodissociation (~8000 – 9500 cm^{-1} depending on the system of interest). This high TKER hydrogen signal is attributed to dissociation along the $^1\pi\sigma^*$ state. Interestingly, the outer ring displays clear anisotropy for imidazole and 2-MI, with the H^+ signal being localised mostly perpendicular to the laser polarization axis (vertical arrow on image a)). This is reflected in the β_2 values directly below the associated TKER spectra shown in figure 3.4. The β_2 values obtained in these measurements display non-limiting negative values for the high TKER component in each spectrum. In the case of imidazole, this observation is consistent with previous measurements at 193 nm by Ashfold and co-workers, indicating that the initial recoil anisotropy is preserved due to prompt dissociation, consistent with the transition dipole moment (TDM) for the $^1\pi\pi^* \leftarrow {}^1\pi\pi$ transition being perpendicular to the N-H bond.[4] The retention of the initial recoil anisotropy implies that the $^1\pi\pi^* \rightarrow {}^1\pi\sigma^*$ IC is very fast. A discussion of β_2 parameters and the information one can extract relating to the mechanism will be revisited in the succeeding paragraphs.

The TKER spectra for imidazole, 2-MI, 4-MI and 2,4-DMI are obtained through deconvolution of the raw H^+ images and accounting for the co-fragment's kinetic energy using equation 1.24 by assuming the $C_3N_2H_3$, $C_4N_2H_5$, $C_4N_2H_5$ and $C_5N_2H_7$ radicals. The TKER spectra have been fitted using a Boltzmann distribution for the low TKER component and a Gaussian distribution for the high TKER

component (red and blue plots, respectively) details of which can be found in appendix I. as the partner fragments, respectively.

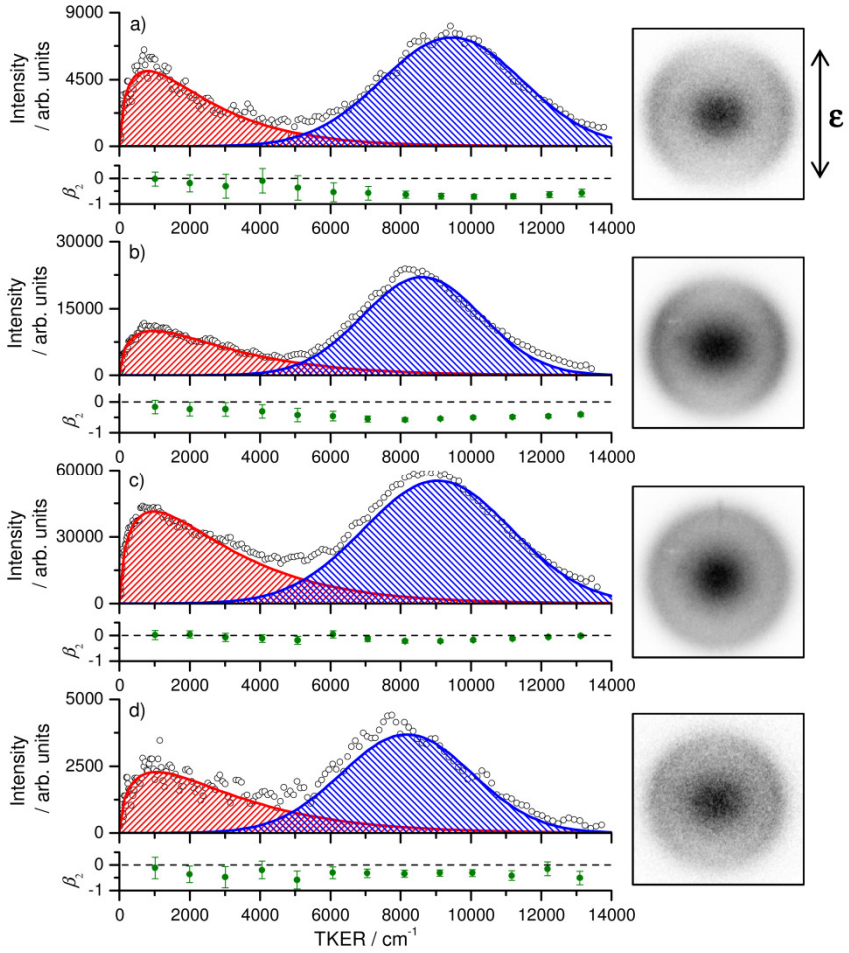

Figure 3.4 – Raw images for H^+ and corresponding TKER spectra following excitation at 200 nm and probing with 243.1 nm for a) imidazole, b) 2-MI, c) 4-MI and d) 2,4-DMI. The pump probe delay was set to +2 ps. The corresponding fits to the TKER spectra include a Boltzmann function (red) and a Gaussian distribution (blue). Also shown below each TKER spectrum is the associated β_2 anisotropy parameter as a function of TKER. The polarization of the pump laser relative to the image is shown by the double-headed arrow (**ε**).

As is clearly evident, the TKER spectra are bimodal, with two clear components peaked at ~1000 cm^{-1} and from 8000 cm^{-1} – 9500 cm^{-1}, depending on the molecule of interest. Interestingly, whilst the peak position for the low TKER component does not change for the different molecules, the high TKER component

does, which could be attributed to slight changes to the N-H bond dissociation energy (D_0) and the energy difference between the $^1\pi\pi^*$ / $^1\pi\sigma^*$ CI and the dissociation asymptote correlated to ground state radical products (red asymptote in figure 3.2 for imidazole).[16] It is important to note that for all TKER spectra recorded, detuning the probe wavelength away from the REMPI transition ($\lambda \neq 243.1$ nm) leads to a considerable reduction in the H^+ signal (>100 fold) indicative that neutral hydrogen is being probed.

The TKER spectrum for imidazole, shown in figure 3.4 a), is similar to that obtained by Ashfold and co-workers following photoexcitation directly to the $^1\pi\pi^*$ state at 193 nm.[4] In their study, the high TKER component was attributed to N-H dissociation along the $^1\pi\sigma^*$ state following $^1\pi\pi^* \rightarrow {}^1\pi\sigma^*$ IC. The low TKER component was postulated to occur *via* sequential $^1\pi\pi^* \rightarrow {}^1\pi\sigma^* \rightarrow {}^1\pi\pi$ IC followed by statistical dissociation of highly vibrational excited ground state molecules through unimolecular decay. While the central peak positions of the high and low TKER components are almost identical between the above TR-VMI measurements and the HRA-PTS measurements of Ashfold and co-workers, there is a striking disparity in the relative peak heights between the high and low TKER components. The TR-VMI measurements have been extended out to a 100 ps pump probe delay (time window of the experiment when these measurements were performed), specifically to monitor the contributions, if any, from statistical unimolecular decay which is anticipated to occur on a much longer timescale as observed by Roberts *et al.* [13] (discussed further below). No noticeable change in the TKER spectra was observed, with almost twice as much high TKER component relative to the low TKER component (obtained by integrating the Gaussian and statistical decay fits in

imidazole) observed independently of pump probe delay in the range $100 > t > 2$ ps. This is in sharp contrast to the HRA-PTS on imidazole, with this ratio seemingly reversed. This seems to suggest that the low TKER component is formed with two time constants. The first is very short whilst the second is long (>100 ps) in agreement with the results observed by Roberts *et al.*[13]

3.2.2 Hydrogen Transients

The transient H^+ signal for imidazole is shown in figure 3.5 a) and b) for the high and low TKER components, respectively. For 2-MI, 4-MI and 2,4-DMI, the corresponding transients are shown in figure 3.6 and the relevant transient data is given in table 3.2. All transients discussed herein are obtained by collecting a series of TKER spectra at different pump probe delays and integrating each TKER spectrum around the high and low TKER features (for energy integral ranges, see table 3.2).

Imidazole Transients

For both transients shown in figure 3.5, when the probe precedes the pump, i.e. $t < 0$, no two-colour probe pump H^+ signal is observed. For $t > 0$, the H^+ sharply rises and plateaus by 500 fs, indicative of very fast N-H dissociation. The normalised experimental data is fit to a convoluted Gaussian and single exponential rise function (see appendix I for details). For imidazole, time constants of $\tau_H = 78 \pm 37$ fs and $\tau_L = 163 \pm 50$ fs are obtained for the high and low TKER components, where the subscripts H and L represent high and low TKER, respectively. The corresponding fits to the data are also shown by the solid black lines. The large uncertainty in the τ_H

time constant, relative to the actual value of τ_H for the high TKER component is a result of the 160 fs instrument response function (IRF).

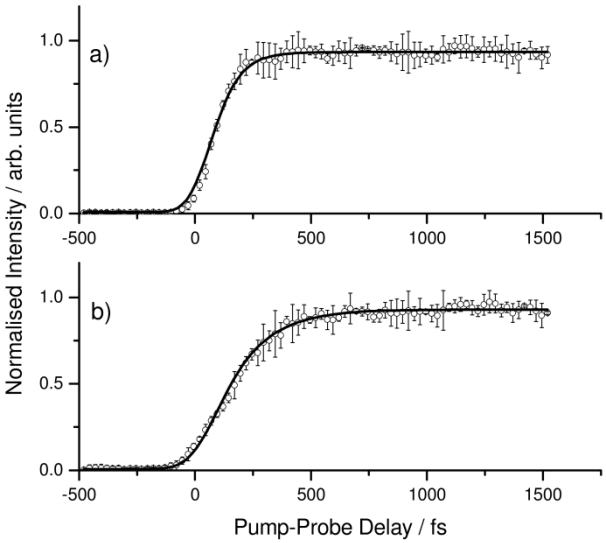

Figure 3.5 – H^+ transients as a function of pump (200 nm) probe (243.1 nm) delay for high and low TKER components, a) and b), respectively, in imidazole. Experimental data is fit with an exponential rise function convolved to the IRF (solid black line) giving time constants τ for the high (τ_H) and low (τ_L) TKER components of a) τ_H = 78 ± 37 fs and b) τ_L = 163 ± 50 fs, respectively. Error bars correspond to a 95% confidence limit.

The short time constant for the high TKER component is apparent in the retention of the initial recoil anisotropy in the raw image in figure 3.4 a) and in previous work.[4] Following photoexcitation at 200 nm in imidazole, $^1\pi\pi^* \rightarrow {}^1\pi\sigma^*$ IC and then dissociation along the $^1\pi\sigma^*$ state occurs in 78 ± 37 fs, meaning that population transfer between $^1\pi\pi^* \rightarrow {}^1\pi\sigma^*$ IC occurs in less than 78 fs. In turn, this suggests the coupling between the relevant potential energy surfaces (PESs) mediated by distortions of the ring leads to very efficient population transfer onto the $^1\pi\sigma^*$ state. Theory suggests that the dominance of the $^1\pi\sigma^*$ channel is no longer assured as compared to direct excitation to the $^1\pi\sigma^*$ state.[11, 12] Whilst the measurements presented here strongly point towards the active participation of the

$^1\pi\sigma^*$ state following excitation to the $^1\pi\pi^*$ state, they are only sensitive to this channel and hence the exclusion of other pathways as a possible photorelaxation pathway is not possible. Such pathways include the ring-puckering and ring-opening channels, suggested by the calculations of Barbatti *et al*., for both imidazole [11] and pyrrole [17] and/or ring deforming dynamics observed in the parent imidazole molecule by Ullrich and co-workers using time-resolve ion yield, which provides a timescale for excited state depopulation through the measurement of other fragment ion generation.[10]

Considering the low TKER component, the time constant for the formation of these hydrogen atoms is also very short, indicating that the dynamics are direct. These scans have been extended up to ~100 ps (not shown) with minimal changes to the TKER spectra observed. One would expect the time constant for statistical unimolecular decay to be much longer than the time constant measured here for the low TKER component (τ_L = 163 ± 50 fs). Based on Rice-Ramsperger-Kassel-Marcus (RRKM) theory, one generally anticipates statistical decay to occur on a minimum time frame of nanoseconds [18] and strongly suggests that the origin of these hydrogen atoms is not through successive $^1\pi\pi^* \rightarrow {}^1\pi\sigma^* \rightarrow {}^1\pi\pi$ IC couplings followed by statistical unimolecular decay of highly vibrational excited ground state molecules. Instead, given the energy difference between the ground ($\tilde{X}$) and electronically excited ($\tilde{A}$) state of the imidazolyl radical is ~7000 cm^{-1},[5] the low TKER energy component could be attributed to adiabatic dissociation at the $^1\pi\sigma^*$ / $^1\pi\pi$ CI. This type of two channel dissociation has previously been observed in measurements of hydrogen elimination in phenol-d_5.[19]

However, inspection of the variation in β_2 as a function of TKER seems to disprove this hypothesis (see anisotropy parameter discussion below).

Methylated Derivative Transients

The effect of ring methylation at the 2-, 4- and 2,4- positions upon the dynamics is summarised by the data shown in table 3.2, which are derived from the fits in figure 3.6. At a first glance, the time constants for both the high and low TKER components are longer than those obtained in imidazole and plausible explanations are given below.

Table 3.2 – Extracted time constants τ for the high (τ_H) and low (τ_L) TKER components obtained in imidazole, 2-MI, 4-MI, 2,4-DMI and 1-MI obtained through convolution of the IRF with an exponential rise (see appendix 1). Also shown are the integral widths for the high and low TKER components used to extract the associated time constants for imidazole and its methylated derivatives.

Molecule	High KER		Low KER	
	Integral / cm^{-1}	**Rise Time (τ_L) / fs**	**Integral / cm^{-1}**	**Rise Time (τ_H) / fs**
Imidazole	7000 – 12000	78 ± 37	500 – 4500	163 ± 50
2-MI	6500 – 11000	131 ± 16	500 – 4500	305 ± 57
4-MI	6500 – 11500	185 ± 37	500 – 4500	334 ± 59
2,4-DMI	5500 – 11000	139 ± 56	500 – 4500	250 ± 105
1-MI	-	-	0 - 10000	< 50

It is also notable in table 3.2 that once again for 2-MI, 4-MI and 2,4-DMI, there is a noticeable difference in the time constants extracted for the high and low TKER components. The transients derived from analysis of the high TKER component are attributed to $^1\pi\pi^* \rightarrow {}^1\pi\sigma^*$ IC followed by direct dissociation *via* the $^1\pi\sigma^*$ state as in imidazole. Given the short time constants extracted for the low

TKER component, this once again strongly suggests that sequential IC from $^1\pi\pi^* \rightarrow {}^1\pi\sigma^* \rightarrow {}^1\pi\pi$ followed by statistical unimolecular decay is very unlikely to be the origin of these low TKER hydrogen. However, in much the same way to the imidazole data discussed above, statistical unimolecular decay is expected0 at longer timescales (> 100 ps) in agreement with the results observed by Roberts *et al.*[13]

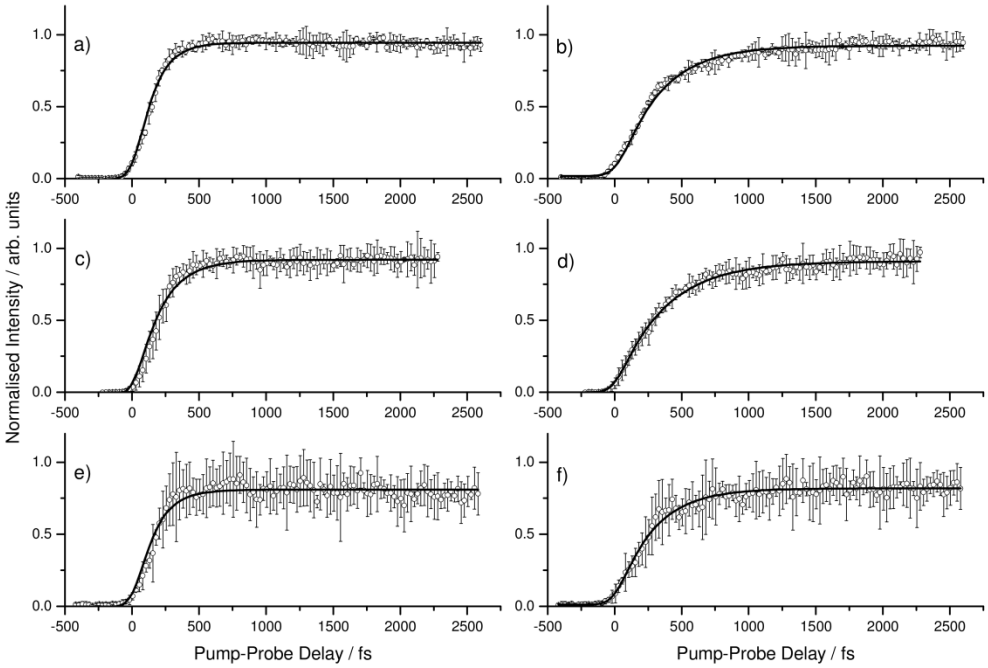

Figure 3.6 – H^+ transients as a function of pump (200 nm) probe (243.1 nm) delay for high and low TKER components for a) and b) 2-MI; c) and d) 4-MI; e) and f) 2,4-DMI. Experimental data is fit with an exponential rise function convolved to the IRF (solid black line) giving time constants τ which are provided in table 3.2. Error bars correspond to a 95% confidence limit.

3.2.3 Anisotropy Parameters

Also included in figure 3.4 a) - d) is a plot of β_2 as a function of TKER in imidazole, 2-MI, 4-MI and 2,4-DMI, respectively. For imidazole, a non-limiting negative β_2 (~-0.75) for the high TKER component is apparent, peaking at ~9500 cm^{-1}. However, within the signal-to-noise, the low TKER component is almost isotropic. If the low TKER component was indeed due to/possesses contributions

from adiabatic dissociation, one would anticipate that *both* the high and low TKER components would display similar β_2 values given that both the ground and excited state imidazolyl radicals originate from the same initially prepared $^1\pi\pi^*$ state, albeit with a different quantum yield. However, the variation between the anisotropies of the two components is notable and therefore very likely rules out adiabatic dissociation at the $^1\pi\sigma^*$ / $^1\pi\pi$ CI as the origin of the low TKER component. Multiphoton processes such as absorption of a further pump photon by the parent cation to generate hydrogen atoms, similar to that postulated in other studies could be a likely candidate.[20]

The β_2 measured for the methylated derivatives shows some notable differences from those measured in imidazole. Whilst for imidazole there is a clear distinction between the measured β_2 values for the high and low TKER components, the high TKER showing non-limiting negative anisotropy (β_2 ~-0.75) while the low TKER a more isotropic value, this is not as clear-cut for all the methylated derivatives (see figure 3.4 b) – d)). For 2-MI the high TKER component displays a negative non-limiting β_2 value (~-0.6), whilst the low TKER component, within the signal-to-noise, is isotropic, much-like imidazole. For 4-MI and 2,4-DMI however, the high TKER components have a much smaller, non-limiting β_2 (~-0.15 and ~-0.3, respectively). As a result, it is concluded that the low TKER component in 2-MI is unlikely a result of dissociation to excited ($\tilde{A}$) state imidazolyl fragments formed via an adiabatic pathway at the $^1\pi\sigma^*$ / $^1\pi\pi$ CI. However for 4-MI and 2,4-DMI, the argument carries less gravitas owing to the less negative β_2 value for the high TKER components. Assessing the TDM for the initial excitation may provide an explanation for the disparity between imidazole/2-MI and 4-MI/2,4-DMI in the high

TKER hydrogen β_2. However, the TD-DFT calculations discussed above did not suggest a significant difference in the TDM between imidazole and the three derivatives.

3.2.4 The Effects of Ring Methylation

Along with the difference in β_2, it is apparent that methylation of the ring in imidazole leads to an increase in the time constant for both the high and low TKER transients. Theory predicts that out-of-plane and in-plane distortions can lead to $^1\pi\pi^* \rightarrow {}^1\pi\sigma^*$ IC [11] and it is conceivable that replacing H with the heavier CH_3 group could hinder this motion. This in turn could subsequently lengthen the timescale for population transfer from $^1\pi\pi^* \rightarrow {}^1\pi\sigma^*$ and hence dissociation along the $^1\pi\sigma^*$ state leading to the high TKER component. For the low TKER component, this is slightly less clear-cut given that the origin of the low TKER hydrogen signal is less definitive, although the more feasible candidate could be multiphoton processes. However, it is notable that both the high *and* low TKER transients for 2-MI, 4-MI and 2,4-DMI are longer than the corresponding transients observed in imidazole which could imply that the low TKER component may also originate from the $^1\pi\sigma^*$ state following IC from $^1\pi\pi^*$.

Alternatively, the increased hydrogen elimination timescales in the methylated imidazole derivatives, relative to imidazole, may be accounted for by considering differences in the density of vibrational states at the excitation energy of 6.2 eV (200 nm). If, as suggested by Barbatti *et al.*,[11] the $^1\pi\pi^* \rightarrow {}^1\pi\sigma^*$ coupling relies on motion along a specific ring deforming coordinate then as the density of vibrational states at the excitation energy increases, the flux imparted to the $^1\pi\pi^*$

state will have a greater probability of sampling orthogonal modes rather than those which could promote coupling between the $^1\pi\pi^*$ and $^1\pi\sigma^*$ surfaces. This will lengthen the time that the system remains on the $^1\pi\pi^*$ state. As a result, the appearance timescales for any subsequent N-H bond fission may be notably slower. Within a Fermi's golden rule [21, 22] model for IC, the transition rate would be expected to increase with greater density of states, evidently this is not the case in imidazole. [11] The density of states in the methylated derivatives can be assessed relative to "bare" imidazole by comparing the energies of the onset of the $^1\pi\pi^*$ state (relative to the $^1\pi\pi$ ground states), the density of vibrational eigenstates should increases with excess energy in the $^1\pi\pi^*$ state (i.e. a typical anharmonic potential).

The computed vertical transitions and assigned experimental $^1\pi\pi^* \leftarrow {}^1\pi\pi$ transition onsets in table 3.1 suggest that upon methylation of the imidazole ring, the $^1\pi\pi^* \leftarrow {}^1\pi\pi$ vertical excitation energies decrease, thus increasing the density of states accessible at 200 nm in the $^1\pi\pi^*$ state. This supports the experimental observation that, relative to imidazole, the time constants for hydrogen yield increase in 2-MI and 4-MI as shown in table 3.2. However, this explanation fails to account for the timescales extracted from experiments on 2,4-DMI (see table 3.2), which are faster than those obtained for 4-MI at high TKER and both 2-MI and 4-MI at low TKER. Based on the arguments made above and the fact that the calculated $^1\pi\pi^* \leftarrow {}^1\pi\pi$ energy is smallest for 2,4-DMI from the various calculations, it is anticipated that 2,4-DMI would exhibit the longest hydrogen elimination timescales. However, these arguments are an over simplification and give no consideration to the topography of the $^1\pi\pi^*$ PES in all the available ($3N-6$, where N is the number of atoms) vibrational degrees of freedom. It is possible that within one of these

dimensions, 2,4-DMI exhibits additional methods of efficiently coupling from $^1\pi\pi^*$ via a CI to the $^1\pi\sigma^*$ state, such as those highlighted by Barbatti *et al.* in "bare" imidazole.[11, 12]

3.2.5 1-Methylimidazole Results

A TKER spectrum, raw H^+ image and transient of low TKER H^+ for hydrogen formed by a 200 / 243.1 nm pump probe scheme in 1-MI is shown in figure 3.7.

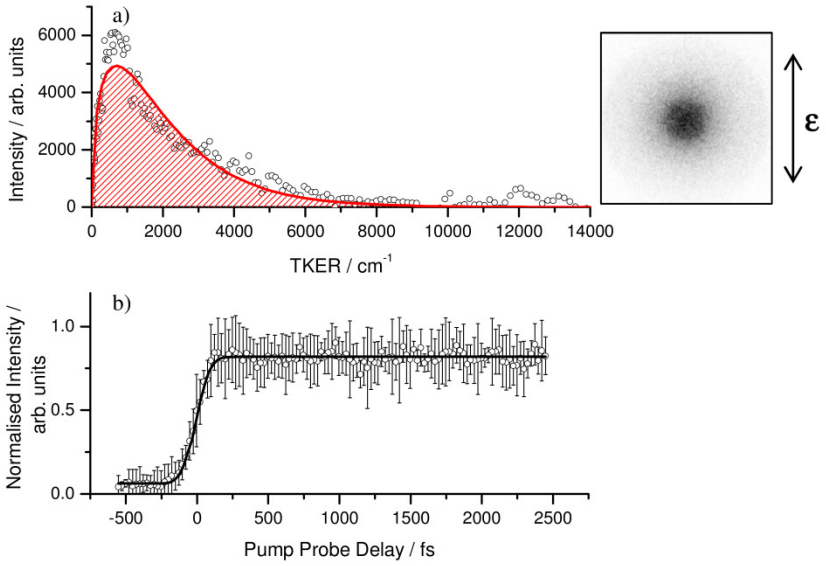

Figure 3.7 – a) Raw H^+ image and corresponding TKER spectrum for hydrogen elimination from 1-MI taken with a 200 nm pump and 243.1 nm probe at a pump probe delay of +2 ps. The polarization of the pump laser relative to the image is shown by the double-headed arrow (**ε**).The corresponding fit to the TKER spectrum is a Boltzmann function (red). b) H^+ transient of hydrogen eliminated from 1-MI at all TKER fit with an exponential rise function convolved to the IRF (solid black line) giving a time constant $\tau < 50$ fs. Error bars correspond to a 95% confidence limit.

From the TKER spectrum and the raw image it is clear that no hydrogen is eliminated with high TKER. This is to be expected, as the N-H coordinate is no longer present. The hydrogen signal observed at low TKER is therefore a result of

dissociation of either ring C-H bonds or the C-H bonds of the methyl group. The process for forming the low TKER hydrogen signal is expected to be the result of multiphoton absorption to a high lying electronic state which can then lead to C-H dissociation yielding neutral hydrogen atoms. From a fit of the transient signal (figure 3.7 b)), yielding a timescale for C-H dissociation of <50 fs, it is apparent that hydrogen formation is an ultrafast process (quicker than the temporal resolution of the TR-VMI setup). This timescale is significantly quicker than the formation of low TKER hydrogen in imidazole and the methylated derivatives, suggesting that at least some proportion of the H^+ signal observed in imidazole (with τ_L = 163 ± 50 fs) originates from N-H dissociation.

3.3 Conclusions

TR-VMI has been used to directly probe hydrogen elimination of imidazole and its methylated derivatives. The measurements show that following photoexcitation at 200 nm, very fast IC from the $^1\pi\pi^*$ to the $^1\pi\sigma^*$ state, potentially mediated by ring distortions, leads to hydrogen atoms eliminated with high TKER. The time constant for this component in imidazole is 78 ± 37 fs and is attributed to $^1\pi\pi^* \rightarrow {}^1\pi\sigma^*$ IC and then N-H dissociation along the $^1\pi\sigma^*$ state. The low TKER component has a time constant of 163 ± 50 fs. Given the timescale on which the low TKER component appears, it seems unlikely this can be due to statistical unimolecular decay and implies a more direct process such as multiphoton processes. Methylation of the ring leads to a discernible increase in the time constants for both the high and low TKER components. This may be due to a combination of: (i) the heavier methyl groups hindering the in-plane and out-of-plane ring distortions that

mediate $^1\pi\pi^* \rightarrow {}^1\pi\sigma^*$ IC; and (ii) an increased density of vibrational states, compared to imidazole, at the excitation energy (6.2 eV) in the $^1\pi\pi^*$ state, causing an increased sampling of orthogonal modes rather than those which mediate efficient coupling between the $^1\pi\pi^*$ and $^1\pi\sigma^*$ states. Given that the time constants for both the high and low TKER components increase upon methylation, this seems to suggest that the low TKER component may also be mediated by $^1\pi\pi^* \rightarrow {}^1\pi\sigma^*$ IC, although the precise mechanism for these low TKER hydrogen is still unclear. Studies of 1-MI suggest that hydrogen elimination from C-H coordinates can occur, through multiphoton absorption processes, within 50 fs.

3.4 References

[1] A. L. Sobolewski and W. Domcke, *Chem. Phys. Lett.*, **310**, 548 (1999).

[2] M. N. R. Ashfold, G. A. King, D. Murdock, M. G. D. Nix, T. A. A. Oliver and A. G. Sage, *Phys. Chem. Chem. Phys.*, **12**, 1218 (2010).

[3] K. L. Wells, D. J. Hadden, M. G. D. Nix and V. G. Stavros, *J. Phys. Chem. Lett.*, **1**, 993 (2010).

[4] A. L. Devine, B. Cronin, M. G. D. Nix and M. N. R. Ashfold, *J. Chem. Phys.*, **125**, 184302 (2006).

[5] G. A. King, T. A. A. Oliver, M. G. D. Nix and M. N. R. Ashfold, *J. Chem. Phys.*, **132**, 064305 (2010).

[6] J. Wei, A. Kuczmann, J. Riedel, F. Renth and F. Temps, *Phys. Chem. Chem. Phys.*, **5**, 315 (2003).

[7] J. Wei, J. Riedel, A. Kuczmann, F. Renth and F. Temps, *Faraday Discuss.*, **127**, 267 (2004).

[8] H. Lippert, H. H. Ritze, I. V. Hertel and W. Radloff, *ChemPhysChem*, **5**, 1423 (2004).

[9] R. l. Montero, A. l. P. Conde, V. Ovejas, M. Fernández-Fernández, F. Castaño and A. Longarte, *J. Phys. Chem. A*, **116**, 10752 (2012).

[10] H. Yu, N. L. Evans, V. G. Stavros and S. Ullrich, *Phys. Chem. Chem. Phys.*, **14**, 6266 (2012).

[11] M. Barbatti, H. Lischka, S. Salzmann and C. M. Marian, *J. Chem. Phys.*, **130**, 034305 (2009).

[12] R. Crespo-Otero, M. Barbatti, H. Yu, N. L. Evans and S. Ullrich, *ChemPhysChem*, **12**, 3365 (2011).

[13] G. M. Roberts, C. A. Williams, M. J. Paterson, S. Ullrich and V. G. Stavros, *Chem. Sci.*, **3**, 1192 (2012).

[14] These and further calculations discussed in this chapter were performed by Dr G. M. Roberts at the University of Warwick, Ms L. T. Bergendahl and Prof. M. J. Paterson at Heriot-Watt University. These results are publish in: *Phys. Chem. Chem. Phys.*, **13**, 10342 (2011)

[15] D. J. Hadden, K. L. Wells, G. M. Roberts, L. T. Bergendahl, M. J. Paterson and V. G. Stavros, *Phys. Chem. Chem. Phys.*, **13**, 10342 (2011).

[16] B. Cronin, M. G. D. Nix, R. H. Qadiri and M. N. R. Ashfold, *Phys. Chem. Chem. Phys.*, **6**, 5031 (2004).

[17] M. Barbatti, M. Vazdar, A. J. A. Aquino, M. Eckert-Maksic and H. Lischka, *J. Chem. Phys.*, **125**, 164323 (2006).

[18] K. A. Holbrook, M. J. Pilling and S. H. Robertson, *Unimolecular Reactions*, John Wiley & Sons, 1996.

[19] A. Iqbal, M. S. Y. Cheung, M. G. D. Nix and V. G. Stavros, *J. Phys. Chem. A*, **113**, 8157 (2009).

[20] M. G. D. Nix, A. L. Devine, B. Cronin, R. N. Dixon and M. N. R. Ashfold, *J. Chem. Phys.*, **125**, 133318 (2006).

[21] P. A. M. Dirac, *Proc. R. Soc. Lond. A*, **114**, 243 (1927).

[22] G. S. Beddard, G. R. Fleming, O. L. J. Gijzeman and G. Porter, *Chem. Phys. Lett.*, **18**, 481 (1973).

4. Time Resolved Velocity Map Imaging Studies of CH_3 Elimination from Photoexcited Anisole

Hydrogen elimination from heteroaromatic molecules following ultraviolet (UV) excitation has been extensively studied, with the focus on key biological molecules such as chromophores of deoxyribonucleic acid (DNA) bases and amino acids. Extending these studies to look at elimination of other non-hydride photoproducts is essential in creating a more complete picture of the photochemistry of these biomolecules in the gas phase. In this chapter, CH_3 elimination in anisole has been studied using time resolved velocity map imaging (TR-VMI) following photoexcitation at 200 nm. The role of $^1\pi\sigma^*$ states in the excited state dynamics of anisole is compared to the hydride counterpart, phenol, which has been the focus of numerous previous investigations. TR-VMI of anisole provides strong evidence that only CH_3 fragments eliminated with high total kinetic energy release (TKER) are due to direct dissociation involving a $^1\pi\sigma^*$ state, which appear in 91 ± 36 fs. These measurements also suggest that indirect mechanisms such as statistical unimolecular decay could be contributing to the dynamics at much longer times.

4.1 Introduction to Anisole Studies

Since the prediction of the $^1\pi\sigma^*$ relaxation pathway by Domcke and Sobolweski [1, 2] an increasing number of experiments have been carried out in the gas phase to investigate these $^1\pi\sigma^*$ states that are dissociative along the X-H coordinate (where X is typically O, N or S). Whilst a flurry of both experiment and theory has been directed towards $^1\pi\sigma^*$ states in hydrides, in contrast much less effort has been directed at studying these dissociative states localised on other coordinates such as X-C. The velocity map ion imaging (VMI) work by Ashfold and co-workers was the first to identify the role of $^1\pi\sigma^*$ state induced bond dissociation in non-hydride heteroaromatic systems.[3] Their work on N-methylpyrrole clearly showed the bimodal distribution of CH_3 photoproducts following excitation with UV radiation. In keeping with their hydrogen TKER spectra, the appearance of high and low TKER components in their spectra were attributed to direct dissociation along the $^1\pi\sigma^*$ state resulting in high TKER CH_3 fragments and indirect dissociation, in which highly excited ground state molecules decay, resulting in low TKER CH_3 fragments. This work was further complemented by Becucci and co-workers whose combined experimental and theoretical studies showed the existence of two low-lying dissociative $^1\pi\sigma^*$ states localised on the X-CH_3 coordinate in the same system.[4] Using multi-mass ion-imaging, Tseng *et al.* carried out a series of experiments on anisole, N-methylindole and N-methylpyrrole, clearly showing the appearance of high and low TKER CH_3 fragments following photodissociation at 248 nm and 193 nm, to which they once again rationalised these findings by invoking the presence of a $^1\pi\sigma^*$ state localised on the X-CH_3 coordinate.[5] Most

recently, Lim and Kim studied the photodissociation of thioanisole (C_6H_5S-CH_3), observing dissociation mediated by the dissociate $^1\pi\sigma^*$ state that leads to a branching of photoproducts between the ground ($\tilde{X}$) and excited ($\tilde{A}$) radical products.[6]

4.1.1 Aims and Procedure

Although these measurements have provided significant insight into the underlying photophysics of these systems, with clear evidence for the active participation of $^1\pi\sigma^*$ states along X-CH_3 coordinates, very little is known about the timescales of these processes which is critical in unravelling the complex interplay between adiabatic and non-adiabatic dynamics and the factors which affect these. In previous studies on phenol (both deuterated and undeuterated) and imidazole (see chapter 3)[7-10] it has been shown that *both* the high and low TKER components of the hydrogen TKER spectra possess appearance timescales on the order of 100 femtoseconds. Whilst this timescale is unsurprising for a direct process in which dissociation occurs within one vibrational period (i.e. $^1\pi\sigma^*$ mediated dissociation), what is surprising is the timescale for the low TKER component. As discussed in chapter 3 with reference to imidazole,[9, 11-16] previous work by Ashfold and co-workers has attributed this low TKER hydrogen (and CH_3 in N-methylpyrrole) to statistical unimolecular decay whereby vibrational energy must be localised in the correct mode of the electronic ground state before dissociation can occur.[11, 17] However, this mechanism cannot be used to explain the short time constants observed for these low TKER fragments observed in previous hydrogen elimination studies.[10] This has led to suggestion that the appearance of this low TKER hydrogen (and potentially CH_3) is (at least in part) a result of multiphoton absorption

in the parent molecule, similar to that observed for low TKER hydrogen in imidazole (see chapter 3).[9]

In an attempt to extend existing studies on the dissociation of X-CH_3 coordinates and to bridge the gap between these studies and those of phenol, [18] the O-CH_3 dissociation dynamics in anisole are investigated in this chapter. The aim of this work is to determine firstly, the timescale for $^1\pi\sigma^*$ mediated dissociation through the measurement of the high TKER methyl component of the signal and secondly, to provide information about the origin of the low TKER signal observed previously by Tseng *et al.*[5]

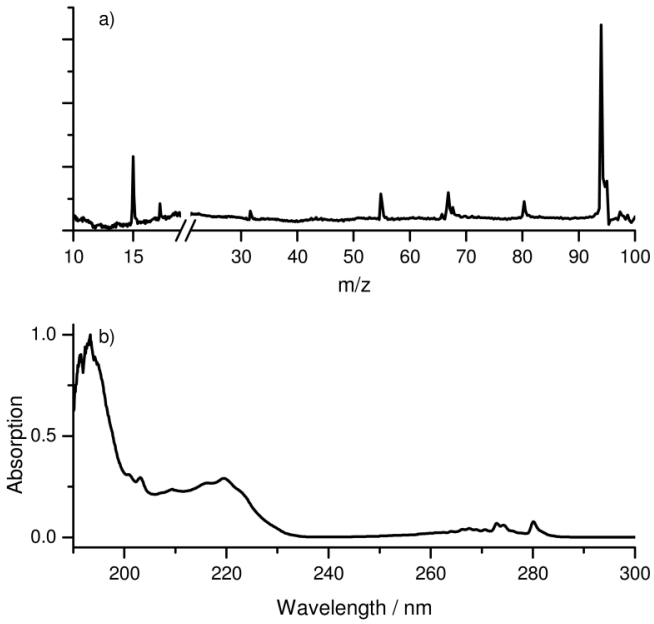

Figure 4.1 – a) Mass spectrum of anisole taken with a 200 nm pump and a 333.4 nm probe at a pump probe delay of 1.5 ps. The spectrum is not continuous across the axis break, the lower m/z signal was collected at higher detector voltages (V_{mcp1} and V_{mcp2}) b) Gas phase UV absorption spectrum of anisole.

All experiments herein were performed following excitation at 200 nm. The CH_3 fragments were probed with 333.4 nm which resonantly ionises CH_3 radicals via

the two-photon 3p $^2A_2'' \leftarrow \widetilde{X}\ ^2A_2''$ transition.[19] A comparative set of experiments were also performed, at 322.5 nm, to assess the contribution to the total CH_3 signal from background CH_3^+ generated through multiphoton absorption processes in the parent anisole. The valve operating conditions are summarised in table 2.2 with a typical mass spectrum of anisole shown in figure 4.1 a), taken with a 200 and 333.4 nm pump probe setup at a 1.5 ps pump probe delay. The UV absorption spectrum of anisole is also shown in figure 4.1 b), with a pronounced absorption at 200 nm which is assigned to a transition to a high lying $^1\pi\pi^*$ state, similar to the high lying states observed in phenol.[20, 21]

4.2 Anisole Studies Results

4.2.1 Total Kinetic Energy Release Spectrum

Figure 4.2 b) and c) shows raw images of CH_3^+ at two pump probe delays. Figure 4.2 c) corresponds to a delay (*t*) between the pump and probe pulses of +1.5 ps, where the pump precedes the probe while figure 4.2 c) corresponds to a pump probe delay of -1.5 ps, the probe now preceding the pump. When the probe precedes the pump, there is considerably less CH_3^+ signal as compared to when the pump precedes the probe (approximately 10 times less total CH_3^+ signal), indicative of a two colour pump probe signal in comparison to a combined pump alone and probe alone signal at negative delays. The TKER of the CH_3 fragment following dissociation is reflected in the distance of the corresponding CH_3^+ from the centre of the image. In figure 4.2 b), there is a small rise in the CH_3^+ signal around 180 pixels from the centre of the image (or 18000 cm^{-1}) which is attributed to CH_3 formed

through dissociation via the $^1\pi\sigma^*$ state localised along the O-CH_3 coordinate and is more noticeable in the TKER spectrum shown in figure 4.3 (solid line).

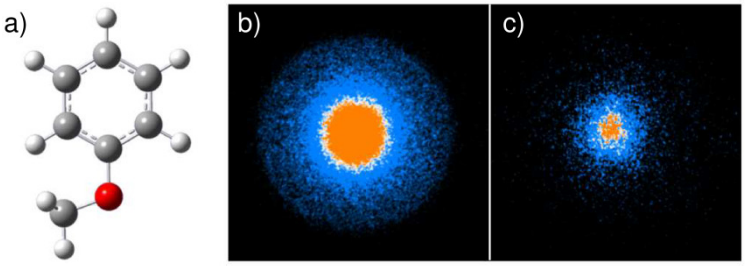

Figure 4.2 – a) Molecular structure of anisole. Velocity map images of CH_3^+ taken with a pump and probe of 200 and 333.4 nm, respectively, taken at a pump probe delay of b) + 1.5 ps and c) – 1.5 ps.

Figure 4.3 shows the TKER distributions derived from deconvolution of the raw CH_3^+ images and assuming C_6H_5O (mass 93) as the partner co-fragment, following photoexcitation at 200 nm and probing CH_3 through resonance enhanced multiphoton ionisation (REMPI) at 333.4 nm and multiphoton ionisation (MPI) at 322.5 nm (solid and dashed lines, respectively). The delay between the pump and probe pulses was set at 1.5 ps. The spectra are dominated by a low TKER CH_3 component, which extends towards high TKER. On close inspection of the on-resonance TKER distribution (solid line) one is able to discern a high TKER component embedded within the tail of the low TKER component, manifested by the noticeable rise in the signal around 18000 cm^{-1}, highlighted in blue for clarity. When detuning from the 333.4 nm resonance, the high TKER component is notably reduced, which indicates that probing of neutral CH_3 through REMPI is occurring following photodissociation. The neutral CH_3 eliminated at high TKER is assigned to dissociation mediated by the $^1\pi\sigma^*$ state.

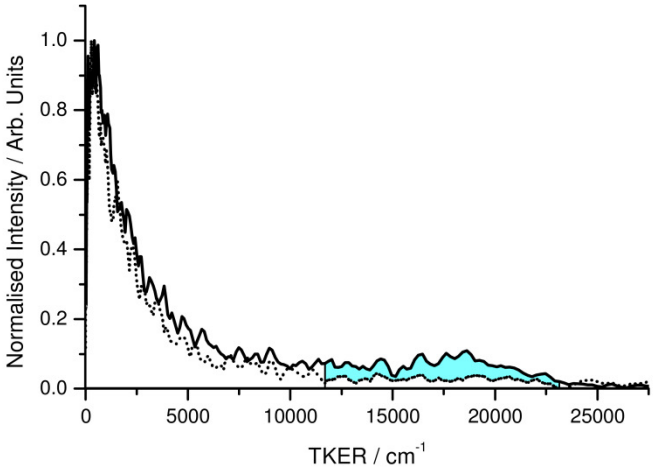

Figure 4.3 – Total kinetic energy release spectra for anisole taken with a 200 nm pump and a 333.4 nm (solid line) or 322.5 nm (dashed line) probe at a pump probe delay of + 1.5 ps. The highlighted area shows the neutral CH_3 from 200 nm induced dissociation attributed to $^1\pi\sigma^*$ dissociation.

In recent work on phenol-d_5, which looks at hydrogen eliminated from the O-H group alone,[8] there is a clear bimodal distribution between the low and the high TKER components, with each component sharing almost equal intensity. In contrast, the on-resonance TKER distribution in figure 4.3 shows a much greater contribution of low TKER component as compared to the high TKER counterpart. In addition, the high TKER component in anisole appears at higher values than the corresponding high TKER component in phenol-d_5 following photoexcitation at 200 nm. This is unsurprising given the decrease in the O-CH_3 bond energy (~22500 cm^{-1}) as compared to the O-H bond energy in phenol (~31000 cm^{-1}).[5] The TKER distribution for the on-resonance excitation shown here is in reasonable agreement with that previously reported by Tseng *et al.*, the high TKER feature peaking in their study ~17000 cm^{-1} compared to ~18000 cm^{-1} measured here. The O-CH_3 bond dissociation energy can be estimated from the maximum TKER (see section 1.3.2) of the on-resonance distribution in figure 4.3. This value corresponds to 25000 – 26000 cm^{-1} implying the O-CH_3 bond energy is 25000 – 24000 cm^{-1}. This compares

reasonably well with the literature value of ~22500 cm^{-1}, the difference likely attributed to the limited resolution of the TR-VMI spectrometer and assuming the phenoxyl and CH_3 radicals are formed in their ground vibrational state.

From the on-resonance TKER distribution shown in figure 4.3, it seems unlikely that photodissociation at 200 nm is forming both ground state and electronically excited C_6H_5O radicals. The $\tilde{A}$ -state of C_6H_5O lies ~8900 cm^{-1} [20] above the ground state and as such, one would anticipate a difference between the low TKER and high TKER components to be around this value. The measurements in phenol-d_5 showed this to be so, with the low and high TKER components separated by ~9000 cm^{-1}.[8] In anisole, the low and high TKER components are separated by ~17500 cm^{-1}, the low TKER component peaking around 400 cm^{-1}. One would therefore anticipate an additional peak at ~9000 cm^{-1} (TKER = 18000 – 8900 cm^{-1}) which is not immediately apparent in figure 4.3 unless this is buried beneath the tail of the low TKER component. As such, the low TKER component in anisole peaking at 400 cm^{-1} cannot be attributed to CH_3 associated with the partner C_6H_5O radical in the $\tilde{A}$ -state.

4.2.2 High TKER Methyl Transients

Figure 4.4 shows the real-time CH_3 elimination of the high TKER feature in anisole. The transients are shown as a function of pump probe delay in figure 4.4 a), 4.4 b) in which the probe was set at 333.4 nm (4.4 a)) and 322.5 nm (4.4 b)) with insets displaying extended time delays. Both transients are obtained by collecting a series of TKER spectra at various pump probe delays (t) and integrating each TKER spectrum around the high TKER feature; 11500 – 23000 cm^{-1}, respectively for both probe wavelengths. Whilst the dynamics are insensitive to the size of the spectral

window in the high TKER region (i.e. between 11500 and 23000 cm^{-1}), the choice of large spectral window for the high TKER component provides an appreciable signal-to-noise. Perhaps the most notable difference in the two transients is the step-like growth of the on-resonance high TKER component (figure 4.4 a)) whilst in the off-resonance high TKER component (figure 4.4 b)), the signal rises around t = 0 and then decays.

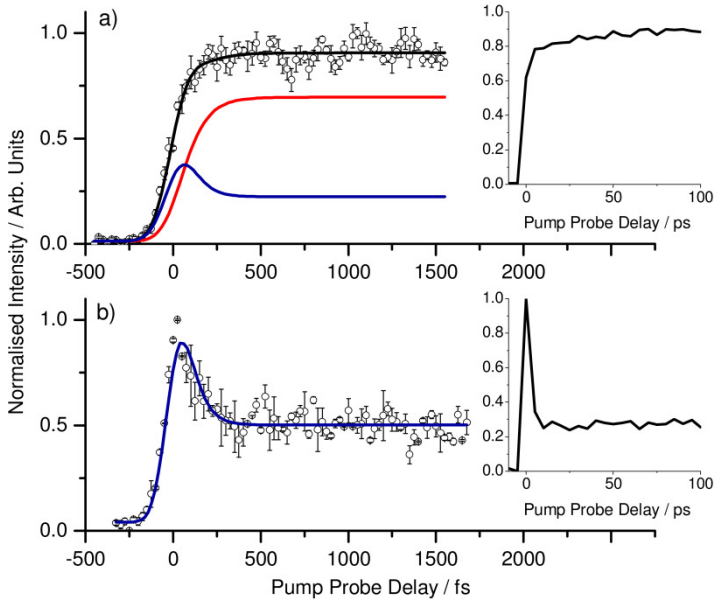

Figure 4.4 – CH_3^+ transients as a function of pump (200 nm) probe delay for high TKER CH_3 molecules probed using a) 333.5 nm and b) 322.5 nm respectively. At negative delays, there is no appreciable 2-colour signal. Experimental data in a) and b) were fitted with an off resonance decay and step function with lifetimes $\tau_{ORdecay} < 65$ fs and $\tau_{ORstep} < 50$ fs, respectively and an additional step function in a) with $\tau_R = 91 \pm 36$ fs, where OR and R correspond to off-resonance and on-resonance respectively.

From figure 4.3, it is evident that the TKER distribution of the on-resonance high TKER component will contain both an on-resonance and off-resonance contribution. As a result, any fitting of the corresponding on-resonance transient shown in figure 4.4 a) must reflect this. The off-resonance transient shown in figure 4.4 b) (probe set at 322.5 nm) requires an exponential decay and step function to fit

the data (solid blue line) with lifetimes $\tau_{ORdecay} < 65$ fs and $\tau_{ORstep} < 50$ fs, where OR denotes off-resonance. The exact values for $\tau_{ORdecay}$ and τ_{ORstep} are too short to be quoted accurately, resulting in large uncertainties in the time-constants. However, both processes are very fast and are likely due to multiphoton excitations that generate CH_3^+ directly, such as: (i) dissociative ionisation of the parent ion through a short lived intermediate state accessed by the pump (fast decay) and; (ii) pump generated anisole$^+$ (or associated fragment) which is further excited by the probe undergoing dissociative ionisation to yield CH_3^+ (fast step).

To fit the on-resonance transient, a combination of the function obtained from the off-resonance transient with an additional step function was used, to yield a time-constant of $\tau_R = 91 \pm 36$ fs, where R denotes on-resonance. Interestingly, this time-constant is similar to that observed in the hydride counterpart (phenol) which was previously measured as $\tau = 88 \pm 30$ fs and is very likely indicative of direct dissociation along the dissociative $^1\pi\sigma^*$ state. The two components of the fit, i.e. the off-resonance component and the step function are shown in figure 4.4 a) by the blue and red lines respectively. To cross-check the validity of this approach, the amplitudes of the off-resonance component and step function (approximately 1:3 respectively) are in very good agreement with the TKER spectra shown in figure 4.3; i.e. multiplying the high TKER component of the off-resonance TKER spectrum by approximately 3 almost overlays the two spectra in the high TKER region.

The appearance time of $\tau = 91 \pm 36$ fs compared to the hydride counterpart of $\tau_R = 88 \pm 30$ fs is much faster than one would anticipate based on the differences in reduced masses of the two systems and peak positions of the high TKER features, ~12000 cm^{-1} and ~18000 cm^{-1} in phenol and anisole, respectively. Indeed, this would

correspond to an almost 3-fold difference between hydrogen and CH_3 elimination, i.e. ~260 fs for CH_3 elimination. However, one very important factor, which determines the time-constant (appearance time) of the fragment being probed, is the minimum internuclear separation upon which the fragment can be ionised and detected. Unfortunately, these measurements are unable to determine the internuclear separation beyond which one is able to detect CH_3 (or hydrogen) fragments.

4.2.3 Low TKER Methyl Transients

Interestingly the low TKER transients at the two probe wavelengths are almost identical in comparison to the high TKER transients. Figures 4.5 a) and b) compare the dynamics at probe wavelengths of 333.4 nm and 322.5 nm, respectively, following excitation at 200 nm. In both cases, the transients are dominated by a rise in the signal close to $t = 0$ followed by a decay to an elevated baseline. The low TKER transients have been obtained by integrating the low TKER component (230 – 5200 cm^{-1}) in both the on-resonance and off-resonance TKER spectra. It is tempting to fit the low TKER CH_3^+ transients with an exponential decay and step function, in much the same way to the off-resonance high TKER component (see figure 4.4 b)). However, by extending the transients at the two probe wavelengths to longer time-delays, as shown in the insets of figures 4.5 a) and b), there is an additional longer decay. As a result, in much the same way to the high TKER components described above, the off-resonance transient has been fitted in figure 4.5 b) with an exponential decay and step function with lifetimes $\tau_{ORdecay1} = 85 \pm 15$ fs and $\tau_{ORstep} < 50$ fs, respectively, and a further exponential decay with a lifetime of $\tau_{ORdecay2} = 5.9 \pm 0.7$ ps obtained from the extended transient shown in the inset of figure 4.5 b); the subscripts 1 and 2 representing the short and long decay functions, respectively. This

combined function (solid blue line) is then used to fit the data obtained in the on-resonance low TKER transient, keeping the time-constants identical (figure 4.5 a)). As evident, the fit is very good suggesting that the dynamics of both the on-resonance and off-resonance low TKER components, at least at short times, are very similar, if not identical.

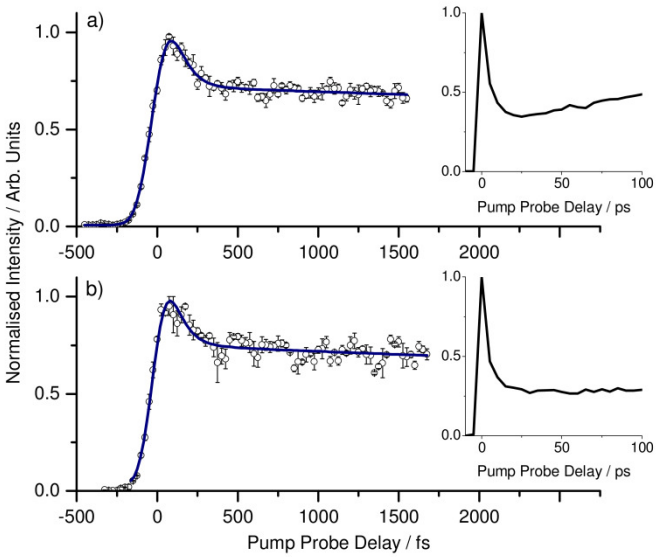

Figure 4.5 – CH_3^+ transients as a function of pump (200 nm) probe delay for low TKER CH_3 molecules probed using a) 333.5 nm and b) 322.5 nm respectively. Experimental data in a) and b) were fitted with two off-resonance decay functions and a step function having lifetimes of $\tau_{ORdecay1}$ = 85 ± 15 fs, $\tau_{ORdecay2}$ = 5.9 ± 0.7 ps and τ_{ORstep} < 50 fs respectively.

The exact mechanisms that are underlying the low TKER transient cannot be exactly quantified; however, it is very likely multicomponent in nature, probably consisting of a multiphoton part giving CH_3^+ directly through dissociative ionisation, as evidenced once again by the appearance of CH_3^+ off-resonance. Interestingly two decay components are present, one with a short lifetime (~85 fs) and one with a longer lifetime (5.9 ps - more visible in figure 4.5 b)) implying that the decay is occurring sequentially through two states, one short lived, the other longer lived. Indeed a decay of 5.9 ps is measured when probing the anisole$^+$ parent transient

through time resolved ion yield, which seems to suggest that this decay is from a short-lived intermediate state in the photoexcited anisole.

4.2.4 Evidence of Statistical Unimolecular Decay?

Whilst statistical unimolecular decay has thus far been ruled out in the *short* time-transients (0 – 1.5 ps), it is clearly evident that for both the on-resonance low *and* high TKER transients collected at *long* time-delays up to 100 ps (insets of figures 4.4 a) and 4.5 a), respectively), there is a slow rise in the CH_3^+ signal. Such behaviour is absent, within the signal-to-noise, in the off resonance transients (insets of figures 4.4 b) and 4.5 b), respectively) and is suggestive that CH_3 radicals are being generated through an indirect process such as statistical unimolecular decay following population of the ground state via internal conversion. This may either be through a conical intersection between the $^1\pi\sigma^*$ state and the $^1\pi\pi$ ground state such as that suggested in the hydride counterpart, phenol,[20] or some other non-radiative pathway. Alternatively, CH_3 radicals could be formed through fragmentation of the parent anisole$^+$ or highly excited fragments thereof. It is clear from these insets that the timescale for this process is likely to be very long, potentially on a similar order of magnitude to the time observed for unimolecular decay by Roberts *et al.* in azole molecules.[10] However, due to the limitations of the experimental setup at the time, it is not possible to determine the time constant for this process.

4.3 Conclusions

Using TR-VMI, CH_3 radical elimination has been observed at a range of TKER following excitation of anisole at 200 nm. The TKER spectrum is dominated by a low TKER peak, with a small high TKER feature centred around 18000 cm^{-1}.

Analysis of the CH_3^+ transients indicates that both the low and high TKER components show dynamics on an ultrafast timescale. The dynamics can be modelled using a step function for the high TKER component, which can be accounted for assuming direct dissociation along the $^1\pi\sigma^*$ state localised on the O-CH_3 coordinate. The low TKER component is likely due to multiphoton processes dominating the dynamics such as dissociative ionisation of the parent cation following population of a long-lived state of the parent anisole. At longer timescales a slow rise is observed in the on-resonance transients (at high and low TKER) that may be the result of statistical unimolecular decay, yielding neutral CH_3.

The generalised model for X-H dissociation as suggested by Domcke and Sobolewski [1, 2] seems to apply in non-hydride systems involving a repulsive $^1\pi\sigma^*$ state following photoexcitation with UV light. The timescale for dissociation along this state has been measured as $\tau_R = 91 \pm 36$ fs for CH_3 elimination compared to $\tau = 88 \pm 30$ fs for hydrogen elimination in phenol.[7, 8] One would anticipate an almost 3-fold difference in the elimination time-scales for the two processes and possibly highlights difference between the point at which CH_3 and hydrogen can be probed along the O-CH_3 or O-H reaction coordinate, respectively.

4.4 References

[1] A. L. Sobolewski and W. Domcke, *Chem. Phys. Lett.*, **310**, 548 (1999).

[2] M. N. R. Ashfold, G. A. King, D. Murdock, M. G. D. Nix, T. A. A. Oliver and A. G. Sage, *Phys. Chem. Chem. Phys.*, **12**, 1218 (2010).

[3] A. G. Sage, M. G. D. Nix and M. N. R. Ashfold, *Chem. Phys.*, **347**, 300 (2008).

[4] G. Piani, L. Rubio-Lago, M. A. Collier, T. N. Kitsopoulos and M. Becucci, *J. Phys. Chem. A*, **113**, 14554 (2009).

[5] C. M. Tseng, Y. T. Lee and C. K. Ni, *J. Phys. Chem. A*, **113**, 3881 (2009).

[6] J. S. Lim and S. K. Kim, *Nature Chem.*, **2**, 627 (2010).

[7] A. Iqbal, L. J. Pegg and V. G. Stavros, *J. Phys. Chem. A*, **112**, 9531 (2008).

[8] A. Iqbal, M. S. Y. Cheung, M. G. D. Nix and V. G. Stavros, *J. Phys. Chem. A*, **113**, 8157 (2009).

[9] D. J. Hadden, K. L. Wells, G. M. Roberts, L. T. Bergendahl, M. J. Paterson and V. G. Stavros, *Phys. Chem. Chem. Phys.*, **13**, 10342 (2011).

[10] G. M. Roberts, C. A. Williams, M. J. Paterson, S. Ullrich and V. G. Stavros, *Chem. Sci.*, **3**, 1192 (2012).

[11] A. L. Devine, B. Cronin, M. G. D. Nix and M. N. R. Ashfold, *J. Chem. Phys.*, **125**, 184302 (2006).

[12] M. Barbatti, H. Lischka, S. Salzmann and C. M. Marian, *J. Chem. Phys.*, **130**, 034305 (2009).

[13] G. A. King, T. A. A. Oliver, M. G. D. Nix and M. N. R. Ashfold, *J. Chem. Phys.*, **132**, 064305 (2010).

[14] R. Crespo-Otero, M. Barbatti, H. Yu, N. L. Evans and S. Ullrich, *ChemPhysChem*, **12**, 3365 (2011).

[15] H. Yu, N. L. Evans, V. G. Stavros and S. Ullrich, *Phys. Chem. Chem. Phys.*, **14**, 6266 (2012).

[16] R. Montero, A. P. Conde, V. Ovejas, M. Fernández-Fernández, F. Castaño and A. Longarte, *J. Phys. Chem. A*, **116**, 10752 (2012).

[17] K. A. Holbrook, M. J. Pilling and S. H. Robertson, *Unimolecular Reactions*, John Wiley & Sons, 1996.

[18] D. J. Hadden, C. A. Williams, G. M. Roberts and V. G. Stavros, *Phys. Chem. Chem. Phys.*, **13**, 4494 (2011).

[19] J. W. Hudgens, T. G. Digiuseppe and M. C. Lin, *J. Chem. Phys.*, **79**, 571 (1983).

[20] M. G. D. Nix, A. L. Devine, B. Cronin, R. N. Dixon and M. N. R. Ashfold, *J. Chem. Phys.*, **125**, 133318 (2006).

[21] R. N. Dixon, T. A. A. Oliver and M. N. R. Ashfold, *J. Chem. Phys.*, **134**, 194303 (2011).

5. Exploring Quantum Phenomena in the σ* Mediated Photochemistry of Thioanisole

This chapter presents an investigation of more exotic phenomena involved in σ* mediated dynamics: firstly, the role of purely quantum mechanical behaviour; and secondly, controlling the contribution of non-adiabatic photochemistry by "vibration-specific control". This is achieved by investigating S-CH_3 bond fission via a $^1n\sigma^*$ potential energy surface (PES) in thioanisole ($C_6H_5SCH_3$). Using time resolved velocity map imaging (TR-VMI) techniques, together with frequency resolved velocity map imaging (VMI) and *ab initio* calculations performed by collaborators,[1, 2] it is demonstrated that excitation to the $^1\pi\pi^* \leftarrow {}^1\pi\pi$ origin (*i.e.* $^1\pi\pi^* \, 0_0^0 \leftarrow {}^1\pi\pi \, 0_0^0$) results in S-$CH_3$ bond fission on the $^1n\sigma^*$ state, despite an apparent energetic barrier to dissociation formed by a CI between the $^1\pi\pi^*$ and $^1n\sigma^*$ PESs ($^1\pi\pi^*$ / $^1n\sigma^*$ CI). This process occurs by accessing "classically forbidden" regions of the excited state potential energy landscape where the barrier to dissociation becomes negligible, aided by torsional motion of the S-CH_3 group out of the plane of the phenyl ring. Control over these dynamics was previously observed in ns VMI studies by populating a single quantum of the S-CH_3 stretch mode in the $^1\pi\pi^*$ ($v_{7a} = 1$) state, which mirrors the nuclear motion required to promote coupling through the $^1\pi\pi^*$ / $^1n\sigma^*$ CI, resulting in a marked change in the electronic branching in the C_6H_5S radical products. This observation is not matched in the fs TR-VMI investigations, where this change in the electronic branching is absent, neatly highlighting the difference between narrowband ns and broadband fs experiments.

5.1 Introduction to Thioanisole Studies

5.1.1 Previous Studies of Thioanisole

Non-adiabatic dynamics of the first singlet state possessing σ* character (in this case ^{1}nσ* - formed by the promotion of a sulphur lone pair electron to the σ* orbital centred on the S-CH_3 bond) in thioanisole ($C_6H_5SCH_3$ – see structure in figure 5.1 a)) has been studied previously using ns VMI by Lim and Kim. [3] The ^{1}nσ* state mediated S–CH_3 bond cleavage in thioanisole was shown to proceed in a manner qualitatively similar to ^{1}πσ* governed S–H bond fission dynamics in thiophenol (C_6H_5SH), which has received more attention in both the gas [4-12] and solution phases.[10, 11]

With respect to the schematic PESs depicted in figure 5.1 b), after initial excitation of thioanisole to its ^{1}ππ* state with a pump laser, excited state population may couple onto a dissociative ^{1}nσ* PES and evolve to radical photoproducts:

$$\begin{aligned} &C_6H_5S\text{-}CH_3 + h\nu_{pu} \rightarrow \\ &C_6H_5S\left(\tilde{X}\right) + CH_3 \text{ [A]} \\ &C_6H_5S\left(\tilde{A}\right) + CH_3 \text{ [B]} \end{aligned} \qquad (5.1)$$

The ns VMI studies performed by Lim and Kim [3] upon excitation at the ^{1}ππ* ← ^{1}ππ origin (*i.e.* $^1\pi\pi^* 0_0^0 \leftarrow {}^1\pi\pi\ 0_0^0$) suggest that a small fraction (~5%) of the dissociating flux undergoes non-adiabatic coupling through the ^{1}nσ* / ^{1}ππ CI (designated CI2 in figure 5.1 b)) to yield CH_3 and $\tilde{X}$ state thiophenoxyl radical (C_6H_5S) products, while the remainder evolves adiabatically, avoiding the ^{1}nσ* / ^{1}ππ

CI, yielding CH_3 and $\tilde{A}$ state thiophenoxyl radical products. These two dissociation pathways are labelled channels [A] and [B], respectively, in equation 5.1.

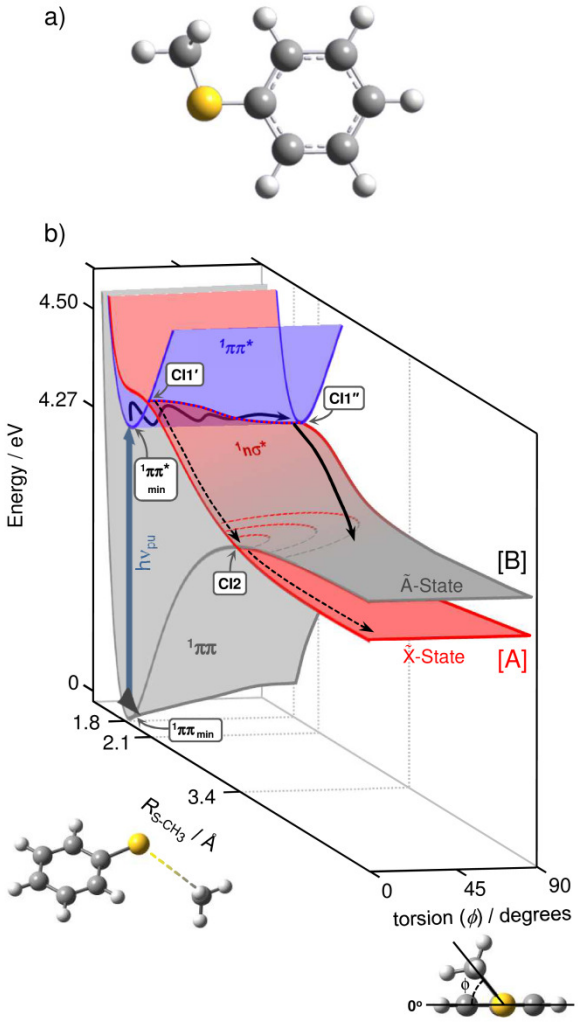

Figure 5.1 – a) Molecular structure of thioanisole. b) PES of the ground state ($^1\pi\pi$) and first two singlet excited states ($^1\pi\pi^*$ and $^1n\sigma^*$), with respect to the S-CH_3 separation ($R_{S\text{-}CH_3}$) and the out-of-plane C-C-S-CH_3 angle (ϕ). The "quasi-seam of intersection" CI1 (black dotted line) and $^1n\sigma^*$ / $^1\pi\pi$ CI (CI2) are shown. Also included is the pathway for channel [A] – dissociation to the $\tilde{A}$ state radical products (black arrows); and channel [B] – the formation of $\tilde{X}$ state product by excitation of the "dynamic resonance" ν_{7a} vibrational mode (black dashed arrows).

The dominance of adiabatic dynamics at the $^1n\sigma^*$ / $^1\pi\pi$ CI was qualitatively interpreted by Lim and Kim in terms of the geometric phase effect,[13] where the

dissociating flux bifurcates around $^1n\sigma^*$ / $^1\pi\pi$ CI, destructively interferes and diminishes the population evolving non-adiabatically into channel [A]. Lim and Kim also identified an anomalous "dynamic resonance" when exciting a $^1\pi\pi^* \leftarrow {}^1\pi\pi$ feature at 283.9 nm, which is assigned to population of the in-plane C-S-CH_3 stretch vibrational eigenstate (the ν_{7a} vibrational eigenstate) lying 722 cm^{-1} above the $^1\pi\pi^*$ origin.

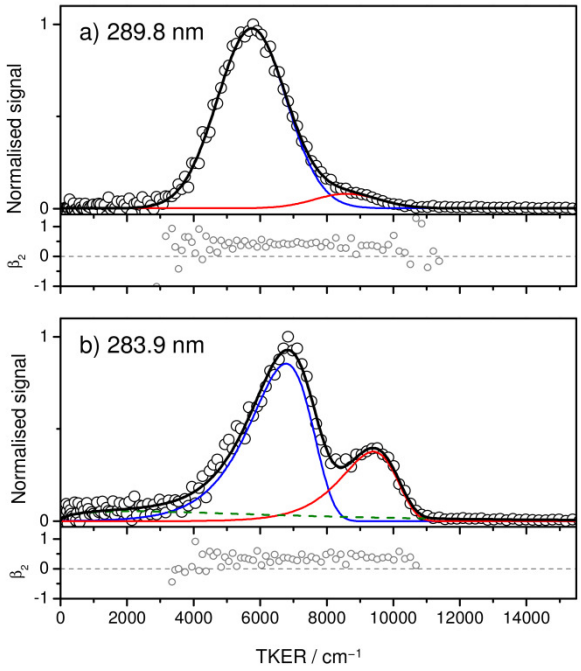

Figure 5.2 – TKER spectra obtained following photoexcitation of thioanisole with a ns excitation pulse centred at a) 289.8 nm and b) 283.9 nm collected at $t \approx 20$ ns. Solid black lines correspond to fits to the TKER spectra, with individual components of the fit associated with the channel [A] (red), channel [B] (blue) and Boltzmann-like background (dashed green) signals. β_2 anisotropy parameters (grey circles) extracted are provided below each spectrum.

Excitation of this "dynamic resonance" results in a striking enhancement of the relative yield of channel [A] photoproducts.[3] Lim and Kim suggested that exciting at this specific wavelength led to simultaneous population of both the $^1\pi\pi^*$ and $^1n\sigma^*$ states, the $^1n\sigma^*$ component then evolved directly through the $^1\pi\pi^*$ / $^1n\sigma^*$

CI (labelled CI1′ in figure 5.1 b)) and that the increased flux along the S–CH_3 stretch coordinate ($R_{S\text{-}CH_3}$), induced by ν_{7a}, encouraged non-adiabatic transfer from $^1n\sigma^*$ through $^1n\sigma^*$ / $^1\pi\pi$ CI into channel [A].[14] This mechanism is shown by the dashed arrows in figure 5.1 b).

Total kinetic energy release (TKER) spectra from VMI, performed with ns pulses, highlight the difference between the formation of CH_3 following photoexcitation at the $^1\pi\pi^* \leftarrow {}^1\pi\pi$ origin (289.8 nm) and at the "dynamic resonance" vibrational eigenstate (283.9 nm) and are shown in figure 5.2 a) and b); these experiments were performed by collaborators [1] show good agreement with the spectra obtained by Lim and Kim.[3] Spectra obtained at excitation wavelengths away from the dynamic resonance are similar the figure 5.2 a).

5.1.2 Aims and Procedure

These previous studies have gone some way to elucidating the source of the intriguing fragmentation dynamics displayed by thioanisole, but many aspects remain un-assessed. In particular the mechanism for $^1n\sigma^*$ mediated CH_3 elimination when excitation occurs to the $^1\pi\pi^*$ state below the $^1\pi\pi^*$ / $^1n\sigma^*$ CI, which forms an apparent barrier to S-CH_3 dissociation.[3]

The work in this chapter aims to study several issues that are unresolved by the findings of Lim and Kim. The aims are: (i) to elucidate the source of $^1n\sigma^*$ mediated CH_3 elimination when excitation occurs below the $^1\pi\pi^*$ / $^1n\sigma^*$ CI; (ii) determine the timescale for CH_3 dissociation at a series of excitation wavelengths; and (iii) to observe whether excitation with the large spectral bandwidth fs pulses, implemented in TR-VMI, at the "dynamic resonance" vibrational eigenstate will still

show the notable change in electronic branching observed by Lim and Kim with ns pulses.[3]

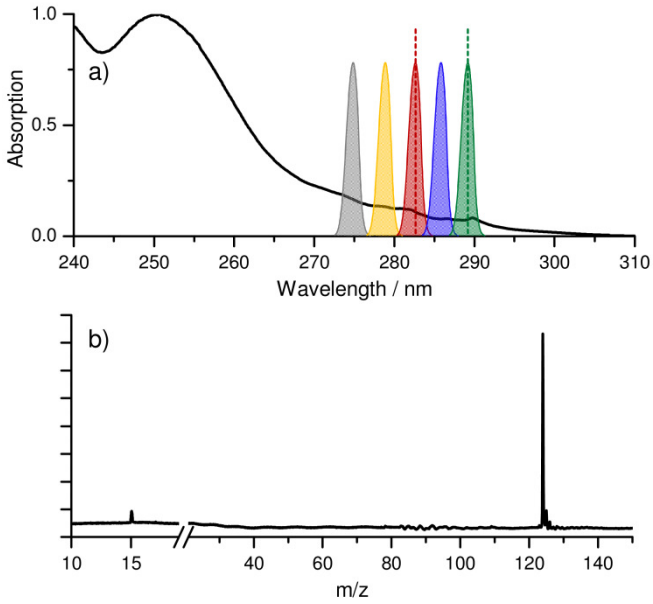

Figure 5.3 – a) Ultraviolet absorption spectrum for thioanisole, with the five excitation wavelengths highlighted (Gaussian distributions). The origin transition (green dashed line) and the "dynamic resonance" transition (red dashed line) are highlighted. b) Mass spectrum of thioanisole parent and methyl taken with a 279 nm pump and 333.4 nm probe, at t = 1.2 ns. The spectrum is not continuous over the break in axis and the lower m/z peak was collected at higher detector voltages (V_{mcp1} and V_{mcp2}).

In this chapter TR-VMI results are presented for S-CH_3 dissociation in thioanisole with pump wavelengths at the $^1\pi\pi^* \leftarrow {}^1\pi\pi$ origin (289.8 nm), the "dynamic resonance" (283.9) and three other transitions to the $^1\pi\pi^*$ state at 286.8, 279 and 275 nm. All wavelengths were provided by the pump TOPAS-C setup (see chapter 2). The ultraviolet (UV) absorption spectrum of thioanisole is shown in figure 5.3 a), with the corresponding photoexcitation wavelengths studied highlighted by the coloured Gaussian distributions. Probing of CH_3 was carried out by a 333.4 nm probe inducing (2+1) resonance enhanced multiphoton ionisation via the two-photon 3p $^2A_2'' \leftarrow \tilde{X}\ ^2A_2''$ transition.[15] The presence of a methyl signal is

apparent in the mass spectrum shown in figure 5.3 b), which was taken with a 279 and 333.4 nm pump probe scheme at a 1.2 ns pump probe delay (*t*). Valve operating conditions are as described in section 2.2 and the specifics are summarised in table 2.2. The TR-VMI work in this chapter was supported by ns VMI studies [1] and high level theoretical calculations,[2] both of which were performed by collaborators.[16]

5.2 Results of Thioanisole Studies

5.2.1 Comparison of fs TR-VMI and ns VMI results at the $^1\pi\pi^* \leftarrow {}^1\pi\pi$ Origin

The TKER spectrum and corresponding image (raw and deconvoluted) for CH_3 elimination in thioanisole following excitation at the $^1\pi\pi^* \leftarrow {}^1\pi\pi$ origin, with a fs 289.8 and 333.4 nm pump and probe, respectively, is shown in figure 5.4. The spectrum was acquired at t = 1.2 ns. The major feature, centred at a TKER of ~5500 cm^{-1}, is attributed to dissociation mediated by the $^1n\sigma^*$ state that proceeds adiabatically around the $^1n\sigma^*$ / $^1\pi\pi$ CI to give CH_3 and the $\tilde{A}$ state thiophenoxyl radical product. The maximum TKER ($TKER_{max}$) of the observed CH_3 with the $\tilde{A}$ state thiophenoxyl radical product is ~8000 cm^{-1}. This matches well with the $TKER_{max}$ predicted by equation 5.2:

$$TKER_{max} = h\nu - D_0(S\text{-}CH_3) - \Delta E(\tilde{A} \leftarrow \tilde{X}) \qquad (5.2)$$

In equation 5.2, $h\nu$ is the photon energy; $D_0(S\text{-}CH_3)$ is the S-CH_3 bond dissociation energy (24400 cm^{-1} – determined from ns VMI studies [1]); and $\Delta E(\tilde{A} \leftarrow \tilde{X})$ is the separation between the ground ($\tilde{X}$) and excited ($\tilde{A}$) state thiophenoxyl radical product (3000 cm^{-1} [17]). Using equation 5.2, the $TKER_{max}$ for dissociation at 289.8 nm is predicted to be 7100 cm^{-1}.

The TKER spectrum at this wavelength closely resembles the TKER spectrum collected through ns VMI, in figure 5.2 a). However, a significant broadening of the major peak is observed when using fs pulses due to the larger spectral bandwidth of the fs pulses.

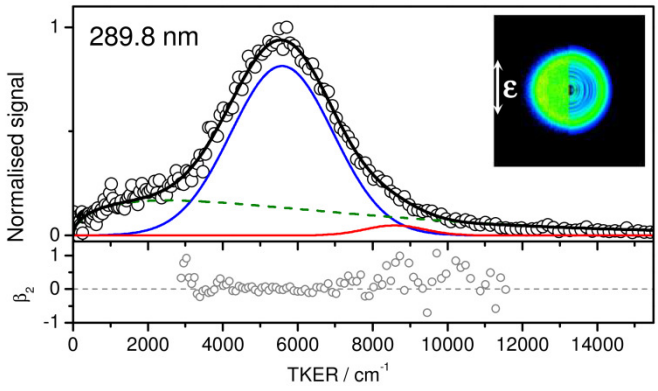

Figure 5.4 – TKER spectra of the CH_3 radical products obtained following photoexcitation of thioanisole at 289.8 and REMPI-probing at 333.4 nm, recorded at t = 1.2 ns. Associated velocity map images from which the TKER spectra are derived are shown inset (left halves are raw recorded images, right halves are deconvoluted slices, white arrows represent **ε**). Solid black lines correspond to fits to the TKER spectra, with individual components of the fit associated with the channel [A] (red), channel [B] (blue) and Boltzmann-like background (dashed green) signals. β_2 anisotropy parameters (grey circles) extracted from the images are provided below.

From the raw and deconvoluted images, inset in figure 5.4, it is clear that the distribution of the CH_3 formed is isotropic relative to the laser electric field polarisation (labelled **ε**). This is reflected in the β_2 parameter which is plotted over a range of TKER below each TKER spectrum. The value of β_2 (approximately zero) in the fs TR-VMI experiments is different to that observed previously in ns VMI studies, $\beta_2 \approx 0.4$, shown in figure 5.2 a) and the S-CH_3 bond / transition dipole moment angle determined by theory. The reason for this discrepancy between the ns and fs VMI studies could be attributed to the fs excitation of thioanisole yielding a ro-vibrational wavepacket on $^1\pi\pi^*$. Large spectral bandwidth fs pulses will therefore

generate a coherent ensemble of rotational states in $^1\pi\pi^*$ which will evolve as a function of time, leading to rotational dephasing. This rapid scrambling of rotational coherences, which must occur on a timescale faster than S-CH_3 bond dissociation, offers an explanation for the isotropic nature of the fs velocity map images.

Also notable in the fs TKER spectrum is the minimal contribution of this $\tilde{X}$ state product signal, in figure 5.4, from the amplitude of the fit component attributed to this product channel (red Gaussian distribution). In fact the presence of this component is not necessary to provide an adequate total fit (black line) to the entire TKER spectrum and is only included as the presence of CH_3 with $\tilde{X}$ state thiophenoxyl is observed in the ns VMI experiments.

The Origin of $^1n\sigma^*$ Mediated Signal Below the $^1\pi\pi^*$ / $^1n\sigma^*$ Conical Intersection

The dynamics in thioanisole upon excitation to the $^1\pi\pi^* \leftarrow {}^1\pi\pi$ origin can be explained with reference to the schematic potential energy surfaces (PESs), of the $^1\pi\pi^*$, $^1n\sigma^*$ and $^1\pi\pi$ states, in terms of the S-CH_3 separation and the out-of-plane C-C-S-CH_3 torsion (ϕ), shown in figure 5.1 b). Theoretical calculations [2] suggest that the branching space of the $^1\pi\pi^*$ / $^1n\sigma^*$ CI contains the S-CH_3 stretching motion and the C-C-S-CH_3 out-of-plane torsional motion, while the molecule is planar (in C_s symmetry). However once out of this planar geometry, at $\phi \neq 0°$, the C_s symmetry is broken and the interaction between the $^1\pi\pi^*$ and $^1n\sigma^*$ states exists as a weakly avoided crossing that is preserved during the torsional motion (in ϕ). The CI (when in C_s symmetry) and avoided crossing (when in C_1 symmetry) can be considered a "quasi-seam of intersection" between the two states and is signified by the dashed line in figure 5.1 b). The "quasi-seam of intersection" CI1 is predicted to reach a

maximum at $\phi = 0°$ (labelled CI1′), with an energy of ~720 cm^{-1} [3] above the $^1\pi\pi^*$ origin, and reach a minimum at $\phi \approx 90°$ (labelled CI1″).

Upon excitation close to the $^1\pi\pi^*$ state origin (minimum energy geometry - $^1\pi\pi^*_{min}$ in figure 5.1 b)) the prepared wavepacket cannot dissociate due to the barrier formed by CI1′. However by propagating along the torsional coordinate to $\phi >> 0°$, conceivably into the "non-classical" extremities of the wavepacket motion (*i.e.* tunnelling), the barrier to dissociation is reduced in energy allowing population to transfer from the $^1\pi\pi^*$ state onto the $^1n\sigma^*$ state yielding CH_3. It is expected that $^1\pi\pi^* \rightarrow {}^1n\sigma^*$ IC will only occur at the extremities of the wavepacket's motion along the ϕ coordinate, suggesting that the rate of IC will be small. Therefore the timescale for dissociation is dependent on the rate of IVR, typically on the order of 100s-1000s of picoseconds (see timescales for dissociation below).

Predominance of the CH_3 and $\tilde{A}$ State Thiophenoxyl Photoproduct

Both the fs TR-VMI and ns VMI studies have shown the predominance of S-CH_3 dissociation yielding CH_3 and the $\tilde{A}$ state thiophenoxyl co-fragment (over the $\tilde{X}$ state product). *Ab initio* calculations suggest that the $^1n\sigma^*$ / $^1\pi\pi$ CI (labelled CI2 in figure 5.1 b)) exists at a point of degeneracy at a larger S-CH_3 separation and $\phi = 0$, with motion in ϕ lifting the degeneracy (unlike the quasi-seam linking CI1′ and CI1″).[2] If $^1\pi\pi^* \rightarrow {}^1n\sigma^*$ IC occurs at the extremity of wavepacket motion in ϕ (i.e. $\phi >> 0°$) the possibility for torsional rearrangement to allow for sampling of CI2 (at $\phi = 0°$) is low and prompt dissociation along the $^1n\sigma^*$ state predominantly generates

channel [B] photoproducts. This overall mechanism for S-CH_3 dissociation to the $\tilde{A}$ state thiophenoxyl product asymptote is shown by the black arrows in figure 5.1 b).

5.2.2 Results at the "Dynamic Resonance" Transition Wavelength: 283.9 nm

The velocity map image (raw and deconvoluted), TKER spectrum and β_2 values from fs TR-VMI studies of thioanisole excited at the "dynamic resonance" transition are shown in figure 5.5. The major feature of the TKER spectrum is a Gaussian distribution centred at ~6000 cm^{-1} (blue line), which is attributed to CH_3 elimination along with $\tilde{A}$ state thiophenoxyl products. The predicted $TKER_{max}$ for this channel at 283.9 nm from equation 5.2 is 7860 cm^{-1}, is in reasonable accord with the $TKER_{max} \approx 9000$ cm^{-1} observed in figure 5.5. However, the TKER spectrum and image show notable differences from the ns VMI images previously collected [1, 3] and an example is shown in figure 5.2 b). The main difference between the ns and fs spectra is the absence of any notable CH_3 signal corresponding to dissociation with the $\tilde{X}$ state thiophenoxyl radical co-fragment. As with ns TKER spectra and the fs TKER spectrum at the $^1\pi\pi^*$ origin, fitting of the TKER spectrum in figure 5.5 has been performed with a Boltzmann distribution and two Gaussian functions. It has been previously suggested that excitation at 283.9 nm lead to the creation of a superposition of the $^1\pi\pi^*$ and $^1n\sigma^*$ state, the population in the $^1n\sigma^*$ state then evolved non-adiabatically through CI2. However, ns VMI experiments performed by collaborators [1] along with theoretical calculations,[2] alternatively suggest that only the $^1\pi\pi^*$ state is populated at 283.9 nm. As the ν_{7a} mode (S-CH_3 stretching motion) is the derivative coupling mode of the CI1′ branching space, promotion of the $^1\pi\pi^*(\nu_{7a} = 1) \leftarrow {}^1\pi\pi$ "dynamic resonance" transition will lead to prompt non-adiabatic passage through CI1 at $\phi \approx 0°$ onto the $^1n\sigma^*$ state.

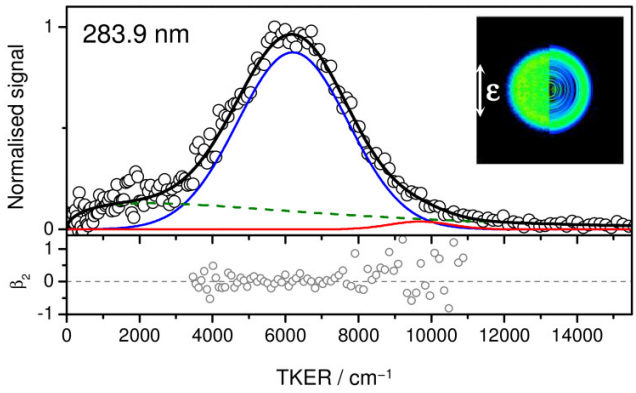

Figure 5.5 – TKER spectra of the CH_3 radical products obtained following photoexcitation of thioanisole at 283.9 and REMPI-probing at 333.4 nm, recorded at t = 1.2 ns. Associated velocity map images from which the TKER spectra are derived are shown inset (left halves are raw recorded images, right halves are deconvoluted slices, white arrows represent **ε**). Solid black lines correspond to fits to the TKER spectra, with individual components of the fit associated with the channel [A] (red), channel [B] (blue) and Boltzmann-like background (dashed green) signals. β_2 anisotropy parameters (grey circles) extracted from the images are provided below.

Once on the $^1n\sigma^*$ state at $\phi \approx 0°$ the probability of accessing CI2 (which only exists at $\phi = 0$) is greatly increased, leading to a non-adiabatic transition through CI2 and dissociation towards the $\tilde{X}$ state radical asymptote. This increased probability of accessing CI2 accounts for the sharp resonance observed in the $\tilde{X}/\tilde{A}$ state branching when ν_{7a} is excited with a narrowband pulse at 283.9 nm (shown as a black dashed arrow in figure 5.1 b)). However, the ν_{7a} mode will be one of many modes in a superposition of eigenstates excited when using a fs laser pulse centred at 283.9 nm and the formation of a wavepacket at energies around the 722 cm^{-1} "dynamic resonance" will occur. Therefore, the ν_{7a} mode specific dynamics will be lost in the dynamics of all the eigenstates populated, this neatly highlights the mode specific nature of the "dynamic resonance" and difference between narrowband ns and broadband fs experiments

5.2.3 CH_3 Elimination at 286.3, 279 and 275 nm.

TKER spectra along with the corresponding velocity map images and β_2 values for S-CH_3 dissociation from thioanisole at 286.3, 279 and 275 nm are shown in figure 5.6 a), b) and c), respectively.

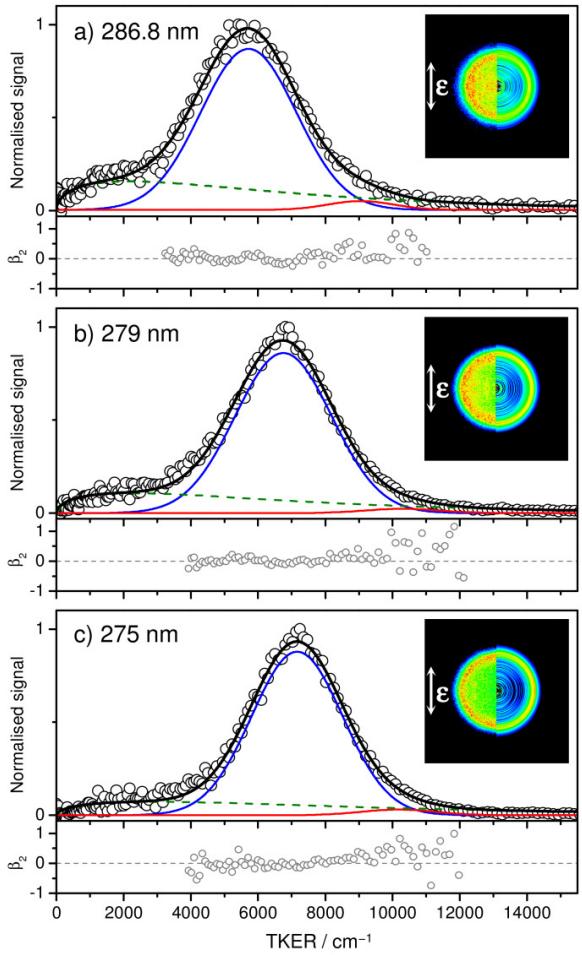

Figure 5.6 – TKER spectra of the CH_3 radical products obtained following photoexcitation of thioanisole at a) 286.8, b) 279 and c) 275 nm and REMPI-probing at 333.4 nm, recorded at t = 1.2 ns. Associated velocity map images from which the TKER spectra are derived are shown inset (left halves are raw recorded images, right halves are deconvoluted slices and white arrows represent **ε**). Solid black lines correspond to fits to the TKER spectra, with individual components of the fit associated with the channel [A] (red), channel [B] (blue) and Boltzmann-like background (dashed green) signals. β_2 anisotropy parameters (grey circles) extracted from the images are provided below.

In all cases, minimal CH_3 and $\tilde{X}$ state thiophenoxyl product is observed, signified by the small amplitudes of the corresponding fit functions (red Gaussian distributions). The centre of the CH_3 and the $\tilde{A}$ state thiophenoxyl product feature (blue Gaussian distribution) is noticeably shifted to higher TKER (blue-shifted) as the pump photon energy is increased and the $TKER_{max}$ is also observed to shift, as predicted by equation 5.2, when $h\nu$ is increased. The β_2 parameter is ~0 for all excitation wavelengths, including the origin and "dynamic resonance" transition, suggesting that the same mechanism for forming CH_3 is occurring at all wavelengths studied.

5.2.4 CH_3^+ Transients

TR-VMI transients of CH_3^+ formed by $^1n\sigma^*$ mediated photodissociation are shown in figure 5.7 at 289.8 (green), 286.8 (blue), 283.9 (red), 279 (orange) and 275 nm (grey). The transients were produced by collecting a series of velocity map images at different *t* and integrating a 2000 cm^{-1} window centred on the CH_3 and $\tilde{A}$ state thiophenoxyl product feature in the TKER spectra. Each transient is fit with two exponential rises, one for the short timescale dynamics ($\tau < 500$ fs) and one for the long timescale dynamics ($\tau > 50$ ps); both functions are convoluted with a Gaussian representing the instrument response function (IRF - Full width at half maximum ≈ 120 fs). The short timescale dynamics, involving the first exponential rise, are nearly identical for all five excitation wavelengths and are attributed to multiphoton absorption of parent thioanisole which can then fragment to yield CH_3^+. This CH_3^+ is associated with the underlying Boltzmann feature observed in all TKER spectra (figure 5.4, 5.5 and 5.6) and will be briefly discussed below. Beyond $t > 1$ ps the transients show that the CH_3 and $\tilde{A}$ state thiophenoxyl radical products are forming

over hundreds to thousands of picoseconds and at an increased rate when more internal energy is imparted into the $^1\pi\pi^*$ state, (see table 5.1 for $^1\pi\pi^*$ internal energy, time constants and rates). These fits return time constants (τ) for adiabatic dissociation to CH_3 and the $\tilde{A}$ state thiophenoxyl radical products of 1430 ± 240, 840 ± 100, 670 ± 50, 189 ± 10 and 74 ± 10 ps for excitation centred at 289.8, 286.8, 283.9, 279 and 275 nm, respectively.

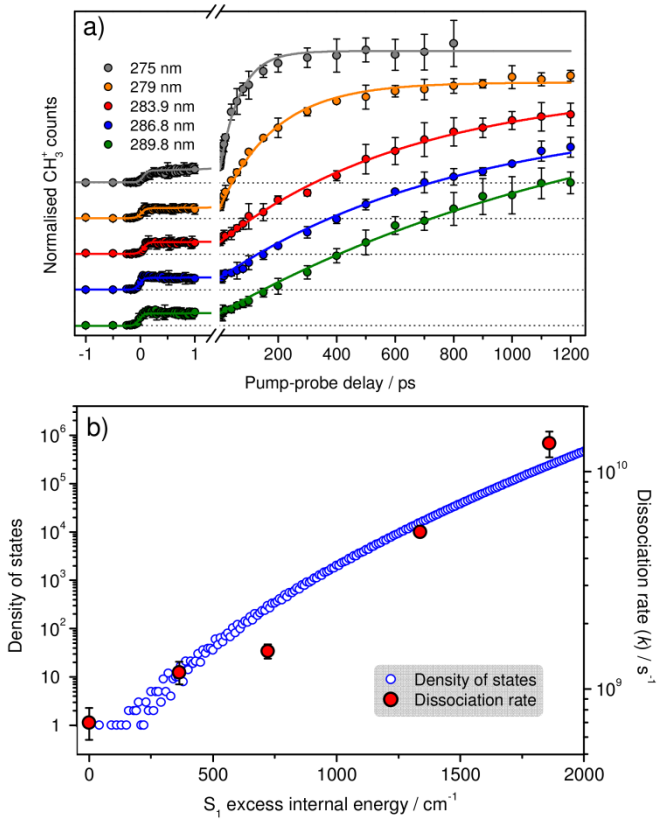

Figure 5.7 – a) Normalised integrated CH_3^+ signal transients for the CH_3 and $\tilde{A}$ state thiophenoxyl channel feature (circles) from fs TR-VMI following excitation centred at 289.8 (green), 286.8 (blue), 283.9 (red), 279 (orange) and 275 nm (grey) plotted as a function of pump probe delay (t). Error bars correspond to 2 standard deviations the mean signal values and the solid lines show kinetic fits which consist of two exponential rises (one <500 fs and one >50 ps) and an exponential decay convoluted with the IRF (see appendix I for details). b) Dissociation rate ($k = 1/\tau$) as a function of mean internal (vibrational) energy imparted to the $^1\pi\pi^*$ molecules by photoexcitation (red circles), compared to the calculated density of vibrational states in $^1\pi\pi^*$ at 25 cm^{-1} energy intervals (blue circles).

The timescales determined are typically on the order expected for IVR in small aromatic species.[18, 19] Given that the mechanism for dissociation to the CH_3 and the $\tilde{A}$ state thiophenoxyl radical products (see above) relies on IVR into the torsional motion (varying ϕ), leading to a reduction in the CI1 barrier energy, and the S-CH_3 stretching mode, these timescales are unsurprising. The rate of IVR into these vibrational modes can be accounted for by invoking a Fermi's golden rule model, where the increased density of vibrational states initially excited will lead to quicker IVR.[20] The density of states in the $^1\pi\pi^*$ state can be approximated through calculation of the harmonic vibrational frequencies [2, 21] and a plot of the density of states along with the experimentally determined rate is shown in figure 5.7 b). This plot shows that the increasing density of states accessed in the $^1\pi\pi^*$ state with higher pump energies correlates nicely with the increasing dissociation rates observed.

Table 5.1 – Adiabatic S–CH_3 dissociation to CH_3 and $\tilde{A}$ state thiophenoxyl time constants (τ) and associated dissociation rates ($k = 1/\tau$) obtained from kinetic fits to the CH_3^+ signal transients presented in Fig. 5(a). Errors correspond to 2 standard deviations.

λ / nm	**$^1\pi\pi^*$ internal energy / cm^{-1}**	**τ / ps**	**Rate / 10^9 s^{-1}**
289.8	0	1430 ± 240	0.70 ± 0.12
286.8	360	840 ± 100	1.19 ± 0.14
283.9	720	670 ± 50	1.49 ± 0.11
279	1340	189 ± 10	5.29 ± 0.28
275	1860	74 ± 10	13.5 ± 1.83

5.2.5 Low TKER CH_3 signal

The TKER spectra shown above (figure 5.4, 5.5 and 5.6) show a low TKER Boltzmann distribution, similar to the low TKER signal previously observed in anisole (chapter 4) and other molecules, such as phenol.[22-26] The origin of this low TKER signal can be assessed by "detuning" the probe wavelength away from the CH_3 REMPI transition (at 333.4 nm) to 323 nm,[15] which will highlight the contribution from multiphoton generation of CH_3^+. The comparison of on-resonance and the "detuned" off-resonance CH_3^+ signal is provided in figure 5.8. From the TKER spectra in figure 5.8 a) it is apparent that the low TKER is predominantly the result of multiphoton absorption of the parent thioanisole molecule and dissociation to directly yield CH_3^+.

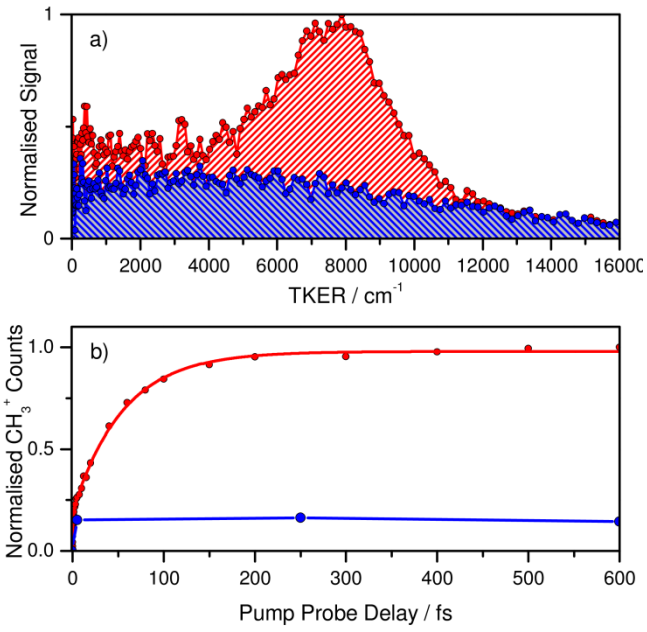

Figure 5.8 – a) TKER spectra from thioanisole dissociation at 275 nm and probing at either 333.4 nm (red) or 323 nm (blue), at t = 1.2 ns. b) Transient CH_3^+ signal at varying t, taken with a 275 nm pump and probing at either 333.4 nm (red) or 323 nm (blue).

Conversely, the signal attributed to dissociation into CH_3 and $\tilde{A}$ state thiophenoxyl radicals at high TKER, is formed as neutral CH_3 before probing, hence the dependence on the probe wavelength. The transients in figure 5.8 b) suggest, as speculated above, that the fast exponential rise feature in the transients in figure 5.7 a) is the result of this low TKER Boltzmann distribution.

5.3 Conclusions

The excited state photodynamics of thioanisole have been studied using TR-VMI and related studies which utilised fs VMI and *ab initio* calculations. $^1\pi\pi^* \rightarrow {}^1n\sigma^*$ IC and subsequent adiabatic dissociation to yield CH_3 and $\tilde{A}$ state thiophenoxyl was observed at a range of wavelengths, including below the apparent barrier to dissociation formed by the $^1\pi\pi^*$ / $^1n\sigma^*$ CI at zero C-C-S-CH_3 torsional angle (ϕ). Theoretical calculations suggest that the $^1\pi\pi^*$ / $^1n\sigma^*$ CI exists as a "quasi-seam" of intersection at a range of ϕ and decreases in energy as $\phi >> 0°$. Dissociation when excited at the origin $^1\pi\pi^* \leftarrow {}^1\pi\pi$, with a fs laser pulse, occurs via IC to the $^1n\sigma^*$ state at the extremities of wavepacket motion in ϕ (once accessed through IVR), where the "quasi-seam" of intersection (CI1) is lower in energy. This proposed mechanism matches the mechanism suggested for dissociation at the origin in the ns VMI studies, although in the ns case a single vibrational eigenstate is excited rather than a wavepacket.[16] As only the extremities of wavepacket motion lead to $^1\pi\pi^* \rightarrow {}^1n\sigma^*$ IC and the correct motion needs to be accessed through IVR, the rate of dissociation is low and a timescale of 1430 ± 240 ps is measured.

When higher internal (vibrational) energy is imparted to the $^1\pi\pi^*$ state the rate of IC and successive dissociation is increased. The rate of dissociation has been shown to correlate well with the density of vibrational states in the $^1\pi\pi^*$ state, suggesting that the rate of IVR into the appropriate motion in ϕ follows a Fermi's golden rule model.[20]

Direct comparison of the fs TR-VMI and ns VMI studies show a notable difference when excitation occurs at the $^1\pi\pi^*(\nu_{7a} = 1) \leftarrow {}^1\pi\pi$ "dynamic resonance". In the ns VMI studies branching to the CH_3 and $\tilde{X}$ state thiophenoxyl product channel is drastically increased. This increase is not seen in the fs TR-VMI results due to the excitation of numerous vibrational eigenstates around the $\nu_{7a} = 1$ level, forming a superposition of vibrational eigenstates. As a result the ν_{7a} dependent dynamics are lost in the ensemble of all the contributing vibrational eigenstates. This neatly highlights the potential for differing dynamics between the mode specific ns studies and broadband fs TR-VMI studies, both of which have been used extensively in previous research.[22-24, 27-36]

5.4 References

[1] These experiments were performed by Dr. A. M. Wenge, Miss S. J. Harris, Mr T. N. V. Karsili and Prof. M. N. R. Ashfold at the University of Bristol and are published in: *Chem. Sci.*, **4** (2013) 993.

[2] These and further calculations discussed in this chapter were performed by Dr G. M. Roberts at the University of Warwick, Ms L. T. Bergendahl and Prof. M. J. Paterson at Heriot-Watt University. These results are publish in: *Chem. Sci.*, **4** (2013) 993.

[3] J. S. Lim and S. K. Kim, *Nature Chem.*, **2**, 627 (2010).

[4] J. S. Lim, I. S. Lim, K. S. Lee, D. S. Ahn, Y. S. Lee and S. K. Kim, *Angew. Chem. Int. Ed.*, **45**, 6290 (2006).

[5] I. S. Lim, J. S. Lim, Y. S. Lee and S. K. Kim, *J. Chem. Phys.*, **126**, 034306 (2007).

[6] A. L. Devine, M. G. D. Nix, R. N. Dixon and M. N. R. Ashfold, *J. Phys. Chem. A*, **112**, 9563 (2008).

[7] M. N. R. Ashfold, A. L. Devine, R. N. Dixon, G. A. King, M. G. D. Nix and T. A. A. Oliver, *Proc. Natl. Acad. Sci. USA*, **105**, 12701 (2008).

[8] J. S. Lim, Y. S. Lee and S. K. Kim, *Angew. Chem. Int. Ed.*, **47**, 1853 (2008).

[9] J. S. Lim, H. Choi, I. S. Lim, S. B. Park, Y. S. Lee and S. K. Kim, *J. Phys. Chem. A*, **113**, 10410 (2009).

[10] T. A. A. Oliver, Y. Zhang, M. N. R. Ashfold and S. E. Bradforth, *Faraday Discuss.*, **150**, 439 (2011).

[11] Y. Y. Zhang, T. A. A. Oliver, M. N. R. Ashfold and S. E. Bradforth, *Faraday Discuss.*, **157**, 141 (2012).

[12] T. A. A. Oliver, G. A. King, D. P. Tew, R. N. Dixon and M. N. R. Ashfold, *J. Phys. Chem. A*, 10.1021/jp308804d (2012).

[13] S. C. Althorpe, in *Conical Intersections: Theory, Computation and Experiments*, eds. W. Domcke, D. R. Yarkony and H. Köppel, World Scientific Publishing Co. Pte. Ltd., 2011, pp. 155-194.

[14] C. Wittig, *J. Phys. Chem. B*, **109**, 8428 (2005).

[15] J. W. Hudgens, T. G. Digiuseppe and M. C. Lin, *J. Chem. Phys.*, **79**, 571 (1983).

[16] G. M. Roberts, D. J. Hadden, L. T. Bergendahl, A. M. Wenge, S. J. Harris, T. N. V. Karsili, M. N. R. Ashfold, M. J. Paterson and V. G. Stavros, *Chem. Sci.*, **4** (2013) 993.

[17] J. B. Kim, T. I. Yacovitch, C. Hock and D. M. Neumark, *Phys. Chem. Chem. Phys.*, **13**, 17378 (2011).

[18] D. Boyall and K. L. Reid, *Chem. Soc. Rev.*, **26**, 223 (1997).

[19] K. L. Reid, *Int. Rev. Phys. Chem.*, **27**, 607 (2008).

[20] P. A. M. Dirac, *Proc. R. Soc. Lond. A*, **114**, 243 (1927).

[21] S. E. Stein and B. S. Rabinovitch, *J. Chem. Phys.*, **58**, 2438 (1973).

[22] A. Iqbal, M. S. Y. Cheung, M. G. D. Nix and V. G. Stavros, *J. Phys. Chem. A*, **113**, 8157 (2009).

[23] D. J. Hadden, K. L. Wells, G. M. Roberts, L. T. Bergendahl, M. J. Paterson and V. G. Stavros, *Phys. Chem. Chem. Phys.*, **13**, 10342 (2011).

[24] D. J. Hadden, C. A. Williams, G. M. Roberts and V. G. Stavros, *Phys. Chem. Chem. Phys.*, **13**, 4494 (2011).

[25] G. M. Roberts, C. A. Williams, M. J. Paterson, S. Ullrich and V. G. Stavros, *Chem. Sci.*, **3**, 1192 (2012).

[26] C. M. Tseng, Y. T. Lee and C. K. Ni, *J. Phys. Chem. A*, **113**, 3881 (2009).

[27] A. L. Devine, B. Cronin, M. G. D. Nix and M. N. R. Ashfold, *J. Chem. Phys.*, **125**, 184302 (2006).

[28] M. G. D. Nix, A. L. Devine, B. Cronin, R. N. Dixon and M. N. R. Ashfold, *J. Chem. Phys.*, **125**, 133318 (2006).

[29] M. G. D. Nix, A. L. Devine, R. N. Dixon and M. N. R. Ashfold, *Chem. Phys. Lett.*, **463**, 305 (2008).

[30] A. Iqbal, L. J. Pegg and V. G. Stavros, *J. Phys. Chem. A*, **112**, 9531 (2008).

[31] A. Iqbal and V. G. Stavros, *J. Phys. Chem. Lett.*, **1**, 2274 (2010).

[32] M. N. R. Ashfold, G. A. King, D. Murdock, M. G. D. Nix, T. A. A. Oliver and A. G. Sage, *Phys. Chem. Chem. Phys.*, **12**, 1218 (2010).

[33] G. A. King, T. A. A. Oliver and M. N. R. Ashfold, *J. Chem. Phys.*, **132**, 214307 (2010).

[34] G. A. King, T. A. A. Oliver, M. G. D. Nix and M. N. R. Ashfold, *J. Chem. Phys.*, **132**, 064305 (2010).

[35] G. M. Roberts, C. A. Williams, J. D. Young, S. Ullrich, M. J. Paterson and V. G. Stavros, *J. Am. Chem. Soc.*, **134**, 12578 (2012).

[36] H. Yu, N. L. Evans, V. G. Stavros and S. Ullrich, *Phys. Chem. Chem. Phys.*, **14**, 6266 (2012).

6. Competing $^1\pi\sigma^*$ Mediated Dynamics in Mequinol

Chapter 6 focuses on the competition between dynamics along two different dissociative coordinates, both mediated by $^1\pi\sigma^*$ potential energy surfaces (PESs). The work presented herein utilises ultrafast time resolved velocity map imaging (TR-VMI) to study competing dissociation pathways along $^1\pi\sigma^*$ PESs in mequinol (*p*-methoxyphenol), localised at O-H and O-CH_3 bonds yielding hydrogen or CH_3 radicals, respectively, over an excitation wavelength range of 298 – 238 nm and at 200 nm. Hydrogen elimination is found to be operative via either tunnelling under a $1^1\pi\pi^*$ / $^1\pi\sigma^*_{O\text{-}H}$ conical intersection (CI) ($298 \geq \lambda \geq 280$ nm), occurring in nanoseconds, or ultrafast internal conversion through appropriate CIs ($\lambda \leq 245$ nm), both of which provide mechanisms for coupling onto the dissociative $^1\pi\sigma^*_{O\text{-}H}$ state associated with the O-H bond. In the intermediate wavelength range of $280 \geq \lambda \geq 245$ nm, $^1\pi\sigma^*_{O\text{-}H}$ mediated hydrogen elimination is not observed. In contrast, $^1\pi\sigma^*_{O\text{-}CH_3}$ state driven CH_3 radical elimination is observed in the excitation range $264 \geq \lambda \geq 238$ nm and is attributed to either (i) direct population of a "quasi-bound" region of the $^1\pi\sigma^*_{O\text{-}CH_3}$ state or (ii) an ultrafast $2^1\pi\pi^*$ to $^1\pi\sigma^*_{O\text{-}CH_3}$ internal conversion (IC), potentially via subsequent IC through the intermediate $1^1\pi\pi^*$ state. When exciting mequinol at 200 nm, $^1\pi\sigma^*_{O\text{-}H}$ mediated O-H dissociation is seen to dominate over $^1\pi\sigma^*_{O\text{-}CH_3}$ mediated O-CH_3 dissociation and a similar mechanism to that proposed for O-H dissociation in phenol at 200 nm is expected to be operative.

6.1 Introduction to Mequinol Studies

The ubiquitous presence of $^1\pi\sigma^*$ states in heteroaromatic molecules offers numerous systems for study, allowing one to vary the electronic properties of molecules and assess the contribution of $^1\pi\sigma^*$ states to the excited state dynamics of these system. [1, 2] Recently, a few experiments have been performed on heteroaromatic systems that contain two heteroatom containing coordinates which possess dissociative $^1\pi\sigma^*$ states, to observe if competition will occur between the two coordinates. The first of these by Wells *et al.* in adenine,[3] when exciting above the onset for dissociation along either the azole (N_9-H) and amino (NH_2) coordinates (see figure 1.1), found ultrafast processes compete on both coordinates. The results of this study proved pertinent as the N_9 atom forms the glycosidic bond to the backbone in DNA bound adenine. Elsewhere, work by Oliver *et al.* in 4-hydroxyindole and 5-hydroxyindole [4] has found that differing structural isomers with two dissociative coordinates showed preferential elimination from one coordinate over the other, with phenol-like or indole-like dynamics observed depending on the position of the hydroxyl functional group in hydroxyindole. It is with the above in mind that the experiments presented here focus on mequinol (*p*-methoxyphenol – molecular structure in figure 6.1 a)), which has the potential for displaying competing $^1\pi\sigma^*$ dynamics along O-H and O-CH_3 bond coordinates. The dynamics along each coordinate are examined experimentally through TR-VMI imaging, by probing the resultant hydrogen atom and CH_3 radical photoproducts. This work is complemented by high level equation-of-motion couple cluster with singles and doubles excitations (EOM-CCSD) and complete active space with second order perturbation theory (CASPT2) calculations performed by

collaborators,[5, 6] which, together with TR-VMI, enables detailed insight into any competition between these two dynamical pathways. Specifically, the work aims to merge together previous investigations into the photodissociation of phenol [7-11] and anisole (from chapter 4),[12, 13] where $^1\pi\sigma^*$ mediated bond fission has been observed to occur along their O-H and O-CH_3 coordinates, respectively.

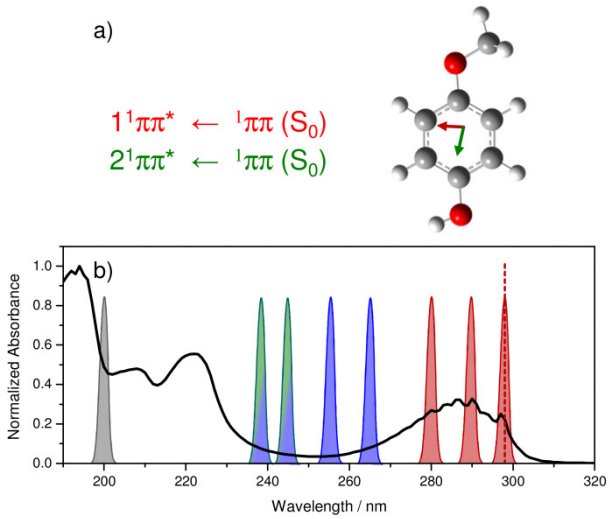

Figure 6.1 – a) Molecular structure of mequinol, overlaid with arrows representing the direction of the transition dipole moment for excitation to the $1^1\pi\pi^*$ (red) and $2^1\pi\pi^*$ (green) states calculated using EOM-CCSD.[6] b) Vapour phase UV absorption spectrum of mequinol, with the excitation wavelengths studied using TR-VMI highlighted (Gaussian distributions). These highlighted wavelengths are assigned to a $1^1\pi\pi^* \leftarrow {}^1\pi\pi$ transition (red), a $2^1\pi\pi^* \leftarrow {}^1\pi\pi$ transition (green), a transition to a higher lying state (grey) and a $^1\pi\sigma^*_{O\text{-}CH_3} \leftarrow {}^1\pi\pi$ transition (blue).

6.1.1 The Electronic Structure of Mequinol

Figure 6.1 b) presents a vapour phase ultraviolet (UV) absorption spectrum of mequinol over the range 190 – 320 nm and is qualitatively similar to the profile of the UV spectrum previously reported for phenol.[14] Interpretation of figure 6.1 b) is guided by the calculated vertical and optimised excitation energies from EOM-CCSD [6] and CASPT2(12/11) [5] calculations, respectively, summarised in table

6.1, which indicate the presence of two $^1\pi\pi^*$ states, $1^1\pi\pi^*$ (the π (HOMO) to π^* transition) to and $2^1\pi\pi^*$ (the π (HOMO-1) to π^* transition), at 4.53 and 5.91 eV, respectively (based upon the EOM-CCSD calculations). The calculations also indicate vertical transitions to two $^1\pi\sigma^*$ states localised along the O-H ($^1\pi\sigma^*_{O\text{-}H}$) and O-$CH_3$ ($^1\pi\sigma^*_{O\text{-}CH_3}$) bonds, respectively. However, the calculations suggest that the oscillator strengths (see table 6.1) to these $^1\pi\sigma^*$ states are one to two orders of magnitude less than that to the two $^1\pi\pi^*$ states and the experimentally observed increases in absorbance at ~298 and ~240 nm (~4.15 and ~5.15 eV) in the UV spectrum are therefore assigned to the onsets for absorption to the $1^1\pi\pi^*$ and $2^1\pi\pi^*$ states, respectively.

Table 6.1 – EOM-CCSD vertical energies (ΔE_{vert}) [6] and oscillator strengths (*f*) in addition to CASPT2(12/11) optimised energies (ΔE_{opt}) [5] for the singlet electronic state transitions in mequinol. Where available, experimentally determined values (Expt) are also provided from [a] reference [15] and [b] TR-VMI results.

Transition	EOM-CCSD/aug-cc-pVDZ		CASPT2(12/11)/aug-cc-pVTZ	Expt. / eV
	ΔE_{vert} / eV	f	ΔE_{opt} / eV	
$1^1\pi\pi^* \leftarrow S_0$	4.53	0.0480	4.29	4.17[a]
$^1\pi\sigma^*_{O\text{-}H} \leftarrow S_0$	5.09	0.0006	5.13	…
$^1\pi\sigma^*_{O\text{-}CH3} \leftarrow S_0$	5.43	0.0043	5.23	…
$2^1\pi\pi^* \leftarrow S_0$	5.91	0.0691	…	~5.05[b]

The weaker oscillator strengths for one-photon excitation to both the $^1\pi\sigma^*$ states is also supported by the minimal absorbance between ~260 to ~245 nm in figure 6.1 b),

correlating to a region where the Franck-Condon overlap for excitation to highly vibrationally excited levels of the $1^1\pi\pi^*$ state is poor and before the onset of the higher lying $2^1\pi\pi^*$ state.

Potential Energy Cuts

Potential energy cuts (PECs) through the first four singlet excited states in mequinol, calculated using CASPT2(12,11), with respect to the O-H ($R_{O\text{-}H}$) and O-CH_3 ($R_{O\text{-}CH_3}$) coordinates are shown in figure 6.2 a) and b), respectively.

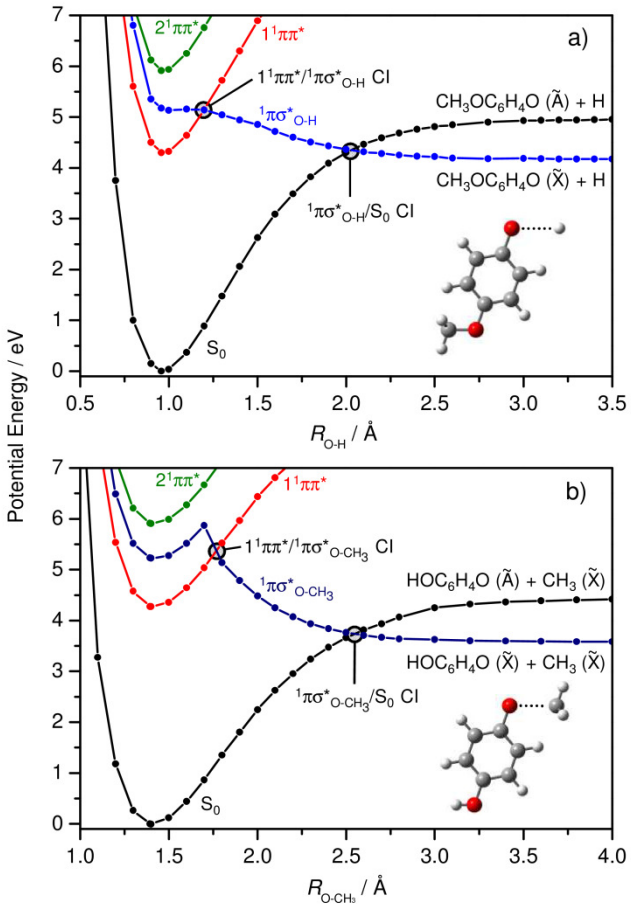

Figure 6.2 – PECs of the ground state and first four singlet excited states ($1^1\pi\pi^*$, $2^1\pi\pi^*$, $^1\pi\sigma^*_{O\text{-}H}$ and $^1\pi\sigma^*_{O\text{-}CH_3}$) in mequinol calculated at the CASPT2(12,11) level, with respect to a) O-H separation ($R_{O\text{-}H}$) and b) O-CH_3 separation ($R_{O\text{-}CH_3}$). Also labelled are the relevant CIs between states and the radical states that correspond to each asymptote.[5]

Qualitatively, the PECs along $R_{O\text{-}H}$ in mequinol resemble those previously calculated in phenol,[11, 16] showing a degeneracy between the bound $1^1\pi\pi^*$ and dissociative $^1\pi\sigma^*_{O\text{-}H}$ states ($1^1\pi\pi^*$ / $^1\pi\sigma^*_{O\text{-}H}$ CI) and between the $^1\pi\sigma^*_{O\text{-}H}$ and $^1\pi\pi$ states ($^1\pi\sigma^*_{O\text{-}H}$ / $^1\pi\pi$ CI). More generally, these match the relatively common characteristics of electronic state PECs along X-H bond coordinates in heteroaromatic molecules.[2] The computed PECs in figure 6.2 a) also show that following excitation to the origin of the $1^1\pi\pi^*$ state (below the $1^1\pi\pi^*$ / $^1\pi\sigma^*_{O\text{-}H}$ CI), population transfer onto the $^1\pi\sigma^*_{O\text{-}H}$ surface is hindered by an energetic barrier (~0.8 eV). Again, this is notionally similar to that previously computed in phenol,[16] with both molecules displaying similar calculated barrier heights. It has been demonstrated by Roberts *et al.*,[17] that dissociation in phenol proceeds by hydrogen tunnelling through this barrier. Due to the similarity of the mequinol PECs with those of phenol, hydrogen tunnelling below the $1^1\pi\pi^*$ / $^1\pi\sigma^*_{O\text{-}H}$ CI is expected.

The O-H bond dissociation energy, D_0(O-H), has been obtained by high Rydberg atom photofragment translation spectroscopy (HRA-PTS) which gives a value of D_0 = 28620 cm^{-1}.[18] This value of D_0(O-H) is lower than for the equivalent bond in phenol, which is to be expected as the electron-donating character of the *para* methoxy group will lead to the stabilisation of the electron deficient radical product.[19-21] From figure 6.2 a) it is also apparent that dissociation may occur to either the $\tilde{X}$ or $\tilde{A}$ state methoxyphenoxyl ($H_3COC_6H_4O$) radical, with the energy separation between these two states ($\Delta E(\tilde{A} \leftarrow \tilde{X})$) predicted to be ~6300 cm^{-1}.

The PECs along the O-CH_3 bond coordinate ($R_{O\text{-}CH_3}$) are shown in figure 6.2 b). Similar to the PECs along $R_{O\text{-}H}$, a degeneracy between the $1^1\pi\pi^*$ and $^1\pi\sigma^*_{O\text{-}CH_3}$

surfaces ($1^1\pi\pi^*$ / $^1\pi\sigma^*_{O\text{-}CH_3}$ CI) is found at an $R_{O\text{-}CH_3}$ close to the vertical Franck-Condon (vFC) region. This CI may provide a viable pathway for population to couple from an initially excited $1^1\pi\pi^*$ state onto the dissociative $^1\pi\sigma^*_{O\text{-}CH_3}$ state, enabling O-CH_3 bond fission. Furthermore, the PECs in figure 6.2 b) also display a degeneracy between the dissociative $^1\pi\sigma^*_{O\text{-}CH_3}$ state and $^1\pi\pi$ ($^1\pi\sigma^*_{O\text{-}CH_3}$ / $^1\pi\pi$ CI) at larger O-CH_3 separation. Interestingly, unlike the $^1\pi\sigma^*_{O\text{-}H}$ state, the $^1\pi\sigma^*_{O\text{-}CH_3}$ state shows a significant amount of bound character in the vFC region, resulting from a large mixing contribution from the oxygen centered 3s Rydberg orbital (on the O-CH_3 coordinate), which then evolves into σ* valence character at extended O-CH_3 distances. The calculated "quasi-bound" character of this surface in the vFC region suggests that the $^1\pi\sigma^*_{O\text{-}CH_3}$ state can support bound vibrational levels, as previously reported in aniline which exhibits a $^1\pi\sigma^*_{N\text{-}H}$ state with a similar "quasi-bound" profile.[22-26]

The D_0 for the O-CH_3 bond, D_0(O-CH_3), has previously been determined to be ~21800 cm^{-1}.[27] The difference between $\tilde{X}$ and $\tilde{A}$ state hydroxyphenoxyl (HOC_6H_4O) radical can also be approximated from figure 6.2 b), $\Delta E(\tilde{A} \leftarrow \tilde{X}) \approx$ 6900 cm^{-1}.

6.1.2 Aims and Procedure

The aim of this chapter is to understand the competition between two $^1\pi\sigma^*$ surfaces that are dissociative along two different bond coordinates in mequinol through the use of TR-VMI at a range of excitation wavelengths. It is anticipated that mequinol will display competing "phenol-like" dynamics along the O-H coordinate and "anisole-like" behaviour with respect to the O-CH_3 coordinate. By measuring the

timescale and total kinetic energy release (TKER) of dissociated hydrogen and CH_3 (and corresponding co-fragment) it should be possible to ascertain whether the radical products are formed via an ultrafast mechanism or slower (>10 ps) process, such as tunnelling or statistical unimolecular decay. TR-VMI allows one to isolate radicals formed by $^1\pi\sigma^*$ mediated processes and study their dynamics independently.

The experimental procedure is carried out as described in chapter 2. Pump wavelengths are provided by both the pump TOPAS-C (238 – 298 nm) and the series of β-barium borate (BBO) crystals (200 nm). Probing of radical products is carried out at 243.1 nm, for hydrogen by 2+1 resonance enhanced multiphoton ionisation (REMPI) via the 2s ← 1s transition, and 333.4 nm, for CH_3 by 2+1 REMPI via the $3p\ ^2A_2'' \leftarrow \tilde{X}\ ^2A_2''$ transition.[28]

The formation of a molecular beam of mequinol is described in section 2.2 and the specific conditions summarised in table 2.2. Previous studies have shown that mequinol exists as either a *cis* or *trans* conformer with respect to torsional motion around either the C-O-H or C-O-CH_3 moieties,[15] with minimal energy separation (~10 cm^{-1}) between conformers in the ground state.[29] Based upon the valve temperature and molecular beam temperature, mequinol is expected to freeze into nearly equal proportions of *cis* and *trans* conformers in the molecular beam. The difference between the $1^1\pi\pi^* \leftarrow {}^1\pi\pi$ transition energy in the two conformers is small (~100 cm^{-1} – determined by HR-PTS studies [18]) and an ensemble average of the dynamics of both conformers is expected when excitation occurs with a broad energy (~500 cm^{-1}) fs laser pulse.

6.2 Results of Mequinol Studies

6.2.1 Hydrogen Elimination upon Excitation at λ = 280 – 298 nm

Following photoexcitation to the lowest energy $1^1\pi\pi^*$ state, the general O-H dissociation dynamics of mequinol are summarised in figures 6.3 and 6.4 for excitation wavelengths of 298, 290 and 280 nm (shown as red Gaussians in figure 6.1). Velocity map images of REMPI-probed hydrogen elimination (H^+) at these wavelengths are shown inset in the respective panels in figure 6.3, for a pump probe delay (t) of 1200 ps; the top halves present the raw images while the lower halves show deconvoluted images. All three images are dominated by a single ring at large radii, which possesses an isotropic signal distribution with respect to the electric field polarisation of the pump laser ($\boldsymbol{\varepsilon}$), indicated by the white arrow. The isotropic nature of this single ring is attributed to dissociation that occurs on a slower timescale than the rotational dephasing of any molecular alignment.[30]

The corresponding TKER spectra derived from the H^+ velocity map images at 298, 290 and 280 nm (t = 1200 ps) are shown in figures 6.3 a) – c) (black lines), together with TKER spectra obtained from images at t = 1 ps (red lines). All three TKER spectra in figure 6.3 show a large H^+ signal with a Gaussian-like profile centred at 4000 – 5000 cm^{-1}, correlating to the isotropic ring at larger radii in the H^+ images. This Gaussian-like signal is also convoluted with a minor Boltzmann-like background signal. Such well-defined Gaussian H^+ signal profiles at high TKER are characteristic of $^1\pi\sigma^*$ mediated hydrogen elimination dynamics proceeding along the $R_{O\text{-}H}$ coordinate.[8, 9, 17] This Gaussian-like signal is absent from the TKER spectra

acquired at t = 1 ps, suggesting that the rise time (τ) for $^1\pi\sigma^*_{O\text{-}H}$ mediated hydrogen formation is longer than 1 ps.

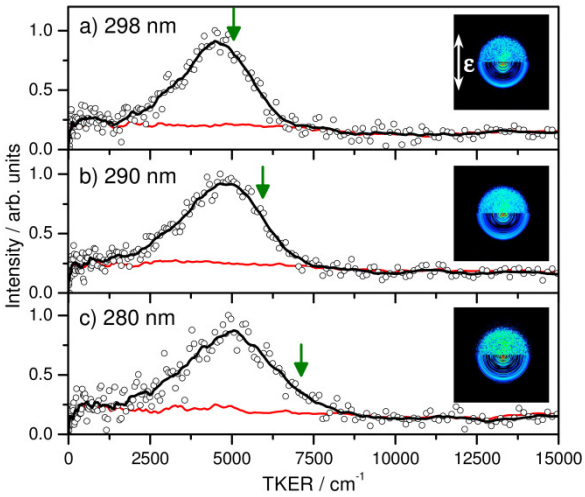

Figure 6.3 – TKER spectra (circles), overlaid with 10 point averages (black lines), and corresponding H^+ velocity map images (inset) recorded for hydrogen elimination from mequinol at pump wavelengths of a) 298, b) 290 and c) 280 nm with a 1200 ps delayed probe of 243.1 nm. Also included are 10 point averaged TKER spectra taken with a 1 ps delayed probe (red lines). Vertical green arrows represent the predicted $TKER_{max}$ derived from equation 6.1 (see text). The inset images consist of raw (top) and deconvoluted images (bottom) where the pump electric field polarisation, **ε**, is indicated by the white arrow.

Excitation at 298 nm corresponds to the $1^1\pi\pi^* \leftarrow {}^1\pi\pi$ origin transition, while 290 and 280 nm corresponds to a scenario where excess energy (as vibrational energy orthogonal to $R_{O\text{-}H}$) is imparted into the $1^1\pi\pi^*$ state. The corresponding increase in photon energy is observed in the blue-shifting of the maximum TKER ($TKER_{max}$) in the TKER spectra in figure 6.3 ($TKER_{max}$ is ~6200, ~6700 and ~7500 cm^{-1} at 298, 290 and 280 nm, respectively). However, minimal change in the centre (mean) TKER of the Gaussian feature at high TKER is observed, suggesting that coupling onto the $^1\pi\sigma^*_{O\text{-}H}$ state proceeds from a similar energy within the $1^1\pi\pi^*$ potential (defined with respect to O–H stretching motion) at all excitation

wavelengths in the range 298 – 280 nm. This mimics the dissociation behaviour observed previously in phenol by both Dixon *et al.*[11] and Roberts *et al.*[17] following excitation at energies above the $1^1\pi\pi^*$ state origin and below the $1^1\pi\pi^*$ / $^1\pi\sigma^*_{O\text{-}H}$ CI. As in that case, the observed energy disposal can be understood by recognising that hydrogen tunnels under the $1^1\pi\pi^*$ / $^1\pi\sigma^*_{O\text{-}H}$ CI at an energy close to that of the $1^1\pi\pi^*$ zero point energy (ZPE) level in the O-H stretch (see PECs in figure 6.2 a)), with any additional vibrational energy in the photo-prepared $1^1\pi\pi^*$ molecules mapping through into the $\tilde{X}$ state methoxyphenoxyl radical product.

The $TKER_{max}$ for dissociation at each wavelength can be predicted by equation 6.1:

$$TKER_{max} = h\nu - D_0(O\text{-}H) \qquad (6.1)$$

D_0(O-H) is experimentally determined to be 28620 cm^{-1} (from HR-PTS studies [18]) and $h\nu$ is the energy of the excitation photon. Based upon equation 6.1, the $TKER_{max}$ at 298, 290 and 280 nm is 5000, 5900 and 7100 cm^{-1}, respectively; these theoretical $TKER_{max}$ are represented by the green arrows in figure 6.3. It is clear from figure 6.3 that each TKER spectra extends beyond this theoretical maximum; this difference is accounted for by the large energy bandwidth of the fs lasers pulse employed and the low resolution of the spectrometer ($\Delta E/E \approx 15\%$ at this energy range). However, the green arrows determined from equation 6.1 do imply that dissociation is occurring to the hydrogen and $\tilde{X}$ state methoxyphenoxyl radical asymptote (blue asymptote in figure 6.2).

H^+ Transients at λ = 280 – 298 nm

Figure 6.4 a) – c) shows transients of H^+ signal from a series of hydrogen TKER spectra (at varying *t*) at 298, 290 and 280 nm, respectively, integrated in a 2000 cm^{-1} window around the peak of the Gaussian-like feature. The transients show a combination of dynamics occurring over different timescales, consisting of an ultrafast rise (<100 fs) around t = 0 ps and a slower signal increase (≥1200 ps), which corresponds to the appearance of the underlying Boltzmann-like and Gaussian distributions, respectively. From the spectra it is clear that the rise in the slowly increasing signal has not terminated by 1200 ps (the temporal limit of the setup) and kinetic fitting of the data is therefore not feasible.

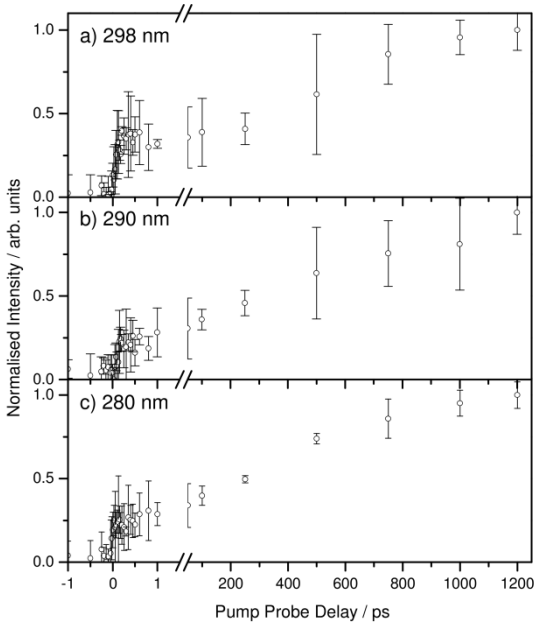

Figure 6.4 – H^+ signal transients in mequinol, taken at pump wavelengths of a) 298, b) 290 and c) 280 nm, with a probe of 243.1 nm. Transients are obtained by integrating the measured H^+ signal over the TKER range of 2000 cm^{-1} around the Gaussian-like feature peak at a series of pump probe delays (*t*). Error bars correspond to two standard deviations.

From comparison to similar spectra acquired in phenol by Roberts *et al.*,[17] when exciting below the $1^1\pi\pi^*$ / $^1\pi\sigma^*_{O\text{-}H}$ CI barrier, this suggests that an analogous mechanism is leading to $^1\pi\sigma^*_{O\text{-}H}$ mediated hydrogen elimination. The timescale for hydrogen elimination in phenol was attributed to hydrogen tunnelling from the $1^1\pi\pi^*$ state to the $^1\pi\sigma^*_{O\text{-}H}$ state, which can then subsequently dissociate to yield hydrogen and phenoxyl radicals. The similarity in the timescale and the unchanging mean TKER in figure 6.3 strongly imply that hydrogen elimination mediated by tunnelling is taking place in mequinol.

An estimation of the tunnelling lifetime in mequinol can be determined from the computed one dimensional PECs along $R_{O\text{-}H}$ using a semiclassical Brillouin-Kramers-Wentzel (BKW) calculation, a method that has previously been applied in phenol[17] and substituted phenols clustered with NH_3.[10] Using a set of PECs in mequinol, similar to those in figure 6.2 a), a lifetime can be obtained by using the BKW theory equation:

$$\tau = \left[\nu_{OH} \exp\left(-2\int_{u_1}^{u_2} \sqrt{\frac{2m}{\hbar^2}(V(u)-E)}\,du \right) \right]^{-1} \qquad (6.2)$$

In equation 6.2 u is the O-H bond coordinate, ν_{OH} is the O-H stretch frequency (3740 cm^{-1}), m is the mass of a hydrogen atom, $V(u)$ is the potential barrier (taken from the calculated PECs), and E is the kinetic energy of the hydrogen at the ZPE of the $1^1\pi\pi^*$ state O-H stretch ($½\nu_{OH}$). For mequinol this returns an estimated timescale for hydrogen tunnelling of 9.8 ns, which is on the order expected by inspection of the transients in figure 6.4. This is a reasonable estimate for the order of magnitude for hydrogen tunnelling, but is significantly longer than the timescale expected form

figure 6.4 which shows a significant signal by t = 1.2 ns. It should be noted that, equation 6.2 has limits that may account for the overestimation: (i) these calculations involve a 1-D approximation in the $R_{O\text{-}H}$ coordinate, whereas the experimental dynamics occur on a full multi-dimensional potential energy landscape. Additional degrees of freedom can reduce the effective barrier area and as such 1-D tunneling calculations provide an upper limit of the actual tunneling lifetime. (ii) The BKW calculations do not account for the fact that in mequinol's C_s symmetry group, population transfer between the $1^1\pi\pi^*$ and the $^1\pi\sigma^*_{O\text{-}H}$ states must be mediated by an out-of-plane vibration of a'' symmetry.

6.2.2 Hydrogen Elimination upon Excitation at λ = 254 and 264 nm

At shorter wavelengths (λ = 264 and 254 nm), still below the onset of the higher lying $2^1\pi\pi^*$ state (solid blue Gaussian features in figure 6.1 b)), no characteristic signatures for $^1\pi\sigma^*_{O\text{-}H}$ driven hydrogen elimination via either tunnelling, or by direct coupling through the $1^1\pi\pi^*$ / $^1\pi\sigma^*_{O\text{-}H}$ CI, are observed in the TR-VMI measurements. In fact, negligible probed hydrogen signal, at both high and low TKER (see figure 6.5), is observed in this wavelength region. The absence of any significant signal at all TKER is expected due to the poor cross-section for one-photon absorption at 264 and 254 nm (see figure 6.1 b)) than at longer wavelengths (λ = 298 – 280 nm) resulting in minimal population in the $1^1\pi\pi^*$ state. The reduction in absorbance to the $1^1\pi\pi^*$ state is likely due to significantly poorer Franck-Condon overlap between $^1\pi\pi$ and $1^1\pi\pi^*$ at shorter wavelengths. As demonstrated in table 6.1 the oscillator strength to the $^1\pi\sigma^*_{O\text{-}H}$ state is particularly low (two orders of magnitude less than the $1^1\pi\pi^*$ and $2^1\pi\pi^*$ states) ruling out direct excitation to this state.

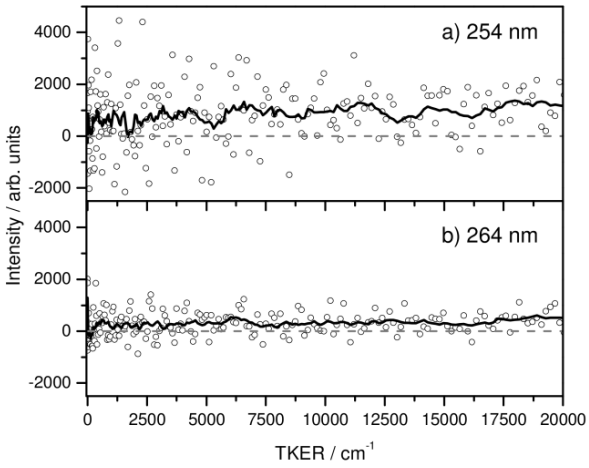

Figure 6.5 – TKER spectra for hydrogen elimination in mequinol (circles) at pump wavelengths of a) 254 and b) 264 nm, with a 1200 ps delayed 243.1 nm probe. Data is overlaid with a 10 point average (black line).

However, TR-VMI measurements of CH_3 elimination in mequinol (section 6.2.4), provide some evidence that one-photon excitation is occurring in this energy region. Specifically, population may be imparted into the "quasi-bound" well of the $^1\pi\sigma^*_{O\text{-}CH_3}$ state, the calculated oscillator strength for which is an order of magnitude larger than the $^1\pi\sigma^*_{O\text{-}H}$ state (see table 6.1). The non-observation of hydrogen at λ = 264 and 254 nm, particularly at low TKER, may therefore be rationalised by considering that the majority of excitation occurs to the $^1\pi\sigma^*_{O\text{-}CH_3}$ state at these wavelengths, thus localising electron density onto the O-CH_3 coordinate, away from the O-H bond (and ring C-H bonds), reducing the probability of hydrogen elimination through both $^1\pi\sigma^*$ mediated dissociation and multiphoton processes.

6.2.3 Hydrogen Elimination upon Excitation at λ = 200 – 245 nm

The resultant TKER distributions for hydrogen elimination at pump wavelengths of 245 and 238 nm are shown in figure 6.6 a) and b) (recorded at t = 10 ps), respectively, with the corresponding H^+ velocity map images inset.

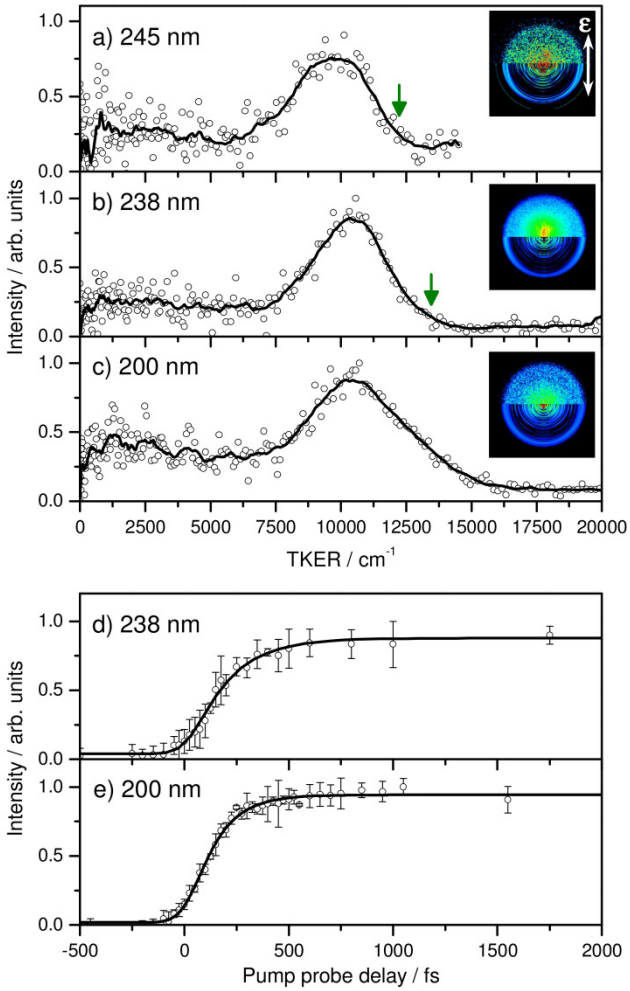

Figure 6.6 – TKER spectra for hydrogen elimination from mequinol (circles) at pump wavelengths of a) 245, b) 238 and c) 200 nm, with a 10 ps delayed probe of 243.1 nm. Spectra are overlaid with a 10 point average (black line). Corresponding images are shown inset and consist of raw (top) and deconvoluted images (bottom) with the pump electric field polarisation, **ε**, indicated by the white arrow. Vertical green arrows represent the predicted $TKER_{max}$ derived from equation 6.1 (see text). H^+ signal transients from the high TKER Gaussian feature are shown for d) 238 and e) 200 nm (circles), obtained by integrating signal over the TKER range 9500 - 11500 cm^{-1} for spectra recorded at a series of *t*. Error bars correspond to two standard deviations. Transients are fitted with an exponential rise function convoluted with the Gaussian IRF (black line).

Excitation at 245 and 238 nm corresponds to energies close to the second rising feature in the UV absorption spectrum (figure 6.1 b)). This, coupled with the poor absorption to the $^1\pi\sigma^*_{O\text{-}H}$ state observed at 254 and 264 nm, suggests that excitation at these wavelengths corresponds to a $2\,^1\pi\pi^* \leftarrow {}^1\pi\pi$ transition (shown as

green / blue Gaussian features in figure 6.1 b)). Similar to below the $1^1\pi\pi^*$ / $^1\pi\sigma^*_{O\text{-}H}$ CI ($\lambda \geq 280$ nm), both TKER spectra contain a broad Boltzmann-like distribution peaked at low TKER (~2500 cm^{-1}) and a Gaussian-like distribution centred at high TKER (~10500 cm^{-1}). From a comparison of figures 6.6 a) and b) to the TKER spectra from tunnelling mediated dissociation ($\lambda \geq 280$ nm – figure 6.3) it is evident that the mean TKER of the Gaussian-like feature is blue-shifted by ~5000 cm^{-1}. This implies that a tunnelling mechanism is no longer operative, which is also apparent from Gaussian-like signals present at only t = 10 ps. The corresponding $TKER_{max}$ for dissociation at each wavelength closely matches that predicted by equation 6.1 (green arrows in figure 6.6 a) and b)) suggesting that excitation at these wavelengths is leading to the formation of hydrogen and $\tilde{X}$ state methoxyphenoxyl radical products.

Inspection of the velocity map image anisotropy for the high TKER feature upon excitation at 245 nm (inset, figure 6.6 a)) suggests that hydrogen atoms are preferentially ejected perpendicular to $\boldsymbol{\varepsilon}$ with a measured value of $\beta_2 = -0.32$. This perpendicular anisotropy confirms that: (i) hydrogen elimination is occurring faster than the timescale for rotational dephasing;[30] and (ii) dissociation is occurring from the $2^1\pi\pi^*$ state as this, unlike the $1^1\pi\pi^*$ state, has a transition dipole moment (TDM) perpendicular to the O-H coordinate (see calculated TDMs in figure 6.1 a)). The overall mechanism for dissociation at 245 nm that yields the high TKER Gaussian-like feature in figure 6.6 a) is therefore population of the $2^1\pi\pi^*$ state, which then undergoes $^1\pi\sigma^*_{O\text{-}H}$ mediated dissociation through either a direct $2^1\pi\pi^*$ / $^1\pi\sigma_{O\text{-}H}$ CI coupling or a cascaded $2^1\pi\pi^* \rightarrow 1^1\pi\pi^* \rightarrow {}^1\pi\sigma^*_{O\text{-}H}$ pathway.

A similar conclusion can be drawn from the anisotropic image obtained following excitation at 238 nm (see inset figure 6.6 b)), where the hydrogen, once again, is preferentially formed perpendicular to $\boldsymbol{\varepsilon}$ where $\beta_2 = -0.35$. The same mechanism for $2^1\pi\pi^*$ to $^1\pi\sigma_{O\text{-}H}$ transfer is proposed for hydrogen elimination at both 245 and 238 nm. Furthermore, the increased H^+ signal levels at 238 nm, relative to those at 245 nm (see inset images figure 6.6 a) and b)), suggest that the cross-section for absorption to the $2^1\pi\pi^*$ state is increasing. This increase is likely the result of improved Franck-Condon factors for the $2^1\pi\pi^* \leftarrow {}^1\pi\pi$ transition at shorter wavelengths. This increasing cross-section is also apparent in figure 6.1 b) and appears to continue up to $\lambda \approx 220$ nm.

In addition to excitation at 245 and 238 nm, measurements have also been performed at 200 nm (figure 6.6 c)), yielding a similar high TKER Gaussian signal centred at ~10800 cm^{-1}. This Gaussian-like feature displays a noticeable asymmetry towards high TKER, on account of the large amount of excess energy imparted at 200 nm, which will be mapped through into a broad distribution of vibrational eigenstates in the methoxyphenoxyl radical co-fragment upon O-H dissociation. Despite the asymmetry of the Gaussian-like feature, the signal does not extend out to the predicted $TKER_{max}$ (using equation 6.1) which is at ~21400 cm^{-1} (not shown in figure 6.6 c)). The origin of this $^1\pi\sigma^*_{O\text{-}H}$ mediated hydrogen elimination upon excitation at 200 nm is unclear as the excited state initially accessed is undetermined due to the significantly increased density of electronic states at this energy. It seems likely, based upon the extra rising features in figure 6.1 b) around 200 nm, that excitation to a state other than $2^1\pi\pi^*$ is most likely (potentially an even higher lying $^1\pi\pi^*$ state). This inability to assign the initially excited state at 200 nm is

compounded by the minimal information that can be obtained from the hydrogen recoil distribution of the Gaussian-like TKER feature, which returns a value of $\beta_2 \approx 0$ and is apparent in the image inset in figure 6.6 c). Due to the pump probe delay at which figure 6.6 c) was acquired (t = 10 ps) it is unlikely that the isotropic distribution observed is caused by rotational dephasing.[30] In spite of the absence of information about the initially excited state, the high TKER feature in figure 6.6 c) confirms that coupling onto $^1\pi\sigma^*_{O\text{-}H}$ is operative following 200 nm excitation, whether it be via a series of CI couplings from the initially excited state or direct coupling through a single CI onto $^1\pi\sigma^*_{O\text{-}H}$.

H^+ Transients at λ = 238 and 200 nm

An H^+ signal transient of the high TKER Gaussian feature at 238 nm (integrated between 9500 – 11500 cm^{-1} at each t) is presented in figure 6.6 d), providing a measure of the timescale for $^1\pi\sigma^*_{O\text{-}H}$ mediated O-H bond dissociation following excitation to $2^1\pi\pi^*$. Unfortunately, a similar transient could not be obtained at 245 nm due to the reduced H^+ signal levels. A kinetic fit to this transient (black line) with an exponential rise function convoluted with our Gaussian IRF (FWHM ≈ 120 fs for a 238 / 243.1 nm pump / probe combination – see section 2.4.4) returns an ultrafast timescale for the appearance of high TKER hydrogen of τ = 181 ± 28 fs, correlating to the time taken for the overall $^1\pi\sigma^*_{O\text{-}H}$ promoted hydrogen elimination mechanism to occur, via either a $2^1\pi\pi^* \rightarrow 1^1\pi\pi^* \rightarrow {}^1\pi\sigma^*_{O\text{-}H}$ series of ICs or a direct $2^1\pi\pi^* \rightarrow {}^1\pi\sigma^*_{O\text{-}H}$ IC.

Figure 6.6 e) presents an analogous H^+ signal transient for the high TKER feature at 200 nm, which when fitted using the same kinetic model at 238 nm (but

with a longer Gaussian IRF of ~160 fs for the 200 / 243.1 nm pump / probe scheme – see section 2.4.4), provides a timescale of τ = 128 ± 16 fs, also confirming that the measured $\beta_2 \approx 0$ value of this feature in the H^+ velocity map image is not due rotational dephasing of the parent molecule.[30] In phenol, Iqbal *et al*.[9] have previously reported a timescale of ~90 fs for O-H bond fission along the $^1\pi\sigma^*_{O\text{-}H}$ state at 200 nm, which is marginally quicker than (but comparable to) the ultrafast timescale observed in mequinol.

The timescale from O-H dissociation along the $^1\pi\sigma^*_{O\text{-}H}$ at 200 nm is, however, marginally quicker than at 238 nm, which may be a direct result of the higher electronic state density at 200 nm, possibly offering an enhanced rate for CI couplings onto $^1\pi\sigma^*_{O\text{-}H}$.

6.2.4 CH_3 Elimination

The TKER spectra following CH_3 elimination in mequinol are summarised in figure 6.7 a) – f) across a pump wavelength range of 280 – 200 nm.

CH_3 Elimination at λ = 280 – 298 nm

Figure 6.7 a) displays a TKER spectrum for CH_3 elimination following excitation at 280 nm with a 333.4 nm probe (t = 1200 ps). This spectrum is representative of all TKER spectra recorded in the range of 298 ≥ λ ≥ 280 nm. As discussed above, excitation in this energy range corresponds to a region of the $1^1\pi\pi^*$ below the barrier to hydrogen dissociation formed by the $1^1\pi\pi^*$ / $^1\pi\sigma^*_{O\text{-}H}$ CI and a similar barrier is expected to be present along $R_{O\text{-}CH_3}$ (formed by the $1^1\pi\pi^*$ / $^1\pi\sigma^*_{O\text{-}CH_3}$ CI – see PECs in figure 6.2 b)).

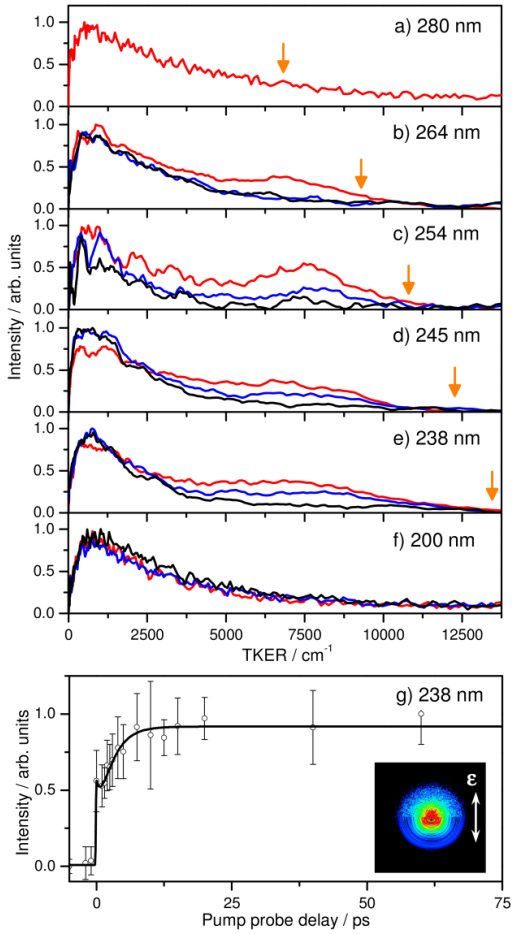

Figure 6.7 – TKER spectra obtained for CH_3 elimination from mequinol, taken at pump wavelengths of a) 280, b) 264, c) 254, d) 245, e) 238 and f) 200 nm, with a t = 1 (black), t = 10 (blue) and t = 1200 ps (red) delayed 333.3 nm probe. Spectra b) – e) show a 10 point average of the raw collected data (not shown). Vertical orange arrows in a) – e) indicate the predicted $TKER_{max}$ value determined from equation 6.3 (see text). g) CH_3^+ signal transient (circles) obtained by integrating in the TKER range 6000 - 8000 cm^{-1} taken with a 238 and 333.3 nm pump and probe arrangement. The black line in g) represents a kinetic fit to the data, while the inset CH_3^+ velocity map image was recorded at a 238 nm pump wavelength with t = 1200 ps. The pump electric field polarisation, **ε**, is shown by the white arrow.

While hydrogen tunnelling from $1^1\pi\pi^*$ to $^1\pi\sigma^*_{O\text{-}H}$ occurring over a nanosecond timeframe was observed, a similar mechanism for CH_3 is not expected and high TKER Gaussian signals for $O\text{-}CH_3$ dissociation via the $^1\pi\sigma^*_{O\text{-}CH_3}$ state is not observed in the range λ = 280 – 298 nm. Due to the 15-times greater mass of CH_3

relative to hydrogen, CH_3 tunnelling onto $^1\pi\sigma^*_{O\text{-}CH_3}$ from the $1^1\pi\pi^*$ state is not anticipated to be kinetically competitive to the hydrogen tunnelling process. Hence, the TKER spectrum for CH_3 elimination is exclusively composed of a broad Boltzmann distribution peaked at ~1000 cm^{-1}.

CH_3 Elimination at λ = 238 – 264 nm

Figures 6.7 b) and c) show TKER spectra for CH_3 elimination from mequinol following photoexcitation at 264 and 254 nm, respectively, at t = 1 (black), 10 (blue) and 1200 ps (red). In both cases, the t = 1200 ps TKER spectra contain a high TKER Gaussian-like feature, centred between 7000 – 7500 cm^{-1}, nested on top of a broad background Boltzmann signal. In a similar interpretation to the $^1\pi\sigma^*_{O\text{-}H}$ mediated hydrogen elimination, these high TKER Gaussian signals are attributed to O-CH_3 dissociation along the $^1\pi\sigma^*_{O\text{-}CH_3}$ state. Using equation 6.7 (with D_0(O-H) replaced by D_0(O-CH_3) (~21800 cm^{-1}) [27]) fails to model the observed $TKER_{max}$ at both 264 and 254 nm (predicting ~16100 and ~17600 cm^{-1}, respectively). This value far exceeds the observed $TKER_{max}$ of ~10000 and ~11500 cm^{-1} for the Gaussian feature in figures 6.7 b) and c), respectively.

A better estimate for the observed $TKER_{max}$ of the Gaussian-like signal can be attained by assuming that dissociation yields CH_3 and the $\tilde{A}$ state hydroxyphenoxyl radical photoproducts, where the difference in energy is calculated to be $\Delta E(\tilde{A} \leftarrow \tilde{X}) \approx 6900$ cm^{-1}. A $TKER_{max}$ for dissociation to CH_3 and the $\tilde{A}$ state hydroxyphenoxyl radical can be determined with equation 6.3:

$$TKER_{max} = h\nu - \left[D_0\left(O\text{-}CH_3\right) + \Delta E\left(\tilde{A} \leftarrow \tilde{X}\right) \right] \qquad (6.3)$$

Equation 6.3 predicts $TKER_{max}$ for dissociation at 264 and 254 nm of ~9300 and ~10800 cm^{-1}, respectively. These values for $TKER_{max}$ provide a much better estimate and are shown as orange arrows in figure 6.7. From the energies predicted by equation 6.7 it can be concluded that O-CH_3 dissociation is occurring by evolving adiabatically motion around the $^1\pi\sigma^*_{O\text{-}CH_3}$ / $^1\pi\pi$ CI leading to the formation of CH_3 and the $\tilde{A}$ state hydroxyphenoxyl radical. Similar adiabatic dissociation was observed previously in thioanisole (chapter 5) for $^1n\sigma^*$ mediated CH_3 elimination and was rationalised by suggesting that the $^1\pi\pi^*$ to $^1n\sigma^*$ coupling occurs at a nuclear geometry that is far from that required for non-adiabatic passage through the $^1n\sigma^*$ / $^1\pi\pi$ CI. Alternatively, the absence of non-adiabatic dynamics may be accounted for by the geometric phase effect,[31] where the dissociating flux enters the $^1\pi\sigma^*$ / $^1\pi\pi$ CI, bifurcates and then destructively interferes (due to a difference in phase) such that the flux exiting this CI resides primarily on the adiabatic pathway leading to $\tilde{A}$ state hydroxyphenoxyl photoproducts.

As excitation at 264 and 254 nm is known to lie below the onset for excitation to the $2^1\pi\pi^*$ state, O-CH_3 dissociation at these wavelengths is rationalised by one of two mechanisms. The first mechanism requires population of a set of high vibrational eigenstates in the $1^1\pi\pi^*$ state, which can couple through the $1^1\pi\pi^*$ / $^1\pi\sigma^*_{O\text{-}CH_3}$ CI leading to dissociation. This mechanism seems unlikely as the low Franck-Condon factors for excitation to $1^1\pi\pi^*$ at 264 and 254 nm was apparent from the absence of any hydrogen signal at these wavelengths. A more likely mechanism is via direct excitation to the "quasi-bound" well of $^1\pi\sigma^*_{O\text{-}CH_3}$ state in the vFC region. The population will then take time to escape the "quasi-bound" well and dissociate.

Figure 6.7 b) reveals that no signature for O-CH_3 fission along $^1\pi\sigma^*_{O\text{-}CH_3}$ is present at 1 and 10 ps (black and blue lines, respectively), but is clearly visible by 1200 ps (red line). Based on this limited temporal information, this would imply that transfer from the "quasi-bound" well onto the dissociative region of the $^1\pi\sigma^*_{O\text{-}CH_3}$ state takes a significant amount of time, occurring on a timeframe of hundreds to thousands of picoseconds. By 254 nm (figure 6.7 c)), some signal associated with $^1\pi\sigma^*_{O\text{-}CH_3}$ based dynamics is observed at 10 ps, but increases in intensity by 1200 ps, suggesting that the rate of transfer has increased due to excitation closer to the top of the "quasi-bound" well. For completeness it is noted that the velocity map images at these wavelengths shows an isotropic ring ($\beta_2 \approx 0$), preventing determination of the state initially accessed and suggesting that rotational dephasing may be occuring.[30]

Excitation at shorter wavelengths of 245 nm and 238 nm results in TKER spectra with similar profiles to those at 264 and 254 nm, shown in figure 6.7 d) and e), respectively. The high TKER Gaussian feature centred around ~7500 cm^{-1} in both spectra is attributed to dissociation to CH_3 and the $\tilde{A}$ state hydroxyphenoxyl radical products along the $^1\pi\sigma^*_{O\text{-}CH_3}$ state as the observed $TKER_{max}$ for this channel matches that predicted by equation 6.3 (vertical orange arrows). Similarly, these features possess an isotropic recoil distribution (as shown by the inset image in figure 6.7 g) at 238 nm), making it difficult to determine the exact mechanism for their formation. As excitation to the $2^1\pi\pi^*$ state is known to occur at 245 and 238 nm (figure 6.1 b) and section 6.2.3), population may initially be imparted to the $2^1\pi\pi^*$ state leading to subsequent coupling onto $^1\pi\sigma^*_{O\text{-}CH_3}$ through appropriate CIs. However, similar to the mechanism observed at 264 and 254 nm, direct excitation to the $^1\pi\sigma^*_{O\text{-}CH_3}$ state may

also play a role at these shorter wavelengths. From the TKER spectra in figure 6.7 d) and e) it can be tentatively suggested that the timescale for the formation of the high TKER Gaussian-like feature is shorter than at 264 and 254 nm, in keeping with the trend observed in these two longer wavelengths.

CH_3^+ Transients at 238 nm

At 238 nm the signal levels were sufficient that a CH_3^+ signal transient could be obtained for the high TKER Gaussian feature. This is generated by integrating the signal in this feature (6000 – 8000 cm^{-1}) at a series of *t* and is presented in figure 6.7 g). Fitting this signal transient to the sum of an exponential rise and an exponential decay function (accounting for contributions from the underlying Boltzmann-like feature) convoluted with the Gaussian IRF (solid black line), returns an appearance timescale of τ = 2.5 ± 1.3 ps for CH_3 and the $\tilde{A}$ state hydroxyphenoxyl radical products formed via the $^1\pi\sigma^*_{O\text{-}CH_3}$ surface at 238 nm.

Surprisingly the timescale for high TKER CH_3 dissociation is an order of magnitude longer than that observed for high TKER hydrogen dissociation at the same wavelength. Assuming that high TKER hydrogen and CH_3 radical signals observed at these wavelengths are both the result of initial excitation to $2^1\pi\pi^*$, implies that the timeframes for coupling from the $2^1\pi\pi^*$ state onto the two different $^1\pi\sigma^*$ states, through appropriate CIs, are both ultrafast and kinetically competitive. The substantial difference in the overall O-CH_3 and O-H dissociation timescales may be attributed to the significantly different topographies of the $^1\pi\sigma^*_{O\text{-}CH_3}$ and $^1\pi\sigma^*_{O\text{-}H}$ potentials, as population feeding into the "quasi-bound" region of the $^1\pi\sigma^*_{O\text{-}CH_3}$ state

will be highly impeded by the apparent barrier to O-CH_3 bond dissociation, whereas the $^1\pi\sigma^*_{O-H}$ surface is expected to dissociate in a purely "ballistic" fashion.

CH_3 Elimination at 200 nm

The results of studying CH_3 radical elimination at 200 nm in mequinol are shown in figure 6.7 f). Unlike longer wavelengths, photoexcitation at 200 nm fails to yield any distinguishable signature for CH_3 radicals eliminated along the $^1\pi\sigma^*_{O-CH_3}$ state. This is unlike the dynamics previously observed in anisole (chapter 4) at 200 nm, where a distinct signature for $^1\pi\sigma^*_{O-CH_3}$ mediated O-CH_3 cleavage is taking place within ~90 fs.[13] *Para*-hydroxy substitution of anisole would therefore appear to deactivate any possibility of coupling onto the $^1\pi\sigma^*_{O-CH_3}$ state following 200 nm excitation, leaving ultrafast coupling onto the $^1\pi\sigma^*_{O-H}$ state to dominate in mequinol and exhibit "phenol-like" dynamics.

6.2.5 Low TKER Hydrogen and CH_3 Elimination

Briefly it is noted that at all wavelengths studied and when probing both hydrogen and CH_3 (except when studying hydrogen at 264 and 254 nm) a significant H^+ or CH_3^+ signal is observed at low TKER. By detuning the probe laser pulse away from the corresponding REMPI transitions (243.1 nm for hydrogen and 333.4 nm for CH_3) the low TKER signal was found to be multicomponent in nature. The low TKER Boltzmann feature is therefore assigned to multiphoton absorption of the parent mequinol molecule and subsequent dissociation yielding both neutral and cationic hydrogen and CH_3. This resembles the low TKER features observed in previous chapters and in other studies.[32] However, no rise in the low TKER hydrogen and CH_3 elimination signal was observed at longer pump probe delays (t >

100 ps) ruling out contribution from statistical unimolecular decay processes which were observed in anisole (chapter 4) and azole-based molecules.[33]

6.3 Conclusions

The results of this TR-VMI study on $^1\pi\sigma^*$ mediated dissociation pathways in mequinol, reveals competing dynamics along the $^1\pi\sigma^*_{O\text{-}H}$ and $^1\pi\sigma^*_{O\text{-}CH_3}$ surfaces and a strong excitation wavelength dependence upon the propensity for either O-H or O-CH_3 bond dissociation, respectively. Specifically, the findings highlight that at excitation wavelengths below the $1^1\pi\pi^*$ / $^1\pi\sigma^*_{O\text{-}H}$ CI ($\lambda \geq 280$ nm), dynamics are dominated by hydrogen tunnelling under the $1^1\pi\pi^*$ / $^1\pi\sigma^*_{O\text{-}H}$ CI from the initially populated $1^1\pi\pi^*$ state onto $^1\pi\sigma^*_{O\text{-}H}$ on a timescale >1.2 ns. The kinetic dominance of this hydrogen tunnelling channel subsequently results in an absence of CH_3 tunnelling onto the $^1\pi\sigma^*_{O\text{-}CH_3}$ state and therefore no $^1\pi\sigma^*_{O\text{-}CH_3}$ mediated O-CH_3 dissociation is observed at $\lambda = 280 – 298$ nm.

At wavelengths between 264 – 254 nm a switch in the dominance of hydrogen and CH_3 elimination channels occurs, relative to longer wavelengths. Hydrogen elimination is absent in this excitation region, whereas CH_3 elimination via the $^1\pi\sigma^*_{O\text{-}CH_3}$ surface is a significant feature of the TR-VMI experiments. Such an observation is rationalised by recognising that direct excitation into the “quasi-bound” oxygen 3s Rydberg well of the $^1\pi\sigma^*_{O\text{-}CH_3}$ state occurs at these wavelengths. This localises excited state electron density onto the methoxy group, causing $^1\pi\sigma^*_{O\text{-}CH_3}$ driven CH_3 elimination to dominate over alternative hydrogen elimination pathways.

As a result of the large oscillator strength for the higher lying $2^1\pi\pi^* \leftarrow {}^1\pi\pi$ transition, excitation to the $2^1\pi\pi^*$ state begins to dominate at even shorter wavelengths (λ = 245 and 238 nm). Here, dynamics involving both the ${}^1\pi\sigma^*_{O\text{-}H}$ and ${}^1\pi\sigma^*_{O\text{-}CH_3}$ surfaces are observed, leading to both ultrafast hydrogen elimination (181 ± 28 fs) and CH_3 elimination on a timeframe an order of magnitude slower (2.5 ± 1.3 ps). The significant differences in these dissociation timescales are attributed to the very different topographies of the ${}^1\pi\sigma^*_{O\text{-}H}$ and ${}^1\pi\sigma^*_{O\text{-}CH_3}$ surfaces, the strong "quasi-bound" character of the ${}^1\pi\sigma^*_{O\text{-}CH_3}$ state in the vFC region slows dissociation. These dynamics are initially mediated by IC from the $2^1\pi\pi^*$ state onto the respective ${}^1\pi\sigma^*$ states via appropriate CIs. Given the significant differences in the overall dissociation timescales recorded for O-H and O-CH_3 bond dissociation, this suggests that the initial coupling processes from the $2^1\pi\pi^*$ state to either the ${}^1\pi\sigma^*_{O\text{-}H}$ or ${}^1\pi\sigma^*_{O\text{-}CH_3}$ state must be kinetically competitive for both hydrogen and CH_3 elimination channels to be active at these excitation wavelengths. However, exciting higher lying singlet states, at 200 nm, shows a return to the dominance of ${}^1\pi\sigma^*_{O\text{-}H}$ mediated hydrogen elimination, taking place in 128 ± 16 fs, while, in contrast, O-CH_3 dissociation along the ${}^1\pi\sigma^*_{O\text{-}CH_3}$ state is inactive.

6.4 References

[1] A. L. Sobolewski and W. Domcke, *Chem. Phys. Lett.*, **310**, 548 (1999).

[2] M. N. R. Ashfold, G. A. King, D. Murdock, M. G. D. Nix, T. A. A. Oliver and A. G. Sage, *Phys. Chem. Chem. Phys.*, **12**, 1218 (2010).

[3] K. L. Wells, D. J. Hadden, M. G. D. Nix and V. G. Stavros, *J. Phys. Chem. Lett.*, **1**, 993 (2010).

[4] T. A. A. Oliver, G. A. King and M. N. R. Ashfold, *Phys. Chem. Chem. Phys.*, **13**, 14646 (2011).

[5] These and further calculations discussed in this chapter were performed by Mr T. N. V. Karsili and Prof. M. N. R. Ashfold at the University of Bristol and are published in: *Phys. Chem. Chem. Phys.*, **14**, 13415 (2012)

[6] These and further calculations discussed in this chapter were performed by Dr G. M. Roberts at the University of Warwick, Ms L. T. Bergendahl and Prof. M. J. Paterson at Heriot-Watt University. These results are publish in: *Phys. Chem. Chem. Phys.*, **14**, 13415 (2012)

[7] C. M. Tseng, Y. T. Lee, M. F. Lin, C. K. Ni, S. Y. Liu, Y. P. Lee, Z. F. Xu and M. C. Lin, *J. Phys. Chem. A*, **111**, 9463 (2007).

[8] A. Iqbal, L. J. Pegg and V. G. Stavros, *J. Phys. Chem. A*, **112**, 9531 (2008).

[9] A. Iqbal, M. S. Y. Cheung, M. G. D. Nix and V. G. Stavros, *J. Phys. Chem. A*, **113**, 8157 (2009).

[10] G. A. Pino, A. N. Oldani, E. Marceca, M. Fujii, S. I. Ishiuchi, M. Miyazaki, M. Broquier, C. Dedonder and C. Jouvet, *J. Chem. Phys.*, **133**, 124313 (2010).

[11] R. N. Dixon, T. A. A. Oliver and M. N. R. Ashfold, *J. Chem. Phys.*, **134**, 194303 (2011).

[12] C. M. Tseng, Y. T. Lee and C. K. Ni, *J. Phys. Chem. A*, **113**, 3881 (2009).

[13] D. J. Hadden, C. A. Williams, G. M. Roberts and V. G. Stavros, *Phys. Chem. Chem. Phys.*, **13**, 4494 (2011).

[14] T. Etzkorn, B. Klotz, S. Sorensen, I. V. Patroescu, I. Barnes, K. H. Becker and U. Platt, *Atmos. Environ.*, **33**, 525 (1999).

[15] G. N. Patwari, S. Doraiswamy and S. Wategaonkar, *J. Phys. Chem. A*, **104**, 8466 (2000).

[16] O. P. J. Vieuxmaire, Z. Lan, A. L. Sobolewski and W. Domcke, *J. Chem. Phys.*, **129** (2008).

[17] G. M. Roberts, A. S. Chatterley, J. D. Young and V. G. Stavros, *J. Phys. Chem. Lett.*, **3**, 348 (2012).

[18] D. J. Hadden, G. M. Roberts, T. N. V. Karsili, M. N. R. Ashfold and V. G. Stavros, *Phys. Chem. Chem. Phys.*, **14**, 13415 (2012).

[19] A. L. Devine, M. G. D. Nix, B. Cronin and M. N. R. Ashfold, *Phys. Chem. Chem. Phys.*, **9**, 3749 (2007).

[20] G. A. King, A. L. Devine, M. G. D. Nix, D. E. Kelly and M. N. R. Ashfold, *Phys. Chem. Chem. Phys.*, **10**, 6417 (2008).

[21] C.-M. Tseng, Y. T. Lee, C.-K. Ni and J.-L. Chang, *J. Phys. Chem. A*, **111**, 6674 (2007).

[22] T. Ebata, C. Minejima and N. Mikami, *J. Phys. Chem. A*, **106**, 11070 (2002).

[23] G. A. King, T. A. A. Oliver and M. N. R. Ashfold, *J. Chem. Phys.*, **132**, 214307 (2010).

[24] G. M. Roberts, C. A. Williams, J. D. Young, S. Ullrich, M. J. Paterson and V. G. Stavros, *J. Am. Chem. Soc.*, **134**, 12578 (2012).

[25] R. Spesyvtsev, O. M. Kirkby, M. Vacher and H. H. Fielding, *Phys. Chem. Chem. Phys.*, **14**, 9942 (2012).

[26] R. Spesyvtsev, O. M. Kirkby and H. H. Fielding, *Faraday Discuss.*, **157**, 165 (2012).

[27] M. M. Suryan, S. A. Kafafi and S. E. Stein, *J. Am. Chem. Soc.*, **111**, 1423 (1989).

[28] J. W. Hudgens, T. G. Digiuseppe and M. C. Lin, *J. Chem. Phys.*, **79**, 571 (1983).

[29] Based upon B3LYP/6-311+G(d,p) level calculations

[30] R. N. Zare, *Angular Momentum: Understanding Spatial Aspects in Chemistry and Physics*, Wiley-Blackwell, 1988.

[31] W. Domcke, D. R. Yarkony and H. Köppel, *Conical Intersections: Theory, Computation and Experiments*, World Scientific Publishing Co. Pte. Ltd., 2011.

[32] C. A. Williams, G. M. Roberts, H. Yu, N. L. Evans, S. Ullrich and V. G. Stavros, *J. Phys. Chem. A*, **116**, 2600 (2011).

[33] G. M. Roberts, C. A. Williams, M. J. Paterson, S. Ullrich and V. G. Stavros, *Chem. Sci.*, **3**, 1192 (2012).

7. Concluding Remarks

7.1 Summary of Thesis

The work in this thesis has aimed to expand on previous research into the role of $^1\pi\sigma^*$ and $^1n\sigma^*$ states in the photochemistry of heteroaromatic molecules. These excited electronic states exist in a myriad of molecular systems and actively participate in excited state relaxation pathways, which may contribute to the photostability of deoxyribonucleic acid (DNA) bases and amino acids. Initially these studies looked at $^1\pi\sigma^*$ mediated dynamics in imidazole (localised on the N-H coordinate), which serves as a model for the five-membered ring of adenine, specifically the N_9-H coordinate. Recent studies identifying $^1\pi\sigma^*$ mediated dynamics along non-hydride coordinates led to the investigation of methylated counterparts, specifically the investigation of anisole and thioanisole whose hydride analogues, phenol and thiophenol, have been the subject of a number of previous studies. Finally the competition between two dissociative coordinates (O-H and O-CH_3) in mequinol, each possessing a $^1\pi\sigma^*$ state, was investigated to determine whether the $^1\pi\sigma^*$ state localised along the hydride or non-hydride coordinate would drive the excited state photochemistry.

The introduction of this thesis provided a background to the photophysical and photochemical processes that can occur in molecules and how the implementation of ultrafast time resolved spectroscopy can be used to track the evolution of molecules following photoexcitation.[1] Chapter 1 also outlined the relevance of these studies to understanding the dissipation of undesirable energy in excited biological molecules.[2] In particular, the implication that excited state

population in a potentially reactive excited state could undergo fast relaxation mediated by a $^1\pi\sigma^*$ state prompted the experiments undertaken in this thesis. By obtaining a complete understanding of the interplay between potential energy surfaces (PESs) in sub-units of biomolecules and their analogues, it may be possible to understand how biological systems, such as DNA strands and proteins, deal with harmful UV radiation.

An outline of the time resolved velocity map imaging (TR-VMI) setup utilised was presented in chapter 2. This included a summary of how the pump and probe laser pulses and the molecular beam were generated, as well as the principles of velocity map imaging (VMI).[3] The TR-VMI setup allows for the study of small molecules, independent of intermolecular interactions, at a range of ultraviolet (UV) excitation wavelengths. This enables measurements of the timescales for characteristic $^1\pi\sigma^*$ mediated bond dissociation, generating radical products with a characteristic kinetic energy, from which it is possible to infer information about the rate of coupling onto the $^1\pi\sigma^*$ state from the initially photoexcited state.

TR-VMI was applied to study the hydrogen elimination process, upon excitation at 200 nm, in imidazole and methylated derivatives. These results, presented in chapter 3, showed that ultrafast N-H dissociation in imidazole, occurring in 78 ± 37 fs, was attributed to internal conversion (IC) from the initially excited $^1\pi\pi^*$ state to the $^1\pi\sigma^*$ state leading to N-H dissociation. Based on theoretical calculations, it was previously speculated that IC occurred via a conical intersection (CI) between the $^1\pi\pi^*$ and $^1\pi\sigma^*$ states found along a ring distortion coordinate.[4] Upon methylation of the imidazole ring, N-H dissociation was still observed

however, the rate of IC decreased and the timescale for $^1\pi\sigma^*$ mediated dissociation increased, taking approximately 130 – 190 fs. The increasing timescale for hydrogen elimination, upon methylation of imidazole, was attributed to either: (i) the heavier methyl groups impeding the motion along the ring distortion coordinates which allows access to the appropriate $^1\pi\pi^*$ / $^1\pi\sigma^*$ CI; or (ii) the increased density of vibrational eigenstates in the $^1\pi\pi^*$ state leading to a greater sampling of modes orthogonal to the required ring distortion coordinates.[5]

The dynamics of O-CH_3 dissociation in anisole, following photoexcitation at 200 nm, was investigated in chapter 4. This work formed the first time resolved study of $^1\pi\sigma^*$ mediated CH_3 elimination in such heteroaromatic molecules, which complemented previous studies at 248 and 193 nm that were performed using the multimass imaging technique.[6] TR-VMI showed that O-CH_3 dissociation in anisole is dominated by signal at low TKER. This signal was attributed to: (i) multiphoton absorption of the anisole parent species, to yield an ultrafast CH_3 signal (<50 fs rise and 85 ± 15 fs decay); and (ii) statistical unimolecular decay at much longer timescales (>20 ps). A small CH_3 signal at high TKER was also observed, attributed to $^1\pi\sigma^*$ mediated O-CH_3 dissociation. A timescale of 91 ± 36 fs was measured for this process.[7]

Chapter 5 presented TR-VMI studies investigating S-CH_3 dissociation in thioanisole at a range of wavelengths (289.8 – 275 nm) and allowed comparison of these fs studies to related ns VMI studies. This work showed that $^1n\sigma^*$ mediated CH_3 elimination was possible when exciting below the apparent barrier to dissociation, formed by a $^1\pi\pi^*$ / $^1n\sigma^*$ CI, at 289.8 nm. Complementary calculations suggested that

this barrier is significantly reduced by wavepacket motion in the C-C-S-CH_3 torsional coordinate (ϕ) to a region where the $^1\pi\pi^*$ / $^1n\sigma^*$ degeneracy, which exists as a "quasi-seam of intersection" with respect to ϕ, is lower in energy. Motion to this region of the $^1\pi\pi^*$ PES where IC occurs induces a rearrangement away from the nuclear geometry required to access the $^1n\sigma^*$ / $^1\pi\pi$ CI at extended S-CH_3, reducing the amount of ground state radical product formed, an interpretation supported by fs and ns experimental results. The timescale for dissociation was found to be dependent on the rate of intramolecular vibrational energy redistribution (IVR) into the required torsional motion, typically taking 10 – 1000 ps. The rate of IVR was found to increase with excess vibrational energy in the $^1\pi\pi^*$ state in line with the increasing density of vibrational eigenstates, which fits a Fermi's golden rule model.[8] Corresponding ns VMI studies showed vibrational eigenstate specific dynamics when exciting the ν_{7a} mode (the S-CH_3 stretching motion), leading to a notable change in the branching of the thiophenoxyl radical product's electronic state. This mode specific "dynamic resonance" was not observed in fs studies, as excitation with a broad spectral bandwidth fs pulse leads to population of a range of vibrational eigenstates.[9]

Finally, $^1\pi\sigma^*$ mediated hydrogen and CH_3 elimination was examined in mequinol upon excitation at a variety of wavelengths, corresponding to excitation to either the $1^1\pi\pi^*$, $2^1\pi\pi^*$ or $^1\pi\sigma^*_{O\text{-}CH_3}$ state. TR-VMI results showed that tunnelling from the $1^1\pi\pi^*$ state (280 – 298 nm) lead to the preferential $^1\pi\sigma^*_{O\text{-}H}$ mediated hydrogen elimination, the dynamics of which are similar to that previously observed in phenol.[10] At higher excitation energies, once Franck-Condon overlap for $1^1\pi\pi^* \leftarrow {}^1\pi\pi$ transition was significantly reduced, direct population of a "quasi-bound" well

in the $^1\pi\sigma^*_{O\text{-}CH_3}$ state was observed (254 – 264 nm). This leads to the exclusive formation of $^1\pi\sigma^*_{O\text{-}CH_3}$ mediated CH_3 once population has escaped the "quasi-bound" well. Exciting to the $2^1\pi\pi^*$ state at shorter wavelengths (238 – 245 nm) resulted in ultrafast coupling onto both $^1\pi\sigma^*$ states, although differing timescales for hydrogen and CH_3 production were observed and attributed to the different topographies of the $^1\pi\sigma^*_{O\text{-}H}$ and $^1\pi\sigma^*_{O\text{-}CH_3}$ states, as supported by complementary theoretical calculations. The dominance of O-H dissociation was then seen to return upon excitation at 200 nm, showing similar dynamics to hydrogen elimination at the same wavelength in phenol.[11, 12] No O-CH_3 fission via the $^1\pi\sigma^*_{O\text{-}CH_3}$ state was observed at 200 nm.

7.2 Outlook

The work in this thesis has demonstrated the versatility of $^1\pi\sigma^*$ and $^1n\sigma^*$ states as a pathway for bond dissociation and potentially excited state relaxation in a range of biomolecules. However, the molecules focused on in this work have been sub-units or models of biological molecules. The role of $^1\pi\sigma^*$ mediated dynamics, compared to other photorelaxation pathways, in large biological systems is still unclear. Hopefully, advances in techniques for introducing larger molecules into the gas phase (i.e. laser desorption techniques [13, 14] or electrospray ionisation [15]) will allow one to study more complex structures, extending this "bottom-up" approach to more relevant, realistic systems. The comparison of gas phase studies to liquid phase studies, where important solvent effects are introduced, is also essential for understanding how these biological systems behave in nature. Comparative studies performed on molecules in both the gas and liquid phase have shown

similarities in the dynamics. However, studies of this ilk are few and more advances are required before a general understanding can be achieved.

The investigation of molecular photodissociation dynamics has now become a major area of physical chemistry however there is still a lot that is not yet understood about the role of $^1\pi\sigma^*$ and $^1n\sigma^*$ states in the general photochemistry of molecules. The role of CI as mediators for photophysical processes that can populated these states has long been understood, however the aspects of a molecule's PES that influence the efficiency of the adiabatic vs non-adiabatic processes at such CI are still unclear and further studies will, hopefully, provide more details about the nature of these couplings. Greater understanding of the factors affecting mechanisms for populating these states could be achieved through more investigations of substituted phenol molecules, expanding on the work in chapter 6 and previous studies by Ashfold and co-workers,[16-19] with a particular focus on the rate of $^1\pi\pi^* \rightarrow {}^1\pi\sigma^*$ tunnelling.

The later chapters of this thesis concentrated on some of the more unusual phenomena of $^1\pi\sigma^*$ and $^1n\sigma^*$ mediated dynamics which have not been extensively studied. These unusual effects, such as "quasi-seams of intersection" and excitation to "quasi-bound" wells, will play an important role in determining the quantum yield of $^1\pi\sigma^*$ mediated dynamics, relative to other pathways, such as CI mediated dynamics and tunnelling, in the photochemistry of a molecular system. Future studies of less investigated molecular systems, such as aniline and substituted thiophenols,[20, 21] will hopefully strive to develop a more complete picture of when these more exotic mechanisms occur and how they contribute to the general role played by $^1\pi\sigma^*$ and $^1n\sigma^*$ in molecular photochemistry and photophysics.

7.3 References

[1] A. H. Zewail, *Angew. Chem. Int. Ed.*, **39**, 2587 (2000).

[2] C. T. Middleton, K. de La Harpe, C. Su, Y. K. Law, C. E. Crespo-Hernandez and B. Kohler, *Annu. Rev. Phys. Chem.*, **60**, 217 (2009).

[3] A. T. J. B. Eppink and D. H. Parker, *Rev. Sci. Instrum.*, **68**, 3477 (1997).

[4] M. Barbatti, H. Lischka, S. Salzmann and C. M. Marian, *J. Chem. Phys.*, **130**, 034305 (2009).

[5] D. J. Hadden, K. L. Wells, G. M. Roberts, L. T. Bergendahl, M. J. Paterson and V. G. Stavros, *Phys. Chem. Chem. Phys.*, **13**, 10342 (2011).

[6] C. M. Tseng, Y. T. Lee and C. K. Ni, *J. Phys. Chem. A*, **113**, 3881 (2009).

[7] D. J. Hadden, C. A. Williams, G. M. Roberts and V. G. Stavros, *Phys. Chem. Chem. Phys.*, **13**, 4494 (2011).

[8] P. A. M. Dirac, *Proc. R. Soc. Lond. A*, **114**, 243 (1927).

[9] G. M. Roberts, D. J. Hadden, L. T. Bergendahl, A. M. Wenge, S. J. Harris, T. N. V. Karsili, M. N. R. Ashfold, M. J. Paterson and V. G. Stavros, *Chem. Sci.*, **4** (2013) 993.

[10] G. M. Roberts, A. S. Chatterley, J. D. Young and V. G. Stavros, *J. Phys. Chem. Lett.*, **3**, 348 (2012).

[11] A. Iqbal, M. S. Y. Cheung, M. G. D. Nix and V. G. Stavros, *J. Phys. Chem. A*, **113**, 8157 (2009).

[12] D. J. Hadden, G. M. Roberts, T. N. V. Karsili, M. N. R. Ashfold and V. G. Stavros, *Phys. Chem. Chem. Phys.*, **14**, 13415 (2012).

[13] K. Tanaka, *Angew. Chem. Int. Ed.*, **42**, 3860 (2003).

[14] V. V. Golovlev, S. L. Allman, W. R. Garrett, N. I. Taranenko and C. H. Chen, *Int. J. Mass Spectrom.*, **169**, 69 (1997).

[15] J. B. Fenn, *Angew. Chem. Int. Ed.*, **42**, 3871 (2003).

[16] A. L. Devine, M. G. D. Nix, B. Cronin and M. N. R. Ashfold, *Phys. Chem. Chem. Phys.*, **9**, 3749 (2007).

[17] G. A. King, A. L. Devine, M. G. D. Nix, D. E. Kelly and M. N. R. Ashfold, *Phys. Chem. Chem. Phys.*, **10**, 6417 (2008).

[18] M. N. R. Ashfold, G. A. King, D. Murdock, M. G. D. Nix, T. A. A. Oliver and A. G. Sage, *Phys. Chem. Chem. Phys.*, **12**, 1218 (2010).

[19] G. A. King, T. A. A. Oliver, R. N. Dixon and M. N. R. Ashfold, *Phys. Chem. Chem. Phys.*, **14**, 3338 (2012).

[20] T. A. A. Oliver, G. A. King, D. P. Tew, R. N. Dixon and M. N. R. Ashfold, *J. Phys. Chem. A*, **116**, 12444 (2012).

[21] G. M. Roberts, C. A. Williams, J. D. Young, S. Ullrich, M. J. Paterson and V. G. Stavros, *J. Am. Chem. Soc.*, **134**, 12578 (2012).

Appendix I

Total Kinetic Energy Release Fitting Functions

The fitting of total kinetic energy release (TKER) spectra uses a combination of functions to fit the low energy statistical feature and high energy symmetric or asymmetric features. These functions are listed below and are a Boltzmann distribution, a Gaussian distribution and a Gumbel distribution, respectively.

The Boltzmann distribution has the form:

$$F(x) = Y_0 + \frac{A\sqrt{x}}{\exp(x/W)} \tag{1}$$

where Y_0 is the baseline offset, A is the functions magnitude and W is the distribution width.

The Gaussian distribution has the form:

$$F(x) = Y_0 + A\exp\left(-\frac{(x-z)^2}{2\sigma^2}\right) \tag{2}$$

where Y_0 is the baseline offset, A is the functions magnitude, z is the peak centre of the function and σ is the variance.

The Gumbel distribution has the form:

$$F(x) = Y_0 + A\exp\left(-\frac{(-x+z)}{\sigma}\right)\exp\left[-\exp\left(-(-x+z)/\sigma\right)\right] \tag{3}$$

where Y_0 is the baseline offset, A is the functions magnitude, z is the peak centre of the function and σ is the variance.

Transient Signal Fitting Functions

The fitting of time resolved ion yield and velocity map imaging transients requires the use of a series of fitting functions; in particular a Gaussian distribution, an instrument response function (IRF) convoluted exponential decay and an IRF convoluted exponential rise. The mathematical functions for these distributions are below:

The Gaussian distribution in terms of pump probe delay (t) has the form:

$$F(t) = Y_0 + A\exp\left(-\frac{2.77(t-z)^2}{FWHM^2}\right) \tag{4}$$

where Y_0 is the baseline offset, A is the functions magnitude, z is the offset from time zero and $FWHM$ is the full width at half maximum of the distribution. N.B. this function differs from that used for TKER spectra which is based upon the variance.

The IRF convoluted exponential decay has the form:

$$F(t) = Y_0 + A\left[G(t) * \exp\left(-\frac{(t-z)}{\tau_d}\right)\right] \tag{5}$$

The IRF convoluted exponential rise has the form

$$F(t) = Y_0 + A\left[G(t) * \left(1-\exp\left(-\frac{(t-z)}{\tau_r}\right)\right)\right] \tag{6}$$

In equations 4 and 5, Y_0 is the baseline offset, A is the functions magnitude, z is the offset from time zero, τ_d is the decay lifetime, τ_r is the rise time and $G(t)$ is the convoluted Gaussian, from equation 4, that models the IRF.